



**UNIVERSIDADE ESTADUAL DE CAMPINAS**  
Faculdade de Engenharia Mecânica

**RODRIGO LIMA PEREIRA**

**Otimização Topológica Acústica Multidomínio e  
Multimaterial Baseada em uma Abordagem Evolucionária**

**Multimaterial and Multidomain Acoustic Topology  
Optimization Based on an Evolutionary Approach**

Campinas

2023

**RODRIGO LIMA PEREIRA**

**Multimaterial and Multidomain Acoustic Topology  
Optimization Based on an Evolutionary Approach**

**Otimização Topológica Acústica Multidomínio e  
Multimaterial Baseada em uma Abordagem Evolucionária**

Tese de Doutorado apresentada à Faculdade de Engenharia Mecânica da Universidade Estadual de Campinas como parte dos requisitos exigidos para a obtenção do título de Doutor em Engenharia Mecânica, na Área de Mecânica dos Sólidos e Projeto Mecânico

Doctoral Thesis presented to the School of Mechanical Engineering of the University of Campinas in partial fulfillment of the requirements for the degree of Doctor in Mechanical Engineering, in the Area of Solid Mechanics and Mechanical Design.

Orientador: Prof. Dr. Renato Pavanello

ESTE TRABALHO CORRESPONDE À VERSÃO FINAL DA TESE DE DOUTORADO DEFENDIDA PELO ALUNO RODRIGO LIMA PEREIRA, E ORIENTADA PELO PROF. DR. RENATO PAVANELLO.

Campinas

2023

Ficha catalográfica  
Universidade Estadual de Campinas  
Biblioteca da Área de Engenharia e Arquitetura  
Rose Meire da Silva - CRB 8/5974

P414m Pereira, Rodrigo Lima, 1992-  
Multimaterial and multidomain acoustic topology optimization based on an evolutionary approach / Rodrigo Lima Pereira. – Campinas, SP : [s.n.], 2023.

Orientador: Renato Pavanello.  
Tese (doutorado) – Universidade Estadual de Campinas, Faculdade de Engenharia Mecânica.

1. Otimização topológica. 2. Materiais porosos. 3. Simulação multifísica. 4. Vibração. 5. Acustica. I. Pavanello, Renato, 1959-. II. Universidade Estadual de Campinas. Faculdade de Engenharia Mecânica. III. Título.

#### Informações Complementares

**Título em outro idioma:** Otimização topológica acústica multidomínio e multimaterial baseada em uma abordagem evolucionária

**Palavras-chave em inglês:**

Topology optimization

Porous materials

Multiphysics simulations

Vibrations

Acoustics

**Área de concentração:** Mecânica dos Sólidos e Projeto Mecânico

**Titulação:** Doutor em Engenharia Mecânica

**Banca examinadora:**

Renato Pavanello [Orientador]

José Maria Campos dos Santos

Alberto Luiz Serpa

Marcelo Areias Trindade

Olavo Mecias da Silva Júnior

**Data de defesa:** 10-03-2023

**Programa de Pós-Graduação:** Engenharia Mecânica

**Identificação e informações acadêmicas do(a) aluno(a)**

- ORCID do autor: <https://orcid.org/0000-0002-0442-4666>

- Currículo Lattes do autor: <https://lattes.cnpq.br/8648415987292827>

**UNIVERSIDADE ESTADUAL DE CAMPINAS  
FACULDADE DE ENGENHARIA MECÂNICA**

**TESE DE DOUTORADO**

**Multimaterial and Multidomain Acoustic Topology  
Optimization Based on an Evolutionary Approach**

**Otimização Topológica Acústica Multidomínio e  
Multimaterial Baseada em uma Abordagem Evolucionária**

Autor: Rodrigo Lima Pereira

Orientador: Prof. Dr. Renato Pavanello

A Banca Examinadora composta pelos membros abaixo aprovou esta Tese de Doutorado:

**Prof. Dr. Renato Pavanello, Presidente**  
**DMC/FEM/UNICAMP**

**Prof. Dr. Marcelo Areias Trindade**  
**SEM/EESC/USP**

**Prof. Dr. Olavo Mecias da Silva Junior**  
**LVA/EMC/UFSC**

**Prof. Dr. Alberto Luiz Serpa**  
**DMC/FEM/UNICAMP**

**Prof. Dr. José Maria Campos dos Santos**  
**DMC/FEM/UNICAMP**

A Ata de Defesa com as respectivas assinaturas dos membros encontra-se no SIGA/Sistema de Fluxo de Dissertação/Tese e na Secretaria do Programa da Unidade.

Campinas, 10 de Março de 2023

## **DEDICATÓRIA**

Aos meus queridos pais, Edvaldo e Magna, e ao meu grande amor, Juliana.

## AGRADECIMENTOS

Aos meus pais, Edvaldo e Magna, e família, Edvaldo Júnior, Lígia, Adriana, Alexandre, Jacqueline, Bruna e Raimunda. Agradeço por sempre estarem presentes ao longo de minha formação como cidadão.

À minha noiva, Juliana, e família, Joaquim, Consolação, Gabriel, Regina e Hugo, pela atenção, carinho e cuidado.

Ao querido professor Renato Pavanello, pelo compromisso e amizade. Um verdadeiro exemplo a ser seguido.

Ao amigo Heitor N. Lopes pela parceria acadêmica de sucesso e pela amizade construída ao longo desses anos.

Aos amigos e colegas do Laboratório de Otimização Topológica e Análises Multifísicas, em especial à Marcela, Breno, Daniel, Gisele, Valter, Rafael, Rodrigo, Márcio e Luiz. Sou grato pelo companheirismo, momentos de descontração e ensinamentos nas mais diversas áreas.

Agradeço também aos demais colegas e amigos que de alguma forma me ajudaram a concluir mais essa etapa da vida, bem como aos orientadores da Graduação, Roberto de Araújo Bezerra (UFC), e Mestrado, Jorge Luiz de Almeida Ferreira (UnB), por me iniciarem na carreira acadêmica.

À Faculdade de Engenharia Mecânica da UNICAMP pelo apoio e oportunidade, bem como à Coordenação de Aperfeiçoamento de Pessoal de Nível Superior Brasil (CAPES) pelo financiamento (código 001).

*“Eu sou de uma terra que o povo padece  
Mas nunca esmorece, procura vencê,  
Da terra adorada, que a bela caboca  
De riso na boca zomba no sofrê.  
Não nego meu sangue, não nego meu nome,  
Olho para fome e pergunto: o que há?  
Eu sou brasileiro fio do Nordeste,  
Sou cabra da peste, sou do Ceará.”*

*—Patativa do Assaré, Sou cabra da peste*

## RESUMO

PEREIRA, Rodrigo Lima. Otimização Topológica Acústica Multidomínio e Multimaterial Baseada em uma Abordagem Evolucionária. 2023. Tese (Doutorado). Faculdade de Engenharia Mecânica, Universidade Estadual de Campinas, Campinas, Brasil.

O projeto de estruturas para atenuação sonora é um ramo relevante da engenharia, sendo de fundamental importância para a promoção do bem-estar das pessoas, principalmente após a industrialização. Em grande parte das aplicações, cavidades internas a paredes de edifícios, aviões, automóveis ou trens, por exemplo, são totalmente preenchidas com materiais porosos, visando o aumento da dissipação de energia sonora no interior dos poros. No entanto, essa abordagem nem sempre é a solução mais eficaz, já que a maioria desses meios atenua o som principalmente em altas frequências. Ademais, o desenvolvimento de algoritmos de otimização topológica vem recebendo muita atenção nos setores acadêmico e industrial, uma vez que a grande parte das estruturas otimizadas são altamente eficazes, apresentando *design* contra-intuitivo e arquitetura instigante. A reestruturação completa do domínio de projeto inicial ao longo da maximização ou minimização de alguma função específica, respeitando restrições, é um dos aspectos mais interessantes de tais abordagens. Com base nisso, este trabalho detalha uma nova metodologia de otimização topológica acústica com aplicações no projeto de sistemas de isolamento sonora compostos por materiais rígidos, pororígidos (ou fluido equivalente), elásticos e poroelásticos. Várias extensões para a abordagem *Bi-directional Evolutionary Structural Optimization* (BESO) são propostas, a fim de levar em conta as particularidades das composições elasto-poroelasto-acústicas e rígido-pororígido-acústicas aqui investigadas. A metodologia proposta utiliza o método dos elementos finitos em todos os procedimentos numéricos, enquanto considera novos esquemas de interpolação material nas otimizações bifásicas e multifásicas. Neste último cenário, as equações de Helmholtz e de Biot são consideradas, dependendo da aplicação. Funções objetivo como nível de pressão sonora, coeficiente de absorção, perda de transmissão e potências dissipadas são aqui tratadas, respectivamente, no projeto de metassuperfícies rígido-acústicas, sistemas poro-acústicos, silenciadores multi-câmaras e sistemas fechados de atenuação sonora. Vários exemplos bidimensionais são apresentados e amplamente discutidos.

**Palavras-chave:** Otimização topológica, BESO, Material poroso, Sistemas Multifísicos, Vibroacústica

## ABSTRACT

PEREIRA, Rodrigo Lima. Multimaterial and Multidomain Acoustic Topology Optimization Based on an Evolutionary Approach. 2023. Thesis (Ph.D.). School of Mechanical Engineering, University of Campinas, Campinas, Brazil.

The design of structures for sound attenuation is a relevant engineering branch, as it is of fundamental importance for the promotion of people's well-being, especially after industrialization. In the majority of applications, cavities inside walls of buildings, airplanes, automobiles or trains, for example, are fully filled with porous materials, aiming at the increase of sound energy dissipation inside the pores. However, this approach may not always be the most effective solution, as much of these medium attenuate sound mainly at high frequencies. In addition to this, the development of topology optimization algorithms has been receiving a lot of attention in the academic and industrial sectors, since many designs are highly effective, counter-intuitive and architecturally exciting. The complete restructuring of the initial design domain to maximize or minimize some specific function, while respecting constraints, is one of the mainly interesting aspects of these approaches. On that basis, this work details a new acoustic topology optimization methodology with applications on the design of soundproof systems composed of rigid, pororigid (or equivalent fluid), elastic and poroelastic materials. Several extensions to the Bi-directional Evolutionary Structural Optimization (BESO) approach are proposed, in order to account for the particularities of the elastic-poroelastic-acoustic and rigid-pororigid-acoustic investigated compositions. The proposed methodology uses the Finite Element Method (FEM) along all numerical procedures, while establishes new material interpolation schemes in the biphasic and multiphase optimizations. In the later, Helmholtz and Biot's expressions are considered, depending on the application. Objective functions such as Sound Pressure Level (SPL), absorption coefficient, Transmission Loss (TL) and Dissipated Power Levels ( $PL_D$ ) are here treated in the design of acoustic-rigid metasurfaces, poro-acoustic systems, multi-chamber mufflers and closed-space structures for sound attenuation, respectively. Several bidimensional examples are presented and thoroughly discussed.

**Keywords:** Topology optimization, BESO, Porous materials, Multiphysics Systems, Vibroacoustics

## LIST OF FIGURES

Figure 1.1 – The three optimization types, (a) size, (b) shape and (c) topology ( <a href="#">Bendsøe; Sigmund, 2004</a> ) . . . . .	24
Figure 1.2 – Basic example of a 0 – 1 topology ( <a href="#">Maute et al., 1999</a> ) . . . . .	26
Figure 3.1 – $r_{\min}$ subdomain created in the $i$ th element . . . . .	49
Figure 3.2 – Flowchart of the BESO method . . . . .	52
Figure 7.1 – Mesh configuration of Problem 1 – Application 1 . . . . .	125
Figure 7.2 – Mesh configuration of Problem 2 – Application 1 . . . . .	125
Figure 7.3 – Mesh configuration of Application 2 . . . . .	126
Figure 7.4 – Mesh configuration of Application 3 . . . . .	126

## LIST OF TABLES

Table A.1 – Indication of variable changes: papers to thesis . . . . .	140
--	-----

## **LIST OF ABBREVIATIONS AND ACRONYMS**

BESO	Bi-directional Evolutionary Structural Optimization
ESO	Evolutionary Structural Optimization
FEM	Finite Element Method
mdBESO	Multidomain BESO
$PL_D$	Dissipated Power Level
SIMP	Solid Isotropic Material with Penalization
SPL	Sound Pressure Level
TL	Transmission Loss
UMP	Unified Multiphase
VTM	Virtual Temperature Method

# LIST OF SYMBOLS

## *Latin Letters*

$\bar{a}$	Imposed acceleration
AR	Addition Ratio
AR <sub>max</sub>	Maximum Addition Ratio
$\tilde{A}$	First Lamé constant of the poroelastic material
$\hat{A}$	First Lamé constant of the structural phase.
$A_{n=1}^{N_{el}}$	Assembly operator related with the entire domain
$A_{n=1}^{N_{bc}}$	Assembly operator related with the considered boundary
$\tilde{b}$	Viscous damping coefficient
$c_a$	Speed of sound in air
$C$	Mean Compliance
$\tilde{C}_{p1}$	Global coupling matrix of poroelastic materials – Part 1
$\tilde{C}_{p2}$	Global coupling matrix of poroelastic materials – Part 2
$D_a$	Global damping matrix of the acoustic domain
$e^{(\cdot)}$	Exponential function
$err$	Stop criterion variable
ER	Evolutionary Rate
$E_e$	Young's modulus of the elastic material
$E_p$	Young's modulus of the poroelastic material
$E_e$	Elasticity matrix related to $\Omega_e$
$E_p$	Elasticity matrix related to $\Omega_p$
$\hat{\mathbf{f}}$	Global load vector (multiphysics related)
$\hat{\mathbf{f}}$	Global load vector of the structure

$\hat{\mathbf{f}}_a$	Global load vector of the acoustic domain
$\mathbf{f}_e$	Imposed boundary load vector
$\hat{\mathbf{f}}_e$	Global load vector of the elastic domain
$\hat{\mathbf{f}}_f$	Global load vector of the fluid phase of poroelastic materials
$\hat{\mathbf{f}}_s$	Global load vector of the structural phase of poroelastic materials
$g$	Inequality constraint function
$h$	Equality constraint function
$\mathbf{H}_a$	Global kinetic energy matrix of the acoustic domain
$\tilde{\mathbf{H}}_p$	Global kinetic energy matrix of the poroelastic domain
$I$	List of nodes that are inside the $r_{\min}$ subdomain
$\mathbf{I}$	Identity tensor
$j$	Imaginary unit
$k_a$	Air wavenumber
$K_b$	Bulk modulus of the frame at constant air pressure
$\tilde{K}_f$	Bulk modulus of the fluid in the pores
$K_s$	Bulk modulus of the elastic material from which the structural skeleton is made
$\mathbf{K}$	Global stiffness matrix of the structure
$\mathbf{K}_e$	Global stiffness matrix of the elastic domain
$\tilde{\mathbf{K}}_p$	Global stiffness matrix of the poroelastic domain
$\mathbf{L}_{ae}$	Global acoustic-elastic coupling matrix
$\mathbf{L}_{ap}$	Global acoustic-poroelastic coupling matrix
$M$	Amount of elements connect to the $n_d$ th node
$\mathbf{M}_e$	Global mass matrix of the elastic domain
$\tilde{\mathbf{M}}_p$	Global mass matrix of the poroelastic domain

$n_g$	Number of inequality constraints
$n_h$	Number of equality constraints
$n_x$	Number of design variables
$\mathbf{n}_a$	Outward unit normal vector to the acoustic domain
$\mathbf{n}_e$	Outward unit normal vector to the elastic domain
$\mathbf{n}_p$	Outward unit normal vector to the poroelastic domain
$N$	Number of iterations considered in the historical average
$\tilde{N}$	Shear modulus of the poroelastic material (and shear modulus of the structural skeleton)
$N_{el}$	Total number of elements in the domain
$N_{elD}$	Total number of elements in the design domain
$N_{bc}$	Total number of elements in the considered boundary
$\mathbf{N}_a$	Acoustic (or fluid) shape function matrix
$\mathbf{N}_e$	Elastic (or structural) shape function matrix
$p_a$	Pressure field in the acoustic domain
$p_f$	Pressure field in the fluid phase of poroelastic materials
$\bar{p}$	Imposed pressure
$\hat{\mathbf{p}}_a$	Global pressure vector of the acoustic domain
$\hat{\mathbf{p}}_f$	Global pressure vector of the fluid phase of poroelastic materials
$\tilde{Q}$	Coupling coefficient that account for volumetric changes in the structural phase
$\mathbf{Q}_a$	Global compression matrix of the acoustic domain
$\tilde{\mathbf{Q}}_p$	Global compression matrix of the poroelastic domain
$r_{in}$	Distance from the centroid of the $i$ th element to the $n_d$ th node
$r_{min}$	Mesh independent filter radius
$\tilde{R}$	Coupling coefficient that account for volumetric changes in the fluid phase

$t$	Time
$\bar{\mathbf{u}}$	Imposed displacement
$\hat{\mathbf{u}}$	Global displacement vector of the structure
$\mathbf{u}_e$	Displacement field in the elastic domain
$\hat{\mathbf{u}}_e$	Global displacement vector of the elastic domain
$\hat{\mathbf{u}}_s$	Global displacement vector of the structural phase of poroelastic materials
$\mathbf{u}_s$	Displacement field in the structural phase of poroelastic materials
$\mathbf{U}_f$	Displacement field in the fluid phase of poroelastic materials
$\bar{v}$	Imposed velocity
$V$	Volume fraction
$V^*$	Final volume fraction
$w_i$	Weight factor regarding the $i$ th element
$w(r_{\text{in}})$	Linear weight factor
$x_i$	Elemental design variable
$x_{\text{min}}$	Lower bound of $x_i$
$\mathbf{x}$	Vector of design variables
$\mathbf{x}^l$	Lower bound of $\mathbf{x}$
$\mathbf{x}^u$	Upper bound of $\mathbf{x}$
$Z_0$	Air characteristic impedance
$\mathbf{Z}$	Global dynamic matrix of the acoustic domain
$\tilde{\mathbf{Z}}$	Global dynamic matrix (multiphysics related)

### ***Greek Letters***

$\tilde{\alpha}$	Dynamic tortuosity
$\alpha_\infty$	Tortuosity
$\alpha_i$	Elemental sensitivity number

$\alpha_{\max}$	Maximum sensitivity number
$\alpha_{\min}$	Minimum sensitivity number
$\alpha_{n,d}$	$n$ d th node sensitivity number
$\alpha_{\text{th}}$	Threshold sensitivity number
$\gamma_0$	Specific heat ratio
$\tilde{\gamma}$	Coupling coefficient of the poroelastic phases
$\Gamma_1$ to $\Gamma_5$	Boundaries of $\Omega_a$
$\Gamma_{\text{ae}}$	Common acoustic-elastic boundary
$\Gamma_{\text{ap}}$	Common acoustic-poroelastic boundary
$\Gamma_{\text{ea}}$	Common elastic-acoustic boundary
$\Gamma_{\text{ep}}$	Common elastic-poroelastic boundary
$\Gamma_{\text{pp}}$	Common poroelastic-poroelastic boundary
$\Gamma_{e1}, \Gamma_{e2}$	Boundaries of $\Omega_e$
$\Gamma_p$	Outer boundaries of $\Omega_p$
$\delta(\cdot)$	Test function variable
$\underline{\epsilon}_e$	Elastic strain tensor
$\underline{\epsilon}^s$	Structural phase strain tensor
$\zeta$	Penalty coefficient
$\eta_0$	Dynamic viscosity of the interstitial fluid
$\eta_e$	Structural loss factor of the elastic material
$\eta_p$	Structural loss factor of the poroelastic material
$\hat{\theta}$	Global solution vector
$\kappa_a$	Bulk modulus of air
$\Lambda$	Viscous characteristic length
$\Lambda'$	Thermal characteristic length

$\nu_e$	Poisson's ratio of the elastic material
$\nu_p$	Poisson's ratio of the poroelastic material
$\tilde{\xi}$	Newly introduced coupling coefficient
$\rho$	Mass density
$\tilde{\rho}$	Major effective density
$\rho_{11}$	Homogenized density: inertial damping in the structural phase
$\tilde{\rho}_{11}$	Minor effective density: inertial and viscous damping in the structural phase
$\rho_{12}$	Homogenized density: inertial damping in both phases
$\tilde{\rho}_{12}$	Minor effective density: inertial and viscous damping in both phases
$\rho_{22}$	Homogenized density: inertial damping in the fluid phase
$\tilde{\rho}_{22}$	Minor effective density: inertial and viscous damping in the fluid phase
$\rho_a$	Air density
$\rho_e$	Elastic material density
$\rho_f$	Fluid phase density
$\rho_s$	Structural phase density
$\sigma$	Static flow resistivity
$\underline{\sigma}_e$	Elastic Stress tensor
$\hat{\underline{\sigma}}^s$	Stress tensor of the poroelastic material in vacuo
$\underline{\sigma}^t$	Total stress tensor of the poroelastic material
$\tau$	Tolerance
$\phi$	Porosity
$\Phi$	Objective function
$\omega$	Angular frequency
$\Omega_a$	Acoustic domain
$\Omega_d$	Design domain

$\Omega_e$	Elastic domain
$\Omega_{nd}$	Non-design domain
$\Omega_p$	Poroelastic domain

***Subscripts and Superscripts***

$(\cdot)_a$	Acoustic (or air) properties
$(\cdot)_r$ or $(\cdot)^{(r)}$	Iteration counter
$(\cdot)_e$	Elastic properties
$(\cdot)_f$	Fluid phase properties of poroelastic materials
$(\cdot)_i$ or $(\cdot)^i$	$i$ th finite element related variable
$(\cdot)_p$	Poroelastic properties
$(\cdot)_s$	Structural phase properties of poroelastic materials

# CONTENTS

<b>1</b>	<b>Introduction</b>	<b>22</b>
1.1	Structural Optimization	23
1.1.1	Types of Structural Optimization	24
1.1.2	Structural Topology Optimization	25
1.2	Goals and Contributions	27
1.3	Thesis Organization	29
<b>2</b>	<b>Vibroacoustic Systems Governing Equations</b>	<b>30</b>
2.1	Helmholtz-based Media Formulation	31
2.2	Poroelastic Media Formulation	33
2.3	General Fluid-Structure Interactions: Governing Equations	39
2.3.1	Coupled Acoustic-Poroelastic-Elastic Boundary Conditions	40
2.3.1.1	Poroelastic-Elastic	41
2.3.1.2	Poroelastic-Acoustic	42
2.3.1.3	Poroelastic-Poroelastic	43
2.3.2	Coupled Acoustic-Poroelastic-Elastic Equilibrium Equations	43
<b>3</b>	<b>Bi-directional Evolutionary Structural Optimization Method</b>	<b>45</b>
3.1	Topology Optimization Problem: Structural Compliance Minimization	46
3.2	Sensitivity Analysis	47
3.3	Mesh-Independent Filter Scheme	48
3.4	Sensitivity Stabilization Procedure and Normalization	49
3.5	Heuristic Design Update and Stop Criterion	50
3.6	BESO Algorithm	51
3.7	Acoustic Topology Optimization Based on the BESO Approach	52
<b>4</b>	<b>A Multiconstrained Evolutionary Approach</b>	<b>54</b>
<b>5</b>	<b>An Evolutionary Multidomain Method Applied to Multiphase Mufflers</b>	<b>69</b>
<b>6</b>	<b>Evolutionary Design of Mutiphysics Systems with Poroelastic Materials</b>	<b>92</b>
<b>7</b>	<b>Discussion</b>	<b>124</b>
7.1	Number of Elements per Wavelength and Mesh Configuration	124
7.2	Definition of Target Volume Fractions	126
7.3	Computational Costs of the Multidomain/Multiphase Application	127
7.4	Performance Against Design Complexity of the Multiphysics Application	128
<b>8</b>	<b>Concluding Remarks</b>	<b>129</b>
	<b>Bibliography</b>	<b>133</b>

<b>APPENDIX A</b>	<b>Extended Sensitivity Analysis</b>	<b>140</b>
A.1	Sound Pressure Level	141
A.2	Absorption Coefficient	144
A.3	Transmission Loss	145
A.4	Dissipated Power Level	148
<b>APPENDIX B</b>	<b>Publications in International Conferences</b>	<b>155</b>
<b>APPENDIX C</b>	<b>Permission to Use Content – Elsevier and Springer Nature</b>	<b>183</b>

# 1 | Introduction

In general terms, noise can be understood as an unpleasant, undesirable, unexpected or unwanted sound, mainly originated from human activities (Singh; Davar, 2004) and dependent on the excitation frequency of the source, the proximity to the receiver, the exposure duration, among other factors (Bala; Verma, 2020). If divided into indoor and outdoor noise pollutants, one can cite the sound emitted from televisions, refrigerators, blenders, vacuum cleaners and washing machines as indoor, while the outdoor ones may come from road traffic, jet planes, garbage trucks, construction sites, manufacturing processes, religious ceremonies, etc (Birgitta; Lindvall, 1995; Bala; Verma, 2020).

Following a report from EEA (2019), around 12000 premature deaths and 48000 new cases of ischemic heart disease per year may be attributed to long-term exposure to hazardous noise levels in Europe alone. In this same region, chronic high annoyance is reported by 22 million people, while 6.5 million are said to have sleep disturbances. According to the same report, mitigation actions are most effective at the source, being railroads or airports for example, followed by combined policies to reduce air pollution and environmental noise. As specified by Cavalcante *et al.* (2013), in Brazil, noise levels above 85 dB are considered to be an imminent risk to the health of workers, if no appropriate protection is used. Nevertheless, these researchers have found that some lumber and metallurgical companies commonly reach more than 100 dB in its industrial activities, exposing more than half of its workers to these damaging noises.

As another example, military vehicles, aircrafts and ships mostly lack in noise control treatments (Jokel *et al.*, 2019), as well as offshore platforms in general. The reasons range from the increase of carrying capacity, to reductions of weight for fuel savings. Consequently, in such platforms, most of the crew is subjected to noise levels greater than 85 dB for about 8 hours a day, reaching up to 110 dB on a daily basis. On board of typical military ships, the personnel is also subjected to highly noisy environments (exceeding 100 dB), even when running basic activities, such as doing laundry, getting meals or even sleeping.

Despite the individual hearing protection that is usually applied by the companies and military, and some Hearing Conservation Programs placed by Governments, it is perceptible that more effective methods of noise reduction should be implemented for a better quality of life. This can be achieved by using porous materials properly arranged over movable and immovable compositions, as well as by building structures that prioritize Sound Pressure Level (SPL) reductions in specific locations, while maintaining ventilation, such as in residential facades and hospitals. But how these porous materials should be arranged to reduce noise levels in these working places? How elastic/rigid structures should be built to increase acoustic comfort, while maintaining permissibility? Topology optimization methods may offer some insight.

## 1.1 Structural Optimization

In an optimization problem, the main goal is to find the best possible solution among the ones that satisfy a set of previously imposed constraints. It goes without saying that such optimal result depends on the problem itself, which can be the minimization of costs of a factory or the maximization of efficiency of a specific machine, for example (Arora, 2015). In an engineering perspective, the objective is to find the best performance of a particular structure, such as a bridge or space vehicle, while constrained by a certain weight, load capacity, displacements, geometry, and so on (Xie; Steven, 1997).

To give a broader view of the optimization stage in the design process, Kirsch (1993) presented the following roadmap:

- (a) *Formulation*: Establishment of functional requirements that are paramount to the correct use of the final structure.
- (b) *Conceptualization*: The designer chooses the overall topology, material and type of structure to achieve the predefined functionalities.
- (c) *Optimization*: Within the scope of the ideas gathered and the decisions made in the previous steps, the designer seeks, at this level, to find the best possible solution to the problem at hand, while respecting the imposed constraints. Many are the ways to conduct this step; by try-and-error or by the use of numerical simulations, for example.
- (d) *Detailing*: Here the experience of the engineer is crucial to judge if the optimal result fulfills the expectations of the company, the market and the regulatory institutions. If necessary, the design should return to one of the previous steps for improvements.

In any structural design optimization, the best possible solution is obtained by the maximization or minimization of a performance function, e.g., mean compliance, stress norm or vibration characteristics, named as objective function,  $\Phi$ . The constraints are restriction functions imposed to the optimization problem, being usually set in a form of inequality,  $g$ , or equality,  $h$ , equations. The working domain is then described by the design variables,  $\mathbf{x}$ , which can change along the entire optimization process, beyond being continuous or discrete values (Christensen; Klarbring, 2009; Arora, 2015). Therefore, a typical optimization problem can be stated as,

$$\text{Minimize: } \Phi, \quad (1.1)$$

$$\text{Subjected to: } \begin{cases} g(\mathbf{x}) \leq 0, \\ h(\mathbf{x}) = 0, \\ \mathbf{x}^l \leq \mathbf{x} \leq \mathbf{x}^u, \end{cases} \quad (1.2)$$

where  $\Phi$ ,  $g = [g_1(\mathbf{x}), g_2(\mathbf{x}), \dots, g_{n_g}(\mathbf{x})]^T$ ,  $h = [h_1(\mathbf{x}), h_2(\mathbf{x}), \dots, h_{n_h}(\mathbf{x})]^T$  and  $\mathbf{x} = [x_1, x_2, \dots, x_{n_x}]^T$  are defined on  $\mathfrak{R}^{n_x}$ . The number of inequality and equality constraints are  $n_g$  and  $n_h$ , respectively, while  $n_x$  is the number of design variables;  $\mathbf{x}^l$  and  $\mathbf{x}^u$  are the lower and upper bounds of  $\mathbf{x}$ . (Bazaraa *et al.*, 2006; Kim *et al.*, 2002).

### 1.1.1 Types of Structural Optimization

Based on the geometrical and structural characteristics of the body to be optimized, three are the types of structure optimization that are usually considered: size, shape and topology, as illustrated in Fig. 1.1.

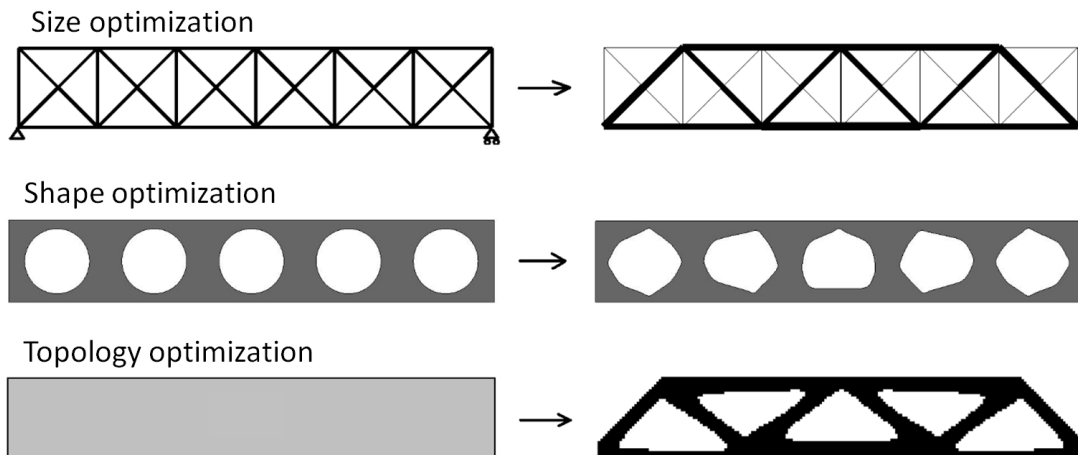


Figure 1.1 – The three optimization types, (a) size, (b) shape and (c) topology (Bendsøe; Sigmund, 2004)

Particularly, size optimization concerns with changing the lengths and cross sectional geometric properties of beams, trusses and frames, that are part of a larger structure, aiming to enhance the observed system characteristic (Fig. 1.1(a)). This is the earliest form of structural optimization, in a way that the domain is fixed and the finite element model of the structure do not need to be modified (Bendsøe; Kikuchi, 1988; Rozvany *et al.*, 1995).

In shape optimization (Fig. 1.1(b)), the contours of the structure are changed as to promote the maximization or minimization of the objective function. In this case, the boundaries are not broken, nor are new ones formed, in a way that the structural connectivity remains the same (Christensen; Klarbring, 2009). Besides that, shape optimization is way more flexible than the one based on sizing, as the finite elements need to be integrated to the course of the optimization procedure (the domain changes, but the topology does not) (Haftka; Grandhi, 1986; Ding, 1986).

Not only combining both optimization types previously cited, but also expanding the concept of “the best solution available”, the structural topology optimization (Fig. 1.1(c)) promotes the search for the optimal distribution of material within the limits of the design domain, while allowing the appearance and modification of internal cavities. In this scenario, it is common for the resulted design to be completely different from the initial one.

### 1.1.2 Structural Topology Optimization

With the possibility of using several iterative algorithms, structural topology optimization techniques may provide the optimal material arrangement of a closed design space, even though its initial form is of arbitrary nature. The advantages of such approach are diverse, ranging from economic savings (reductions of time invested in try-and-error simulations and in raw materials used) to the improvement of basic structural aspects (increase of global stiffness or a better distribution of stresses, for example) (Das *et al.*, 2011).

Combining the use of homogenization techniques with structural optimization methods, Bendsøe and Kikuchi (1988) lead the field of topology optimization research in the late 1980s with its landmark paper entitled “Generating optimal topologies in structural design using a homogenization method”. Here, the idea of turning the optimization approach into a material distribution problem emerged (Maute *et al.*, 1999). From this groundbreaking work, a high number of methodologies emanated such as the ones based on density (Bendsøe, 1989; Zhou; Rozvany, 1991), level-set functions (Allaire *et al.*, 2002; Wang *et al.*, 2003), topological derivative (Sokolowski; Zochowski, 1999), phase field (Bourdin; Chambolle, 2003), evolution-

ary procedures (Xie; Steven, 1992; Yang *et al.*, 1999), among several others (Sivapuram; Picelli, 2018; Ramamoorthy *et al.*, 2021).

An important example among the ones cited is the density-based class of methods. In these approaches, the entire domain, in which the topology optimization problem is based, is discretized into several finite elements, with elemental or nodal design variables,  $x_i$ , describing the disposition of material along the given area, as can be seen in Fig. 1.2. The presence of a material is treat as “full” ( $x_i = 1$ ) and its absence as “void” ( $x_i = 0$ ). Besides, the variable  $x_i$  is often called as density, or pseudo-density, and should not be confused with a true property, such as the mass density (Dilgen *et al.*, 2019).

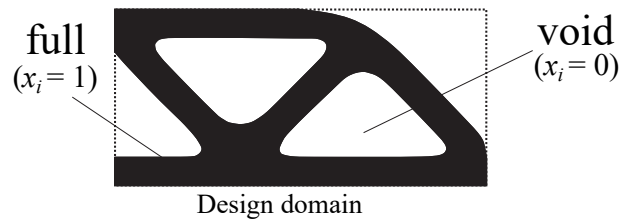


Figure 1.2 – Basic example of a 0 – 1 topology (Maute *et al.*, 1999)

By the definition of a power-law interpolation scheme, e.g.  $U(x_i) = x_i^\zeta U_0$ , where  $U(x_i)$  is an investigated material property,  $\zeta$  is a penalty coefficient, and  $x_i$  is redefined as a continuous design variable ( $0 \leq x_i \leq 1$ ), the Solid Isotropic Material with Penalization (SIMP) method (Bendsøe, 1989) was able to simplify the homogenization approach and enhance the convergence for full-void solutions. Nevertheless, in light of the relaxation of the original discrete optimization problem to a continuous one, regions with intermediate materials, known as gray areas, were also a common trait of the SIMP approach, despite of the penalization of intermediate densities ( $\zeta > 1$  for most cases) (Sigmund; Maute, 2013).

Furthermore, the adoption of linear elements of low-order caused a few numerical issues, such as the appearance of checkerboard patterns (Jog; Haber, 1996) and mesh dependence (Sigmund, 1997), presenting challenges in the generation of reasonably manufacturable topologies. Propositions such as the use of numeric filters and stabilization schemes (Zhou; Rozvany, 1991; Bendsøe; Sigmund, 1999; Jog; Haber, 1996; Sigmund, 1997; Sigmund; Petersson, 1998) were made in order to circumvent these problems. The relative success of this combination of ideas revolutionized the field of research in topology optimization and propelled these numerical methods to be used in a wide range of applications, such as the design of a complete airplane wing using more than 1 billion three-dimensional elements, carried out by Aage *et al.* (2017).

Also based on density, the methods entitled Evolutionary Structural Optimization (ESO),

and Bi-directional Evolutionary Structural Optimization (BESO), have been widely considered in applications concerning structural topology optimization due to their discrete behavior, robustness and ease of computational implementation. Being considered by [Sigmund and Maute \(2013\)](#) as a discrete variation of the SIMP approach, these evolutionary class of methods also make use of power-law interpolations and numeric filters for the calculation of the objective function gradients. As a consequence, the generated topologies have well-defined boundaries, despite of some convergence difficulties due to the discrete density updates.

As the BESO approach allows that materials be reintroduce into the design domain if considered advantageous to the objective function, which is an enhancement to the ESO approach that only removes material, and considering the expertise of the Laboratory of Topology Optimization and Multiphysics Analysis of UNICAMP on this topic of study, this work proposes several modifications to the BESO basic algorithm ([Huang; Xie, 2010a](#)) in order to consider acoustic, rigid, pororigid, elastic or poroelastic material elements in the design of general soundproof system settings. Besides, many are the gaps that still exist in the implementation of topology optimization techniques involving multiple materials, domains, restrictions and frequencies to achieve a greater proximity to real-world applications. This is even more pronounced when considering evolutionary procedures applied in the design of soundproof systems. Thus, many of these gaps are here faced with the goal of generating systematic and functional solutions for such situations.

## 1.2 Goals and Contributions

Since the main goal of this work is to contribute to the development of evolutionary acoustic topology optimization methodologies in the design of general soundproof system settings, three different BESO-based topology optimization studies are presented in paper-based formats, shown in Chapters 4, 5 and 6. Most of these works were published in international journals with the following bibliographic descriptions:

### ◇ International Journal Papers

Chapter 4: Pereira, R. L.; Lopes, H. N.; Pavanello, R. Topology optimization of acoustic systems with a multiconstrained BESO approach. *Finite Element in Analysis and Design*, v. 201, p. 103701, 2022. <https://doi.org/10.1016/j.finel.2021.103701>

Chapter 5: Pereira, R. L.; Lopes, H. N.; Moura, M. S.; Pavanello R. Multi-domain acoustic topology optimization based on the BESO approach: applications on the design of

multi-phase material mufflers. *Structural and Multidisciplinary Optimization*, v. 66, p. 25, 2023. <https://doi.org/10.1007/s00158-022-03479-4>

Chapter 6: Pereira, R. L.; Anaya-Jaimes, L. M.; Pavanello, R. Evolutionary topology optimization approach to design multiphase soundproof systems with poroelastic media (Manuscript submitted for publication), 2023.

On that basis, the original contributions may be synthesized as,

- Contribute to the dissemination of information about evolutionary topology optimization techniques and the use of semi-phenomenological porous models in this context;
- Implement the Virtual Temperature Method (VTM) in the multiconstrained BESO algorithm for connectivity of acoustic systems;
- Develop the multidomain BESO algorithm (mdBESO) and apply it in the design of multiphase muffler chambers;
- Adapt the BESO technique to be applied in the design of fully coupled acoustic, poroelastic and elastic systems;
- Propose new material interpolation schemes to account for acoustic-pororigid-rigid and acoustic-poroelastic-elastic relations;
- Propose several designs of soundproof systems with clearly defined topologies.

Moreover, beyond the aforementioned works produced in the current PhD period, a few publications on international conferences were also made, usually prior to the journal papers. Hence, these conference contributions are not comprised on the main body of the thesis due to content overlap with the included ones, but being added to Appendix B in a chronological order of publication. The bibliographic descriptions for these works are:

#### ◇ **International Conference Papers**

- Pereira, R. L.; Anaya-Jaimes, L. M.; Pavanello, R. Design of periodic noise barriers using the bi-directional evolutionary optimization method. In: *e-Forum Acusticum*. v. 1, p.209–215, 2020. <https://doi.org/10.48465/fa.2020.1068>.
- Pereira, R. L.; Anaya-Jaimes, L. M.; Pavanello, R. Topology optimization of acoustic-poroelastic-elastic structures for sound attenuation. In: *15th World Congress on Computational Mechanics & 8Th Asian Pacific Congress on Computational Mechanics*, 2022. <https://doi.org/10.23967/wccm-apcom.2022.117>

- Pereira, R. L.; Pavanello, R. Topology optimization design of acoustic-poroelastic-elastic structures by the BESO Approach. In: 8th International Symposium on Solid Mechanics, 2022. <https://doi.org/10.26678/ABCM.MECSOL2022.MSL22-0197>

It is highlighted that the part of this work regarding the publication: Pereira, R.L.; Lopes, H.N.; Pavanello, R. Topology optimization of acoustic systems with a multiconstrained BESO approach. *Finite Element in Analysis and Design*, v. 201, p. 103701, (2022), is reproduced with permission of Elsevier. Also, part of this work referring to the publication: Pereira, R.L.; Lopes, H.N.; Moura, M.S.; Pavanello R. Multi-domain acoustic topology optimization based on the BESO approach: applications on the design of multi-phase material mufflers. *Structural and Multidisciplinary Optimization*, v. 66, p. 25 (2023), is reproduced with permission of Springer Nature (see Appendix C for a complete description of the copyright clearances).

### 1.3 Thesis Organization

The organization of this thesis is presented as follows: In Chapter 1 the introduction is given, with basic presentations of structural optimization types, their definitions and applications. In Chapter 2 the governing equations and the FEM procedures employed in the simulation of Helmholtz, Biot and fluid-structure based domains are thoroughly detailed. Chapter 3 introduces the Bi-directional evolutionary Structural Optimization method following the minimization of compliance example. General steps for the computational implementation are also provided. A multiconstrained optimization methodology is presented in Chapter 4. Here, the BESO algorithm is employed to solve two different acoustic topology optimization problems, while considering the Virtual Temperature Method (VTM) to avoid seclusion of air holes inside rigid and pororigid structures.

Chapter 5 displays the multiphase BESO-based methodology for the design of multidomain systems, named as mdBESO. Acoustic-rigid and acoustic-pororigid material phases are considered in the topology optimization of one-chamber mufflers, while the acoustic-pororigid-rigid case is combined with the one, two and three-chamber scenario. In Chapter 6 the design of closed-space systems for sound attenuation is treated, with acoustic, poroelastic, and elastic material elements being part of the design process. The optimization problem is posed as to maximize dissipated power levels, and different combinations of its structural, viscous and thermal partitions, throughout single and multiple frequencies. Chapter 7 introduces further discussions on the topics brought in previous chapters. Conclusions are drawn in Chapter 8.

## 2 | Vibroacoustic Systems Governing Equations

It is common to find in nature examples of interaction between bodies, at different temperatures, subject to oscillatory pressures and even at unequal phases. In the same way, there are many approaches to simulate such encounters, being purely numerical or using experimental data. One of the most popular numerical approaches for solving complex structural problems is called the Finite Element Method (FEM) (Cook *et al.*, 2001). This technique consists in finding the solution of a field problem, that is, a spatial distribution of one or more dependent variables that are usually described in a form of differential or integral expressions. To apply the FEM, the intricate observed domain is first subdivided into small parts, with well-defined geometry and material characteristics, called elements. For these reduced regions, governing mathematical equations are constructed with various boundary conditions, in order to contemplate the most diverse relations between bodies. Many are the numerical simulations that can be performed, even for multiphysics systems subjected to different loads at distinct moments. The possibilities are very broad, being the bases of several works in sciences and engineering (Aage *et al.*, 2017).

On that scenario, this chapter introduces the governing equations and the mathematical procedures employed in the discretization of Helmholtz, Biot and fluid-structural based domains. In a step-wise manner, the Weighted Residuals Method is applied to these fundamental expressions, generating their weak forms (or variational formulations), to only then include Galerkin's procedures and the FEM to find the elemental information. Even though this chapter has similar discussions to those found in sections number 2 of the embedded papers (Chapters 4, 5 and 6), the author has chosen to expand this theoretical background due to its key importance for a complete understanding of the methodologies proposed. Finally, it is remarked that the properties of acoustic, poroelastic and elastic regions are mostly referred, in this chapter, by the subscripts  $(\cdot)_a$ ,  $(\cdot)_p$  and  $(\cdot)_e$ , respectively. The structural and fluid phases of the poroelastic domain are subjected to the subscripts  $(\cdot)_s$  and  $(\cdot)_f$ .

## 2.1 Helmholtz-based Media Formulation

In the frequency domain, the equation that governs a steady-state perfect fluid (inviscid, incompressible, homogeneous and isotropic) region,  $\Omega_a$ , with sound pressure as a time-harmonic function ( $e^{j\omega t}$ ), may be written as the following scalar Helmholtz equation (Atalla; Sgard, 2015),

$$\nabla \cdot \left( \frac{\nabla p_a}{\rho_a} \right) + \frac{\omega^2}{\kappa_a} p_a = 0 \quad \text{with} \quad \kappa_a = \rho_a c_a^2 \quad \text{in} \quad \Omega_a, \quad (2.1)$$

where  $\rho_a$  is the density,  $\kappa_a$  is the bulk modulus,  $p_a$  is the pressure in an Eulerian field,  $c_a$  is the speed of sound,  $j$  is the imaginary unit ( $j^2 = -1$ ),  $\omega$  is the angular frequency,  $t$  is time and  $\nabla$  is the gradient operator.

As a general aspect, the pressure field can be solved by the combination of equation (2.1) with some of the following boundary conditions (Yoon, 2013),

$$\text{Pressure} \quad \rightarrow \quad p_a = \bar{p}, \quad \text{over} \quad \Gamma_1, \quad (2.2)$$

$$\text{Rigid wall} \quad \rightarrow \quad \nabla p_a \cdot \mathbf{n}_a = 0, \quad \text{over} \quad \Gamma_2, \quad (2.3)$$

$$\text{Impedance} \quad \rightarrow \quad \frac{\nabla p_a \cdot \mathbf{n}_a}{\rho_a} = -\frac{j\omega p_a}{Z_0}, \quad \text{over} \quad \Gamma_3, \quad (2.4)$$

$$\text{Particle acceleration} \quad \rightarrow \quad \frac{\nabla p_a \cdot \mathbf{n}_a}{\rho_a} = \bar{a}, \quad \text{over} \quad \Gamma_4, \quad (2.5)$$

$$\text{Particle velocity} \quad \rightarrow \quad \frac{\nabla p_a \cdot \mathbf{n}_a}{\rho_a} = -j\omega \bar{v}, \quad \text{over} \quad \Gamma_5, \quad (2.6)$$

where  $\mathbf{n}_a$  is the outward unit normal vector to the acoustic domain;  $\bar{p}$ ,  $\bar{v}$  and  $\bar{a}$  are the imposed pressure, particle velocity and particle acceleration, respectively. The symbols  $\Gamma_1$  to  $\Gamma_5$  refer to the different boundary types of  $\Omega_a$ , in which Eqs. (2.2) to (2.4) are valid. The air characteristic impedance is represented by  $Z_0 = \rho_a c_a$ . The impedance matching between the inner and outer acoustic fluids is simulated by a termination with practically no reflection of incident waves (Eq. (2.4)), known as anechoic (Munjaj, 2014).

The weak form of the boundary value problem defined by Eqs. (2.1) to (2.4) can then be obtained by the adoption of the Weighted Residuals Method and the Divergence Theorem,

$$\begin{aligned} \frac{1}{\rho_a} \int_{\Omega_a} \nabla p_a \cdot \nabla \delta p_a \, d\Omega_a - \frac{\omega^2}{\kappa_a} \int_{\Omega_a} p_a \delta p_a \, d\Omega_a + \int_{\Gamma_3} \frac{j\omega p_a}{Z_0} \delta p_a \, d\Gamma_3 \\ - \int_{\Gamma_4} \bar{a} \delta p_a \, d\Gamma_4 + \int_{\Gamma_5} j\omega \bar{v} \delta p_a \, d\Gamma_5 = 0, \end{aligned} \quad (2.7)$$

where  $\delta p_a$  is the test function. Usually, in the finite element implementation, the kinematic boundary (Eq. (2.2)) is explicitly imposed on  $\Gamma_1$ , while the rigid wall condition (Eq. (2.3)) is automatically satisfied, hence not appearing in the above expression.

The discretization of the field variable,  $p_a$ , is established by the consideration of the following forms,

$$p_a = \sum_{i=1}^{N_{el}} \mathbf{N}_a \hat{\mathbf{p}}_a^i, \quad (2.8)$$

$$\nabla p_a = \sum_{i=1}^{N_{el}} (\nabla \mathbf{N}_a) \hat{\mathbf{p}}_a^i, \quad (2.9)$$

where  $\mathbf{N}_a$  is the elemental shape function matrix regarding the fluid element domain,  $\Omega_a^i$ , and  $\hat{\mathbf{p}}_a^i$  is the elemental pressure vector. The gradient operator  $\nabla$  is mathematically defined, in a bidimensional perspective, as,

$$\nabla = \left\{ \begin{array}{l} \partial/\partial x \\ \partial/\partial y \end{array} \right\}. \quad (2.10)$$

Following Galerkin's approach, the test function and its gradient can be written in a similar manner,

$$\delta p_a = \sum_{i=1}^{N_{el}} \mathbf{N}_a \delta \hat{\mathbf{p}}_a^i, \quad (2.11)$$

$$\nabla \delta p_a = \sum_{i=1}^{N_{el}} (\nabla \mathbf{N}_a) \delta \hat{\mathbf{p}}_a^i, \quad (2.12)$$

with  $\delta \hat{\mathbf{p}}_a^i$  being the test function vector defined in  $\Omega_a^i$  and  $N_{el}$  the number of elements contained in the global domain. Applying the elemental forms of Eqs. (2.8) to (2.12) into (2.7), the kinetic energy, compression and damping matrices are respectively obtained, in  $\Omega_a^i$ , as

$$\mathbf{H}_a^i = \frac{1}{\rho_a} \int_{\Omega_a^i} (\nabla \mathbf{N}_a)^T \nabla \mathbf{N}_a d\Omega_a^i, \quad (2.13)$$

$$\mathbf{Q}_a^i = \frac{1}{\kappa_a} \int_{\Omega_a^i} \mathbf{N}_a^T \mathbf{N}_a d\Omega_a^i, \quad (2.14)$$

$$\mathbf{D}_a^i = \frac{1}{Z_0} \int_{\Gamma_3^i} \mathbf{N}_a^T \mathbf{N}_a d\Gamma_3^i. \quad (2.15)$$

Also, the element load vector defined in  $\Gamma_4^i$  and  $\Gamma_5^i$  boundaries of  $\Omega_a^i$  is,

$$\hat{\mathbf{f}}_a^i = \bar{a} \int_{\Gamma_4^i} \mathbf{N}_a^T d\Gamma_4^i - j\omega \bar{v} \int_{\Gamma_5^i} \mathbf{N}_a^T d\Gamma_5^i. \quad (2.16)$$

Following the standard finite element assembly procedure,

$$\mathbf{H}_a = \underset{n=1}{\overset{N_{\text{el}}}{A}} \mathbf{H}_a^i, \quad (2.17)$$

$$\mathbf{Q}_a = \underset{n=1}{\overset{N_{\text{el}}}{A}} \mathbf{Q}_a^i, \quad (2.18)$$

$$\mathbf{D}_a = \underset{n=1}{\overset{N_{\text{bc}}}{A}} \mathbf{D}_a^i, \quad (2.19)$$

$$\hat{\mathbf{f}}_a = \underset{n=1}{\overset{N_{\text{bc}}}{A}} \hat{\mathbf{f}}_a^i, \quad (2.20)$$

the acoustic dynamic system can finally be written,

$$\underbrace{(\mathbf{H}_a + j\omega\mathbf{D}_a - \omega^2\mathbf{Q}_a)}_{\mathbf{Z}} \hat{\mathbf{p}}_a = \hat{\mathbf{f}}_a, \quad (2.21)$$

where  $A_{n=1}^{N_{\text{el}}}$  and  $A_{n=1}^{N_{\text{bc}}}$  are assembly operators,  $N_{\text{el}}$  is the total number of elements in the fluid domain and  $N_{\text{bc}}$  is the total number of elements in the considered boundary. The global kinetic energy, compression and damping matrices are represented by  $\mathbf{H}_a$ ,  $\mathbf{Q}_a$  and  $\mathbf{D}_a$ , while the global fluid load and pressure vectors are  $\hat{\mathbf{f}}_a$  and  $\hat{\mathbf{p}}_a$ , respectively.

## 2.2 Poroelastic Media Formulation

According to the works of [Biot \(1956a\)](#) and [Biot \(1956b\)](#), a poroelastic media may be viewed as a collection of fluid and structural phases superimposed in a homogenized manner. In this theory, the existing pores are considered to be fully saturated with air, with the elastic skeleton subjected to small displacements, and the entire poroelastic domain modeled as isotropic. Since the mixed  $\mathbf{u}/p$  approach, as proposed by [Atalla \*et al.\* \(1998\)](#) and later enhanced by [Atalla \*et al.\* \(2001\)](#), is based on the macroscopic interstitial fluid phase pressures,  $p_f$ , and solid phase displacements,  $\mathbf{u}_s$ , the porous medium may then be treated as homogeneous ([Silva Júnior, 2007](#); [Bécot; Jaouen, 2013](#); [Atalla; Sgard, 2015](#)). Hence, for a time-harmonic motion, the wave behavior is described, in the poroelastic medium, by the following relations,

$$\nabla \cdot \hat{\boldsymbol{\sigma}}^s + \omega^2 \tilde{\rho} \mathbf{u}_s + \tilde{\gamma} \nabla p_f = \mathbf{0}, \quad (2.22)$$

$$\nabla^2 p_f + \omega^2 \frac{\tilde{\rho}_{22}}{\tilde{R}} p_f - \omega^2 \frac{\tilde{\rho}_{22}}{\phi^2} \tilde{\gamma} \nabla \cdot \mathbf{u}_s = 0, \quad (2.23)$$

where the tilde symbol indicates a frequency-dependent and complex valued variable,  $\tilde{\rho}$  is the combined effective density,  $\tilde{\gamma}$  is the coupling coefficient,  $\hat{\boldsymbol{\sigma}}^s$  is the stress tensor of the porous material in vacuum,  $\tilde{\rho}_{22}$  is related to the saturated fluid effective density,  $\tilde{R}$  is the coupling coefficient that account for volumetric changes in the fluid phase and  $\phi$  is the porosity. To find

the combined effective density,  $\tilde{\rho}$ , and the coupling coefficient,  $\tilde{\gamma}$ , one may write,

$$\tilde{\rho} = \tilde{\rho}_{11} - \frac{\tilde{\rho}_{12}^2}{\tilde{\rho}_{22}}, \quad (2.24)$$

$$\tilde{\gamma} = \phi \left( \frac{\tilde{\rho}_{12}}{\tilde{\rho}_{22}} - \frac{\tilde{Q}}{\tilde{R}} \right), \quad (2.25)$$

with the individual effective densities being defined as,

$$\tilde{\rho}_{11} = \rho_{11} + \frac{\tilde{b}}{j\omega}, \quad (2.26)$$

$$\tilde{\rho}_{22} = \rho_{22} + \frac{\tilde{b}}{j\omega}, \quad (2.27)$$

$$\tilde{\rho}_{12} = \rho_{12} - \frac{\tilde{b}}{j\omega}. \quad (2.28)$$

The homogenized densities  $\rho_{11}$  and  $\rho_{22}$  account for the inertia effects in the structural and fluid phases, while  $\rho_{12}$  considers the interactions between the inertia forces of both phases. The physical interpretation of  $\tilde{b}$  may be divided into two aspects, depending on its real and imaginary parts. The first is related to the dissipative effect of viscous forces, and the second to the added mass effect that happens due to these same viscous interactions ([Dazel et al., 2008](#)). Following [Allard and Atalla \(2009\)](#), these homogenized densities may also be expressed as,

$$\rho_{11} = (1 - \phi)\rho_s - \rho_{12}, \quad (2.29)$$

$$\rho_{22} = \phi\rho_f - \rho_{12}, \quad (2.30)$$

$$\rho_{12} = -\phi\rho_f(\alpha_\infty - 1), \quad (2.31)$$

and,

$$\tilde{b} = \phi^2 \sigma \tilde{G}, \quad (2.32)$$

where  $\phi$  is the porosity,  $\alpha_\infty$  is the tortuosity,  $\sigma$  is the static flow resistivity,  $\rho_f$  is the fluid phase density and  $\rho_s$  is the solid phase density. As  $\tilde{G}$  defines  $\tilde{b}$ , it also accounts for viscous effects. Based on [Johnson et al. \(1987\)](#), this variable is stated as,

$$\tilde{G} = \sqrt{1 + j \frac{4\alpha_\infty^2 \eta_0 \rho_f \omega}{\sigma^2 \Lambda^2 \phi^2}}, \quad (2.33)$$

with  $\Lambda$  being the viscous characteristic length and  $\eta_0$  the dynamic viscosity of the interstitial fluid. Related only to the structural skeleton, the stress tensor of the porous material in vacuum,  $\hat{\sigma}^s$ , also has a mathematical expression associated to it,

$$\hat{\sigma}^s = \underbrace{\left( \tilde{A} - \frac{\tilde{Q}^2}{\tilde{R}} \right)}_{\tilde{A}} \nabla \cdot \mathbf{u}_s \mathbf{I} + 2\tilde{N} \underline{\underline{\epsilon}}^s, \quad (2.34)$$

where  $\mathbf{I}$  is the identity tensor,  $\boldsymbol{\varepsilon}^s$  is the structural phase strain tensor,  $\tilde{A}$  is the first Lamé constant of the poroelastic material and  $\tilde{N}$  is the shear modulus of the poroelastic material. The variables  $\tilde{Q}$  and  $\tilde{R}$  are the coupling coefficients that account for volumetric changes in structural and fluid phases, and  $\hat{A}$  is the first Lamé constant of the structural phase (poroelastic material in vacuum).

The complete description of the variables  $\tilde{N}$ ,  $\tilde{A}$ ,  $\tilde{Q}$  and  $\tilde{R}$  have been obtained by [Biot and Willis \(1957\)](#), which suggested the ‘‘Gendaken Experiments’’. Being divided into three parts, the first Gendaken Experiment consisted of subjecting the poroelastic material to a pure shear stress, leading to the confirmation that  $\tilde{N}$  is indeed the shear modulus of the elastic skeleton, as that is no contribution from the fluid phase to the shear restoring force. The second experiment placed the studied material under a constant hydrostatic pressure, which provided the definition of the bulk modulus of the frame at constant air pressure,  $K_b$ . Finally, in the third experiment, the material was subjected to an increasing pressure, without the help of a jacketed support. At this moment, two more variables were defined, being  $K_s$  the bulk modulus of the elastic material from which the porous skeleton is made, and  $\tilde{K}_f$  the bulk modulus of the fluid in the pores ([Allard; Atalla, 2009](#)). On that basis, the aforementioned variables can now be described as,

$$\tilde{A} = \frac{(1 - \phi) \left(1 - \phi - \frac{K_b}{K_s}\right) K_s + \phi \frac{K_s}{\tilde{K}_f} K_b}{1 - \phi - \frac{K_b}{K_s} + \phi \frac{K_s}{\tilde{K}_f}} - \frac{2}{3} \tilde{N}, \quad (2.35)$$

$$\tilde{Q} = \frac{\left(1 - \phi - \frac{K_b}{K_s}\right) \phi K_s}{1 - \phi - \frac{K_b}{K_s} + \phi \frac{K_s}{\tilde{K}_f}}, \quad (2.36)$$

$$\tilde{R} = \frac{\phi^2 K_s}{1 - \phi - \frac{K_b}{K_s} + \phi \frac{K_s}{\tilde{K}_f}}, \quad (2.37)$$

$$\tilde{N} = \frac{E_p(1 + j\eta_p)}{2(1 + \nu_p)}, \quad (2.38)$$

with  $E_p$ ,  $\eta_p$  and  $\nu_p$  being the Young’s modulus, the loss factor and the Poisson’s ratio of the poroelastic material, respectively.

Since, in many cases,  $K_s$  is not available due to difficulties in determine the Youngs modulus of the base elastic material by measurement, the variables  $\tilde{A}$ ,  $\tilde{Q}$  and  $\tilde{R}$  can be rewritten in a simplified manner ([Lee, 2009](#)),

$$\tilde{A} = \frac{\nu_p E_p (1 + j\eta_p)}{(1 + \nu_p)(1 - 2\nu_p)}, \quad (2.39)$$

$$\tilde{Q} = (1 - \phi)\tilde{K}_f, \quad (2.40)$$

$$\tilde{R} = \phi\tilde{K}_f. \quad (2.41)$$

As an alternative to this, [Yamamoto \*et al.\* \(2009\)](#) considered the Hashin-Shtrikman's bounds ([Hashin; Shtrikman, 1963](#)) to find an estimated value for  $K_s$ . Nevertheless, as the majority of poroelastic media has high porosity values, Eqs. (2.39), (2.40) and (2.41) in fact become a suitable choice for the current formulations.

Furthermore, as highlighted by [Cao \*et al.\* \(2018\)](#), one of the most used models to account for thermal losses inside porous domains is attributed to [Champoux and Allard \(1991\)](#), due to the reduced amount of variables introduced in the formulations. So, with the adoption of this model in the present work,  $\tilde{K}_f$  can finally be defined,

$$\tilde{K}_f = \gamma_0 P_0 \left[ \gamma_0 - (\gamma_0 - 1) \left( 1 - j \frac{8\eta_0}{\Lambda'^2 P d \rho_f \omega} \sqrt{1 + j \frac{\Lambda'^2 P d \rho_f \omega}{16\eta_0}} \right)^{-1} \right]^{-1}, \quad (2.42)$$

where  $\gamma_0$  is the specific heat ratio,  $Pd$  is the Prandtl number,  $P_0$  is the atmospheric pressure and  $\Lambda'$  is the thermal characteristic length.

Again, the variational formulation of the coupled problem stated in Eqs. (2.22) and (2.23) may be obtained by the Weighted Residuals Method and the application of the Divergence Theorem,

$$\begin{aligned} \int_{\Omega_p} \{ \hat{\boldsymbol{\sigma}}^s(\mathbf{u}_s) : \boldsymbol{\varepsilon}^s(\delta \mathbf{u}_s) - \omega^2 \tilde{\rho} \mathbf{u}_s \cdot \delta \mathbf{u}_s - \tilde{\gamma} \nabla p_f \cdot \delta \mathbf{u}_s \} d\Omega_p \\ - \int_{\Gamma_p} \{ \hat{\boldsymbol{\sigma}}^s(\mathbf{u}_s) \cdot \mathbf{n}_p \} \cdot \delta \mathbf{u}_s d\Gamma_p = 0, \end{aligned} \quad (2.43)$$

$$\begin{aligned} \int_{\Omega_p} \left\{ \frac{\phi^2}{\omega^2 \tilde{\rho}_{22}} \nabla p_f \cdot \nabla \delta p_f - \frac{\phi^2}{\tilde{R}} p_f \delta p_f - \tilde{\gamma} \nabla \delta p_f \cdot \mathbf{u}_s \right\} d\Omega_p \\ + \int_{\Gamma_p} \left\{ \tilde{\gamma} \mathbf{u}_s \cdot \mathbf{n}_p - \frac{\phi^2}{\omega^2 \tilde{\rho}_{22}} \nabla p_f \cdot \mathbf{n}_p \right\} \delta p_f d\Gamma_p = 0, \end{aligned} \quad (2.44)$$

where  $\Gamma_p$  represents the outer boundary of the poroelastic domain  $\Omega_p$ ,  $\mathbf{n}_p$  is outward unit normal vector to  $\Gamma_p$ , and  $\delta \mathbf{u}_s$  and  $\delta p_f$  are admissible functions ([Atalla \*et al.\*, 1998](#)). An alternative way to rewrite the above equations was given by [Atalla \*et al.\* \(2001\)](#), who considered only physical quantities that can be directly specified on the surface of two distinct poroelastic materials. Knowing that the total stress tensor,  $\boldsymbol{\sigma}^t$ , and the average relative displacement vector,  $\phi(\mathbf{U}_f -$

$\mathbf{u}_s$ ), are related to,

$$\boldsymbol{\sigma}^t \cdot \mathbf{n}_p = \hat{\boldsymbol{\sigma}}^s \cdot \mathbf{n}_p - \phi \left( 1 + \frac{\tilde{Q}}{\tilde{R}} \right) p_f \mathbf{I} \cdot \mathbf{n}_p, \quad (2.45)$$

$$\phi(\mathbf{U}_f - \mathbf{u}_s) \cdot \mathbf{n}_p = -\tilde{\gamma} \mathbf{u}_s \cdot \mathbf{n}_p + \frac{\phi^2}{\omega^2 \tilde{\rho}_{22}} - \phi \left( 1 + \frac{\tilde{Q}}{\tilde{R}} \right) \mathbf{u}_s \cdot \mathbf{n}_p, \quad (2.46)$$

(see [Atalla et al. \(1998\)](#) for the origin of these expressions), the Divergence Theorem can again be applied to the surface integrals of Eqs. (2.43) and (2.44), together with the vector relation:  $\nabla \cdot (u\mathbf{h}) = \nabla u \cdot \mathbf{h} + u \nabla \cdot \mathbf{h}$ , enhancing the aforementioned weak form to the following set of expressions ([Atalla et al., 2001](#); [Rigobert et al., 2003](#); [Allard; Atalla, 2009](#)),

$$\int_{\Omega_p} \left\{ \hat{\boldsymbol{\sigma}}^s(\mathbf{u}_s) : \boldsymbol{\varepsilon}^s(\delta \mathbf{u}_s) - \omega^2 \tilde{\rho} \mathbf{u}_s \cdot \delta \mathbf{u}_s - (\tilde{\gamma} + \tilde{\xi}) \nabla p_f \cdot \delta \mathbf{u}_s - \tilde{\xi} p_f \nabla \cdot \delta \mathbf{u}_s \right\} d\Omega_p - \int_{\Gamma_p} (\boldsymbol{\sigma}^t \cdot \mathbf{n}_p) \cdot \delta \mathbf{u}_s d\Gamma_p = 0, \quad (2.47)$$

$$\int_{\Omega_p} \left\{ \frac{\phi^2}{\omega^2 \tilde{\rho}_{22}} \nabla p_f \cdot \nabla \delta p_f - \frac{\phi^2}{\tilde{R}} p_f \delta p_f - (\tilde{\gamma} + \tilde{\xi}) \nabla \delta p_f \cdot \mathbf{u}_s - \tilde{\xi} \delta p_f \nabla \cdot \mathbf{u}_s \right\} d\Omega_p - \int_{\Gamma_p} \phi(\mathbf{U}_f - \mathbf{u}_s) \cdot \mathbf{n}_p \delta p_f d\Gamma_p = 0, \quad (2.48)$$

where  $\tilde{\xi} = \phi(1 + \tilde{Q}/\tilde{R})$  is a coupling coefficient introduced for conciseness ([Lee et al., 2012](#)). An interesting aspect of Eqs. (2.47) and (2.48) is that the coupling between the structural and fluid phases are of volumetric nature, while the boundary quantities  $\boldsymbol{\sigma}^t \cdot \mathbf{n}_p$  and  $\phi(\mathbf{U}_f - \mathbf{u}_s)$  allow a natural coupling between poroelastic-elastic domains, as well as two dissimilar poroelastic materials. Nonetheless, special treatments are needed to correctly simulate acoustic-poroelastic interfaces (see Section 2.3.1).

In this scenario, the Finite Element Method (FEM) has been employed in the discretization of Eqs. (2.47) and (2.48). Knowing that  $\hat{p}_f^i$  and  $\hat{\mathbf{u}}_s^i$  are the nodal pressure and displacement vectors regarding the poroelastic element  $i$ , and that both fluid and structure elemental shape function matrices are respectively denoted as  $\mathbf{N}_a$  and  $\mathbf{N}_e$ , the fields  $p_f$  and  $\mathbf{u}_s$  may finally be stated,

$$p_f = \sum_{i=1}^{N_{el}} \mathbf{N}_a \hat{\mathbf{p}}_f^i, \quad (2.49)$$

$$\mathbf{u}_s = \sum_{i=1}^{N_{el}} \mathbf{N}_e \hat{\mathbf{u}}_s^i, \quad (2.50)$$

$$\nabla p_f = \sum_{i=1}^{N_{el}} (\nabla \mathbf{N}_a) \hat{\mathbf{p}}_f^i, \quad (2.51)$$

$$\nabla \mathbf{u}_s = \sum_{i=1}^{N_{el}} (\nabla \mathbf{N}_e) \hat{\mathbf{u}}_s^i, \quad (2.52)$$

where the differential operator  $\nabla$  may be written, in a bidimensional perspective, as,

$$\nabla = \begin{bmatrix} \partial/\partial x & 0 \\ 0 & \partial/\partial y \\ \partial/\partial y & \partial/\partial x \end{bmatrix}. \quad (2.53)$$

By Galerkin's approach, all admissible functions of pressure and displacement are respectively similar to  $p$ ,  $\mathbf{u}$  and their gradients,

$$\delta p_f = \sum_{i=1}^{N_{el}} \mathbf{N}_a \delta \hat{\mathbf{p}}_f^i, \quad (2.54)$$

$$\delta \mathbf{u}_s = \sum_{i=1}^{N_{el}} \mathbf{N}_e \delta \hat{\mathbf{u}}_s^i, \quad (2.55)$$

$$\nabla \delta p_f = \sum_{i=1}^{N_{el}} (\nabla \mathbf{N}_a) \delta \hat{\mathbf{p}}_f^i, \quad (2.56)$$

$$\nabla \delta \mathbf{u}_s = \sum_{i=1}^{N_{el}} (\nabla \mathbf{N}_e) \delta \hat{\mathbf{u}}_s^i, \quad (2.57)$$

which leads to the following system of equations,

$$\begin{bmatrix} \tilde{\mathbf{K}}_p - \omega^2 \tilde{\mathbf{M}}_p & -(\tilde{\mathbf{C}}_{p1} + \tilde{\mathbf{C}}_{p2}) \\ -(\tilde{\mathbf{C}}_{p1} + \tilde{\mathbf{C}}_{p2})^T & \tilde{\mathbf{H}}_p/\omega^2 - \tilde{\mathbf{Q}}_p \end{bmatrix} \begin{Bmatrix} \hat{\mathbf{u}}_s \\ \hat{\mathbf{p}}_f \end{Bmatrix} = \begin{Bmatrix} \hat{\mathbf{f}}_s \\ \hat{\mathbf{f}}_f/\omega^2 \end{Bmatrix}. \quad (2.58)$$

Here,  $\tilde{\mathbf{K}}_p$ ,  $\tilde{\mathbf{M}}_p$ ,  $\tilde{\mathbf{H}}_p$  and  $\tilde{\mathbf{Q}}_p$  are the global poroelastic stiffness, mass, kinetic and compression matrices, respectively, while the poroelastic phases are coupled with the help of the matrices  $\tilde{\mathbf{C}}_{p1}$  and  $\tilde{\mathbf{C}}_{p2}$ . The global displacement and pressure vectors are  $\hat{\mathbf{u}}_s$  and  $\hat{\mathbf{p}}_f$ , where  $\hat{\mathbf{f}}_s$  and  $\hat{\mathbf{f}}_f$  are their correspondent global load vectors.

In an elemental view,  $\Omega_p^i$  and  $\Gamma_p^i$ , the above matrices and load vectors assume the following forms,

$$\tilde{\mathbf{K}}_p^i = \int_{\Omega_p^i} (\nabla \mathbf{N}_e)^T \mathbf{E}_p \nabla \mathbf{N}_e d\Omega_p^i, \quad (2.59)$$

$$\tilde{\mathbf{M}}_p^i = \int_{\Omega_p^i} \tilde{\rho} \mathbf{N}_e^T \mathbf{N}_e d\Omega_p^i, \quad (2.60)$$

$$\tilde{\mathbf{H}}_p^i = \int_{\Omega_p^i} \frac{\phi^2}{\tilde{\rho}_{22}} (\nabla \mathbf{N}_a)^T \nabla \mathbf{N}_a d\Omega_p^i, \quad (2.61)$$

$$\tilde{\mathbf{Q}}_p^i = \int_{\Omega_p^i} \frac{\phi^2}{\tilde{R}} \mathbf{N}_a^T \mathbf{N}_a d\Omega_p^i, \quad (2.62)$$

$$\tilde{\mathbf{C}}_{p1}^i = \int_{\Omega_p^i} \frac{\phi}{\tilde{\alpha}} \mathbf{N}_e^T \nabla \mathbf{N}_a d\Omega_p^i, \quad (2.63)$$

$$\tilde{\mathbf{C}}_{p2}^i = \int_{\Omega_p^i} \phi \tilde{\xi} (\nabla \cdot \mathbf{N}_e)^T \mathbf{N}_a d\Omega_p^i, \quad (2.64)$$

$$\hat{\mathbf{f}}_s^i = \int_{\Gamma_p^i} \mathbf{N}_e^T (\boldsymbol{\sigma}^t \cdot \mathbf{n}_p) d\Gamma_p^i, \quad (2.65)$$

$$\hat{\mathbf{f}}_f^i = \int_{\Gamma_p^i} \phi (\mathbf{U}_f - \mathbf{u}_s) \cdot \mathbf{n}_p \mathbf{N}_a^T d\Gamma_p^i, \quad (2.66)$$

with  $\mathbf{E}_p$  being the elasticity matrix of the poroelastic domain,

$$\mathbf{E}_p = \begin{bmatrix} \hat{A} + 2\tilde{N} & \hat{A} & 0 \\ \hat{A} & \hat{A} + 2\tilde{N} & 0 \\ 0 & 0 & \tilde{N} \end{bmatrix}, \quad (2.67)$$

and,

$$\tilde{\alpha} = \alpha_\infty - j \frac{\phi \sigma \tilde{G}}{\omega \rho_f}, \quad (2.68)$$

being the dynamic tortuosity variable introduced by [Johnson \*et al.\* \(1987\)](#). Finally, according to [Sgard \*et al.\* \(2005\)](#), [Lee \*et al.\* \(2015\)](#) and [Allard and Atalla \(2009\)](#) the following relations are also valid,

$$\frac{\phi}{\tilde{\alpha}} = \tilde{\gamma} + \tilde{\xi} = \frac{\phi(\tilde{\rho}_{12} + \tilde{\rho}_{22})}{\tilde{\rho}_{22}} = \frac{\phi^2 \rho_f}{\tilde{\rho}_{22}}. \quad (2.69)$$

### 2.3 General Fluid-Structure Interactions: Governing Equations

As this work also deals with interactions of explicit acoustic-elastic regions (not to be confused with the implicit kind of poroelastic media), the linear elastodynamic equation, as well as the boundary conditions applied over the elastic domain,  $\Omega_e$ , are respectively introduced, for time-harmonic motion ( $e^{j\omega t}$ ), as ([Atalla; Sgard, 2015](#); [Vicente \*et al.\*, 2015](#)),

$$\nabla \cdot \boldsymbol{\sigma}_e + \rho_e \omega^2 \mathbf{u}_e = \mathbf{0} \quad \text{in } \Omega_e, \quad (2.70)$$

and,

$$\text{Displacements imposition} \quad \rightarrow \quad \mathbf{u}_e = \bar{\mathbf{u}} \quad \text{over} \quad \Gamma_{e1}, \quad (2.71)$$

$$\text{External load distribution} \quad \rightarrow \quad \boldsymbol{\sigma}_e \cdot \mathbf{n}_e = \mathbf{f}_e \quad \text{over} \quad \Gamma_{e2}, \quad (2.72)$$

$$\text{Equilibrium of loads} \quad \rightarrow \quad \boldsymbol{\sigma}_e \cdot \mathbf{n}_e = p_a \mathbf{n}_a \quad \text{over} \quad \Gamma_{ae}. \quad (2.73)$$

Here,  $\boldsymbol{\sigma}_e$  is the elastic stress tensor,  $\bar{\mathbf{u}}$  is the imposed displacement and  $\mathbf{n}_e$  is the outward unit normal vector to the elastic region ( $\mathbf{n}_e = -\mathbf{n}_a$ ). The symbols  $\Gamma_{e1}$  and  $\Gamma_{e2}$  refer to the different boundary types of  $\Omega_e$  (Dirichlet and Neumann, respectively), where Eqs. (2.71) and (2.72) are valid. Finally,  $\Gamma_{ae}$  concerns to the common acoustic-elastic frontier (Eq. (2.73)).

In the acoustic side, the coupling boundary condition applied over  $\Gamma_{ae}$  also has a mathematical contributor,

$$\text{Displacements continuity} \quad \rightarrow \quad \frac{\nabla p_a \cdot \mathbf{n}_a}{\rho_a} = \omega^2 \mathbf{u}_e \cdot \mathbf{n}_a \quad \text{over} \quad \Gamma_{ae}. \quad (2.74)$$

Following similar procedures to those performed for poroelastic and acoustic materials, adding Eq. (2.74) to the variational form of Helmholtz-based domains (Eq. (2.7)), and combining Eqs. (2.70) to (2.73) together, the weak forms of the coupled acoustic-elastic domains are respectively presented,

$$\begin{aligned} & \frac{1}{\rho_a} \int_{\Omega_a} \nabla p_a \cdot \nabla \delta p_a \, d\Omega_a - \frac{\omega^2}{\kappa_a} \int_{\Omega_a} p_a \delta p_a \, d\Omega_a + \int_{\Gamma_3} \frac{j\omega p_a}{Z_0} \delta p_a \, d\Gamma_3 \\ & - \int_{\Gamma_4} \bar{a} \delta p_a \, d\Gamma_4 + \int_{\Gamma_5} j\omega \bar{v} \delta p_a \, d\Gamma_5 - \omega^2 \int_{\Gamma_{ae}} \mathbf{u}_e \cdot \mathbf{n}_a \delta p_a \, d\Gamma_{ae} = 0, \end{aligned} \quad (2.75)$$

$$\begin{aligned} & \int_{\Omega_e} \boldsymbol{\sigma}_e(\mathbf{u}_e) : \boldsymbol{\varepsilon}_e(\delta \mathbf{u}_e) \, d\Omega_e - \int_{\Omega_e} \rho_e \omega^2 \mathbf{u}_e \cdot \delta \mathbf{u}_e \, d\Omega_e \\ & - \int_{\Gamma_{e2}} \mathbf{f}_e \cdot \delta \mathbf{u}_e \, d\Gamma_{e2} - \int_{\Gamma_{ae}} p_a \mathbf{n}_a \cdot \delta \mathbf{u}_e \, d\Gamma_{ae} = 0, \end{aligned} \quad (2.76)$$

where  $\mathbf{f}_e$  is a load vector applied over  $\Gamma_{e2}$ ,  $\boldsymbol{\varepsilon}_e$  is the elastic strain tensor and both  $\delta p_a$ ,  $\delta \mathbf{u}_e$  are admissible functions. Once more, the kinetic condition (Eq. (2.71)) is explicitly applied over  $\Gamma_{e1}$  in the finite element implementation.

### 2.3.1 Coupled Acoustic-Poroelastic-Elastic Boundary Conditions

As treated in the works of [Atalla \*et al.\* \(2001\)](#), the main coupling conditions involving poroelastic media are of four types, that is poroelastic-poroelastic, poroelastic-elastic, poroelastic-acoustic and poroelastic-septum, together with the two loading conditions of imposed pressure and displacements. Considering the current weak form of the mixed  $\mathbf{u}/p$  expressions, Eqs. (2.47) and (2.48), the poroelastic media couples to others through the following

boundary terms,

$$I^p = - \int_{\Gamma_p} (\boldsymbol{\sigma}^t \cdot \mathbf{n}_p) \cdot \delta \mathbf{u}_s \, d\Gamma_p - \int_{\Gamma_p} \phi(\mathbf{U}_f - \mathbf{u}_s) \cdot \mathbf{n}_p \delta p_f \, d\Gamma_p. \quad (2.77)$$

In this section, only the first three coupling cases are shown, since these are the conditions used in the problems investigated, together with the acoustic-elastic one presented previously. It is emphasized that a complete overview of the many ways to simulate porous materials are presented in the works of [Allard and Atalla \(2009\)](#).

### 2.3.1.1 Poroelastic-Elastic

Knowing that the elastic media couples with the following surface integral expression (shown in Eqs. (2.72) and (2.76)),

$$I^e = - \int_{\Gamma_e} (\boldsymbol{\sigma}_e \cdot \mathbf{n}_e) \cdot \delta \mathbf{u}_e \, d\Gamma_e, \quad (2.78)$$

where  $\mathbf{n}_e = -\mathbf{n}_p$ , the combination of both Eqs. (2.77) and (2.78) may be written as,

$$I^p + I^e = - \int_{\Gamma_{ep}} (\boldsymbol{\sigma}^t \cdot \mathbf{n}_p) \cdot \delta \mathbf{u}_s \, d\Gamma_{ep} - \int_{\Gamma_{ep}} \phi(\mathbf{U}_f - \mathbf{u}_s) \cdot \mathbf{n}_p \delta p_f \, d\Gamma_{ep} + \int_{\Gamma_{ep}} (\boldsymbol{\sigma}_e \cdot \mathbf{n}_p) \cdot \delta \mathbf{u}_e \, d\Gamma_{ep}. \quad (2.79)$$

The coupling conditions at the common boundary  $\Gamma_{ep}$  are defined in a way that the continuity of the total stress, the lack of relative mass flux through the impervious wall and the continuity of the solid phase vectors at such interface are all ensured. Mathematically, this can be respectively stated as,

$$\boldsymbol{\sigma}^t \cdot \mathbf{n}_p = \boldsymbol{\sigma}_e \cdot \mathbf{n}_p, \quad (2.80)$$

$$\phi(\mathbf{U}_f - \mathbf{u}_s) \cdot \mathbf{n}_p = 0, \quad (2.81)$$

$$\mathbf{u}_s = \mathbf{u}_e. \quad (2.82)$$

Substituting Eqs. (2.80), (2.81) and (2.82) into Eq. (2.79) one may find that  $I^p + I^e = 0$ , which means that the poroelastic-elastic coupling is natural (no additional efforts are necessary). Nevertheless, the kinematic boundary condition, Eq. (2.82), needs to be explicitly imposed in  $\Gamma_{ep}$ , which may be done automatically by the FEM.

### 2.3.1.2 Poroelastic-Acoustic

Consider that the weak form of the scalar Helmholtz expression, Eq. (2.7), has been rewritten as the following,

$$\frac{1}{\rho_a} \int_{\Omega_a} \nabla p_a \cdot \nabla \delta p_a \, d\Omega_a - \frac{\omega^2}{\kappa_a} \int_{\Omega_a} p_a \delta p_a \, d\Omega_a - \int_{\Gamma_a} \frac{\nabla p_a \cdot \mathbf{n}_a}{\rho_a} \delta p_a \, d\Gamma_a = 0, \quad (2.83)$$

where  $\Gamma_a = \Gamma_2 \cup \Gamma_3 \cup \Gamma_4 \cup \Gamma_5$ . Hence, the surface integral of such equation is,

$$I^a = - \int_{\Gamma_a} \frac{\nabla p_a \cdot \mathbf{n}_a}{\rho_a} \delta p_a \, d\Gamma_a, \quad (2.84)$$

which leads to,

$$\begin{aligned} I^p + I^a = & - \int_{\Gamma_{ap}} (\boldsymbol{\sigma}^t \cdot \mathbf{n}_p) \cdot \delta \mathbf{u}_s \, d\Gamma_{ap} - \int_{\Gamma_{ap}} \phi(\mathbf{U}_f - \mathbf{u}_s) \cdot \mathbf{n}_p \delta p_f \, d\Gamma_{ap} \\ & + \int_{\Gamma_{ap}} \frac{\nabla p_a \cdot \mathbf{n}_p}{\rho_a} \delta p_a \, d\Gamma_{ap}, \end{aligned} \quad (2.85)$$

for  $\mathbf{n}_a = -\mathbf{n}_p$ .

In the common  $\Gamma_{ap}$  boundary, the interface conditions are,

$$\boldsymbol{\sigma}^t \cdot \mathbf{n}_p = -p_a \mathbf{n}_p, \quad (2.86)$$

$$\frac{\nabla p_a \cdot \mathbf{n}_p}{\rho_a} = \mathbf{u}_s \cdot \mathbf{n}_p + \phi(\mathbf{U}_f - \mathbf{u}_s) \cdot \mathbf{n}_p, \quad (2.87)$$

$$p_f = p_a, \quad (2.88)$$

where the continuity of all normal stresses, acoustic and total poroelastic displacements, and pressure are respectively represented, across  $\Gamma_{ap}$ , by Eqs. (2.86), (2.87) and (2.88). Substituting these later expressions in Eq. (2.85), one gets,

$$I^p + I^a = \int_{\Gamma_{ap}} \delta(p_a \mathbf{n}_p \cdot \mathbf{u}_s) \, d\Gamma_{ap}, \quad (2.89)$$

which is the standard acoustic-elastic coupling term. Once again, the kinematic boundary condition, Eq. (2.88), needs to be explicitly imposed in  $\Gamma_{ap}$ . This may be done automatically by the FEM.

### 2.3.1.3 Poroelastic-Poroelastic

Let two different poroelastic materials be identified by the subscript numbers  $(\cdot)_1$  and  $(\cdot)_2$ . Therefore, in the common  $\Gamma_{pp}$  boundary,

$$\begin{aligned} I_1^p + I_2^p = & - \int_{\Gamma_{pp}} (\boldsymbol{\sigma}_1^t \cdot \mathbf{n}_{p1}) \cdot \delta \mathbf{u}_{s1} d\Gamma_{pp} - \int_{\Gamma_{pp}} \phi(\mathbf{U}_{f1} - \mathbf{u}_{s1}) \cdot \mathbf{n}_{p1} \delta p_{f1} d\Gamma_{pp} \\ & + \int_{\Gamma_{pp}} (\boldsymbol{\sigma}_2^t \cdot \mathbf{n}_{p1}) \cdot \delta \mathbf{u}_{s2} d\Gamma_{pp} + \int_{\Gamma_{pp}} \phi(\mathbf{U}_{f2} - \mathbf{u}_{s2}) \cdot \mathbf{n}_{p1} \delta p_{f2} d\Gamma_{pp}, \end{aligned} \quad (2.90)$$

for  $\mathbf{n}_{p2} = -\mathbf{n}_{p1}$ . To properly couple two dissimilar poroelastic materials, the conditions are of four types. The first one concerns the continuity of normal stresses, while the second ensures continuity of mass flow across the boundary. The third and fourth ones also establish the solid phase displacements and pore fluid pressure fields across  $\Gamma_{pp}$ . In a mathematical point of view, these conditions are,

$$\boldsymbol{\sigma}_1^t \cdot \mathbf{n}_{p1} = \boldsymbol{\sigma}_2^t \cdot \mathbf{n}_{p1}, \quad (2.91)$$

$$\phi(\mathbf{U}_{f1} - \mathbf{u}_{s1}) \cdot \mathbf{n}_{p1} = \phi(\mathbf{U}_{f1} - \mathbf{u}_{s1}) \cdot \mathbf{n}_{p1}, \quad (2.92)$$

$$\mathbf{u}_{s1} = \mathbf{u}_{s2}, \quad (2.93)$$

$$p_{f1} = p_{f2}. \quad (2.94)$$

The combination of Eqs. (2.91), (2.92), (2.93) and (2.94) with (2.90) leads to  $I_1^p + I_2^p = 0$ , which represents a natural coupling between both media. Same as before, the kinematic conditions, Eqs. (2.93) and (2.94), need to be explicitly imposed in  $\Gamma_{pp}$ . In a finite element implementation, this may be done automatically through assembling.

## 2.3.2 Coupled Acoustic-Poroelastic-Elastic Equilibrium Equations

Considering the structural layouts and topologies investigated throughout this work, whenever poroelastic materials are treated, acoustic and elastic domains are also present. Therefore, it is convenient to introduce the fully coupled acoustic-poroelastic-elastic equilibrium equations at this point. Again, with the adoption of the FEM, Eqs. (2.47), (2.48), (2.75) and (2.76) can be discretized by following similar procedures as the ones adopted in Eqs. (2.49) to (2.57), which generates,

$$\underbrace{\begin{bmatrix} \mathbf{K}_e - \omega^2 \mathbf{M}_e & \mathbf{0} & \mathbf{0} & -\mathbf{L}_{ae} \\ \mathbf{0} & \tilde{\mathbf{K}}_p - \omega^2 \tilde{\mathbf{M}}_p & -(\tilde{\mathbf{C}}_{p1} + \tilde{\mathbf{C}}_{p2}) & -\mathbf{L}_{ap} \\ \mathbf{0} & -(\tilde{\mathbf{C}}_{p1} + \tilde{\mathbf{C}}_{p2})^T & \tilde{\mathbf{H}}_p/\omega^2 - \tilde{\mathbf{Q}}_p & \mathbf{0} \\ -\mathbf{L}_{ae}^T & -\mathbf{L}_{ap}^T & \mathbf{0} & \mathbf{H}_a/\omega^2 + j\mathbf{D}_a/\omega - \mathbf{Q}_a \end{bmatrix}}_{\tilde{\mathbf{Z}}} \underbrace{\begin{Bmatrix} \hat{\mathbf{u}}_e \\ \hat{\mathbf{u}}_s \\ \hat{\mathbf{p}}_f \\ \hat{\mathbf{p}}_a \end{Bmatrix}}_{\hat{\boldsymbol{\theta}}} = \underbrace{\begin{Bmatrix} \hat{\mathbf{f}}_e \\ \hat{\mathbf{f}}_s \\ \hat{\mathbf{f}}_f/\omega^2 \\ \hat{\mathbf{f}}_a/\omega^2 \end{Bmatrix}}_{\hat{\mathbf{f}}}. \quad (2.95)$$

The introduced global elastic stiffness and mass matrices are denoted as  $\mathbf{K}_e$  and  $\mathbf{M}_e$ , respectively, with  $\mathbf{L}_{ae}$  and  $\mathbf{L}_{ap}$  being the standard acoustic-elastic coupling matrices at  $\Gamma_{ae}$  and  $\Gamma_{ap}$ , respectively. In the  $\Omega_e^i$  domain, and boundaries  $\Gamma_{ae}^i$  and  $\Gamma_{ap}^i$ , these matrices are described as,

$$\mathbf{K}_e^i = \int_{\Omega_e^i} (\nabla \mathbf{N}_e)^T \mathbf{E}_e \nabla \mathbf{N}_e d\Omega_e^i, \quad (2.96)$$

$$\mathbf{M}_e^i = \int_{\Omega_e^i} \rho_e \mathbf{N}_e^T \mathbf{N}_e d\Omega_e^i, \quad (2.97)$$

$$\mathbf{L}_{ae}^i = \int_{\Gamma_{ae}^i} \mathbf{N}_e^T \mathbf{n}_a \mathbf{N}_a d\Gamma_{ae}^i, \quad (2.98)$$

$$\mathbf{L}_{ap}^i = \int_{\Gamma_{ap}^i} \mathbf{N}_e^T \mathbf{n}_a \mathbf{N}_a d\Gamma_{ap}^i, \quad (2.99)$$

and,

$$\hat{\mathbf{f}}_e^i = \int_{\Gamma_{e2}^i} \mathbf{N}_e^T \mathbf{f}_e d\Gamma_{e2}^i, \quad (2.100)$$

where  $\mathbf{E}_e$  is the elasticity matrix related to  $\Omega_e$ .

As previously stated, the adopted poroelasticity equations do not require coupling matrices to connect dissimilar poroelastic or poroelastic-elastic domains. However, for the acoustic-poroelastic case, a  $\mathbf{L}_{ap}$  fluid-structural coupling matrix need to be implemented for the correct description of forces that are exchanged between both media. To comply with this, two methodologies can be used. The first consists of tracking the boundaries between the different materials throughout the optimization process, in order to implement the  $\mathbf{L}_{ae}$  and  $\mathbf{L}_{ap}$  matrices in all acoustic-elastic and poroelastic-acoustic boundaries. The second methodology avoid such time consuming calculations by ignoring the tracking of borders, as Biot's equations are used to simulate all acoustic, elastic and poroelastic elements by the manipulation of specific variables. This last approach, named as Unified Multiphase (UMP) modeling technique (Lee, 2009; Lee *et al.*, 2012; Lee *et al.*, 2015), is the one adopted in the optimization procedure presented in Chapter 6. Moreover, the descriptions related to the scalar Helmholtz equation given in Section 2.1 are thoroughly used in the works brought by Chapters 4 and 5.

## 3 | Bi-directional Evolutionary Structural Optimization Method

First introduced by [Xie and Steven \(1992\)](#), [Xie and Steven \(1993\)](#), the Evolutionary Structural Optimization (ESO) methodology aims to gradually remove inefficient material from the structure, evolving the design towards an optimal form. Since this is a density-based optimization process, the design domain is usually discretized into finite elements, describing the structure through the attribution of pseudo-densities, also called design variables. In this particular approach, there is no possibility of returning elements (only full elements could be turned into void ones), meaning that the optimization procedure is somewhat biased by the first iterations or the initial guess design.

A natural ESO evolution would then be to allow the reentry of material (or the transformation of void elements into full ones), which was proposed by [Querin \*et al.\* \(1998\)](#), [Querin \*et al.\* \(2000\)](#). Here, the ESO algorithm was modified to allow the addition of material to regions with high local stresses. Such numerical procedure gave rise to the Bi-directional ESO methodology, or simply BESO, being latter applied to stiffness optimizations by [Yang \*et al.\* \(1999\)](#). Following the works of [Sigmund and Maute \(2013\)](#), who described the BESO algorithm as a discrete version of the SIMP methodology, and [Cunha \*et al.\* \(2021\)](#), who proposed several finite variation sensitivity analysis for discrete methods, these evolutionary approaches present clear boundaries between different domains, which exclude the need for post-processing to classify gray areas; generate multiple possible solutions throughout the optimization procedure, as valid candidates are obtained in every iteration; and can be implemented with relatively low effort if starting from the SIMP algorithm ([Sigmund, 2001](#)).

In this chapter, the Bi-directional Evolutionary Structural Optimization approach utilizing the material interpolation scheme with penalization ([Huang; Xie, 2009](#); [Huang; Xie, 2010a](#); [Huang; Xie, 2010c](#)) is briefly introduced. Discussions concerning the sensitivity analysis of the mean compliance problem, as well as the presentation of the mesh-independent pro-

jection filter, stabilization procedures, and the heuristic update schemes are presented. Finally, a flowchart of the BESO method is provided.

### 3.1 Topology Optimization Problem: Structural Compliance Minimization

One of the most common problems of structural topology optimization is the minimization of compliance. Hence, in this section, the BESO methodology is considered in its solution, with the statement of the problem being (Huang; Xie, 2010a),

$$\text{Minimize: } C = \frac{1}{2} \hat{\mathbf{f}}^T \hat{\mathbf{u}}, \quad (3.1)$$

$$\text{Subjected to: } \begin{cases} \mathbf{K} \hat{\mathbf{u}} = \hat{\mathbf{f}}, \\ V^* - \sum_{i=1}^{N_{\text{elD}}} V_i x_i = 0, \\ x_i = x_{\min} \text{ or } 1, \end{cases} \quad (3.2)$$

where  $C$  is the mean compliance,  $V^*$  is the prescribed final volume fraction and  $\sum_{i=1}^{N_{\text{elD}}} V_i x_i$  is the design volume fraction obtained in each iterative step.  $N_{\text{elD}}$  is the total number of elements of the design domain. The expression  $\mathbf{K} \hat{\mathbf{u}} = \hat{\mathbf{f}}$  represents a static linear elastic system of equations, with  $\mathbf{K}$  being the global stiffness matrix of the structure;  $\hat{\mathbf{u}}$  and  $\hat{\mathbf{f}}$  are the displacements and load global vectors. The equality constraint imposed by the volume fractions is a common trait of evolutionary algorithms as the volume generally changes throughout the optimization. The equilibrium equation is another important characteristic of most optimizers, being also possible to consider acoustic, thermic, electric or even multiphysics systems in the problem composition.

The design variable is here represented by  $x_i$ , assuming only discrete values of bounds  $x_{\min}$  and 1. In the early ESO algorithms,  $x_{\min}$  was set to 0, meaning that the void element would be completely removed from the design domain. In this approach, the gains are substantial, since the elements/nodes are not accounted for in the subsequent iterations, reducing the overall computational costs. However, these so called hard-kill methods sometimes lead to non-optimal solutions, or presented convergence difficulties (Zhou; Rozvany, 2001; Huang; Xie, 2010a; Huang; Xie, 2010c; Sigmund; Maute, 2013). In the works of Rozvany and Querin (2002) the consideration of a Sequential Element Rejection and Admission (SERA) method was defined, in a way that void elements would be replaced by a soft material with very low density, introducing the concept of soft-kill ( $0 < x_{\min} \ll 1$ ). Later, Huang and Xie (2009) considered a power-law, similar to the one used in SIMP, together with the soft-kill strategy, to calculate the gradients of the objective function instead of the its approximate variations. This procedure is presented next.

### 3.2 Sensitivity Analysis

Aiming to obtain a full-void design, the material interpolation scheme is presented,

$$E(x_i) = E_e x_i^\zeta, \quad (3.3)$$

leading to,

$$\mathbf{K} = \sum_{i=1}^{N_{\text{elD}}} x_i^\zeta \mathbf{K}_e^i, \quad (3.4)$$

where  $E$  is the Young's modulus of the structure,  $E_e$  is the Young's modulus of the elastic material,  $\zeta$  is a penalty coefficient and  $\mathbf{K}_e$  is the global stiffness matrix of the elastic material. Elemental variables are defined with the subscript/superscript  $i$ .

When an element is added or removed from the design domain the objective function is modified as a result of such structural change. This alteration is generally referred as sensitivity number,  $\alpha_i$ , and is attributed to the modified element. In the soft-kill BESO approach, these sensitivities are based on the gradient of the objective function, hence,

$$\frac{dC}{dx_i} = \frac{1}{2} \frac{d}{dx_i} (\hat{\mathbf{f}}^T \hat{\mathbf{u}}) = \frac{1}{2} \left( \frac{\partial \hat{\mathbf{f}}^T}{\partial x_i} \hat{\mathbf{u}} + \hat{\mathbf{f}}^T \frac{\partial \hat{\mathbf{u}}}{\partial x_i} \right). \quad (3.5)$$

As  $\partial \hat{\mathbf{u}}/dx_i$  is unknown, the adjoint method (Tortorelli; Michaleris, 1994) is applied by the introduction of a Lagrange multiplier vector in Eq. (3.1),

$$L = \frac{1}{2} \hat{\mathbf{f}}^T \hat{\mathbf{u}} + \boldsymbol{\lambda}^T (\hat{\mathbf{f}} - \mathbf{K} \hat{\mathbf{u}}). \quad (3.6)$$

Considering  $\partial \hat{\mathbf{f}}/\partial x_i = 0$ , one gets,

$$\frac{dL}{dx_i} = \left( \frac{1}{2} \hat{\mathbf{f}}^T - \boldsymbol{\lambda}^T \mathbf{K} \right) \frac{\partial \hat{\mathbf{u}}}{\partial x_i} - \boldsymbol{\lambda}^T \frac{\partial \mathbf{K}}{\partial x_i} \hat{\mathbf{u}}. \quad (3.7)$$

To eliminate the unknown variable,  $\partial \hat{\mathbf{u}}/dx_i$ , from Eq. (3.7),  $\boldsymbol{\lambda}$  may be chosen such that,

$$\frac{1}{2} \hat{\mathbf{f}}^T - \boldsymbol{\lambda}^T \mathbf{K} = \mathbf{0}. \quad (3.8)$$

From the mechanical equilibrium equation,

$$\hat{\mathbf{f}}^T = \hat{\mathbf{u}}^T \mathbf{K}^T = \hat{\mathbf{u}}^T \mathbf{K}, \quad (3.9)$$

hence,

$$\boldsymbol{\lambda} = \frac{1}{2} \hat{\mathbf{u}}, \quad (3.10)$$

and,

$$\frac{dL}{dx_i} = -\frac{1}{2} \hat{\mathbf{u}}^T \frac{\partial \mathbf{K}}{\partial x_i} \hat{\mathbf{u}}. \quad (3.11)$$

With the help of the material interpolation scheme, Eq. (3.4), the following is obtained,

$$\alpha_i = -\frac{1}{2}\zeta x_i^{\zeta-1}(\hat{\mathbf{u}}_i)^T \mathbf{K}_e^i \hat{\mathbf{u}}_i. \quad (3.12)$$

Knowing that the BESO method is of discrete nature, Eq. (3.12) can be rewritten as,

$$\alpha_i = -\frac{1}{\zeta} \frac{\partial L}{\partial x_i} = \begin{cases} \frac{1}{2}(\hat{\mathbf{u}}_i)^T \mathbf{K}_e^i \hat{\mathbf{u}}_i & \text{when } x_i = 1, \\ \frac{x_{\min}^{\zeta-1}}{2}(\hat{\mathbf{u}}_i)^T \mathbf{K}_e^i \hat{\mathbf{u}}_i & \text{when } x_i = x_{\min}, \end{cases} \quad (3.13)$$

where the exponent  $\zeta$  penalizes only void elements. In most cases,  $x_{\min} = 0.001$  is set.

The presented gradient-based soft-kill approach facilitates the sensitivity analysis of several discrete optimization algorithms, especially those involving multiple materials (Huang; Xie, 2009; Anaya-Jaimes *et al.*, 2022; Pereira *et al.*, 2023) and constraints (Huang; Xie, 2010b; Zuo *et al.*, 2012; Munk *et al.*, 2018; Pereira *et al.*, 2022), and has been used in several works over the past decade, such as in the optimization of natural frequencies (Picelli *et al.*, 2015; Lopes *et al.*, 2021), piezoelectric energy harvesters (Almeida *et al.*, 2019), muffler chambers (Azevedo *et al.*, 2018), fluid-structure based systems (Vicente *et al.*, 2015; Vicente *et al.*, 2016; Kook, 2019; Dilgen *et al.*, 2019), multi-objective and multiscale approaches (Yan *et al.*, 2015), non-linear structures (Xia; Breitkopf, 2017), among others (Zhao, 2014; Xia *et al.*, 2018).

### 3.3 Mesh-Independent Filter Scheme

When discretizing a continuous domain with low-order bilinear (2D) or trilinear (3D) finite elements few issues may arise due to the possibility of the sensitivity numbers become  $C^0$  discontinuous across the element boundaries (Huang; Xie, 2007). Between them are checkerboard patterns (Jog; Haber, 1996) and mesh dependency (Sigmund, 1997), which may be dealt with the adoption of numeric filters. As discussed by Dilgen *et al.* (2019), convolution (Bruns; Tortorelli, 2001) and Helmholtz (Lazarov; Sigmund, 2011) type density filters can be thought as valid choices for the solution of the aforementioned problems. Another common way is based on the projection of the nodal sensitivity numbers along the design domain. A particular form of this last one has been introduced by Huang and Xie (2009), Huang and Xie (2010a), for applications regarding BESO-based optimizations. Therefore, it has been chosen in the current work.

The overall procedure starts with the distribution of the elemental sensitivity numbers between the nodes. As these have no physical meaning, averaged elemental sensitivity numbers must be retrieved. For this, a mesh independent filter radius,  $r_{\min}$ , is placed at the center of each

element. All nodes within this radius are then considered contributors to the sensitivity number that finally result. The  $r_{\min}$  subdomain created in the  $i$ th element is illustrated in Fig. 3.1.

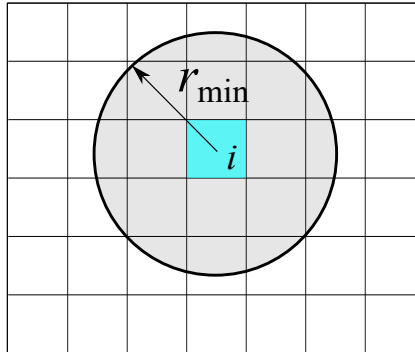


Figure 3.1 –  $r_{\min}$  subdomain created in the  $i$ th element

Considering  $\alpha_{n_d}$  the  $n_d$ th node sensitivity number,  $M$  the amount of elements connected to the  $n_d$ th node,  $w_i$  a weight factor regarding the  $i$ th element (Eq. (3.15)) and  $r_{in}$  the distance from the centroid of the  $i$ th element to the  $n_d$ th node, the nodal sensitivity numbers may be expressed as,

$$\alpha_{n_d} = \sum_{i=1}^M w_i \alpha_i, \quad (3.14)$$

with,

$$w_i = \begin{cases} 1 & \text{if } M = 1, \\ \frac{1}{M-1} \left( 1 - \frac{r_{in}}{\sum_{i=1}^M r_{in}} \right) & \text{if } M > 1. \end{cases} \quad (3.15)$$

Eq. (3.15) indicates that closer nodes to the  $i$ th element have a stronger contribution in obtaining the nodal sensitivity numbers than far ones. Finally, the smoothed elemental sensitivities are,

$$\alpha_i = \frac{\sum^I w(r_{in}) \alpha_{n_d}}{\sum^I w(r_{in})}, \quad (3.16)$$

with  $I$  defined as a list of the nodes that are inside the  $r_{\min}$  subdomain and  $w(r_{in}) = r_{\min} - r_{in}$  being a linear weight factor.

### 3.4 Sensitivity Stabilization Procedure and Normalization

To increase the stability of the optimizer, one common approach is to adopt an additional sensitivity historical averaging, which can be,

$$\alpha_i^{(r)} = \frac{\alpha_i^{(r-1)} + \alpha_i^{(r)}}{2}, \quad (3.17)$$

with the superscript  $(\cdot)^{(r)}$  referring to the ongoing iteration of the topology optimization algorithm.

Another stabilization procedure was proposed by [Zhou \*et al.\* \(2021\)](#), regarding a Min-Max scaling methodology for normalization of values. In many situations, this additional step is recommend to be applied on the sensitivities, as those are filled with positive and negative numbers, hence,

$$\alpha_i^{(r)} = \frac{\alpha_i^{(r)} - \alpha_{\min}^{(r)}}{\alpha_{\max}^{(r)} - \alpha_{\min}^{(r)}}, \quad (3.18)$$

where  $\alpha_{\max}^{(r)}$  and  $\alpha_{\min}^{(r)}$  are the maximum and minimum sensitivity number values of the current iteration, respectively.

### 3.5 Heuristic Design Update and Stop Criterion

To update the design variables it is imperative to first define the target volume for the next iteration. With the use of the Evolutionary Rate (ER) as the change in volume for each iterative step, one may write the expression that relates the volume fraction of the current,  $V_r$ , and next,  $V_{r+1}$ , iterations,

$$V_{r+1} = V_r(1 \pm \text{ER}). \quad (3.19)$$

In evolutionary optimization methods, the sensitivity numbers are local indexes that can be sorted from highest to lowest, leading the material types to be changed accordingly; in other words, the definition of  $V_{r+1}$  establishes a threshold in the sorted sensitivity vector that defines the amount of elements that will be void ( $x_i = x_{\min}$ ) and full ( $x_i = 1$ ), hence,

$$\alpha_i \leq \alpha_{\text{th}} \quad \text{as} \quad \text{void elements}, \quad (3.20)$$

$$\alpha_i > \alpha_{\text{th}} \quad \text{as} \quad \text{full elements}, \quad (3.21)$$

where  $\alpha_{\text{th}}$  is the threshold sensitivity number. Seeing that BESO is a bi-directional procedure, the addition of elements is also possible. The Addition Ratio (AR) is the variable that defines the amount void/full elements that can become full/void. However, in order to control this quantity, the maximum Addition Ratio ( $\text{AR}_{\max}$ ) is required as one of the inputs of the method. If the case  $\text{AR} > \text{AR}_{\max}$  happens, the restriction  $\text{AR} = \text{AR}_{\max}$  has to be enforced. This fact results in the imposition that some elements with the lowest  $\alpha_i$  become void, and some with the highest  $\alpha_i$  become full ([Picelli \*et al.\*, 2015](#)).

At last, the stop criterion is stated,

$$err = \left| \frac{\sum_{m=1}^N C_{r-m+1} - \sum_{m=1}^N C_{r-N-m+1}}{\sum_{m=1}^N C_{r-m+1}} \right| \leq \tau, \quad (3.22)$$

where  $\tau$  refers to the tolerance and  $N$  to the number of iterations considered in the historical average. It is remarkable that when the final volume fraction,  $V^f$ , is reached,  $V$  can no longer change until the optimization process is terminated by the fulfillment of Eq. (3.22).

### 3.6 BESO Algorithm

This section presents the overall BESO procedure, which can be expanded to several optimization problems, as shown in the following chapters. The steps are:

- Step 1: Discretize the entire domain, assign proper design variables to the elements of the initial guess design and define BESO parameters in accordance with the optimization problem under investigation;
- Step 2: Execute the finite element procedure (see Chapter 2 for a complete description of various systems governing equations);
- Step 3: Carry out the sensitivity analysis (see Section 3.2 for the compliance problem example). In all the cases presented in this work, the sensitivity numbers were validated by the finite differences method;
- Step 4: Apply the mesh-independent filter scheme to the sensitivity numbers, following Section 3.3;
- Step 5: Apply the sensitivity historical averaging procedure and the Min-Max scaling methodology to the sensitivity numbers, as established in Section 3.4;
- Step 6: Define the volume target for the next iteration, Eq. (3.19);
- Step 7: Add and delete elements according to the update scheme shown in Section 3.5;
- Step 8: Repeat steps 2 to 7 until the final volume is reached and the stop criteria, Eq. (3.22), is satisfied.

Fig. 3.2 illustratively shows the flowchart of the BESO method.

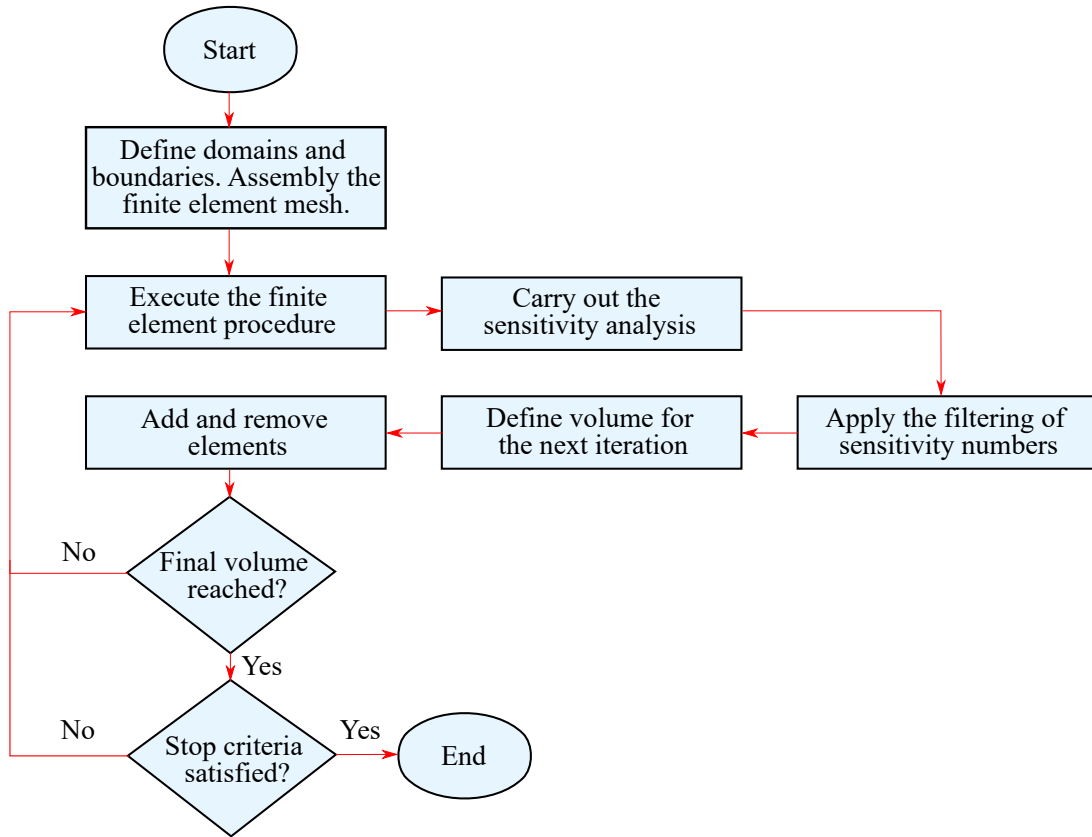


Figure 3.2 – Flowchart of the BESO method

### 3.7 Acoustic Topology Optimization Based on the BESO Approach

In this work, a set of methodologies implemented to solve different Acoustic Topology Optimization (ATO) problems is proposed. Based on BESO method, a multiconstrained approach is investigated in Chapter 4, where the Virtual Temperature Method (VTM) (Liu *et al.*, 2015) has been adapted for use in acoustic domain problems. In Chapter 5, the optimization of multichamber mufflers is investigated, while promoting the addition of poro-rigid and rigid structures within the design domain. For this, a new multiphase material interpolation scheme is proposed, adapting the BESO method for the introduction of more than one material per iteration. In Chapter 6, the multiphysics involving fully modeled acoustic, poroelastic and elastic domains are targeted in the optimization of closed-space soundproof systems. Here, the newly introduced material interpolation scheme of Chapter 5 is modified to account for such complex interactions, leading to the proposition of a new evolutionary methodology.

Furthermore, it is important to note that the BESO algorithm presented in this chapter for the purely structural case of minimizing static compliance can be fully converted to optimizations involving various other physics, such as acoustics, electrical, thermal, and so on.

By implementing the finite element method in systems that describe these different physical models, their respective field problems are solved independently, thus obtaining characteristic field variables such as pressures, potential energies, and temperatures. These results are then provided as input to the BESO algorithm, as well as the objective functions, initiating the evolutionary optimization procedure. It should also be emphasized that sensitivities directly depend on the chosen objective function and therefore need to be calculated accordingly. In this work, the objective functions are Sound Pressure Levels (SPL), absorption coefficient, Transmission Losses (TL) and Dissipated Power Levels ( $PL_D$ ), being thoroughly derived in all sensitivity analysis sections, as they are constantly adopted in vibroacoustic investigations. The BESO algorithm described in this thesis was implemented in the MATLAB<sup>®</sup> software, for the applications presented in Chapters 4 and 5, and in Python, for the study shown in Chapter 6.

## 4 | A Multiconstrained Evolutionary Approach

In this chapter, the original research article entitled “Topology optimization of acoustic systems with a multiconstrained BESO approach” by Rodrigo Lima Pereira, Heitor Nigro Lopes and Renato Pavanello, is presented with permission from Elsevier (see Appendix C for the correspondent copyright clearance). The paper has been published in the *Finite Elements in Analysis and Design*, v. 201, p. 103701, 2022. DOI: 10.1016/j.finel.2021.103701.

The article establishes a new methodology to design simply-connected acoustic systems using the modified Virtual Temperature Method for acoustic applications as an additional constraint, hence configuring a multiconstrained topology optimization approach. This procedure is applied in two completely different acoustic systems, considering porous and rigid materials. Despite the reduced space of solutions imposed by the additional constraint, most of the structures here obtained present highly manufacturable topologies, free of air hole seclusion, and enhanced acoustic characteristics.

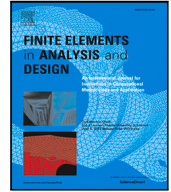
Chapter 7 presents further discussions on the topics and results given here and Appendix A displays detailed extensions of the procedures introduced in the sensitivity analysis sections.



Contents lists available at [ScienceDirect](https://www.sciencedirect.com)

## Finite Elements in Analysis & Design

journal homepage: [www.elsevier.com/locate/finel](http://www.elsevier.com/locate/finel)



# Topology optimization of acoustic systems with a multiconstrained BESO approach

Rodrigo L. Pereira<sup>\*</sup>, Heitor N. Lopes, Renato Pavanello

Department of Computational Mechanics, School of Mechanical Engineering, University of Campinas, Rua Mendeleev 200, 13083-860 Campinas, Brazil

### ARTICLE INFO

#### Keywords:

Topology optimization  
BESO  
Virtual Temperature Method  
Acoustic metasurface  
Porous materials

### ABSTRACT

This work details a new acoustic topology optimization methodology with applications on the design of systems composed of rigid and porous materials. The Bi-directional Evolutionary Structural Optimization (BESO) algorithm is combined with the Virtual Temperature Method to minimize the occurrence of air cavities and rough surfaces inside rigid and porous domains, hence configuring a multiconstrained optimization approach. The modeling of porous materials is done by the Johnson–Champoux–Allard (JCA) formulation, while the Finite Element Method is used to approximate the governing equations of the physical system. Two different optimization problems are considered separately: first, a rigid–acoustic metasurface is optimized to reduce regional sound pressure levels (SPL) in a set of observed frequencies, while also considering wind permeability through the structure. Secondly, a coupled poro-acoustic absorptive system is treated in order to enhance the sound absorption coefficient in the low frequency range. Both problems are systematized by the implementation of acoustic–rigid and acoustic–porous material interpolation schemes, respectively. The effectiveness of the proposed approach is explored through numerical examples. Here, it is remarked that the methodology maintains the uniformity of rigid barriers, by guaranteeing the absence of internal holes to them. In addition, well-defined cavities are formed in porous domains, increasing their absorption coefficients, but without inflicting macroscopic closed spaces within such structures. In these cases, comparison with appropriate literature is also provided.

### 1. Introduction

With the growing demand for efficient engineering projects, efforts have been made to reduce the use of raw materials when manufacturing structures, while enhancing some characteristics of the physical system as a whole. Structural optimization emerged with the goal of assisting engineers in the design of such complex compositions under a series of previously imposed constraints. Combining homogenization techniques with structural optimization methods, Bendsoe and Kikuchi [1] led the field of topology optimization research in the late 1980s. From that moment on, this technique gave rise to a broad range of methods [2–5].

As highlighted by Sigmund and Maute [6] and Xia et al. [7], an important branch of gradient-based topology optimization techniques is the evolutionary one, represented by the Evolutionary Structural Optimization (ESO) and the Bi-directional ESO (BESO) methodologies. Proposed by Xie and Steven [4,8], the ESO method aims at the gradual removal of inefficient material from the structure to improve a chosen objective function.

Nevertheless, since the ESO algorithm only removes material, the optimization procedure is somewhat biased by the first iterations. With

that in mind, Yang et al. [5] proposed the BESO method by including the possibility of material addition to the system. As a gradient-based topology optimization approach, the sensitivity analysis must be performed in all optimization problems. In this context, elementary sensitivity can be understood as the discrete variations that an element would cause in the objective function, when being added or removed from the structure. Thus, elements with lower and higher sensitivity numbers are respectively removed and added to the design domain, in order to make the structure evolve to an optimal topology.

Afterwards, Querin et al. [9] used this newly implemented idea to optimize structures according to their von Mises stress levels, enabling the addition of material to regions with high local stress. It is worth mentioning, however, that the BESO approach had some numerical problems such as checkerboard pattern [10], mesh dependency [11] and unconnected variables for addition and rejection of material. These adversities motivated Huang and Xie [12] to propose the new BESO algorithm, by including sensitivity filters [11, 13], evolutionary stabilization procedures [14] and material interpolations schemes [15] to the methodology. This approach has been

<sup>\*</sup> Corresponding author.

E-mail addresses: [pereira@fem.unicamp.br](mailto:pereira@fem.unicamp.br) (R.L. Pereira), [lopes@fem.unicamp.br](mailto:lopes@fem.unicamp.br) (H.N. Lopes), [pava@fem.unicamp.br](mailto:pava@fem.unicamp.br) (R. Pavanello).

<https://doi.org/10.1016/j.finel.2021.103701>

Received 9 August 2021; Received in revised form 14 October 2021; Accepted 18 October 2021  
0168-874X/© 2021 Elsevier B.V. All rights reserved.

extensively used over the past decade in the optimization of several multiphysical systems, including natural frequencies [16,17], piezoelectric energy harvesters [18] and fluid–structure interactions [19–21]; and motivated the rise of a new range of optimization procedures such as the nodal design variable ESO/BESO method based on Shepard interpolation [22].

The conceptualization of acoustic projects has been largely combined with the use of topology optimization algorithms. Wadbro and Berggren [23] were the first to use such methods to design an acoustic horn, with the goal of enhancing its sound radiation properties. All the acoustic environment was simulated by the scalar Helmholtz equation. Dühring et al. [24] used the SIMP method to optimize indoor and outdoor rigid sound barriers, aiming to reduce the mean squared pressure amplitude in an observed region. For this, the inverses of mass density and bulk modulus were considered as the main variables in the proposed material interpolation scheme.

Lee and Kim [25,26] applied topology optimization techniques to various acoustic systems, being the first to consider such methodologies in the design of internal partitions of reactive mufflers. Oh and Lee [27] optimized an automotive muffler under the influence of temperature gradients. Kook et al. [28] adopted the Zwicker's loudness model [29] as the objective function for the design of rigid sound barriers, while Miyata et al. [30] used the same function for the optimization of multifunctional metasurfaces. Finally, Hu et al. [31] used an ersatz material model, together with a floating projection optimizer, to design dynamic acoustic–mechanical structures without the need for boundary tracking.

To avoid the multiphysical complexities involved in Biot's equations, several studies have adopted simplified porous material formulations when dealing with topology optimization procedures. Silva and Pavanello [32,33] and Yoon et al. [34] adopted equivalent fluid models, such as the Johnson–Champoux–Allard (JCA) [35,36], to describe complex equations for the effective density and bulk modulus of the optimized structures. Furthermore, Yoon [37] and Ferrándiz et al. [38] used the empirical Delany–Bazley formulation [39] to describe the behavior of fibrous materials with porosities close to the unit. However, none of these acoustic topology optimization (ATO) researches adopted the BESO approach as optimizer.

In the BESO context, Picelli et al. [16] and Vicente et al. [19] studied free vibration problems involving acoustic–structural effects. Kook [21] and Dilgen et al. [40] combined the BESO with the mixed ( $u/p$ ) formulation for fluid–structure interactions [41]. Huang and Xie [42] minimized static compliance with an additional displacement constraint for a continuum structure, while Zuo et al. [43] considered multiple displacement and frequency constraints, and Munk et al. [44] adopted additional smart normal constraint to the evolutionary method. Shortly thereafter, Azevedo et al. [45] designed internal partitions of an automotive muffler to maximize sound transmission losses at target frequencies. Here, the authors considered rigid materials to compose the acoustic barriers that appeared in the reactive expansion chamber.

As manufacturing is a crucial part in the design of structures, Liu et al. [46] proposed a connectivity procedure called Virtual Temperature Method (VTM), aiming to avoid enclosed voids inside solid materials. The main idea is that solid materials are considered as thermal insulators, while voids are treated as heat sources and thermal conductors. This virtual composition allows for sudden increases of the system temperature once enclosed voids appear in the design domain. Based on that, one way to provide simply-connected topologies is by constraining the system temperature throughout the entire optimization process. Despite the relative success obtained by this method in mechanical applications [46–48], it appears necessary to verify how acoustic systems behave with the addition of such connectivity constraints in a context of discrete topology optimization treatments. This paper is focused on such investigations.

That being said, the BESO algorithm is employed in this work to solve two different ATO problems, while considering the acoustic VTM to avoid seclusion of air holes inside rigid and porous structures, hence configuring a multiconstrained optimization methodology. Particularly, problem 1 (P1) aims to optimize rigid-acoustic metasurfaces that are able to reduce regional sound pressure levels (SPL) in four different target frequencies, while considering wind permeability through the structure. Problem 2 (P2) proposes the design of coupled poro-acoustic absorptive systems for maximizing the sound absorption coefficient at low frequency range. Since our main goal is to establish a new methodology to design simply-connected acoustic systems, pertinent optimization aspects are explored through numerical examples, such as the evolutionary behavior of acoustic functions in a multiconstrained optimization approach and the manufacturability of the resulting topologies.

The organization of this paper is presented as follows: In Section 2, the acoustic problem is formulated using the finite element approach. In Section 3, the properties of acoustic, porous and rigid materials are discussed, together with the Johnson–Champoux–Allard (JCA) model. Also in this section, appropriate material interpolation schemes are defined for problems 1 and 2. Section 4 introduces the modified Virtual Temperature Method (VTM) for acoustic applications, and in Section 5 the multiconstrained BESO approach is described in detail. Numerical examples and their thorough examinations are provided in Section 6. Finally, conclusions are drawn in Section 7.

## 2. Finite element formulation of acoustic systems

The equation that governs a steady-state inviscid fluid domain  $\Omega$ , with sound pressure as a time-harmonic function ( $p(x, y, t) = p(x, y)e^{i\omega t}$ ), can be written, in the frequency domain, as the following scalar Helmholtz equation,

$$\nabla \cdot \left( \frac{\nabla p(x, y)}{\rho} \right) + \frac{\omega^2}{\kappa} p(x, y) = 0 \quad \text{with } \kappa = \rho c^2 \quad \text{in } \Omega, \quad (1)$$

where  $\rho$  is the density,  $\kappa$  is the bulk modulus,  $p(x, y)$  is the pressure in a bidimensional Eulerian field  $(x, y)$ ,  $c$  is the speed of sound in the fluid,  $j = \sqrt{-1}$  is the complex variable,  $\omega$  is the angular frequency,  $t$  is time and  $\nabla$  is the gradient operator. For simplicity, the pressure field  $p(x, y)$  will be referred only as  $p$ .

As a general aspect, Eq. (1) can be solved when combined with the following boundary conditions [49],

$$p = \bar{p} \quad \text{in } \Gamma_1, \quad (2)$$

$$\nabla p \cdot \mathbf{n} = 0 \quad \text{in } \Gamma_2, \quad (3)$$

$$\nabla p \cdot \mathbf{n} = \bar{a}_n \quad \text{in } \Gamma_3, \quad (4)$$

where  $\mathbf{n}$  refers to the outward unit normal vector,  $\bar{p}$  to imposed pressures and  $\bar{a}_n$  to imposed particle accelerations. The symbols  $\Gamma_1$ ,  $\Gamma_2$  and  $\Gamma_3$  refer to the different boundary types in which Eqs. (2), (3) and (4) are valid. The weighted residuals approach is combined with the divergence theorem to yield the weak form of the scalar Helmholtz equation,

$$\frac{1}{\rho} \int_{\Omega} \nabla p \cdot \nabla \delta p \, d\Omega - \frac{\omega^2}{\kappa} \int_{\Omega} p \delta p \, d\Omega - \int_{\Gamma} \bar{a}_n \delta p \, d\Gamma = 0, \quad (5)$$

where  $\delta p$  is the test function and  $\Gamma$  is the boundary of  $\Omega$ .

To provide a discrete approximation of the continuous problem, the Finite Element Method (FEM) is considered [49,50]. The pressure field and its gradient can be expressed, in the element domain  $\Omega_e$ , as,

$$p = \mathbf{N}_e \mathbf{p}_e, \quad (6)$$

$$\nabla p = \mathbf{B}_e \mathbf{p}_e, \quad (7)$$

where  $\mathbf{N}_e$  and  $\mathbf{B}_e$  are the shape function matrix and its gradient, respectively, with the elemental acoustic pressure vector represented

by  $\mathbf{p}_e$ . Following Galerkin's method, the test function and its gradient can be written in a similar manner,

$$\delta p = \mathbf{N}_e \delta \mathbf{p}_e, \quad (8)$$

$$\nabla \delta p = \mathbf{B}_e \delta \mathbf{p}_e, \quad (9)$$

with  $\delta \mathbf{p}_e$  denoting the test function vector of the  $e$ th element. Applying Eqs. (6), (7), (8) and (9) into (5), the acoustic stiffness and mass matrices in  $\Omega_e$  are obtained,

$$\mathbf{K}_e = \frac{1}{\rho} \int_{\Omega_e} \mathbf{B}_e^T \mathbf{B}_e d\Omega_e, \quad (10)$$

$$\mathbf{M}_e = \frac{1}{\kappa} \int_{\Omega_e} \mathbf{N}_e^T \mathbf{N}_e d\Omega_e, \quad (11)$$

together with the element load vector defined in the  $\Gamma_e$  boundary of  $\Omega_e$ ,

$$\mathbf{f}_e = \bar{a}_n \int_{\Gamma_e} \mathbf{N}_e^T d\Gamma_e. \quad (12)$$

Following the standard finite element assembly procedure,

$$\mathbf{K} = \sum_{e=1}^{N_{el}} \mathbf{K}_e, \quad (13)$$

$$\mathbf{M} = \sum_{e=1}^{N_{el}} \mathbf{M}_e, \quad (14)$$

$$\mathbf{f} = \sum_{e=1}^{N_{bc}} \mathbf{f}_e, \quad (15)$$

the acoustic dynamic system can be finally written,

$$\mathbf{Zp} = (\mathbf{K} - \omega^2 \mathbf{M})\mathbf{p} = \mathbf{f}, \quad (16)$$

where  $A_{e=1}^{N_{el}}$  and  $A_{e=1}^{N_{bc}}$  are assembly operators,  $N_{el}$  is the total number of elements in the fluid domain and  $N_{bc}$  is the total number of elements in the considered boundary. The global acoustic stiffness and mass matrices are represented by  $\mathbf{K}$  and  $\mathbf{M}$ , while the global acoustic load and pressure vectors are  $\mathbf{f}$  and  $\mathbf{p}$ , respectively.

### 3. Properties of acoustic, porous and rigid materials

The main goal of this work is to establish a new methodology to design simply-connected acoustic systems by using a multiconstrained BESO approach in two different ATO problems. For this reason, it is important to clearly define which materials are considered and how they influence the optimization process. According to Lee and Kim [25], it is common practice to consider only density,  $\rho$ , and bulk modulus,  $\kappa$ , as functions of the design variables. This simple approach greatly facilitates the optimization process, as it allows the materials to be continuously governed by the scalar Helmholtz equation, and thus, avoids the complexities involved in fluid–structure formulations. So, apart from air, rigid materials and porous materials with rigid frame (also known as poro-rigid or equivalent fluids) are adopted in this work.

Following many researchers [24,25,34,51], a body can be considered as rigid when a high acoustic impedance is assigned to it, hence resulting in a greatly amplification of the air density and bulk modulus. In order to avoid erroneous values in this approximation, Lee and Kim [25,26] studied simple acoustic settings and concluded that the combination of  $\rho_r \geq 10^5 \rho_a$  and  $c_r \geq 10^1 c_a$  is a safe choice for most problems, where the subscripts  $a$  and  $r$  refer to acoustic and rigid material properties, respectively. With that in mind, the following data are adopted in this work,

$$\rho_a = 1.21 \text{ kg m}^{-3} \quad \text{and} \quad \kappa_a = 1.42 \cdot 10^5 \text{ Pa}, \quad (17)$$

$$\rho_r = 10^7 \rho_a \text{ kg m}^{-3} \quad \text{and} \quad \kappa_r = 10^9 \kappa_a \text{ Pa}. \quad (18)$$

According to Allard and Atalla [52], many semi-phenomenological models are used to describe the propagation of sound in porous bodies, since it is not possible to account for a complete description of their microstructure. A recurring feature of these models is the equivalent fluid

**Table 1**

Parameters related to the JCA model [32,33].

Rock-wool parameters	Values
Porosity $\phi$	0.94
Tortuosity $\alpha_\infty$	2.1
Static flow resistivity $\sigma$ (N s m <sup>-4</sup> )	135,000
Viscous characteristic length $\Lambda$ ( $\mu\text{m}$ )	49
Thermal characteristic length $\Lambda'$ ( $\mu\text{m}$ )	166
Air (20 °C) Parameters	Values
Kinematic viscosity $\eta$ (kg m <sup>-1</sup> s <sup>-1</sup> )	$1.84 \cdot 10^{-5}$
Specific heat ratio $\gamma$	1.401
Prandtl number $Pr$	0.710
Atmospheric pressure $P_0$ (Pa)	101,325

simplification, that considers the long-wavelength condition by stating that the pores are considerably smaller than the wavelength, allowing the porous frame to be set as motionless. Despite that, the visco-inertial and thermal effects are still considered by setting frequency-dependent and complex valued equations to define the effective density,  $\rho_p$ , and effective bulk modulus,  $\kappa_p$  of porous structures, being the only two descriptive variables in an equivalent fluid interpretation.

Taking that into account, the Johnson–Champoux–Allard (JCA) [35, 36] formulations are the ones adopted in this work,

$$\rho_p(\omega) = \frac{\alpha_\infty \rho_a}{\phi} \left( 1 + \frac{\sigma \phi}{j \omega \rho_a \alpha_\infty} \sqrt{1 + j \frac{4 \alpha_\infty^2 \eta \rho_a \omega}{\sigma^2 \Lambda^2 \phi^2}} \right), \quad (19)$$

$$\kappa_p(\omega) = \frac{\gamma P_0}{\phi} \left[ \gamma - (\gamma - 1) \left( 1 - j \frac{8 \eta}{\Lambda'^2 Pr \rho_a \omega} \sqrt{1 + j \frac{\Lambda'^2 Pr \rho_a \omega}{16 \eta}} \right)^{-1} \right]^{-1}, \quad (20)$$

where five intrinsic parameters of porous structures are introduced, being  $\phi$  the porosity,  $\alpha_\infty$  the tortuosity,  $\Lambda$  the viscous characteristic length,  $\Lambda'$  the thermal characteristic length and  $\sigma$  the static flow resistivity. Furthermore, the thermodynamic properties of the air that saturates the porous medium can also be described as the kinematic viscosity  $\eta$ , the specific heat ratio  $\gamma$ , the Prandtl number  $Pr$ , and the atmospheric pressure  $P_0$ . Table 1 lists the parameters related to the JCA model for rock-wool, the chosen porous material, and air at 20 °C.

#### 3.1. Material interpolation scheme

It is quite common to use material interpolation schemes (MIS) in topology optimization problems to change material properties in a systematic manner. In density-based procedures, this interpolation is treated as a polynomial function of the design variables, that vary continuously between 0 and 1. Additionally, these functions can have penalty variables, which work as degrees of the polynomial, in order to assist the solution to nearly full-void designs [12,15]. It is interesting to note, however, that such MIS were introduced to impose an additional relaxation in the original topology optimization discrete problems, transforming those design variables into continuum ones.

Since one of the key features of the BESO approach is related with its discrete nature, one may not be obliged to use a MIS in order to obtain clearly defined topologies. However, many works have been using this resource in order to avoid numerical singularities and to reduce computational costs involved in structural and fluid–structural optimization procedures [12,16,19,20]. These researches have shown that the adoption of an appropriate MIS can even bring stability to the evolutionary process and increase the manufacturability of the optimized topologies, since they enable the evaluation of the objective function gradient [21].

This paper presents two distinct ATO problems, related with the BESO approach, that aims to demonstrate the capabilities of the chosen methodology. The first problem (P1) intends to achieve an optimized metasurface which reduces SPL values by considering rigid and acoustic

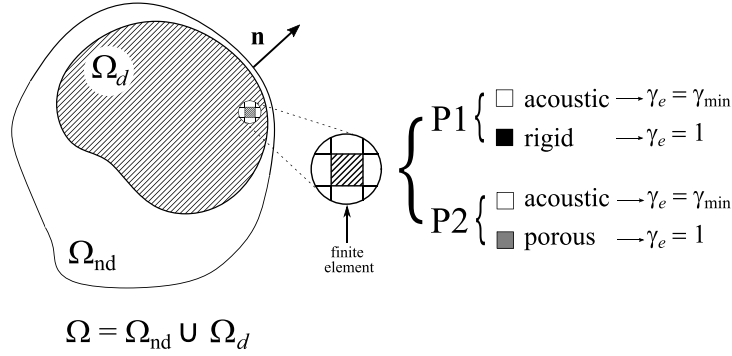


Fig. 1. Finite element model of an acoustic system divided into design,  $\Omega_d$ , and non-design,  $\Omega_{nd}$ , domains, with highlight of the material types and design variable limit values for P1 and P2.

elements in the optimization process. As for the second one (P2), an absorptive system is studied to optimize the absorption coefficient at the low frequency range, with porous and acoustic elements allowed in the design domain.

In this sense, and knowing that the inverses of density and bulk modulus are the variables that multiply directly the acoustic element matrices in a finite element methodology, the set of Eqs. (21) and (22) presents, respectively, the MIS considered in the aforementioned situations,

$$P1 \rightarrow \begin{cases} \frac{1}{\rho(\gamma_e)} = \frac{1}{\rho_a} + \gamma_e^\psi \left( \frac{1}{\rho_r} - \frac{1}{\rho_a} \right), \\ \frac{1}{\kappa(\gamma_e)} = \frac{1}{\kappa_a} + \gamma_e^\psi \left( \frac{1}{\kappa_r} - \frac{1}{\kappa_a} \right), \end{cases} \quad (21)$$

$$P2 \rightarrow \begin{cases} \frac{1}{\rho(\gamma_e)} = \frac{1}{\rho_a} + \gamma_e^\eta \left( \frac{1}{\rho_p} - \frac{1}{\rho_a} \right), \\ \frac{1}{\kappa(\gamma_e)} = \frac{1}{\kappa_a} + \gamma_e^\eta \left( \frac{1}{\kappa_p} - \frac{1}{\kappa_a} \right), \end{cases} \quad (22)$$

with  $\gamma_e$  representing the design variable, the superscripts  $\psi$  and  $\eta$  being the penalty variables, and the subscripts  $a$ ,  $p$  and  $r$  referring to acoustic, porous and rigid materials, respectively. Since the BESO method uses discrete design variables, as stated previously, an investigation was conducted in order to define the limit values of  $\gamma_e$  that would bring stability to the optimization process. So, for all the problems here presented,  $\gamma_e = \gamma_{min} = 0.001$  or  $\gamma_e = 1$  are adopted together with  $\psi = \eta = 2$ .

Fig. 1 illustrates that each optimization problem in consideration allows for specific types of finite elements to be treated in the design domain,  $\Omega_d$ , while in the non-design domain,  $\Omega_{nd}$ , the elements are always kept as air (acoustic elements). The limit values of the design variables and its corresponding element types are also presented, which may be directly related to Eqs. (21) and (22) for both P1 and P2 problems.

#### 4. Connectivity procedure: modified Virtual Temperature Method for acoustic applications

Introduced by Liu et al. in 2015 [46], the Virtual Temperature Method (VTM) is a temperature based procedure, in which the manufacture constraints are taken into account. Such approach consists in converting the connectivity restrictions into an equivalent maximum temperature constraint through the sudden increase of the system temperature, whenever an internal hole appears [47]. As shown at the left side of Fig. 2, air holes are considered to be thermal conductors and active heat sources, which can provoke sudden increases in the system temperature if they are secluded in the insulated material (also referred

as dominant). In the event that these air holes come into contact with the zero temperature boundaries, then, through conduction, the heat from these regions dissipate, lowering their temperatures, as also shown at the right side of Fig. 2.

In this same illustration, variables  $Q$  and  $k_i$  represent the rate of internal heat generation and the thermal conductivity, while  $Q_0$  and  $k_{i0}$  are user defined constants. In addition, the superscripts  $d$  and  $h$  refer to the dominant material and the air holes, respectively. To represent an inactive heat source and avoid singularities, a small number  $\xi = 10^{-6}$  is adopted, while  $\gamma_e$  can only have two discrete values:  $\gamma_{min} = 0.001$  for the dominant material or 1 for the air holes. In this work, the dominant material is considered to be rigid in the first problem and porous in the second one.

Since the adopted methodology aims to achieve a simply-connected structure based on a maximum temperature constraint, the following expression can be written,

$$T_j - T^* \leq 0, \quad (23)$$

where  $T_j$  is the maximum temperature of the system and  $T^*$  is the admissible temperature. The Virtual Scalar Field concept [47] is then particularized to the steady-state temperature field case, which is governed by the heat equation,

$$\nabla \cdot (k_i \nabla T) + Q = 0, \quad (24)$$

where  $T$  is the temperature field variable.

The generally adopted boundaries are typified as insulated,  $T_i$ , and free,  $T_f$ , conditions, as follows,

$$T = 0, \quad \text{in } \Gamma_i, \quad (25)$$

$$k_i \nabla T \cdot \mathbf{n} = 0, \quad \text{in } \Gamma_f, \quad (26)$$

with the FEM being the numerical procedure adopted to solve the above equations. In this way, the heat system expression is also written,

$$\mathbf{K}_T \mathbf{T} = \mathbf{q}, \quad (27)$$

where  $\mathbf{K}_T$  is the global heat conduction matrix,  $\mathbf{T}$  is the nodal temperature vector and  $\mathbf{q}$  is the thermal load vector [47].

Lastly, the basic procedures adopted to choose the user defined variables and the related boundary conditions should be highlighted. It was observed that a free boundary type, Eq. (26), would be an appropriate condition for the up bound surface of both problem domains, while keeping all other boundaries insulated (Eq. (25)). Such choices were made considering the stability of the system, as well as the regions in which the internal voids usually appeared.

Furthermore, several user defined values were considered in order to observe the behavior of  $T_j$ . In these cases, the maximum temperature of the system was expected to be so high in the presence of an internal air hole, as to configure a break in the connectivity constraint. However,  $T_j$  should be low enough not to lengthen the optimization process.

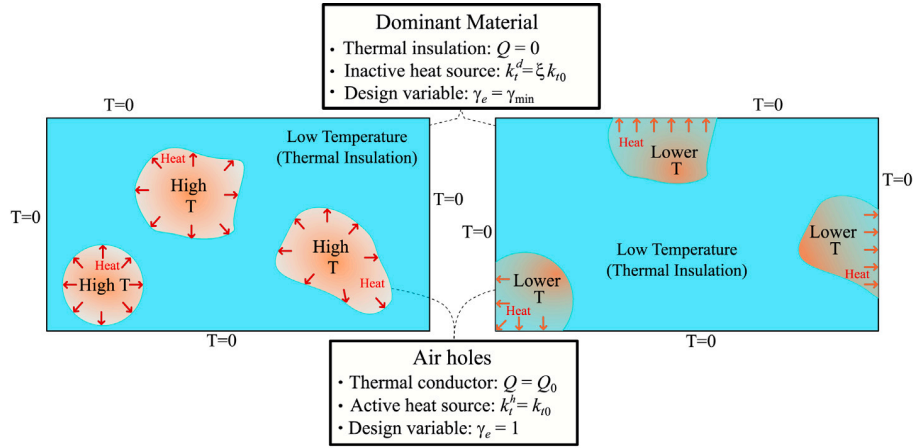


Fig. 2. Virtual Temperature Method illustrated.

This crucial trade-off is particular to any system in consideration and, therefore, should be assessed separately for P1 and P2 problems. The chosen values are presented in Sections 6.1.1 and 6.2.1, respectively.

### 5. Multiconstrained evolutionary approach

Due to the clear identification of element boundaries throughout the iterative process, discrete topology optimization methods showed to be well suited for applications that involve the avoidance of internal air holes in structures. Based on that, this section presents the multiconstrained BESO method for the optimization of two-phase structures (referred here as full-void systems), as proposed by Huang and Xie [12,14] and Zuo et al. [43]. Consider a design problem where the goal is to maximize an objective function,  $\Phi$ , while respecting equilibrium equations, as well as volume and connectivity constraints,

$$\text{Maximize: } \Phi, \quad (28)$$

$$\text{Subjected to: } \begin{cases} \mathbf{Zp} = \mathbf{f}, \\ \mathbf{K}_T \mathbf{T} = \mathbf{q}, \\ V^* - \sum_{e=1}^{N_{el}} V_e \gamma_e = 0, \\ T_j - T^* \leq 0, \\ \gamma_e = \gamma_{min} \text{ OR } 1, \end{cases} \quad (29)$$

with  $\Phi$  specified in Sections 6.1 and 6.2 for P1 and P2, respectively.

In the set of Eq. (29), the volume constraint is described by the relation between the prescribed final volume fraction,  $V^*$ , and the design domain volume fraction, represented by  $\sum_{e=1}^{N_{el}} V_e \gamma_e$ . This is valid since  $\gamma_e$  can only assume discrete values, with bounds  $\gamma_{min}$  and 1, as summarized in Fig. 1. To ensure a simply-connected structure, the VTM is implemented in the form of a thermal inequality expression  $T_j - T^* \leq 0$  (Eq. (23)), which has been described in Section 4. Finally, the expressions  $\mathbf{Zp} = \mathbf{f}$  and  $\mathbf{K}_T \mathbf{T} = \mathbf{q}$  refer to the linear system of acoustic and thermal Eqs. (16) and (27), being solved by the finite element approach.

#### 5.1. Sensitivity analysis

The sensitivity analysis is carried out via differentiation of the objective function. Since this algorithm refers to a multiconstrained optimization problem, the objective function is first transformed into an equivalent Lagrange function of the form [42],

$$L = \Phi + \lambda(T_j - T^* + S_k^2), \quad (30)$$

where  $\lambda$  is the Lagrange multiplier and  $S_k^2$  is a slack variable used to turn an inequality into equality. The sensitivity analysis is now

performed with the differentiation of  $L$ ,

$$\alpha_e = \frac{dL}{d\gamma_e} = \frac{\partial \Phi}{\partial \gamma_e} + \lambda \frac{\partial(T_j - T^* + S_k^2)}{\partial \gamma_e}, \quad (31)$$

where  $\alpha_e$  denote the sensitivity number of the  $e$ th element.

Considering that  $\Phi$  is defined differently in problems 1 and 2, the first term of the right-hand side of Eq. (31) will be discussed later in Sections 6.1 and 6.2. However, the second term is the same for P1 and P2, allowing a single description for both problems. With this in mind, consider Eq. (30) rewritten in the following form,

$$L = \Phi + \lambda(g_k + S_k^2), \quad (32)$$

where  $g_k = T_j - T^*$ . The sensitivities related with the additional variables  $\lambda$  and  $S_k$  are,

$$\frac{\partial L}{\partial \lambda} = g_k + S_k^2, \quad (33)$$

$$\frac{\partial L}{\partial S_k} = 2\lambda S_k. \quad (34)$$

The Karush–Kuhn–Tucker (KKT) condition states that Eqs. (33) and (34) need to vanish in order to fulfill one of the necessary requirements for local optima [43]. For this reason, an initial trend for the value of  $\lambda$  can be set by considering these additional equations and the KKT condition.

In a close examination of Eq. (33), one may notice that if  $g_k$  is positive, then  $g_k + S_k^2 > 0$ , which establishes that  $\lambda$  needs to increase in order to maximize the Lagrange function, and vice versa. However, in the event that Eq. (34) goes to zero,  $\lambda$  will necessarily vanish, since  $S_k \neq 0$ . In conclusion, if  $g_k \leq 0$ , then the constraint is satisfied and  $\lambda$  will not contribute for the maximization of the Lagrange function [44].

Differently from the design variables, the Lagrange multiplier is a continuous non-negative scalar function. So, to turn the search for a solution feasible, Zuo et al. [43] proposed to define  $\lambda$  through a scale function of replacement factors,  $\beta$ , that varies in the [0,1] domain,

$$\lambda = \frac{\beta}{1 - \beta} \quad \text{with } \beta \in [0, 1). \quad (35)$$

It is quite clear that when  $\beta = 0$ ,  $\lambda = 0$  and when  $\beta$  approaches 1,  $\lambda$  goes to infinity. Algorithm 1 shows the procedure adopted to find opportune values of  $\beta$ , and consequently  $\lambda$ , throughout this work.

In Algorithm 1,  $\epsilon = 0.1\%$  is used to regulate the amount of increment allowed in the Lagrange multiplier variable in each step of the optimization procedure.

Also in the second term of the right-hand side of Eq. (31), it is noted that  $T^*$  and  $S_k^2$  are constant variables, while  $T_j$  depends on  $\gamma_e$ .

**Algorithm 1:** Lagrange multiplier determination procedure [43, 44]

---

```

Input:  $T^*$  and  $\epsilon$ 
if  $T_j - T^* > 0$  then
  if  $(T_j - T^*)/T^* > \epsilon$  then
     $\beta = \beta + \epsilon$ 
  else
     $\beta = \beta + (T_j - T^*)/T^*$ 
  end
   $\lambda = \beta/(1 - \beta)$ 
else
   $\lambda = 0$ 
end
Output:  $\lambda$ 

```

---

To find the derivative of  $T_j$ , consider the adjoint load vector  $\partial T_j / \partial \mathbf{T}$  of size [dof, 1], where dof is the total number of degrees of freedom of the system. Since  $T_j$  is the maximum temperature of the system, located in a specific dof,  $\partial T_j / \partial \mathbf{T}$  is completely full of zeros, except at the degree of freedom referred to  $T_j$ , where a value of 1 is placed [53]. The differentiation of  $T_j$  can then be written,

$$\frac{\partial T_j}{\partial \gamma_e} = \left( \frac{\partial T_j}{\partial \mathbf{T}} \right)^T \frac{\partial \mathbf{T}}{\partial \gamma_e}. \quad (36)$$

Considering Eq. (27), the temperature vector differentiation is easily obtained,

$$\frac{\partial \mathbf{T}}{\partial \gamma_e} = -\mathbf{K}_T^{-1} \frac{\partial \mathbf{K}_T}{\partial \gamma_e}. \quad (37)$$

Substituting Eq. (37) in Eq. (36), then,

$$\frac{\partial T_j}{\partial \gamma_e} = -\mathbf{T}_j^T \frac{\partial \mathbf{K}_T}{\partial \gamma_e}, \quad (38)$$

where  $\mathbf{T}_j = \mathbf{K}_T^{-1} (\partial T_j / \partial \mathbf{T})$ . Finally, the expression  $\partial \mathbf{K}_T / \partial \gamma_e$  can be solved by the definition of a particular material interpolation scheme for the VTM case,

$$k_i(\gamma_e) = k_i^d + \gamma_e^2 (k_i^h - k_i^d), \quad (39)$$

with all the thermal variables already defined in Section 4 (see Fig. 2).

### 5.2. Filter scheme and sensitivity stabilization procedure

Due to the  $C^0$  discontinuity of the sensitivity numbers, a few design issues may arise, such as checkerboard patterns [10] and mesh dependency [11]. As a solution, a projection filter scheme is implemented, with a previous step being the determination of the nodal sensitivity numbers [14],

$$\alpha_n = \sum_{e=1}^M w_e \alpha_e, \quad (40)$$

$$w_e = \frac{1}{M-1} \left( 1 - \frac{r_{en}}{\sum_{e=1}^M r_{en}} \right), \quad (41)$$

where  $\alpha_n$  refers to the sensitivity number of the  $n$ th node,  $M$  corresponds to the number of elements connected to the  $n$ th node,  $w_e$  is the weight factor of the  $e$ th element, with  $\sum_{e=1}^M w_e = 1$ , and  $r_{en}$  is the distance from the centroid of the  $e$ th element to the  $n$ th node.

Then, since these nodal sensitivities have no physical meaning, elemental sensitivity numbers must be retrieved. For this, a filter radius,  $r_{\min}$ , centered in the  $e$ th element is chosen to identify the nodes that influence in its sensitivities. Since  $r_{\min}$  is exclusively size based, it does not vary with different meshes. For  $w(r_{en}) = r_{\min} - r_{en}$  being a linear weight factor that can be applied to all  $H$  nodes inside the  $r_{\min}$  subdomain, the filtered  $\alpha_e$  is written as,

$$\alpha_e = \frac{\sum_{n=1}^H w(r_{en}) \alpha_n}{\sum_{n=1}^H w(r_{en})}. \quad (42)$$

Afterwards, the sensitivity historical averaging procedure is employed as an effort to increase the stability of the iterative process,

$$\alpha_e = \frac{(\alpha_e)_{i-1} + (\alpha_e)_i}{2}, \quad (43)$$

where the subscript  $i$  refers to the current iteration.

### 5.3. Design variable update and stop criterion

To update the design variables it is imperative to first define the target volume for the next iteration. With the use of the Evolutionary Rate (ER) as the change in volume for each iterative step, one may write the expression that relates the volume fraction of the current,  $V_j$ , and next,  $V_{j+1}$ , iterations,

$$V_{j+1} = V_j(1 \pm \text{ER}). \quad (44)$$

The sensitivity numbers are then sorted from highest to lowest and the material types are changed accordingly. The definition of  $V_{j+1}$  establishes a threshold, in the sorted sensitivity vector, that defines the amount of elements that will be void ( $\gamma = \gamma_{\min}$ ) and full ( $\gamma = 1$ ) by setting,

$$\alpha_e \leq \alpha_{\text{th}} \quad \text{as void elements}, \quad (45)$$

$$\alpha_e > \alpha_{\text{th}} \quad \text{as full elements}, \quad (46)$$

where  $\alpha_{\text{th}}$  is the threshold sensitivity number. Seeing that BESO is a bi-directional procedure, the addition of elements is also possible. The Addition Ratio (AR) is the variable that defines the amount void/full elements that can become full/void. However, in order to control this quantity, the maximum Addition Ratio ( $\text{AR}_{\max}$ ) is required as one of the inputs of the method. If the case  $\text{AR} > \text{AR}_{\max}$  happens, the restriction  $\text{AR} = \text{AR}_{\max}$  has to be enforced. This fact results in the imposition that some elements with the lowest  $\alpha_e$  become void, and some with the highest  $\alpha_e$  become full [16].

Finally, the stop criterion is stated,

$$\frac{|\sum_{m=1}^N \Phi_{i-m+1} - \sum_{m=1}^N \Phi_{i-N-m+1}|}{\sum_{m=1}^N \Phi_{i-m+1}} \leq \tau, \quad (47)$$

where  $\tau$  represents the tolerance and  $N$  refers to the number of iterations considered in the historical average. It is also important to remark that when the final volume fraction,  $V^*$ , is reached,  $V$  can no longer change until the optimization process is terminated by the fulfillment of Eq. (47). Throughout this work, the values of  $\tau$  and  $N$  are considered to be 0.1% and 10, respectively.

## 6. Topology optimization design of acoustic systems

This section presents numerical examples regarding the use of the multiconstrained BESO methodology, being divided in two distinct ATO problems. The first one (P1) is illustrated in Fig. 3(a). A certain trade-off is in place by relating the amount of wind and sound (acoustic waves) that are allowed to pass through the air holes. If the holes are too large, the structure will be highly permeable to the wind, but good soundproofing will be hard to achieve [30]. Considering that, the goal of P1 is to use the BESO method, with and without active connectivity constraints, to design rigid-acoustic metasurfaces with optimized soundproofing characteristics, as demonstrated at the right side of Fig. 3(a). Lastly, in this case, the issue regarding the appearance of internal air holes in the rigid structure is also explored.

The second problem (P2), shown in Fig. 3(b), is stated as the design of a coupled poro-acoustic absorptive system composed of a periodic arrangement of porous layers backed by a rigid wall. In this application, the porous material is rock-wool (see Table 1), modeled by the JCA formulations (Eqs. (19) and (20)). Here, cases with active constraints are considered, aiming to provide manufacturable topologies with enhanced sound absorption coefficient values in the low frequency spectrum.

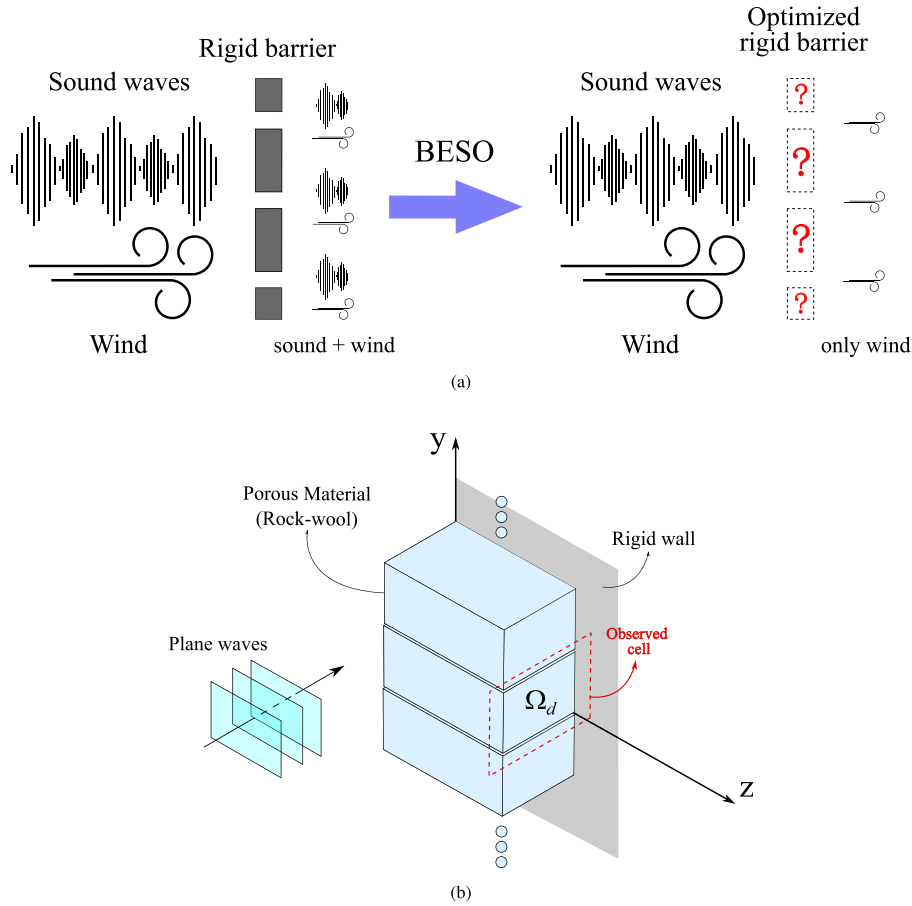


**Fig. 3.** Schematic representation of P1 and P2. (a) Minimization of regional sound pressure levels by topology optimization of an acoustic metasurface and (b) maximization of sound absorption characteristics of porous materials backed by a rigid wall.

### 6.1. Problem 1: Design of acoustic metasurfaces

According to Torresin et al. [54] and Miyata et al. [30], natural ventilation reduces energy consumption in cooling and ventilation of buildings, providing pleasant thermal environments at relatively low cost. As the main connection between indoor–outdoor environments is made through window openings and ventilation apertures, external sounds are, sometimes, a big issue in the design of building façades and even in internal partitions of a residential environment. In this context, the particularization of the procedures shown in Section 5 for the design of wind permeable acoustic metasurfaces can be written as follows,

$$\text{Maximize: } \Phi^{P1} = -\frac{1}{N_f} \sum_{n=1}^{N_f} \text{SPL}_n, \quad (48)$$

$$\text{Subjected to: } \begin{cases} \mathbf{Z}\mathbf{p} = \mathbf{f}, \\ \mathbf{K}_T \mathbf{T} = \mathbf{q}, \\ V^* - \sum_{e=1}^{N_{el}} V_e \gamma_e = 0, \\ T_j - T^* \leq 0, \\ \gamma_e = \gamma_{\min} \text{ OR } 1, \end{cases} \quad (49)$$

where the objective function  $\Phi^{P1}$  corresponds to the arithmetic mean of the SPL values for  $N_f$  target frequencies. In Eq. (48), the negative sign is used to turn a maximization problem into a minimization one [12]. Considering the reference pressure equal to  $P_{\text{ref}} = 20 \mu\text{Pa}$ , the mathematical expression for the frequency dependent SPL calculation

is presented by,

$$\text{SPL} = 10 \log_{10} \left( \frac{P_{\text{avg}}^2}{P_{\text{ref}}^2} \right), \quad (50)$$

where the average squared pressure amplitude is [24,28],

$$P_{\text{avg}}^2 = \frac{1}{\int_{\Omega_r} d\Omega_r} \int_{\Omega_r} |p(\omega, \gamma_e)|^2 d\Omega_r. \quad (51)$$

In the equation above,  $\Omega_r$  corresponds to the receiver domain, the region in which the SPL values must be minimized (see Fig. 4).

Since, in this case,  $\Phi = \Phi^{P1}$ , the sensitivity analysis can now be completely described by solving the first term of the right-hand side of Eq. (31). In this way, one may write,

$$\frac{\partial \Phi}{\partial \gamma_e} = \frac{d\Phi^{P1}}{d\gamma_e} = -\frac{1}{N_f} \sum_{n=1}^{N_f} \left[ \frac{10}{\ln 10} \left( \frac{dP_{\text{avg}}^2/d\gamma_e}{P_{\text{avg}}^2} \right) \right], \quad (52)$$

with,

$$\frac{dP_{\text{avg}}^2}{d\gamma_e} = \frac{\partial P_{\text{avg}}^2}{\partial \gamma_e} + 2\text{Re} \left[ \lambda_1^T \left( \frac{\partial \mathbf{Z}}{\partial \gamma_e} \mathbf{p} - \frac{\partial \mathbf{f}}{\partial \gamma_e} \right) \right]. \quad (53)$$

To find the Lagrange multiplier,  $\lambda_1$ , the following adjoint system needs to be solved,

$$\mathbf{Z} \lambda_1 = -\frac{1}{2} \left( \frac{\partial P_{\text{avg}}^2}{\partial \text{Re}(\mathbf{p})} - j \frac{\partial P_{\text{avg}}^2}{\partial \text{Im}(\mathbf{p})} \right)^T, \quad (54)$$

where,

$$\frac{\partial P_{\text{avg}}^2}{\partial \text{Re}(\mathbf{p})} - j \frac{\partial P_{\text{avg}}^2}{\partial \text{Im}(\mathbf{p})} = \frac{1}{\int_{\Omega_r} d\Omega_r} (2\text{Re}(\mathbf{p})^T - j2\text{Im}(\mathbf{p})^T) \int_{\Omega_r} \mathbf{N}_e^T \mathbf{N}_e d\Omega_r, \quad (55)$$

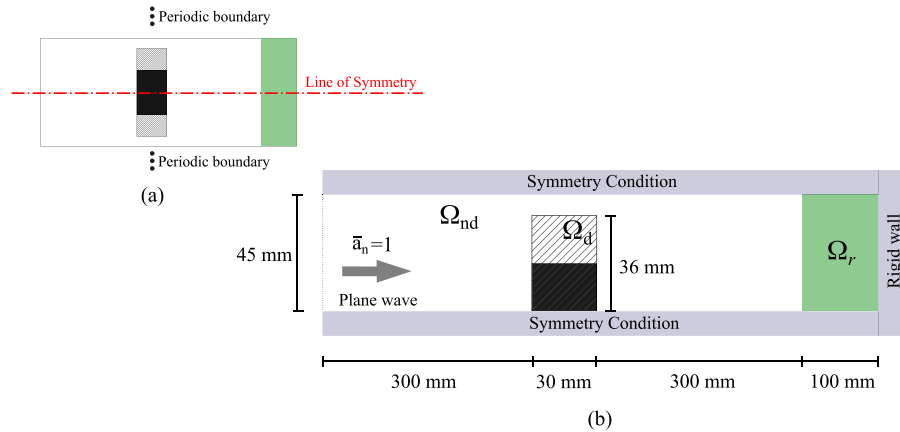


**Fig. 4.** Representation of unit cells (a) with periodic and (b) symmetric conditions. The design domain is equally divided into acoustic (white hatched  $\Omega_d$  area) and rigid (black  $\Omega_r$  area) elements, with the receiver domain represented by  $\Omega_r$  (green area). Only symmetry conditions are adopted in the numerical simulations. (For interpretation of the references to color in this figure legend, the reader is referred to the web version of this article.)

with  $\text{Re}(\mathbf{p})$  and  $\text{Im}(\mathbf{p})$  denoting the real and imaginary parts of  $\mathbf{p}$ . Finally,  $\partial \mathbf{Z} / \partial \gamma_e$  can be found by the use of the MIS presented in Eq. (21).

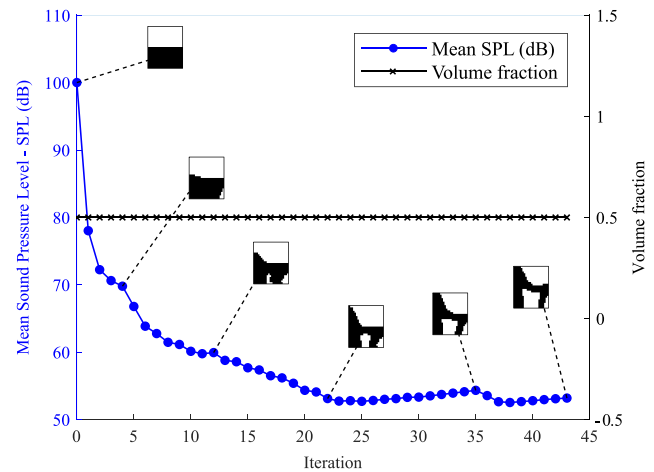
### 6.1.1. Numerical results of P1

Fig. 4 presents the main geometrical aspects adopted in the analysis, being similar to the one considered by Miyata et al. in 2018 [30], where a multifunctional acoustic metasurface was designed using the level set method. It is noted, through Fig. 4(a), that the cell is initially considered as vertically periodic, comprising equal amounts of rigid and acoustic elements in its design domain ( $\Omega_d$ ). Additionally, plane waves are incident in its left side boundary, while rigid wall condition is imposed in the right side. In this general disposition, equal values of sensitivity numbers and nodal pressure would be observed in the upper and lower parts of the domain, due to the symmetry of the system. With this in mind, a symmetric unit cell is adopted, as shown in Fig. 4(b).

The entire fluid domain is discretized into  $584 \times 30$  first order quadrilateral elements, which is way above the minimum recommended per wavelength [49], with  $\Omega_{nd}$  and  $\Omega_r$  (green area) composed exclusively of acoustic elements. The symmetric cell has 730 mm of length and 45 mm of height, with a receiver region of  $100 \times 45 \text{ mm}^2$ . If the individual region lengths were considered (300 mm after and before  $\Omega_d$ , with 100 mm of  $\Omega_r$ ) a 3:3:1 ratio would be observed, which is approximately the wavelengths that acoustic waves would have in these domains for a frequency around 3000 Hz. In addition,  $\Omega_d$  has 30 mm of length, which is approximately 10 times less than the wavelength, and 36 mm of height, holding a 4:1 ratio if compared with the smallest allowable air gap in the metasurface. Finally, the initial topology is set to start from a guess design, with acoustic and rigid elements equally divided in the upper (white hatched area) and lower (black area)  $\Omega_d$  parts, respectively. For this composition, the ratio between the rigid and the through hole areas is 2:3.

For this design problem, the BESO parameters are set as  $\text{ER} = \text{AR}_{\max} = 0.5\%$  and  $r_{\min} = 5.5 \text{ mm}$ , with constant volume fraction of 0.5. The four target frequencies that compose the objective function are 3011 Hz, 3270 Hz, 3480 Hz and 3660 Hz, chosen due to their proximity to peaks in the SPL curve (see Fig. 7). Fig. 5 presents the evolutionary history of mean SPL values, with intermediate designs, while the volume fraction is kept constant and the connectivity constraint is disregarded. From early stages of the optimization process, it is clear that the rigid material tends to migrate to the left side of the design domain, increasing the acoustic shielding effect at the front cavity of the metasurface, but with little reduction to its structural disposition at the back.

Due to the small amount of rigid material that is allowed in  $\Omega_d$ , this tendency induces the formation of air holes inside the rigid structure, but without ever breaching it. From a bidimensional point of view,



**Fig. 5.** Evolutionary history of mean SPL values and volume fraction without considering VTM.

the manufacturing processes of solid structures are mainly conducted through extrusion of the given design plane and, at first analysis, would not be harmed by the presence of internal air holes. However, since no waves are allowed to pass through a rigid barrier, regardless of its thickness, a thin outer layer can present a violation on the rigid material hypothesis, generating issues regarding the accuracy of the material formulation (e.g. the increase of vibrations) and violations of volume constraints.

As a solution to such problems caused by the emergence of air holes, the VTM is considered. Fig. 6 shows the evolution of the mean SPL values with the connectivity constraint set as active. Here, the behavior of the volume fraction and the maximum temperature are also explored. It can be seen that the objective function tends to decrease until the connectivity constraint is breached by the appearance of an internal air hole. A sudden increase of the maximum temperature of the system is then provoked, acting on the sensitivity numbers, so as to immediately redirect rigid materials to fill the hole, also visible in the several intermediate topologies highlighted. This material reorientation, however, causes a momentary increase in the objective function, leading to a sawtooth wave-like evolution that eventually converges to a local minimum.

In all metasurface optimization cases, the VTM variables were set to be  $k_{i0} = 1$ ,  $Q_0 = 10$  and  $T^* = 10$  as an effort to concentrated the study on the influence that the frequencies would have on the final

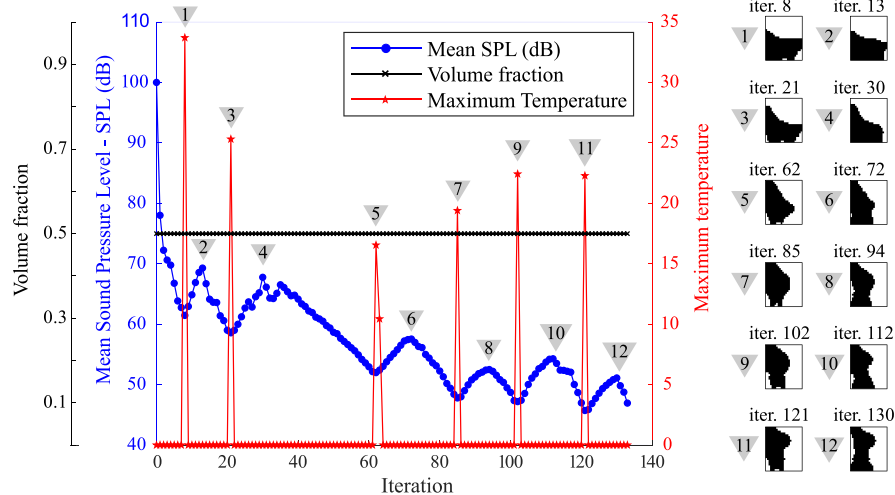


Fig. 6. Evolutionary history of mean SPL values and volume fraction with VTM set as active.

topologies. Such a methodology indeed provided topologies with higher manufacturability and, in many cases, better soundproofing abilities if compared to the ones without active connectivity constraints (see Table 2), but also contributed to the erratic evolutionary behavior that is presented in Fig. 6. This result indicates that particular VTM variables should be set to each optimization procedure considering rigid elements, but that the chosen set of variables also succeeds in avoiding air hole seclusion.

In order to verify the effects of this optimization at the studied frequency range, Fig. 7 is presented. The BESO method succeeds in minimizing SPL values in all four target frequencies at the same time, considering both applications. If one compares only these results, the active VTM case is better than the one without connectivity constraints, presenting the lowest observed SPL values in all targeted frequencies.

Since this optimization problem is of non-convex nature, the BESO method tends to converge to a local minimum, with or without additional restrictions in the space of solutions, as shown in the objective function evolutionary histories (Figs. 5 and 6). This fact helps in the understanding of why some of the active VTM cases present more enhanced soundproofing characteristics than the ones without it. With additional constraints, the original optimization problem changes, presenting a reduced space of solutions with particular local minima.

Such statements are also verified by observing the pressure fields at 3011 Hz, 3270 Hz, 3480 Hz and 3660 Hz for both cases, as shown in Fig. 8. A common aspect of all observed fields is the appearance of evanescent waves at the back cavity of the metasurfaces. They are specially noticeable in the pressure fields from Fig. 8(b), (c), (e) and (g), where relatively high pressure values can be observed.

Evanescence waves are exponentially decaying disturbances that appear due to the reflection of sinusoidal waves at the interfaces between mediums, combined with the boundary continuity condition imposed on them. This aspect was also present in previous works regarding the design of negative effective-mass density acoustic metamaterials [55], acoustic metasurfaces with angular asymmetric-absorption [56] and many other applications on periodic structures. The combination of such mechanisms with the diffraction of incident waves can generate significant pressure drops in the regions after the metasurface, as clearly visible in Fig. 8(d), (g) and (h).

In order to analyze the influence of the target frequency, the optimization procedure is performed for each one of them individually, while keeping the other parameters unchanged. Table 2 presents the optimized topologies, along with the results for the arithmetic mean SPL case. The topologies are displayed inside a rectangle that symbolizes the design domain, with the outside up and down vertical lines representing the periodic bounds associated to each observed region.

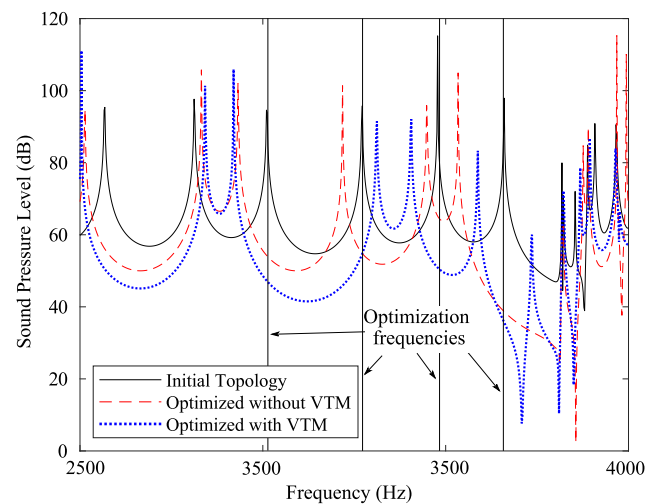


Fig. 7. Sound pressure level responses of the initial and optimized topologies regarding the arithmetic mean SPL case.

In all considered scenarios, the iterative procedure is conducted with and without the connectivity constraints.

For the first three frequencies, it is clear that the VTM did not interfere in the optimization process, since no internal air holes appeared along the iterations. The results, in each of these cases, are therefore identical with and without the activation of the connectivity constraint. Table 2 also shows the initial and final objective function values, along with the number of iterations required until the end of the process (as a subscript of  $\Phi$  in the assigned topology). In all the aforementioned frequencies, the final topologies converged around 60 iterations, showing significant objective function reduction, specially in the 3011 Hz case that presented a 60.35% SPL decrease.

Analyzing the optimized topologies, it is noticeable that the rigid material tends to vertically extend its shape within the design domain, changing the rigid-air disposition to a 4:1 ratio. Such findings are common for all final designs, except for the 3660 Hz case with active VTM, where the topology presents slightly pronunciations in its front cavity. Still, it is remarked that the convergence occurred faster in this case than any other, being mainly attributed to the choice of BESO variables and the reduced space of solutions introduced by the additional constraint application. Despite that, the obtained topology presents a 50.30% SPL reduction and no internal air holes.

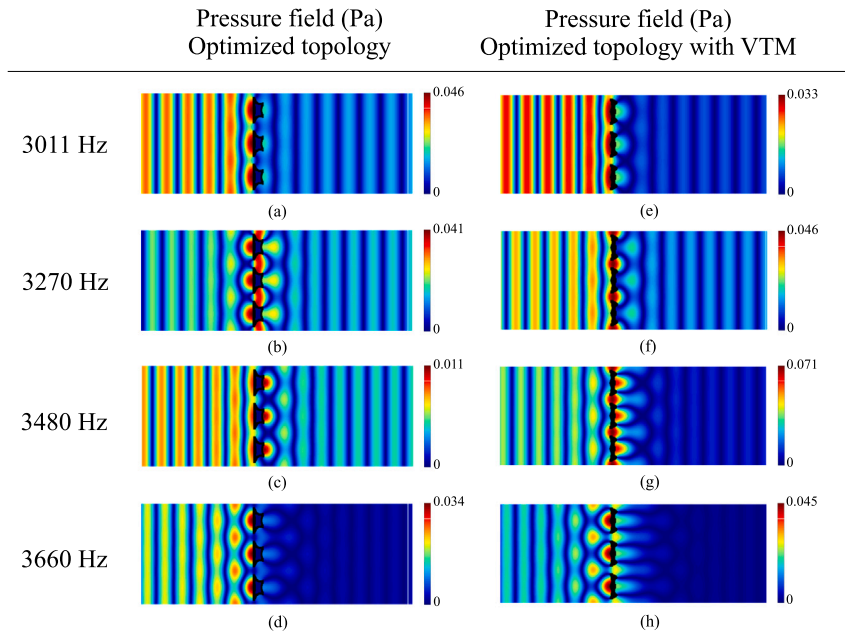


Fig. 8. Pressure fields considering optimized topologies with and without VTM in (a), (e) 3011 Hz, (b), (f) 3270 Hz, (c), (g) 3480 Hz and (d), (h) 3660 Hz for the arithmetic mean SPL case. (For better visualization, three periodic unit cells were used).

## 6.2. Problem 2: Design of poro-acoustic systems

Following a similar procedure adopted in Section 6.1, the ATO problem for the design of porous structures can be written as,

$$\text{Maximize: } \Phi^{P2} = 1 - |R|^2, \quad (56)$$

$$\text{Subjected to: } \begin{cases} \mathbf{Z}\mathbf{p} = \mathbf{f}, \\ \mathbf{K}_T \mathbf{T} = \mathbf{q}, \\ V^* - \sum_{e=1}^{N_{el}} V_e \gamma_e = 0, \\ T_j - T^* \leq 0, \\ \gamma_e = \gamma_{\min} \text{ or } 1, \end{cases} \quad (57)$$

where the objective function  $\Phi^{P2}$  is the sound absorption coefficient of the considered porous material and  $R$  is the reflection coefficient, which in turn can be represented by the following frequency dependent expression [57],

$$R = \frac{-p_2 \exp(-jk_a x_1) + p_1 \exp(-jk_a x_2)}{p_2 \exp(jk_a x_1) - p_1 \exp(jk_a x_2)}, \quad (58)$$

where  $p_1$  and  $p_2$  are pressure amplitudes measured in positions  $x_1$  and  $x_2$  (see Fig. 9), and  $k_a = \omega/c_a$  is the air wavenumber.

Knowing that  $\Phi = \Phi^{P2}$ , the first term of the right-hand side of Eq. (31) can be specified as,

$$\frac{\partial \Phi}{\partial \gamma_e} = -2 \left( \text{Re}(R) \frac{\partial \text{Re}(R)}{\partial \gamma_e} + \text{Im}(R) \frac{\partial \text{Im}(R)}{\partial \gamma_e} \right), \quad (59)$$

with  $\text{Re}(R)$  and  $\text{Im}(R)$  denoting the real and imaginary parts of  $R$ . After a series of mathematical manipulations, the derivative of  $R$  can be found [57],

$$\frac{\partial R}{\partial \gamma_e} = \frac{\left[ -\frac{\partial p_2}{\partial \gamma_e} \exp(-jk_a x_1) + \frac{\partial p_1}{\partial \gamma_e} \exp(-jk_a x_2) \right] \left[ p_2 \exp(jk_a x_1) - p_1 \exp(jk_a x_2) \right] - \left[ p_2 \exp(jk_a x_1) - p_1 \exp(jk_a x_2) \right]^2}{\left[ p_2 \exp(jk_a x_1) - p_1 \exp(jk_a x_2) \right]^2} - \frac{\left[ -p_2 \exp(-jk_a x_1) + p_1 \exp(-jk_a x_2) \right] \left[ \frac{\partial p_2}{\partial \gamma_e} \exp(jk_a x_1) - \frac{\partial p_1}{\partial \gamma_e} \exp(jk_a x_2) \right]}{\left[ p_2 \exp(jk_a x_1) - p_1 \exp(jk_a x_2) \right]^2}, \quad (60)$$

Table 2

Topology designs obtained by BESO, with and without VTM, for different target frequencies. The corresponding objective function values and iterations are also given.

Frequency (Hz)	Initial topology	Optimized topology without VTM	Optimized topology with VTM
3011	$\phi_0 = 122.7$ dB	$\phi_{60} = 48.65$ dB	$\phi_{60} = 48.65$ dB
3270	$\phi_0 = 91.70$ dB	$\phi_{62} = 52.35$ dB	$\phi_{62} = 52.35$ dB
3480	$\phi_0 = 87.76$ dB	$\phi_{60} = 52.84$ dB	$\phi_{60} = 52.84$ dB
3660	$\phi_0 = 97.91$ dB	$\phi_{52} = 32.95$ dB	$\phi_{24} = 48.66$ dB
Mean	$\phi_0 = 100.0$ dB	$\phi_{43} = 53.20$ dB	$\phi_{133} = 46.96$ dB

with  $\partial \text{Re}(R)/\partial \gamma_e$  and  $\partial \text{Im}(R)/\partial \gamma_e$  obtained by taking the real and imaginary parts of  $\partial R/\partial \gamma_e$ . To find  $\partial p_1/\partial \gamma_e$  and  $\partial p_2/\partial \gamma_e$ , similar procedures adopted in the calculation of  $T_j$  can be used, as stated in Eqs. (36), (37) and (38). Lastly,  $\partial \mathbf{Z}/\partial \gamma_e$  is obtained by the use of the appropriate MIS, as presented in Eq. (22).

### 6.2.1. Numerical results of P2

Fig. 9 shows the 2D arrangement considered in this optimization problem. Similarly to P1, the poro-acoustic system is vertically periodic, with rigid wall conditions imposed on the right side boundary, as can be

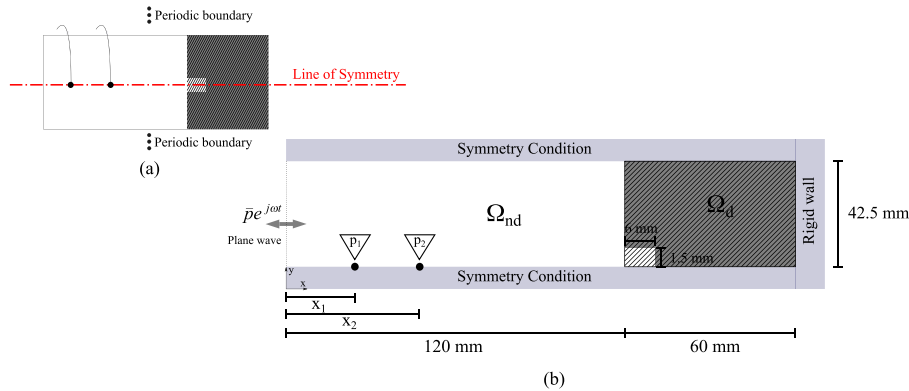


**Fig. 9.** Illustration of P2 unit cells (a) with periodic and (b) symmetric vertical boundaries. The design domain,  $\Omega_d$ , is represented by the hatched area, with porous material in gray color. The acoustic non-design domain,  $\Omega_{nd}$ , is represented in white. Only symmetry conditions are adopted in the numerical simulations.

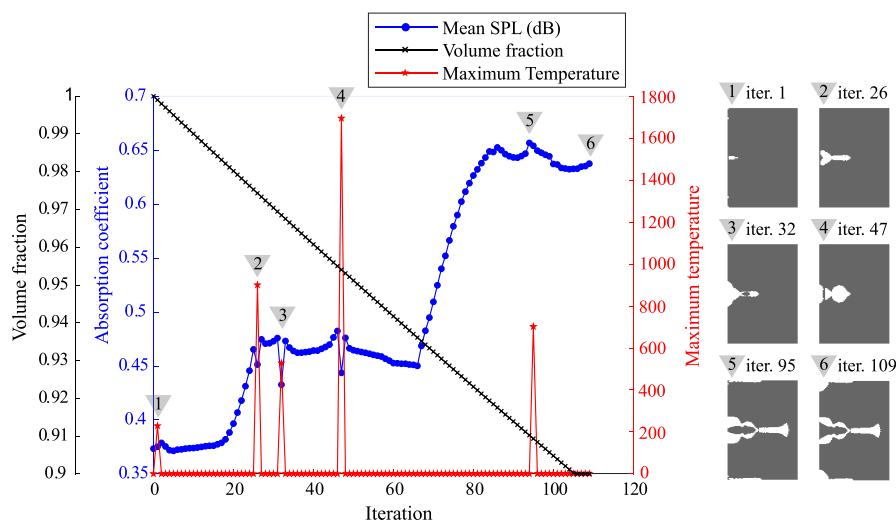


**Fig. 10.** Evolutionary history of the objective function and constraints for 300 Hz as target frequency, as well as presentation of intermediate topologies of interest.

seen in Fig. 9(a). Additionally, plane waves are simulated by Dirichlet conditions (Eq. (2)) and enforced on the left surface of the system. Such combination of settings allows for simpler representation of the porous grid by using a single bidimensional porous strip with upper and lower boundaries treated as symmetric (Fig. 9(b)).

The rock-wool fills an area of  $60 \times 42.5 \text{ mm}^2$ , which is considered as the design domain, while the non-design domain, composed exclusively of acoustic elements, has 120 mm of length by 42.5 mm of height. After several tests, the authors considered that a 2:1 ratio, between the area of acoustic and porous elements, is sufficient to simulate a plane wave propagating in an infinitely long acoustic tube. The entire mesh is composed of  $180 \times 85$  first order quadrilateral elements, while the microphone positions are considered to be  $x_1 = 50 \text{ mm}$  and  $x_2 = 70 \text{ mm}$  from the origin. Finally, a small air inclusion of  $6 \times 1.5 \text{ mm}^2$  is introduced in the symmetric porous design domain, shown in Fig. 9(b), as an initial guess.

Porosity-acoustic systems were also investigated by Silva and Pavanetto [32,33], which adopted the ESO method as optimizer. The current methodology uses different features such as sensitivity filters, connectivity constraints and a bi-directional evolutionary approach to create more manufacturable topologies.

For this particular scenario, the BESO variables are considered to be  $ER = 0.1\%$ ,  $AR_{max} = 0.05\%$ ,  $r_{min} = 10 \text{ mm}$ ,  $V_0 = 0.9965$  and  $V^* = 0.9$ , representing a reduction of 9.965% in volume, since the initial volume is not 1 due to the air inclusion. Two target frequencies are

treated separately, 300 Hz and 500 Hz, which configures two different optimization procedures. Figs. 10 and 11 show the evolution of the objective function, volume fraction and maximum temperature over the optimization, while some intermediate topologies of interest are also highlighted.

Looking at Fig. 10, which deals with the optimization in 300 Hz, one may notice that the maximum temperature is only relevant to the optimization procedure when air regions are trapped inside the porous material, as evidenced when visualizing the intermediate topologies. Comparing these results to the ones from P1 (Fig. 6), the effectiveness of the connectivity procedure in closing secluded air regions is equally observed.

For both P2 optimizations, the VTM variables are defined as  $k_{i0} = 1$ ,  $Q_0 = 100$  and  $T^* = 10$ . In such cases, the VTM is usually activated whenever the objective function suddenly decreases, due to the appearance of an internal air hole. This evolutionary behavior combined with the sensitivity historical averaging procedure and the relatively small addition/removal of material create a stabilization level that endures for a significant number of iterations, but that does not reverse the enhancements already achieved.

Such behavioral differences of  $\Phi^{P1}$  and  $\Phi^{P2}$  are partly due to distinctions in the objective function themselves ( $\Phi^{P1} \neq \Phi^{P2}$ ), but mainly due to the materials involved in the optimizations. In other words, a greater number of porous elements are needed to influence the objective function than rigid ones, since the latter are constitutionally closer

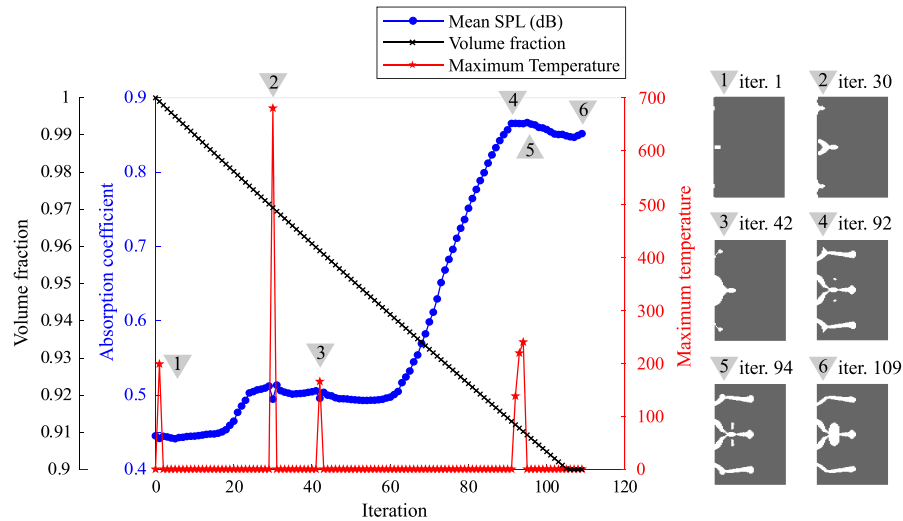


Fig. 11. Evolutionary history of the objective function and constraints for 500 Hz as target frequency, as well as presentation of intermediate topologies of interest.

to acoustic elements than the former. These findings are reinforced by the analysis of Fig. 11, as a similar  $\Phi^{P2}$  performance is observed for the 500 Hz case, compared with the 300 Hz scenario.

Figs. 12 and 13 present a direct comparison between the sound absorption coefficient results found by Silva [32] and by the proposed methodology, for optimizations in 300 Hz and 500 Hz, respectively. In Fig. 12, the topology from Silva presents a significant increase of the sound absorption coefficient around the target frequency, roughly from 0.37 to 0.94; however, it drops considerably for frequencies higher than 400 Hz. In the optimal topology obtained here, an increase is also observed at the target frequency, albeit lower (from 0.37 to 0.87), and the peak only occurs around 480 Hz. Despite that, the obtained topology allows for greater improvements of  $\Phi^{P2}$  from 380 Hz up until the end of the observed frequency range, by maintaining the absorption coefficient around 0.8.

It is perceptible that the root-like topology from Silva increases the sound absorption coefficient at the target frequency more, however, the concentrated air inclusion in the center of the optimal topology obtained, for the 300 Hz case, allows for greater  $\Phi^{P2}$  enhancements in a broader range of frequencies. For the 500 Hz scenario (Fig. 13),  $\Phi^{P2}$  differences between both topologies become less visible, since the proposed structure is composed of multiple air inclusions, approximating itself to the root-like topology of Silva.

Despite of the reduced space of solutions introduced by the additional VTM constraint, the results show major enhancements of the sound absorption coefficient in the overall frequency range, in addition to the increase of the manufacturability of the final topologies.

Finally, it should be remarked that most P2 topologies presented disconnected partitions when considering the proposed approach. Since the standard way to manufacture structures from 2D settings is by extrusion (or by cutting machines for foams), two frames could be added at the edged of the extrusion direction to support the loose parts, therefore not being a manufacturing issue. In addition, the imposition of another VTM constraint considering the dominant material as an active heat source and the acoustic domain as inactive could be a viable solution for general three-dimensional optimizations.

## 7. Conclusions

In this work, a multiconstrained BESO method was applied in two different acoustic systems, aiming to provide topologies that could enhance certain system characteristics, while respecting imposed constraints. The first problem dealt with the optimization of rigid-acoustic metasurfaces, being able to provide SPL reductions up to 60.35% when

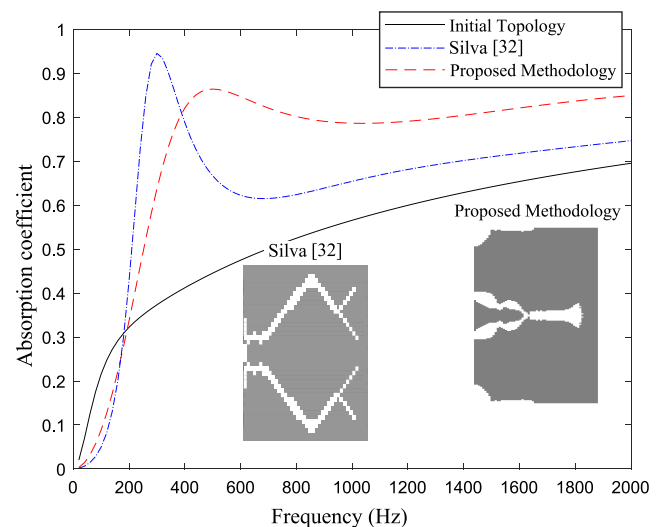


Fig. 12. Behavior of sound absorption coefficient, along low to mid range of frequencies, for the optimization in 300 Hz.

considering the 3011 Hz case. In these analyses, however, some optimized topologies presented internal air holes, which brought problems concerning the rigid material hypothesis and the manufacturability of the obtained structures.

To solve this issue, the modified Virtual Temperature Method (VTM) for acoustic applications was used as a connectivity constraint. The results presented well defined topologies, with no air inclusions, high manufacturability and reduced SPL values in the frequencies targeted. Additionally, the trade-off between the amount of wind that is able to pass through the metasurface holes and its soundproofing effects was successfully established for all cases.

The second problem regarded the optimization of a coupled poro-acoustic absorptive system, aiming to maximize the sound absorption coefficient of the considered porous material, while adopting the VTM as a connectivity constraint. The Johnson–Champoux–Allard (JCA) model was used in this work to simulate the behavior of the porous structure as an equivalent fluid. The results showed well defined topologies with sound absorption coefficients greater than 0.8 in the observed frequency range. Also, a direct comparison with the available

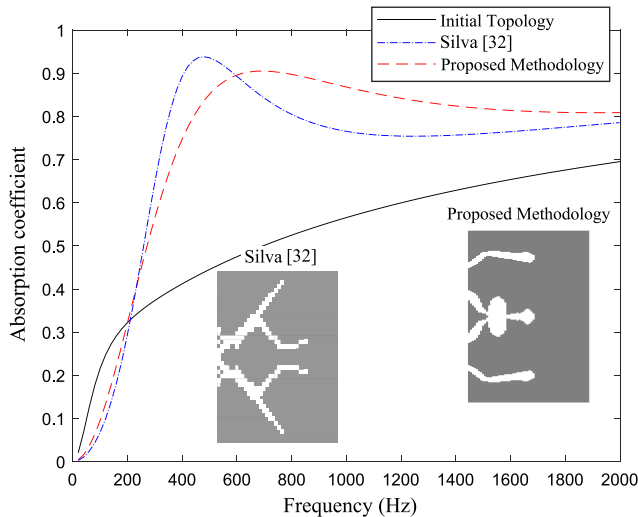


Fig. 13. Behavior of sound absorption coefficient, along low to mid range of frequencies, for the optimization in 500 Hz.

literature was performed. In this respect, it was noted that the obtained topologies presented slightly lower sound absorption coefficient values in the target frequencies of optimization, due to the additional constraint imposed by the VTM. Nonetheless, this same fact also contributed to the improved performances of the obtained topologies in low-to-mid frequency ranges.

A common feature of most multiconstrained problems here presented regards the increase of the iterations required to convergence. The material reorganization that was imposed by VTM proved to be computationally expensive, and, especially when rigid materials were involved, difficult to converge. However, the method succeeded in provide topologies free of air hole seclusions, easy to manufacture and with enhanced characteristics in all the applications considered. This implies that future research should focus in obtain global values of VTM variables, in order to broaden the applications of such approach for other acoustic settings and to reduce the overall computational costs here noticed.

#### CRedit authorship contribution statement

**Rodrigo L. Pereira:** Conceptualization, Methodology, Software, Validation, Data curation, Writing – Original Draft, Visualization, Writing – review & editing. **Heitor N. Lopes:** Conceptualization, Methodology, Writing – review & editing. **Renato Pavanello:** Conceptualization, Resources, Writing – review & editing, Supervision, Project administration.

#### Declaration of competing interest

The authors declare that they have no known competing financial interests or personal relationships that could have appeared to influence the work reported in this paper.

#### Acknowledgments

The authors are grateful for the financial support given by FAPESP (Fundação de Amparo à Pesquisa do Estado de São Paulo), Brazil, project numbers 2013/08293-7 and 2019/05393-7; and by CAPES (Coordenação de Aperfeiçoamento de Pessoal do Nível Superior), Brazil, finance code 001.

#### References

- [1] M.P. Bendsøe, N. Kikuchi, Generating optimal topologies in structural design using a homogenization method, *Comput. Method Appl. M.* 71 (1988) 197–224, [http://dx.doi.org/10.1016/0045-7825\(88\)90086-2](http://dx.doi.org/10.1016/0045-7825(88)90086-2).
- [2] M.P. Bendsøe, Optimal shape design as a material distribution problem, *Struct. Optim. 1* (1989) 193–202, <http://dx.doi.org/10.1007/bf01650949>.
- [3] M. Zhou, G.I.N. Rozvany, The COC algorithm, part II: Topological, geometrical and generalized shape optimization, *Comput. Method Appl. M.* 89 (1991) 309–336, [http://dx.doi.org/10.1016/0045-7825\(91\)90046-9](http://dx.doi.org/10.1016/0045-7825(91)90046-9).
- [4] Y. Xie, G.P. Steven, Shape and layout optimization via an evolutionary procedure, in: *Proceedings of the International Conference on Computational Engineering Science*, 1992.
- [5] X.Y. Yang, Y.M. Xie, G.P. Steven, O.M. Querin, Bidirectional evolutionary method for stiffness optimization, *AIAA J.* 37 (1999) 1483–1488, <http://dx.doi.org/10.2514/2.626>.
- [6] O. Sigmund, K. Maute, Topology optimization approaches: A comparative review, *Struct. Multidiscip. Optim.* 48 (2013) 1031–1055, <http://dx.doi.org/10.1007/s00158-013-0978-6>.
- [7] L. Xia, Q. Xia, X. Huang, Y.M. Xie, Bi-directional evolutionary structural optimization on advanced structures and materials: A comprehensive review, *Arch. Comput. Methods Eng.* 25 (2) (2018) 437–478, <http://dx.doi.org/10.1007/s11831-016-9203-2>.
- [8] Y.M. Xie, G.P. Steven, A simple evolutionary procedure for structural optimization, *Comput. Struct.* 49 (1993) 885–896, [http://dx.doi.org/10.1016/0045-7949\(93\)90035-c](http://dx.doi.org/10.1016/0045-7949(93)90035-c).
- [9] O.M. Querin, V. Young, G.P. Steven, Y.M. Xie, Computational efficiency and validation of bi-directional evolutionary structural optimisation, *Comput. Method Appl. M.* 189 (2) (2000) 559–573, [http://dx.doi.org/10.1016/S0045-7825\(99\)00309-6](http://dx.doi.org/10.1016/S0045-7825(99)00309-6).
- [10] C.S. Jog, R.B. Haber, Stability of finite element models for distributed-parameter optimization and topology design, *Comput. Method Appl. M.* 130 (3) (1996) 203–226, [http://dx.doi.org/10.1016/0045-7825\(95\)00928-0](http://dx.doi.org/10.1016/0045-7825(95)00928-0).
- [11] O. Sigmund, On the design of compliant mechanisms using topology optimization, *Mech. Struct. Mach.* 25 (4) (1997) 493–524, <http://dx.doi.org/10.1080/08905459708945415>.
- [12] X. Huang, M. Xie, *Evolutionary Topology Optimization of Continuum Structures: Methods and Applications*, first Ed., John Wiley & Sons, New Jersey, 2010, <http://dx.doi.org/10.1002/9780470689486>.
- [13] O. Sigmund, J. Petersson, Numerical instabilities in topology optimization: A survey on procedures dealing with checkerboards, mesh-dependencies and local minima, *Struct. Optim.* 16 (1) (1998) 68–75, <http://dx.doi.org/10.1007/BF01214002>.
- [14] X. Huang, M. Xie, Convergent and mesh-independent solutions for the bi-directional evolutionary structural optimization method, *Finite Elem. Anal. Des.* 43 (14) (2007) 1039–1049, <http://dx.doi.org/10.1016/j.finel.2007.06.006>.
- [15] M.P. Bendsøe, O. Sigmund, Material interpolation schemes in topology optimization, *Arch. Appl. Mech.* 69 (1999) 635–654, <http://dx.doi.org/10.1007/s004190050248>.
- [16] R. Picelli, W. Vicente, R. Pavanello, Y. Xie, Evolutionary topology optimization for natural frequency maximization problems considering acoustic–structure interaction, *Finite Elem. Anal. Des.* 106 (2015) 56–64, <http://dx.doi.org/10.1016/j.finel.2015.07.010>.
- [17] H.N. Lopes, J. Mahfoud, R. Pavanello, High natural frequency gap topology optimization of bi-material elastic structures and band gap analysis, *Struct. Multidiscip. Optim.* 63 (2021) 1–16, <http://dx.doi.org/10.1007/s00158-020-02811-0>.
- [18] B.V. de Almeida, D.C. Cunha, R. Pavanello, Topology optimization of bimorph piezoelectric energy harvesters considering variable electrode location, *Smart Mater. Struct.* 28 (8) (2019) 085030, <http://dx.doi.org/10.1088/1361-665x/ab2c3e>.
- [19] W. Vicente, R. Picelli, R. Pavanello, Y. Xie, Topology optimization of frequency responses of fluid–structure interaction systems, *Finite Elem. Anal. Des.* 98 (2015) 1–13, <http://dx.doi.org/10.1016/j.finel.2015.01.009>.
- [20] W. Vicente, Z. Zuo, R. Pavanello, T. Calixto, R. Picelli, Y. Xie, Concurrent topology optimization for minimizing frequency responses of two-level hierarchical structures, *Comput. Method Appl. M.* 301 (2016) 116–136, <http://dx.doi.org/10.1016/j.cma.2015.12.012>.
- [21] J. Kook, Evolutionary topology optimization for acoustic-structure interaction problems using a mixed u/p formulation, *Mech. Base. Des. Struct. Mach.* 47 (3) (2019) 356–374, <http://dx.doi.org/10.1080/15397734.2018.1557527>.
- [22] F. Zhao, A nodal variable ESO (BESO) method for structural topology optimization, *Finite Elem. Anal. Des.* 86 (2014) 34–40, <http://dx.doi.org/10.1016/j.finel.2014.03.012>.
- [23] E. Wadbro, M. Berggren, Topology optimization of an acoustic horn, *Comput. Method Appl. M.* 196 (1) (2006) 420–436, <http://dx.doi.org/10.1016/j.cma.2006.05.005>.
- [24] M.B. Dühring, J.S. Jensen, O. Sigmund, Acoustic design by topology optimization, *J. Sound Vib.* 317 (3) (2008) 557–575, <http://dx.doi.org/10.1016/j.jsv.2008.03.042>.

- [25] J.W. Lee, Y.Y. Kim, Rigid body modeling issue in acoustical topology optimization, *Comput. Method Appl. M.* 198 (9) (2009) 1017–1030, <http://dx.doi.org/10.1016/j.cma.2008.11.008>.
- [26] J.W. Lee, Y.Y. Kim, Topology optimization of muffler internal partitions for improving acoustical attenuation performance, *Internat. J. Numer. Methods Engrg.* 80 (4) (2009) 455–477, <http://dx.doi.org/10.1002/nme.2645>.
- [27] K.S. Oh, J.W. Lee, Topology optimization for enhancing the acoustical and thermal characteristics of acoustic devices simultaneously, *J. Sound Vib.* 401 (2017) 54–75, <http://dx.doi.org/10.1016/j.jsv.2017.04.027>.
- [28] J. Kook, K. Koo, J. Hyun, J.S. Jensen, S. Wang, Acoustical topology optimization for Zwicker's loudness model – Application to noise barriers, *Comput. Method Appl. M.* 237–240 (2012) 130–151, <http://dx.doi.org/10.1016/j.cma.2012.05.004>.
- [29] E. Zwicker, H. Fastl, *Psychoacoustics: Facts and Models*, third Ed., Springer Science & Business Media, Berlin, 2013.
- [30] K. Miyata, Y. Noguchi, T. Yamada, K. Izui, S. Nishiwaki, Optimum design of a multi-functional acoustic metasurface using topology optimization based on Zwicker's loudness model, *Comput. Method Appl. M.* 331 (2018) 116–137, <http://dx.doi.org/10.1016/j.cma.2017.11.017>.
- [31] J. Hu, S. Yao, X. Huang, Topology optimization of dynamic acoustic–mechanical structures using the ersatz material model, *Comput. Method Appl. M.* 372 (2020) 113387, <http://dx.doi.org/10.1016/j.cma.2020.113387>.
- [32] F.I. da Silva Júnior, *Síntese Computacional de Absorvedores Acústicos Porcelásticos [Computational synthesis of poroelastic acoustic absorbers]* (Ph.D. thesis), Department of Computational Mechanics, School of Mechanical Engineering, University of Campinas, 2007.
- [33] F.I. Silva, R. Pavanello, Synthesis of porous–acoustic absorbing systems by an evolutionary optimization method, *Eng. Optim.* 42 (2010) 887–905, <http://dx.doi.org/10.1080/03052150903477184>.
- [34] W.U. Yoon, J.H. Park, J.S. Lee, Y.Y. Kim, Topology optimization design for total sound absorption in porous media, *Comput. Method Appl. M.* 360 (2020) 112723, <http://dx.doi.org/10.1016/j.cma.2019.112723>.
- [35] D.L. Johnson, J. Koplik, R. Dashen, Theory of dynamic permeability and tortuosity in fluid-saturated porous media, *J. Fluid Mech.* 176 (1987) 379, <http://dx.doi.org/10.1017/s0022112087000727>.
- [36] Y. Champoux, J.-F. Allard, Dynamic tortuosity and bulk modulus in air-saturated porous media, *J. Appl. Phys.* 70 (1991) 1975–1979, <http://dx.doi.org/10.1063/1.349482>.
- [37] G.H. Yoon, Acoustic topology optimization of fibrous material with Delany–Bazley empirical material formulation, *J. Sound Vib.* 332 (5) (2013) 1172–1187, <http://dx.doi.org/10.1016/j.jsv.2012.10.018>.
- [38] B. Ferrández, F.D. Denia, J. Martínez-Casas, E. Nadal, J.J. Ródenas, Topology and shape optimization of dissipative and hybrid mufflers, *Struct. Multidiscip. Optim.* (2020) 1–16, <http://dx.doi.org/10.1007/s00158-020-02490-x>.
- [39] M.E. Delany, E.N. Bazley, Acoustical properties of fibrous absorbent materials, *Appl. Acoust.* 3 (2) (1970) 105–116, [http://dx.doi.org/10.1016/0003-682X\(70\)90031-9](http://dx.doi.org/10.1016/0003-682X(70)90031-9).
- [40] C.B. Dilgen, S.B. Dilgen, N. Aage, J.S. Jensen, Topology optimization of acoustic mechanical interaction problems: a comparative review, *Struct. Multidiscip. Optim.* 60 (2019) 779–801, <http://dx.doi.org/10.1007/s00158-019-02236-4>.
- [41] X. Wang, K.-J. Bathe, Displacement/pressure based mixed finite element formulations for acoustic fluid–structure interaction problems, *Internat. J. Numer. Methods Engrg.* 40 (11) (1997) 2001–2017.
- [42] X. Huang, Y.M. Xie, Evolutionary topology optimization of continuum structures with an additional displacement constraint, *Struct. Multidiscip. Optim.* 40 (2010) 409–416, <http://dx.doi.org/10.1007/s00158-009-0382-4>.
- [43] Z.H. Zuo, Y.M. Xie, X. Huang, Evolutionary topology optimization of structures with multiple displacement and frequency constraints, *Adv. Struct. Eng.* 15 (2) (2012) 359–372, <http://dx.doi.org/10.1260/1369-4332.15.2.359>.
- [44] D.J. Munk, T. Kipouros, G.A. Vio, G.T. Parks, G.P. Steven, Multiobjective and multi-physics topology optimization using an updated smart normal constraint bi-directional evolutionary structural optimization method, *Struct. Multidiscip. Optim.* 57 (2) (2018) 665–688, <http://dx.doi.org/10.1007/s00158-017-1781-6>.
- [45] F.M. Azevedo, M.S. Moura, W.M. Vicente, R. Picelli, R. Pavanello, Topology optimization of reactive acoustic mufflers using a bi-directional evolutionary optimization method, *Struct. Multidiscip. Optim.* 58 (2018) 2239–2252, <http://dx.doi.org/10.1007/s00158-018-2012-5>.
- [46] S. Liu, Q. Li, W. Chen, L. Tong, G. Cheng, An identification method for enclosed voids restriction in manufacturability design for additive manufacturing structures, *Front. Mech. Eng.* 10 (2015) 126–137, <http://dx.doi.org/10.1007/s11465-015-0340-3>.
- [47] Q. Li, W. Chen, S. Liu, L. Tong, Structural topology optimization considering connectivity constraint, *Struct. Multidiscip. Optim.* 54 (4) (2016) 971–984, <http://dx.doi.org/10.1007/s00158-016-1459-5>.
- [48] Q. Li, W. Chen, S. Liu, H. Fan, Topology optimization design of cast parts based on virtual temperature method, *Comput. Aided Des.* 94 (2018) 28–40, <http://dx.doi.org/10.1016/j.cad.2017.08.002>.
- [49] N. Atalla, F. Sgard, *Finite Element and Boundary Methods in Structural Acoustics and Vibration*, first Ed., CRC Press, Florida, 2015, <http://dx.doi.org/10.1201/b18366>.
- [50] R.D. Cook, D.S. Malkus, M.E. Plesha, R.J. Witt, *Concepts and Applications of Finite Element Analysis*, fourth ed., John Wiley & Sons, New Jersey, 2001.
- [51] K.H. Kim, G.H. Yoon, Optimal rigid and porous material distributions for noise barrier by acoustic topology optimization, *J. Sound Vib.* 339 (2015) 123–142, <http://dx.doi.org/10.1016/j.jsv.2014.11.030>.
- [52] J.F. Allard, N. Atalla, *Propagation of Sound in Porous Media: Modelling Sound Absorbing Materials*, second Ed., John Wiley & Sons, New Jersey, 2009.
- [53] J.S. Lee, P. Göransson, Y.Y. Kim, Topology optimization for three-phase materials distribution in a dissipative expansion chamber by unified multiphase modeling approach, *Comput. Method Appl. M.* 287 (2015) 191–211, <http://dx.doi.org/10.1016/j.cma.2015.01.011>.
- [54] S. Torresin, R. Albatici, F. Aletta, F. Babich, T. Oberman, J. Kang, Acoustic design criteria in naturally ventilated residential buildings: New research perspectives by applying the indoor soundscape approach, *Appl. Sci.* 9 (24) (2019) 5401, <http://dx.doi.org/10.3390/app9245401>.
- [55] M. Ambati, N. Fang, C. Sun, X. Zhang, Surface resonant states and superlensing in acoustic metamaterials, *Phys. Rev. B* 75 (19) (2007) 195447, <http://dx.doi.org/10.1103/PhysRevB.75.195447>.
- [56] X. Wang, A. Díaz-Rubio, V.S. Asadchy, G. Ptitcyn, A.A. Generalov, J. Ala-Laurinaho, S.A. Tretyakov, Extreme asymmetry in metasurfaces via evanescent fields engineering: Angular-asymmetric absorption, *Phys. Rev. Lett.* 121 (2018) 256802, <http://dx.doi.org/10.1103/PhysRevLett.121.256802>.
- [57] J.S. Lee, Y.Y. Kim, J.S. Kim, Y.-J. Kang, Two-dimensional poroelastic acoustical foam shape design for absorption coefficient maximization by topology optimization method, *J. Acoust. Soc. Am.* 123 (2008) 2094–2106, <http://dx.doi.org/10.1121/1.2839001>.



**Rodrigo Lima Pereira** is a Ph. D. student at the University of Campinas, Brazil, in the School of Mechanical Engineering. He studies topology optimization of poro–acoustic systems at the Laboratory of Topology Optimization and Multiphysics Analysis (LTM). His interests are computational mechanics, multiphysics analysis, vibroacoustics and porous materials.



**Heitor Nigro Lopes** is a Ph. D. student at the University of Campinas, Brazil, in the School of Mechanical Engineering. He studies topology optimization of high-frequency dynamic systems at the Laboratory of Topology Optimization and Multiphysics Analysis (LTM). His interests are computational mechanics, multiphysics analysis and model reduction techniques.



**Renato Pavanello** received the Dr. degree in Mechanics in 1991 from the INSA de Lyon, France. He is Professor at the University of Campinas (Unicamp) in the Laboratory of Topology Optimization and Multiphysics Analysis (LTM). His current research activities are the development of numerical models for analysis and topology optimization of coupled multiphysics and multiscale systems.

## **5 | An Evolutionary Multidomain Method Applied to Multiphase Mufflers**

In this chapter, the original research article entitled “Multi-domain acoustic topology optimization based on the BESO approach: applications on the design of multi-phase material mufflers” by Rodrigo Lima Pereira, Heitor Nigro Lopes, Marcio da Silva Moura and Renato Pavanello, is presented with permission from Springer Nature (see Appendix C for the correspondent copyright clearance). The paper has been published in the *Structural and Multidisciplinary Optimization*, v. 66, p. 25, 2023. DOI: 10.1007/s00158-022-03479-4.

The article establishes a new methodology to design reactive and dissipative multi-chamber mufflers for transmission loss maximization, while based on a multi-domain BESO algorithm, named as mdBESO. In this approach, acoustic, porous and rigid materials are considered simultaneously along up to three design domains, and optimized in a wide frequency range. The obtained topologies shown to be correspondent with literature results, in the comparable cases, and quite effective in providing enhanced transmission loss values for all the observed scenarios.

Chapter 7 presents further discussions on the topics and results given here and Appendix A displays detailed extensions of the procedures introduced in the sensitivity analysis section.



# Multi-domain acoustic topology optimization based on the BESO approach: applications on the design of multi-phase material mufflers

Rodrigo L. Pereira<sup>1</sup> · Heitor N. Lopes<sup>1</sup> · Marcio S. Moura<sup>1,2</sup> · Renato Pavanello<sup>1</sup>

Received: 2 September 2022 / Revised: 22 November 2022 / Accepted: 1 December 2022

© The Author(s), under exclusive licence to Springer-Verlag GmbH Germany, part of Springer Nature 2023

## Abstract

Since the early 1920s, the design of mufflers has become an influential topic of study among engineers, as they have the ability to reduce noise from industrial machinery, combustion engines, refrigerators, etc. However, since its applications are strongly dependent on the target frequencies and the adopted geometries, efficient muffler design methods are still under investigation up to this day. With that in mind, this paper presents a multi-domain acoustic topology optimization methodology applied to the design of reactive and dissipative expansion chamber mufflers. Based on the Bi-directional Evolutionary Structural Optimization (BESO) algorithm, the proposed approach also uses a novel material interpolation scheme that considers acoustic, porous and rigid domains during the optimization process, hence configuring a multi-phase procedure. The simulation of porous materials is performed by the Johnson–Champoux–Allard (JCA) mathematical formulations, while the numerical solution is obtained by the finite element method. To further compose the study, the objective function is defined as the mean value of the sound Transmission Losses (TL) obtained along one, two or three different frequency bands, while the proposed multi-domain BESO (mdBESO) algorithm is applied to the design of single and multi-chamber mufflers. Here, more than one muffler per BESO iteration is considered, being also possible to optimize for specific frequency bands in predefined chambers. The effectiveness of both, the novel material interpolation scheme and the mdBESO algorithm, are highlighted, showing considerable TL enhancements in the broad range of frequencies chosen, while also presenting clear optimized partitions as result.

**Keywords** Topology optimization · BESO · Mufflers · Multi-phase optimization · Multi-domain optimization · Porous materials

## 1 Introduction

The design of mufflers (or silencers) have become an important topic over the years, having started in the 1920s, with strong growth around the 1970s, due to the general concern with the socio-environmental quality of the cities (Munjal 2014). The crucial importance of such systems is clear: to promote the reduction of noise from machinery, exhaust

pipes and other acoustic polluters. To do that, two main physical compositions are generally used, causing the reduction of the net energy flow of the component when in contact with acoustic barriers (Fahy 2000), or the conversion of the overall sound energy into heat, when absorptive structures are in place (Ferrándiz et al. 2020). These configurations may be, respectively, identified as reactive and dissipative mufflers, where the combination of the two is commonly referred as hybrid (Selamet et al. 2003).

An interesting point to note is that both dissipative and reactive mufflers have advantages, such as good sound attenuation performances in high-to-mid and low-to-mid frequency ranges, respectively. Nevertheless, they also have disadvantages, in a way that the first application may be harmed by the fluid flow drag, and the second may produce more engine exhaust backpressure (Panigrahi and Munjal 2005). In this sense, hybrid mufflers have been growing in demand as they combine the aforementioned

---

Responsible Editor: Jianbin Du

✉ Rodrigo L. Pereira  
pereira@fem.unicamp.br

<sup>1</sup> Department of Computational Mechanics, School of Mechanical Engineering, University of Campinas, Rua Mendeleev 200, Campinas, São Paulo 13083-860, Brazil

<sup>2</sup> R & D Engineering, Tenneco Inc, Vereador Marcos Portioli Square 26, Mogi Mirim, São Paulo 13807-900, Brazil

advantages to increase the system performance in a broader frequency range, while reducing its drawbacks (Panigrahi and Munjal 2005). More specifically, this muffler type may provide enhancements in Transmission Loss (TL) values, given that a simple (or empty) expansion chamber cannot reduce sound effectively when close to its x-axial eigenfrequencies (Lee and Kim 2009b).

In addition to the conventional methods of extending the inlet/outlet tubes inside chambers (Munjal 2014) or combining rigid barriers with porous linings in a parametric way (Panigrahi and Munjal 2005), optimization techniques have been widely used in the development of mufflers, as they provide innovative and effective designs for noise attenuation. There are three types of optimization techniques applied to the design of multi-physical systems, namely size, shape and topology (Huang and Xie 2010). The first one concerns with finding the optimal dimensions of the structure, while the second regards the modification of the contours of engineered parts. Finally, the third dictates how the general structures are spatially distributed and connected, fact that promotes the greatest freedom of designs among the techniques cited. Nevertheless, in all these three approaches, constraints are usually imposed by the designers before the procedure starts, being one of the ways of influencing the iterative processes.

In this context, a large number of articles about design methods for active and reactive mufflers have been published. Chang and Chiu (2008) used numerical decoupling methods in conjunction with simulated annealing schemes to design optimal plug/non-plug muffler shapes under a limited space. Barbieri and Barbieri (2006) considered shape optimization and the Zoutendijk's feasible directions method (Zoutendijk 1960) to find the optimal dimensions of an acoustic muffler for TL maximization. Size and shape optimizations were studied by de Lima et al. (2011), jointly with genetic algorithms, in the making of reactive silencers. Afterwards, this last approach was again adopted by Chiu (2011) regarding hybrid mufflers.

After the introduction of topology optimization techniques by Bendsoe and Kikuchi (1988), and its first acoustic application on the maximization of sound radiation properties of a horn (Wadbro and Berggren 2006), silencer compositions were then treated in the studies conducted by Lee and Kim (2009b). Here, the authors designed internal partitions of reactive mufflers with the help of the density-based Solid Isotropic Material with Penalization (SIMP) approach, while considering the scalar Helmholtz equation to simulate the acoustic domain. Besides, the over amplification of acoustic properties was also adopted in the description of rigid barriers (Dühring et al. 2008),

fact that helped avoiding further difficulties regarding fluid-structure formulations. Later, a similar approach for achieving target transmission loss in the design of reactive mufflers was again conducted and validated with experiments (Lee 2015).

Further studies involved the addition of temperature gradients (Oh and Lee 2017), fluid flow characteristics (Lee and Jang 2012) and even the influence of perforated tubes (Yedeg et al. 2016) along the optimization of automotive silencers, in order to bring these multi-objective problems even closer to real applications. In the works of Ferrándiz et al. (2020), the aforementioned characteristics were mostly covered, as the interface of perforated tubes with the general acoustic domain was simulated by impedance matching, while the axial fluid flow and thermal gradients were considered by the adoption of Finite Element Method (FEM) based formulations proposed by Denia et al. (2015). At last, the authors investigated hybrid muffler compositions, where porous structures were simulated by the empirical Delany–Bazley model (1970).

Before that, the above model had already been adopted by Yoon (2013) in the description of porous structures with porosity close to unit. His research showed that by combining acoustic, porous and rigid elements in the muffler chamber, sound attenuation performances were greatly improved, but additional steps were necessary to guarantee the attachment of rigid and porous materials. Another groundbreaking work was performed by Lee et al. (2015), who dealt with the optimization of these same kinds of systems, but now using the Unified Multiphase (UMP) modeling technique (Lee et al. 2012). This approach simulates acoustic, poro-elastic and elastic materials by manipulating the enhanced Biot's equations (Atalla et al. 2001), while also removing the need for boundary tracing throughout the procedure.

Still, it is remarked that the above researches treated only one-chamber mufflers with the SIMP model, leaving a gap for the consideration of other methodologies, such as the discrete Evolutionary Structural Optimization (ESO) (Xie and Steven 1993) and the Bi-directional Evolutionary Structural Optimization (BESO) (Yang et al. 1999; Huang and Xie 2010), in addition to the investigation of multi-domain compositions, that is, design domains that can be treated as a whole or divided in geometrically identical parts. Furthermore, formulations completely based on empirical aspects, as the Delany-Bazley, or on fully-coupled phenomenological characteristics, such as the ones based on Biot's equations (Atalla et al. 1998), may respectively add drawbacks, due to the limitations imposed by working frequencies and high porosity (Bo and Tianning 2009), or further difficulties, as

a result of a greater number of acoustic parameters (Cao et al. 2018) and multi-physical interactions (Lee et al. 2012), in the design of porous materials. Nevertheless, it must be pointed out that Azevedo et al. (2018) performed several analyzes with the BESO method, including two-chamber muffler optimizations for TL maximization, while Pereira et al. (2022), conducted topology optimizations of porous domains with this same approach, aiming to enhance the system absorption characteristics. Despite of these various studies, only bi-material optimizations were investigated.

Based on the above accounts, a multi-phase BESO-based methodology for the design of multi-domain systems, named as mdBESO, is proposed and applied in this paper. Particularly, Acoustic-Rigid (AR) and Acoustic-Porous (AP) material phases are considered in the topology optimization of one-chamber mufflers, while the Acoustic-Porous-Rigid (APR) case is combined with the one, two and three-chamber scenario, as a new multi-phase material interpolation scheme is introduced. Rigid and porous materials with rigid frame are approximated by the over amplification of acoustic properties and by the Johnson–Champoux–Allard (JCA) mathematical formulations, respectively, being the latter the most used semi-phenomenological model in the description of poro-rigid structures (Cao et al. 2018). The mean transmission loss is treated as the objective function, which, in turn, is maximized over a wide frequency range. The proposed approach also allows for the combination of specific domains, according to its previously targeted bands,

to broaden the effects of the resulted topologies (Dong et al. 2020, 2022).

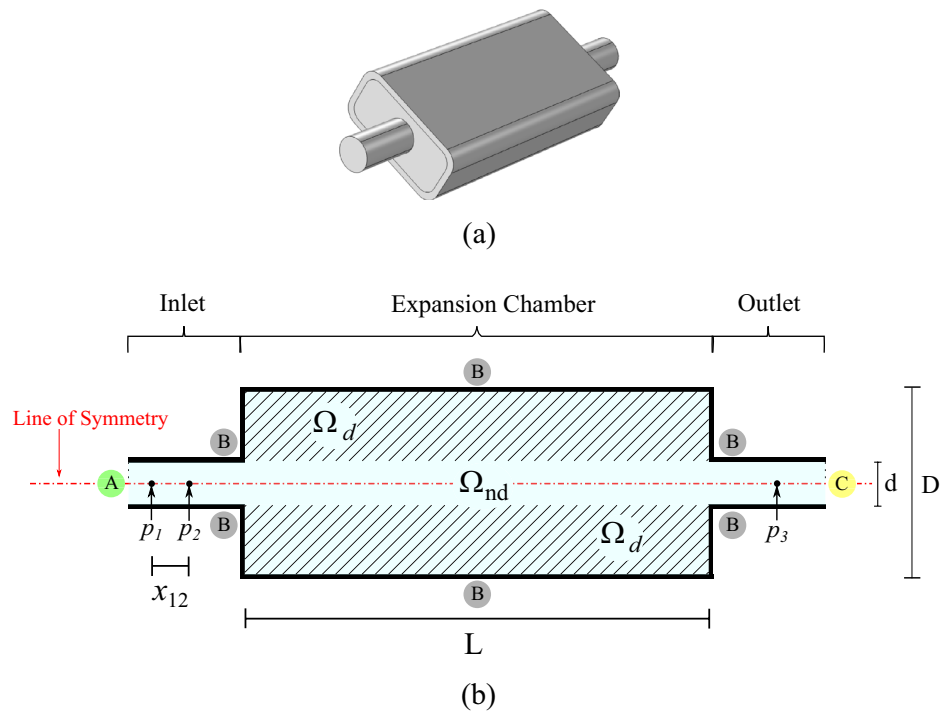
The paper is organized as follows: In Sect. 2, the FEM is introduced, together with the corresponding boundary conditions. Section 3 defines acoustic, porous and rigid material properties, with special attention given to the Johnson–Champoux–Allard (JCA) formulations. Also, material interpolation schemes are defined for the AR, AP and APR configurations. Section 4 presents the multi-domain BESO algorithm, beyond showing the basic features of the discrete topology optimization approach. In Sect. 5, numerical examples and their discussions are treated, with conclusions drawn in Sect. 6.

## 2 Finite element formulation for acoustic muffler systems

In this work, the goal is to optimize muffler systems as generally illustrated in Fig. 1a. To that end, it is modeled a bidimensional symmetric expansion chamber muffler composed of one inlet/outlet tube and filled with an inviscid fluid of negligible flow velocity, as schematically shown in Fig. 1b. For the case of time-harmonic pressure variations ( $p(x, y, t) = p(x, y) \exp(j\omega t)$ ), the system can be described, in the frequency domain, by the subsequent scalar Helmholtz equation,

$$\nabla \cdot \left( \frac{\nabla p(x, y)}{\rho} \right) + \frac{\omega^2}{\kappa} p(x, y) = 0 \quad \text{in } \Omega, \tag{1}$$

**Fig. 1** General representation of a muffler system. **a** Tridimensional muffler model and **b** bidimensional nominal chamber composition with design details. The acoustic domain,  $\Omega$ , is composed of both design,  $\Omega_d$ , and non-design,  $\Omega_{nd}$ , domains, while the symbols (A), (B) and (C) correspond to two Neumann and one Robin boundary condition types, respectively



where the introduced variables are the density  $\rho$ , the bulk modulus  $\kappa = \rho c^2$ , the speed of sound in the fluid  $c$ , the unit imaginary number  $j^2 = -1$ , the radial frequency  $\omega$ , the time  $t$  and the vector differential operator  $\nabla$ . The acoustic domain,  $\Omega$ , is composed of both design,  $\Omega_d$ , and non-design,  $\Omega_{nd}$ , domains, which, in turn, are chosen in order to avoid trivial solutions in a topology optimization process (barrier blockade). Throughout this work, the pressure  $p(x, y)$  in a bidimensional Eulerian field  $(x, y)$  is mentioned only as  $p$ .

As also highlighted in Fig. 1b, two Neumann and one Robin boundary condition types are, respectively, identified by the symbols (A), (B) and (C). Particularly, (A) concerns with the input of plane waves by the assignment of normal particle velocities,  $\bar{v}_n$ , to the inlet section, (B) describes the rigid wall condition that is enforced in the surfaces of the muffler and (C) characterizes the output termination as anechoic, that is a non-reflecting component, by the impedance matching between the inner and outer acoustic fluids (Munjal 2014). Mathematically, such conditions may be written as,

$$\text{(A)} : \frac{\nabla p \cdot \mathbf{n}}{\rho} = -j\omega\bar{v}_n, \tag{2}$$

$$\text{(B)} : \nabla p \cdot \mathbf{n} = 0, \tag{3}$$

$$\text{(C)} : \frac{\nabla p \cdot \mathbf{n}}{\rho} = -\frac{j\omega p}{Z_0}, \tag{4}$$

where  $\mathbf{n}$  is the outward unit normal vector and  $Z_0 = \rho_a c_a$  is the air characteristic impedance, with the subscript  $a$  referring to the acoustic material (air).

The weak form of the boundary value problem defined by Eqs. (1) to (4) can then be obtained by the combination of the Weighted Residuals Method and the Divergence Theorem,

$$\frac{1}{\rho} \int_{\Omega} \nabla p \cdot \nabla \delta p \, d\Omega - \frac{\omega^2}{\kappa} \int_{\Omega} p \delta p \, d\Omega + \int_{\Gamma_1} \frac{j\omega p}{Z_0} \delta p \, d\Gamma_1 + \int_{\Gamma_2} j\omega\bar{v}_n \delta p \, d\Gamma_2 = 0, \tag{5}$$

with  $\Gamma_1$  and  $\Gamma_2$  being, respectively, the boundaries of  $\Omega$  where conditions (A) and (C) (Eqs. (2) and (4)) are valid, and  $\delta p$  is the test function. Since condition (B) (Eq. (3)) is homogeneous, the rigid wall boundary integral vanishes from Eq. (5). The FEM (Atalla and Sgard 2015) is chosen to approximate the continuous problem into a discrete one. By the adoption of Galerkin’s approach, the pressure field and its gradient, together with the test function information, can be written, in the element domain  $\Omega_e$ , as,

$$p = \mathbf{N}_e \mathbf{p}_e \quad \text{and} \quad \delta p = \mathbf{N}_e \delta \mathbf{p}_e, \tag{6}$$

$$\nabla p = \mathbf{B}_e \mathbf{p}_e, \quad \text{and} \quad \nabla \delta p = \mathbf{B}_e \delta \mathbf{p}_e, \tag{7}$$

where  $\mathbf{N}_e$  is the shape function matrix, with  $\mathbf{B}_e$  being its gradient, and  $\mathbf{p}_e$  is the acoustic pressure vector. The variables preceded by  $\delta$  are considered to be test function related.

Placing Eqs. (6) and (7) into Eq. (5), the elemental acoustic stiffness,  $\mathbf{K}_e$ , mass,  $\mathbf{M}_e$ , and damping,  $\mathbf{C}_e$ , matrices, in addition to the element load vector,  $\mathbf{f}_e$ , are reached,

$$\mathbf{K}_e = \frac{1}{\rho} \int_{\Omega_e} \mathbf{B}_e^T \mathbf{B}_e \, d\Omega_e, \tag{8}$$

$$\mathbf{M}_e = \frac{1}{\kappa} \int_{\Omega_e} \mathbf{N}_e^T \mathbf{N}_e \, d\Omega_e, \tag{9}$$

$$\mathbf{C}_e = \frac{1}{Z_0} \int_{\Gamma_{e1}} \mathbf{N}_e^T \mathbf{N}_e \, d\Gamma_{e1}, \tag{10}$$

$$\mathbf{f}_e = -j\omega\bar{v}_n \int_{\Gamma_{e2}} \mathbf{N}_e^T \, d\Gamma_{e2}, \tag{11}$$

where  $\Gamma_{e1}$  and  $\Gamma_{e2}$  can be thought as elemental partitions of  $\Gamma_1$  and  $\Gamma_2$ , respectively. After the standard finite element assembly procedure is conducted, the acoustic dynamic system can be obtained,

$$\mathbf{Z}\mathbf{p} = (\mathbf{K} + j\omega\mathbf{C} - \omega^2\mathbf{M})\mathbf{p} = \mathbf{f}, \tag{12}$$

where  $\mathbf{K}$ ,  $\mathbf{M}$  and  $\mathbf{C}$  are the global acoustic stiffness, mass and damping matrices, with  $\mathbf{f}$  and  $\mathbf{p}$  being the global acoustic load and pressure vectors, respectively.

Lastly, it is noted that the investigated system (Fig. 1b) and the frequency spectrum considered in this work (below the cut off frequency) allow for the assumption of plane waves, not only at the inlet, but also at the outlet regions, where the sound pressure amplitudes ( $p_1$ ,  $p_2$  and  $p_3$ ) are collected and used in the calculation of vibroacoustic indicators, e.g. Transmission Loss (TL). The muffler dimensions, such as chamber length,  $L$ , and height,  $D$ , as well as the distance  $x_{12}$  and the pipe height,  $d$ , are defined later, in the numerical examples section.

### 3 Target material characterization

In this work, rigid and poro-rigid materials are treated as modified fluids, so as to be described by the scalar Helmholtz expression while also avoiding the intricacies related to fluid-structure interactions. The rigid material may be viewed as a

non-vibrating structure, with infinite specific acoustic impedance and total reflective boundaries. In a mathematical perspective, this can be achieved by the over amplification of the density and bulk modulus of the air, as done in previous works (Dühring et al. 2008; Lee and Kim 2009a). In a similar manner, the poro-rigid structure can be derived from an equivalent fluid simplification by the adoption of the long-wavelength condition. Here, the pores are considered to be much smaller than the wavelength, in a way that the porous frame may be treated as motionless. Nevertheless, thermal and visco-inertial effects are still under consideration when the basic features of these poro-rigid materials, such as the effective density,  $\rho_p$ , and the effective bulk modulus,  $\kappa_p$ , are described by frequency-dependent and complex valued equations (Allard and Atalla 2009).

In the researches conducted by Lee and Kim (2009a), the use of rigid materials in simple acoustic settings was investigated, aiming to determine the proper lower limit values of its density,  $\rho_r$ , and bulk modulus,  $\kappa_r$ . They concluded that the values of  $\rho_r \geq 10^5 \rho_a$  and  $c_r \geq 10^1 c_a$  can avoid physically spurious solutions when used in muffler systems, where the subscripts  $a$  and  $r$  refer to acoustic and rigid material properties, respectively. Based on this approximation, the following data are adopted,

$$\rho_a = 1.21 \text{ kg m}^{-3}; \quad \kappa_a = 1.42 \times 10^5 \text{ Pa}, \tag{13}$$

$$\rho_r = 10^7 \rho_a \text{ kg m}^{-3}; \quad \kappa_r = 10^9 \kappa_a \text{ Pa}. \tag{14}$$

In addition, the semi-phenomenological model of Johnson–Champoux–Allard (JCA) (Johnson et al. 1987; Champoux and Allard 1991) is also considered in the simulation of poro-rigid materials,

$$\rho_p = \frac{\alpha_\infty \rho_a}{\phi} + \frac{\sigma}{j\omega} \sqrt{1 + j \frac{4\alpha_\infty^2 \eta \rho_a \omega}{\sigma^2 \Lambda^2 \phi^2}}, \tag{15}$$

$$\kappa_p = \frac{\gamma P_0 / \phi}{\gamma - \frac{1}{1 - j \frac{8\eta}{\Lambda^2 Pr \rho_a \omega} \sqrt{1 + j \frac{\Lambda'^2 Pr \rho_a \omega}{16\eta}}}}, \tag{16}$$

where the porosity is denoted by  $\phi$ , the tortuosity is  $\alpha_\infty$ , the static flow resistivity is  $\sigma$ , the viscous characteristic length is  $\Lambda$  and the thermal characteristic length is  $\Lambda'$ . The four thermodynamic parameters of the air that saturates the pores are also introduced, with  $\eta$  being the kinematic viscosity,  $\gamma$  the specific heat ratio,  $Pr$  the Prandtl number, and  $P_0$  the atmospheric pressure. Table 1 shows the JCA model parameters of rock-wool, as the porous material chosen, and air at 20°C.

**Table 1** JCA model parameters

Parameters of Rock-wool	Value
Porosity $\phi$	0.94
Tortuosity $\alpha_\infty$	2.1
Static flow resistivity $\sigma$ (N s m <sup>-4</sup> )	135, 000
Viscous characteristic length $\Lambda$ ( $\mu$ m)	49
Thermal characteristic length $\Lambda'$ ( $\mu$ m)	166
Thermodynamic Parameters of Air at 20°C	Value
Kinematic viscosity $\eta$ (kg m <sup>-1</sup> s <sup>-1</sup> )	$1.84 \times 10^{-5}$
Specific heat ratio $\gamma$	1.401
Prandtl number $Pr$	0.710
Atmospheric pressure $P_0$ (Pa)	101, 325

### 3.1 Multi-phase material interpolation scheme

Before presenting the three-phase Material Interpolation Scheme (MIS) proposed in this work, two bi-material ones, comprising Acoustic-Rigid (AR) and Acoustic-Porous (AP) relations, are introduced by the set of Eqs. (17) and (18),

$$\begin{cases} \frac{1}{\rho(\gamma_e)} = \frac{1}{\rho_r} + \gamma_e^{\psi_1} \left( \frac{1}{\rho_a} - \frac{1}{\rho_r} \right), \\ \frac{1}{\kappa(\gamma_e)} = \frac{1}{\kappa_r} + \gamma_e^{\psi_2} \left( \frac{1}{\kappa_a} - \frac{1}{\kappa_r} \right), \end{cases} \tag{17}$$

$$\begin{cases} \frac{1}{\rho(\gamma_e)} = \frac{1}{\rho_p} + \gamma_e^{\eta_1} \left( \frac{1}{\rho_a} - \frac{1}{\rho_p} \right), \\ \frac{1}{\kappa(\gamma_e)} = \frac{1}{\kappa_p} + \gamma_e^{\eta_2} \left( \frac{1}{\kappa_a} - \frac{1}{\kappa_p} \right), \end{cases} \tag{18}$$

where  $\gamma_e$  represents the design variable, with the superscripts  $\psi_{1,2}$  and  $\eta_{1,2}$  being penalty variables, and the subscripts  $a$ ,  $p$  and  $r$  referring to acoustic, porous and rigid materials, respectively.

Following Pereira et al. (2022), a recurring practice is to consider  $\gamma_e = \gamma_{\min} = 0.001$  for acoustic and  $\gamma_e = 1$  for rigid/porous materials. However, in this case, the acoustic properties must switch place with the rigid and porous ones, to guarantee an initial domain full of acoustic elements; hence  $\gamma_e = \gamma_{\min} = 0.001$  is adopted for rigid/porous materials, while  $\gamma_e = 1$  is set for the acoustic. In discrete topology optimization algorithms, MIS are often used to enhance the stability of the evolutionary process, as it enables the evaluation of the objective function gradient. In this particular case, Eqs. (17) and (18) are chosen based on the fact that the elemental matrices are proportional to the inverse of the density and bulk modulus (Yoon 2013), as can be seen in Eqs. (8) and (9).

Nevertheless, one of the issues regarding Eq. (17) is due to the considerable differences between the values adopted for  $\rho_r$  and  $\kappa_r$  compared to  $\rho_a$  and  $\kappa_a$ . As the rigid material density and bulk modulus are too large (more than  $10^7$  times the air property values), its inverses are too small, therefore, resulting in interference from the acoustic portion into the rigid one, when considering  $\gamma_{\min} = 0.001$  together with penalty variables smaller than 4. Such fact goes against the expectations regarding the capacity of the chosen MIS be able to address all individual material forms, with as minimum influence of the other phases as possible, when starting from a purely acoustic domain. Based on that, two additional variables ( $\Theta_{1,2}$ ) are introduced in Eq. (17) as an effort to reduce the aforementioned numerical issues,

$$\begin{cases} \frac{1}{\rho(\gamma_e)} = \Theta_1 + \gamma_e^{\psi_1} \left( \frac{1}{\rho_a} - \frac{1}{\rho_r} \right), \\ \frac{1}{\kappa(\gamma_e)} = \Theta_2 + \gamma_e^{\psi_2} \left( \frac{1}{\kappa_a} - \frac{1}{\kappa_r} \right), \end{cases} \quad (19)$$

where,

$$\Theta_1 = \frac{1}{\rho_r} - \gamma_{\min}^{\psi_1} \left( \frac{1}{\rho_a} - \frac{1}{\rho_r} \right), \quad (20)$$

$$\Theta_2 = \frac{1}{\kappa_r} - \gamma_{\min}^{\psi_2} \left( \frac{1}{\kappa_a} - \frac{1}{\kappa_r} \right). \quad (21)$$

From Eqs. (19), (20) and (21) it is perceptive that no further interference is considered over the rigid portion when  $\gamma_{\min} = 0.001$ , while the acoustic phase is also correctly described when  $\gamma_e = 1$  (interference of order of  $0.001^{\psi_{1,2}}$ ).

Following a similar idea, the multi-phase MIS for the Acoustic-Porous-Rigid (APR) problem can finally be introduced,

$$\begin{cases} \frac{1}{\rho(\gamma_{e1}, \gamma_{e2})} = \Theta_3(1 - \gamma_{e2}^{l_2}) + \frac{1}{\rho_p}(\gamma_{e2}^{l_2} - \gamma_{e1}^{l_1}) + \gamma_{e1}^{l_1} \frac{1}{\rho_a}, \\ \frac{1}{\kappa(\gamma_{e1}, \gamma_{e2})} = \Theta_4(1 - \gamma_{e2}^{l_2}) + \frac{1}{\kappa_p}(\gamma_{e2}^{l_2} - \gamma_{e1}^{l_1}) + \gamma_{e1}^{l_1} \frac{1}{\kappa_a}, \end{cases} \quad (22)$$

with,

$$\Theta_3 = \frac{1}{\rho_r} - \left[ \frac{1}{\rho_p}(\gamma_{\min}^{l_2} - \gamma_{\min}^{l_1}) + \gamma_{\min}^{l_1} \frac{1}{\rho_a} \right], \quad (23)$$

$$\Theta_4 = \frac{1}{\kappa_r} - \left[ \frac{1}{\kappa_p}(\gamma_{\min}^{l_2} - \gamma_{\min}^{l_1}) + \gamma_{\min}^{l_1} \frac{1}{\kappa_a} \right], \quad (24)$$

where  $\gamma_{1,2}$  are the problem design variables and  $l_{1,2,3,4}$  are its corresponding penalizers. In addition, acoustic, porous and rigid structures can be clearly obtained

**Table 2** Design variable limiting values according to its corresponding element types and problems under investigation

Problem	Variable	Value	Type
AR (2 phases)	$\gamma_e$	1	Acoustic
		$\gamma_{\min}$	Rigid
AP (2 phases)	$\gamma_e$	1	Acoustic
		$\gamma_{\min}$	Porous
APR (3 phases)	$(\gamma_{e1}, \gamma_{e2})$	(1, 1)	Acoustic
		$(\gamma_{\min}, 1)$	Porous
		$(\gamma_{\min}, \gamma_{\min})$	Rigid

by setting  $(\gamma_{e1}, \gamma_{e2}) = (1, 1)$ ,  $(\gamma_{e1}, \gamma_{e2}) = (\gamma_{\min}, 1)$  and  $(\gamma_{e1}, \gamma_{e2}) = (\gamma_{\min}, \gamma_{\min})$ , respectively. To make matters clearer, Table 2 presents the design variable limiting values according to its corresponding element types, being directly associated with the AR, AP and APR interpolations (Eqs. (19), (18) and (22), respectively). Since the values of  $\psi_{1,2}$ ,  $\eta_{1,2}$  and  $l_{1,2,3,4}$  are problem dependent, they are presented in Sect. 5.

#### 4 Topology optimization of multi-phase mufflers: a BESO-based multi-domain methodology

A topology optimization problem consists in changing the material configuration inside the design domain,  $\Omega_d$ , with the goal of enhancing some objective function, while respecting equilibrium equations and predefined constraints. In density-based optimizations, a design variable is assigned to each  $\Omega_d$  finite element, representing the current material type at that specific  $\Omega_d$  location (see Table 2). Sensitivity numbers are then defined as the derivative of the objective function with respect to the design variables. In a discrete BESO context (Huang and Xie 2010), for example, elements with lower sensitivity numbers are removed from the design, while the ones with higher values are added, thus maximizing the objective function chosen.

As a particularization, consider a topology optimization problem where the goal is to maximize the mean transmission loss,  $\Phi$ , over the angular frequency range  $[\omega_s^{(1)}, \omega_f^{(m)}]$ , when subjected to the acoustic equilibrium system Eq. (12) and  $n - 1$  volume constraints,

$$\max.: \Phi = \frac{1}{\omega_f^{(m)} - \omega_s^{(1)}} \left( \sum_{i=1}^m \int_{\omega_s^{(i)}}^{\omega_f^{(i)}} \text{TL} \, d\Omega_{dm} \right), \quad (25)$$

$$\text{s.t.: } \begin{cases} \mathbf{Zp} = \mathbf{f}, \\ \left\{ \begin{matrix} V_1^* - \left( \sum_{e=1}^{N_{el}} V_e \gamma_e \right)_1 \\ \vdots \\ V_{n-1}^* - \left( \sum_{e=1}^{N_{el}} V_e \gamma_e \right)_{n-1} \end{matrix} \right\} = \begin{Bmatrix} 0 \\ \vdots \\ 0 \end{Bmatrix}, \\ \underline{\gamma} = \left[ \begin{matrix} \gamma_1 \\ \vdots \\ \gamma_{N_{el}} \end{matrix} \right]_1, \dots, \left[ \begin{matrix} \gamma_1 \\ \vdots \\ \gamma_{N_{el}} \end{matrix} \right]_{n-1}. \end{cases} \quad (26)$$

In the above equations,  $m$  is the number of design domains (or muffler chambers) considered in the optimization, while  $\Omega_{dm}$  refers to the specific domain where the mean TL is calculated over the  $[\omega_s^{(m)}, \omega_f^{(m)}]$  frequency range. Additionally,  $n$  indicates the number of material phases treated in the iterative procedure, which are controlled by the relations between the prescribed final volume fractions,  $V^*$ , and the design domain volume fractions,  $\sum_{e=1}^{N_{el}} V_e \gamma_e$ .  $N_{el}$  is the total number of elements in the fluid domain. Furthermore, the general design domain matrix,  $\gamma$ , encompass all the column design domain vectors,  $\gamma$ , of each individual material phase. Table 2 shows the number of material phases and the limit values of the elemental design variables,  $\gamma_e$ , considered in the problems here investigated, while Fig. 2 presents the multi-chamber disposition for up to  $m = 3$ .

Considering the same cross sectional areas of the inlet and outlet tubes, and knowing that only plane waves propagate themselves in those regions, the TL formula can be obtained with the help of the three-point methodology (Wu and Wan 1996),

$$TL = 20 \log_{10} \left( \left| \frac{1}{p_3} \frac{p_1 - p_2 \exp(-jk_a x_{12})}{1 - \exp(-j2k_a x_{12})} \right| \right), \quad (27)$$

where the air wavenumber is denoted by  $k_a = \omega/c_a$ , the sound pressure amplitudes measured at the inlet receivers are  $p_1$  and  $p_2$ , being located  $x_{12}$  from each other (see Fig. 1b), and the sound pressure amplitude taken from the outlet end is  $p_3$ . According to Bilawchuk and Fyfe (2003), and Lee (2015), the compactness of Eq. (27) allows for easier numerical implementation, besides being computationally cheaper, when compared with more traditional methods, such as the 4-pole transfer matrix approach (Young and Crocker 1975).

### 4.1 Sensitivity analysis

As previously highlighted, the contribution of each finite element must be taken into account, in order to maximize the considered objective function. In this muffler optimization problem, such calculation is done by the derivation of  $\Phi$  with respect to  $\gamma_e$ ,

$$\alpha_e = \frac{1}{\omega_f^{(m)} - \omega_s^{(1)}} \left( \sum_{i=1}^m \int_{\omega_s^{(m)}}^{\omega_f^{(m)}} \frac{\partial TL}{\partial \gamma_e} d\Omega_{dm} \right), \quad (28)$$

where  $\alpha_e$  is the sensitivity number of the  $e$ th element. To properly solve Eq. (28), one may first calculate the partial TL derivative (Lee and Kim 2009b),

$$\frac{\partial TL}{\partial \gamma_e} = \frac{10}{\ln 10} \left( \frac{\partial |p_{in}|^2}{\partial \gamma_e} \frac{1}{|p_{in}|^2} - \frac{\partial |p_{out}|^2}{\partial \gamma_e} \frac{1}{|p_{out}|^2} \right), \quad (29)$$

where

$$|p_{in}|^2 = \frac{[\text{Re}(p_1) - \text{Re}(p_2) \cos(k_a x_{12}) - \text{Im}(p_2) \sin(k_a x_{12})]^2}{[1 - \cos(2k_a x_{12})]^2 + [\sin(2k_a x_{12})]^2} + \frac{[\text{Im}(p_1) - \text{Im}(p_2) \cos(k_a x_{12}) + \text{Re}(p_2) \sin(k_a x_{12})]^2}{[1 - \cos(2k_a x_{12})]^2 + [\sin(2k_a x_{12})]^2}, \quad (30)$$

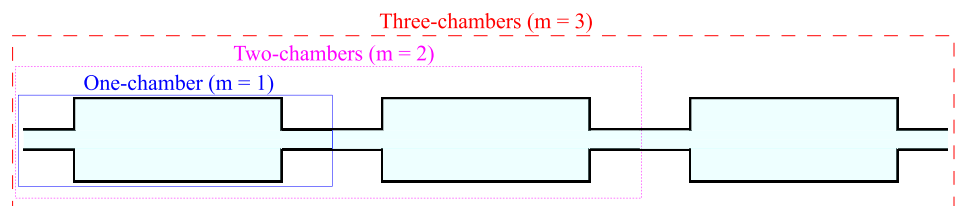
$$|p_{out}|^2 = \text{Re}(p_3)^2 + \text{Im}(p_3)^2, \quad (31)$$

and,

$$\begin{aligned} \frac{\partial |p_{in}|^2}{\partial \gamma_e} = & \frac{2[\text{Re}(p_1) - \text{Re}(p_2) \cos(k_a x_{12}) - \text{Im}(p_2) \sin(k_a x_{12})]}{[1 - \cos(2k_a x_{12})]^2 + [\sin(2k_a x_{12})]^2} \times \\ & \left[ \frac{\partial \text{Re}(p_1)}{\partial \gamma_e} - \frac{\partial \text{Re}(p_2)}{\partial \gamma_e} \cos(k_a x_{12}) - \frac{\partial \text{Im}(p_2)}{\gamma_e} \sin(k_a x_{12}) \right] + \\ & \frac{2[\text{Im}(p_1) - \text{Im}(p_2) \cos(k_a x_{12}) + \text{Re}(p_2) \sin(k_a x_{12})]}{[1 - \cos(2k_a x_{12})]^2 + [\sin(2k_a x_{12})]^2} \times \\ & \left[ \frac{\partial \text{Im}(p_1)}{\partial \gamma_e} - \frac{\partial \text{Im}(p_2)}{\partial \gamma_e} \cos(k_a x_{12}) + \frac{\partial \text{Re}(p_2)}{\gamma_e} \sin(k_a x_{12}) \right], \end{aligned} \quad (32)$$

$$\frac{\partial |p_{out}|^2}{\partial \gamma_e} = 2 \frac{\partial \text{Re}(p_3)}{\partial \gamma_e} \text{Re}(p_3) + 2 \frac{\partial \text{Im}(p_3)}{\partial \gamma_e} \text{Im}(p_3). \quad (33)$$

Fig. 2 General configurations of a muffler system with one, two and three expansion chambers



In Eqs. (30) to (33),  $\text{Re}(p_j)$  and  $\text{Im}(p_j)$  denote the real and imaginary parts of the  $j$ th pressure amplitude, with the values of  $\partial\text{Re}(p_j)/\partial\gamma_e$  and  $\partial\text{Im}(p_j)/\partial\gamma_e$  obtained by, respectively, taking the real and imaginary parts of  $\partial p_j/\partial\gamma_e$ .

By defining an adjoint load vector of form  $\partial p_j/\partial\mathbf{p}$  and size [dof, 1], where dof refers to the total number of degrees of freedom of the system, the investigated nodal pressure,  $p_j$ , is then considered to be addressed to a specific dof, allowing  $\partial p_j/\partial\mathbf{p}$  to be filled with zeros, with the exception of the unitary value that is placed in the dof referred to  $p_j$  (Lee et al. 2015). With this, and the help of Eq. (12), the differentiation of  $p_j$  can be written,

$$\frac{\partial p_j}{\partial\gamma_e} = \left(\frac{\partial p_j}{\partial\mathbf{p}}\right)^T \frac{\partial\mathbf{p}}{\partial\gamma_e}, \tag{34}$$

where,

$$\frac{\partial\mathbf{p}}{\partial\gamma_e} = -\mathbf{Z}^{-1} \frac{\partial\mathbf{Z}}{\partial\gamma_e} \mathbf{p}. \tag{35}$$

Applying Eq. (35) into Eq. (34), and considering  $\mathbf{p}_j = \mathbf{Z}^{-1}(\partial p_j/\partial\mathbf{p})$ , the targeted expression is obtained,

$$\frac{\partial p_j}{\partial\gamma_e} = -\mathbf{p}_j^T \frac{\partial\mathbf{Z}}{\partial\gamma_e} \mathbf{p}. \tag{36}$$

As a final action, one may calculate  $\partial\mathbf{Z}/\partial\gamma_e$  by the assistance of the acoustic finite element equation, Eq. (12), and the appropriated material interpolation scheme. Since this work deals with multi-phase topology optimization problems, all the three MIS expressions Eqs. (18), (19) and (22) are considered when dealing with acoustic-porous, acoustic-rigid and acoustic-porous-rigid compositions, respectively. These expressions have been validated via finite differences method.

### 4.2 Projection filter

When discretizing a continuous domain with the FEM, a few issues may arise due to the  $C^0$  discontinuity across element boundaries. Between them are checkerboard patterns (Jog and Haber 1996) and mesh dependency (Sigmund 1997), which may be dealt with the adoption of numeric filters. As discussed by Dilgen et al. (2019), convolution (Bruns and Tortorelli 2001) and Helmholtz (Lazarov and Sigmund 2011) type density filters can be thought as valid choices for the solution of the aforementioned problems. Another common way is based in the projection of the nodal sensitivity numbers along the design domain. A particular form of this last one has been introduced by Huang and Xie (2007)

for applications regarding BESO-based optimizations. Therefore, it has been chosen in the current work.

The overall procedure consists in distributing the elemental sensitivity numbers between the nodes. Afterwards, a mesh independent filter radius,  $r_{\min}$ , is placed at the center of each element. All nodes within this radius are then considered contributors to the averaged elemental sensitivity numbers that finally result. Based on that, one may write the nodal sensitivity numbers expression as,

$$\alpha_n = \sum_{e=1}^M w_e \alpha_e, \tag{37}$$

$$w_e = \begin{cases} 1 & \text{if } M = 1, \\ \frac{1}{M-1} \left(1 - \frac{r_{en}}{\sum_{e=1}^M r_{en}}\right) & \text{if } M > 1, \end{cases} \tag{38}$$

where  $\alpha_n$  is the  $n$ th node sensitivity number,  $M$  is the amount of elements connected to the  $n$ th node,  $w_e$  is the weight factor of the  $e$ th element and  $r_{en}$  is the distance from the centroid of the  $e$ th element to the  $n$ th node. The filtered sensitivities are,

$$\alpha_e = \frac{\sum^H w(r_{en})\alpha_n}{\sum^H w(r_{en})}, \tag{39}$$

with  $H$  defined as a list of the nodes that are inside the  $r_{\min}$  subdomain and  $w(r_{en}) = r_{\min} - r_{en}$  being a linear weight factor.

At last, to increase the stability of the optimizer, an additional sensitivity historical averaging procedure is adopted,

$$\alpha_e = \frac{\alpha_e^{(i-1)} + \alpha_e^{(i)}}{2}, \tag{40}$$

with the superscript  $i$  referring to the ongoing iteration of the topology optimization algorithm.

### 4.3 Multi-phase design update

To continue the optimization process, the target volume of the following iteration has to be defined. For this, the Evolutionary Rate (ER) is prescribed as the change in volume fraction between the next,  $V^{(i+1)}$ , and the current,  $V^{(i)}$ , iterations, that is,

$$V^{(i+1)} = V^{(i)}(1 \pm \text{ER}). \tag{41}$$

After sorting the sensitivity number values from highest to lowest and considering the threshold established by  $V^{(i+1)}$ , the elements are modified by the following relation,

$$\alpha_e \leq \alpha_{th} \quad \text{as void elements } (\gamma_e = \gamma_{min}), \quad (42)$$

$$\alpha_e > \alpha_{th} \quad \text{as full elements } (\gamma_e = 1), \quad (43)$$

where  $\alpha_{th}$  is the threshold sensitivity number. When  $\alpha_e \leq \alpha_{th}$  the so-called void material is assigned to that specific element by the imposition of  $\gamma_e = \gamma_{min}$ . For the case of  $\alpha_e > \alpha_{th}$ , the full material is then placed. In a multi-phase optimization setting, such element types vary according to the particular materials described by the sensitivity vector under consideration (Huang and Xie 2009, 2010).

As an example, in the APR material configuration  $n = 3$  and  $\underline{\gamma} = [\gamma_1, \gamma_2]$ . This means that two different sensitivity analysis would have to be considered, in order to relate acoustic to porous and then to rigid elements. Such procedure is done with the help of the expressions shown in Sect. 4.1 and the MIS described by Eq. (22). With the derivation of this material interpolation with respect to the elemental design variables,  $(\gamma_{e1}, \gamma_{e2})$ , two sets of sensitivity numbers are generated, becoming then subject to the relations imposed by Eqs. (42) and (43). For a single finite element, the resulted combination of  $(\gamma_{e1}, \gamma_{e2}) = (1, 1)$  describes air, while  $(\gamma_{e1}, \gamma_{e2}) = (\gamma_{min}, 1)$  or  $(\gamma_{min}, \gamma_{min})$  characterizes porous or elastic materials, respectively (see Table 2 for completeness). Such pattern can be repeated for the  $n - 1$  phase materials, in a general case, if more sensitivity vectors are considered and comprehensive MIS are constructed.

One important aspect concerns the meaning of the ER in a multi-phase optimization procedure. While this variable establishes the proportion of volume reduction of the initial structure, composed of material 1, it also controls the increase of the alternative one, material 2. As Eq. (26) restricts the amount of each material volume fraction throughout the optimization, it is understood that material 2 gradually increases, with the reduction of the first, until reaching  $V_2^*$ . Then, such volume is kept constant, while material 3 starts to increase. After  $V_3^*$  is also reached, the next material takes its place, up until all the multiple structures have attained its final volume fractions (Huang and Xie 2009, 2010).

Another important point to note refers to the definition of a variable that allows changes of void/full to full/void elements. This possibility of return of materials (or addition) is controlled by the Addition Ratio (AR), hence representing the bi-directionality of the BESO approach. To apply limitations to this procedure, the maximum Addition Ratio ( $AR_{max}$ ) is established. If the case where  $AR > AR_{max}$  arises, then the  $AR = AR_{max}$  regulation is

imposed to fulfill  $V_{i+1}$ . This entails in the fact that some of the lowest  $\alpha_e$  elements are set to be void and others, with the highest  $\alpha_e$ , to be full.

#### 4.4 Multi-domain evolutionary algorithm

As one of the novelties of the current work, the multi-domain BESO (or mdBESO) method is introduced in Algorithm 1. Initially, all the aforementioned geometry and BESO variables should be imputed to the system, as well as boundary conditions and mesh information. Additionally, the proper number of domains,  $m$ , and material phases,  $n$ , are expected to be known beforehand. In the acoustic topology optimization problems here explored, three types of material configuration are considered, being two bi-phase (AR and AP) and one three-phase (APR), with this last one being also treated in multi-chamber mufflers. The results from such investigations can be found in Sects. 5.1, 5.2 and 5.3.

The natural next step of the mdBESO proposition consists in solving the dynamic equilibrium system, Eq. (12), in order to find the nodal pressure values needed to start the iterative process. At this point, sensitivity analysis, filtering, and multi-phase design update procedures are performed, as previously discussed in Sects. 4.1, 4.2 and 4.3, respectively. However, the new design update matrix and its corresponding volume fraction information are just allowed to be changed outside the multi-domain loop. This methodological decision aims to enhance the stability of the system along the iterative process, since the topological modifications of a chamber will not interfere in the design of the next chamber in the same iteration. Afterwards, the nodal pressure vector is once again obtained, to update the objective function values.

In the current scenario of multi-domain optimizations, it was observed that the superposition of different frequency bands from multiple domains helps to enlarge the frequency spectrum comprised by the optimized structure, fact that justifies the current form of Eq. (25), that is, each frequency range  $[\omega_s^{(m)}, \omega_f^{(m)}]$  is initially considered only in its corresponding design domain,  $\Omega_{dm}$ . This approach has found inspiration in the studies related to the acoustic rainbow trapping phenomenon, which allows broadband trapping of sound by spatial-spectral modulation (Liu et al. 2018), and in the broadband double negativity structures (Dong et al. 2020, 2022), that make use of subwavelength cavities of acoustic metasurfaces/metamaterials to increase the control of certain aspects of the target domains. Finally, the procedure ends when the stop criterion, represented by Eq. (44), and the final volume fractions,  $V^*$ , are reached.

**Algorithm 1** Multi-domain BESO algorithm

---

**Input:** Geometry parameters:  $L, D, d$  and  $x_{12}$   
 BESO parameters:  $\gamma, V^*, r_{\min}, ER, AR_{\max},$   
 $\tau, \psi_{1,2}, \eta_{1,2}$  and  $\iota_{1,2,3,4}$   
 Boundary conditions and mesh  
 Number of domains,  $m$ , and phases,  $n$   
 Nodal pressure values

$i \leftarrow 0$   
**while**  $err < \tau$  **or**  $\sum_{c=2}^n V_{c-1}^{(i)} \neq \sum_{c=2}^n V_{c-1}^*$  **do**  
 $i += 1$   
**for**  $cD \leftarrow 1$  to  $m$  **do**   ▷ multi-domain loop starts  
   Calculate sensitivity numbers of  $cD, \gamma_m^{(i)}$   
   Filter sensitivities of  $cD$   
   Save design update information of  $cD$   
   Save volume update information of  $cD$   
**end for**  
 Update design of all  $m$  domains simultaneously  
 Update volume of all  $m$  domains simultaneously  
 Evaluate nodal pressure values  
 Evaluate objective function  
 Stop criterion verification:  

$$err = \frac{\left| \sum_{p=1}^{10} \Phi^{(i-p+1)} - \sum_{p=1}^{10} \Phi^{(i-9-p)} \right|}{\sum_{p=1}^{10} \Phi^{(i-p+1)}} \leq \tau \quad (44)$$
  
**end while**

**Output:** Optimized topology

---

Figure 3 shows an example of the proposed approach applied to the topology optimization of a bi-chamber muffler ( $m = 2$ ). As can be seen, acoustic, porous and rigid material elements are allowed in the design domains,  $\Omega_d$ , while in the non-design domains,  $\Omega_{nd}$ , the elements are always kept as air (acoustic elements); therefore, multi-phase applications ( $n = 3$ ) are also considered here. After the inputs are given to the mdBESO algorithm, the sensitivity analysis and filtering are performed, as well as both design and volume fraction updated information are gathered in the current design domain,  $cD$ , along iteration  $i$ . Despite of the two chambers being treated separately inside the multi-domain loop, when it ends, they are updated simultaneously, so that the next iteration can consider the new topological system settings. At last, it should be remarked that the multi-chamber mufflers considered in this work are always treated as one single entity, meaning that  $p_3$  values are consistently collected at the outlet tube, even though such position may vary with the number of domains under investigation.

## 5 Numerical examples

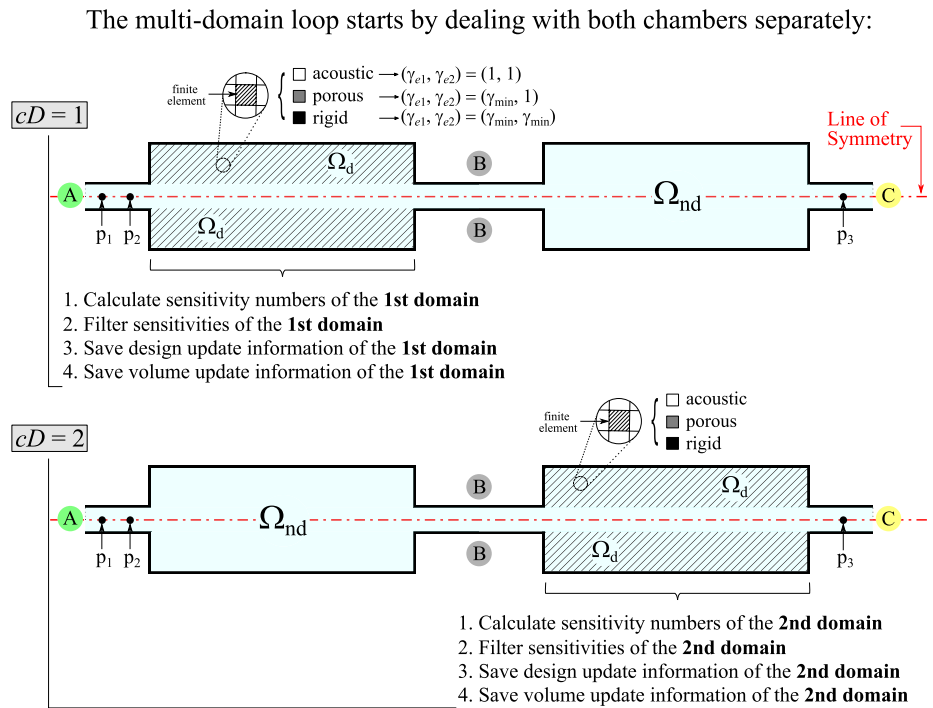
In this section, three major groups comprise the results obtained by the proposed methodology. The first one deals with optimizations of one-chamber mufflers, while

allowing Acoustic–Rigid (AR) or Acoustic–Porous (AP) material phases in the design domain. The second one expands such approach by considering Acoustic–Porous–Rigid (APR) phases in this same type of system. Finally, the third, acknowledges two and three-chamber mufflers, together with the APR case, aiming to investigate a multi-domain optimization problem with a multi-phase material configuration. Here, the periodicity of the system is also examined, highlighting the consequences of such dispositions on TL values.

Figure 1b shows the nominal (or the simple chamber) muffler considered in the current work. Such system has a chamber length of  $L = 500$  mm and height of  $D = 150$  mm. The inlet and outlet terminations are partitions of the same tube, which has  $d = 30$  mm, while the distance between both inlet microphones is chosen to be  $x_{12} = 10$  mm. As stated previously, plane waves are imposed at the inlet boundary by the enforcement of unitary particle velocities on it, while the outlet surface is defined as anechoic. In addition, only the symmetric upper-half chamber structure is considered, as an effort to reduce the computational costs involved in the FEM calculations. Finally, all the other boundaries are set as rigid walls.

Moreover, 3120 first order quadrilateral elements of size 5 mm compose the finite element mesh of the one-chamber muffler system, being numerically above the minimum suggested per wavelength (Atalla and Sgard 2015). To ensure fluid passage, the all acoustic non-design domain,  $\Omega_{nd}$ , covers the inlet, outlet and expansion chamber middle areas. On the other hand, the design domain,  $\Omega_d$ , may allow porous and rigid structures to be placed on it, by following the procedures stated in Sects. 3 and 4. An interesting point to note is that, when it comes to the expansion of any kind of domains in a topology optimization process, some issues may arise such as the number of elements that will be considered in the augmented design domain, the computational costs involved, the behavior of the new system prior to the optimization (the eigenmodes of the structure may change, as well as the choice of the target frequency), the new boundary conditions set up for the study, the position of the microphones (or nodes in a numerical study) to collect pressure/displacement instantaneous values, among others. Here, as the mdBESO has a broader sense of applicability, the geometry and mesh configurations are always kept the same regardless of the number of chambers investigated, that is, the nominal muffler (and its elements) is repeated two and three times, in a series composition, for the two and three-chamber muffler cases, respectively (see Fig. 2). Moreover, the considered inlet/outlet tube lengths comply with the recommendations of Bilawchuk and Fyfe (2003), by being no less than 10% of  $L$ .

**Fig. 3** Visual representation of an  $i$ th iteration of the mdBESO algorithm, when considering two design domains and three material phases



Outside of the multi-domain loop, **all design domains are updated simultaneously**, based on the saved information!

A known behavior of transmission loss curves calculated in expansion chamber mufflers is related to its dome-like disposition, when considering a low-to-mid frequency domain, as shown in Fig. 4. Due to this configuration, TL values almost vanish close to the so called valley frequencies, fact that motivates the design of structures that avoid such kind of performance in the frequencies of interest. Besides, x-axial eigenfrequencies seem to be quite close to these valleys, being one of the main indicators of it (Munjal 2014). Based on that, three different bands are chosen in a way that each of them comprise one of the three first x-axial eigenfrequencies of a nominal expansion chamber muffler, that is, B1: [180, 520] Hz, B2: [520, 860] Hz and B3: [860, 1200] Hz. Initially, in the one-chamber optimization case, these bands are considered individually, but then, in the multi-domain setting, they are combined, broadening the range of frequencies treated by the optimizer, as can also be seen in Fig. 4.

To properly calculated the integrals presented in Eq. (25), the composite Simpson’s numerical integration rule (Atkinson 1989) is considered, with frequency step of 10 Hz. In addition, the BESO parameters are set to vary as little as possible between these different multi-chamber optimizations, while

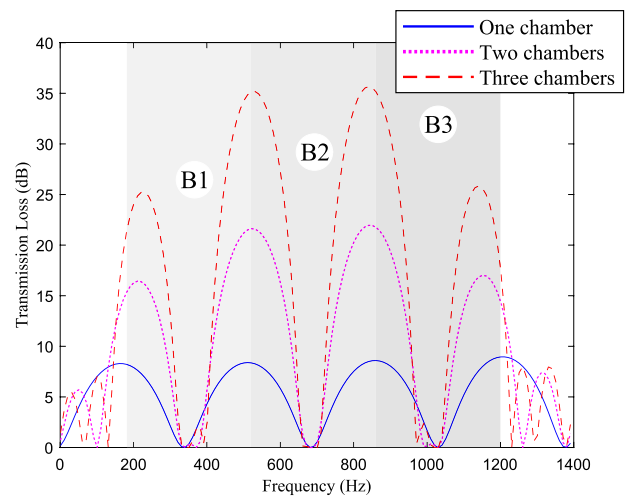


**Fig. 4** TL behaviors of one, two and three empty expansion chambers, together with the frequency bands targeted

still maintaining the particularities of each problem under investigation. With that being said, Table 3 presents all such parameters for these different aforementioned applications.

**Table 3** BESO parameters adopted in the single and multi-chamber muffler optimizations

BESO Parameters	Single-chamber			Multi-chamber
	AR	AP	APR	APR
ER	0.1%	0.1%	0.1%	0.1%
$AR_{max}$	0.1%	0.1%	0.1%	0.1%
$r_{min}$	0.03 m	0.03 m	0.03 m	0.03 m
$\tau$	0.1%	0.1%	0.1%	0.1%
$V_a^*$	96%	80%	76%	76%
$V_p^*$	–	20%	20%	20%
$V_r^*$	4%	–	4%	4%
$(\psi_1, \psi_2)$	(2, 2)	–	–	–
$(\eta_1, \eta_2)$	–	(2, 1)	–	–
$(l_1, l_2, l_3, l_4)$	–	–	(2, 1, 2, 1)	(2, 1, 2, 1)

### 5.1 Single-chamber muffler design: the AR and AP cases

With the goal of investigating the general design trends and dispositions resulting from the application of the proposed approach over a single-chamber muffler system ( $m = 1$ ), while also checking for the validity of Eqs. (17) and (19), two bi-phase ( $n = 2$ ) optimization problems comprising

acoustic-rigid and acoustic-porous materials are treated here. Initially, it is interesting to note that the mdBESO algorithm degenerates to a standard BESO approach when dealing with  $m = 1$  cases. Based on these terms, Fig. 5a–c show the final topologies obtained from the analysis of the AR scenario, when considering the frequency bands B1, B2 and B3, respectively. In the same way, Fig. 5d–f presents the optimized topologies of the AP configuration.

The obtained designs seem to be arranged in a corresponding manner, by looking at the pair of items a–d for B1, b–e for B2 and c–f for B3. These optimized configurations are indeed expected as the barriers break the formation of the modes in the frequencies of interest, enhancing TL values as a result (Lee and Kim 2009b; Lee et al. 2015), shown in Fig. 5g and h. Besides, pure reactive mufflers appear to be effective TL enhancers at low-to-mid frequencies, while dissipative ones tend to perform better as the frequency increases (Panigrahi and Munjal 2005).

Although these findings appear to be sufficient to confirm the effectiveness of the proposed AR and AP material interpolation schemes Eqs. (17) and (19), differences were observed when comparing the AR designs of the current analysis with the ones from Azevedo (2017) and Azevedo et al. (2018), despite of the use of a similar BESO approach in both works. Such contrasting topologies, presented in

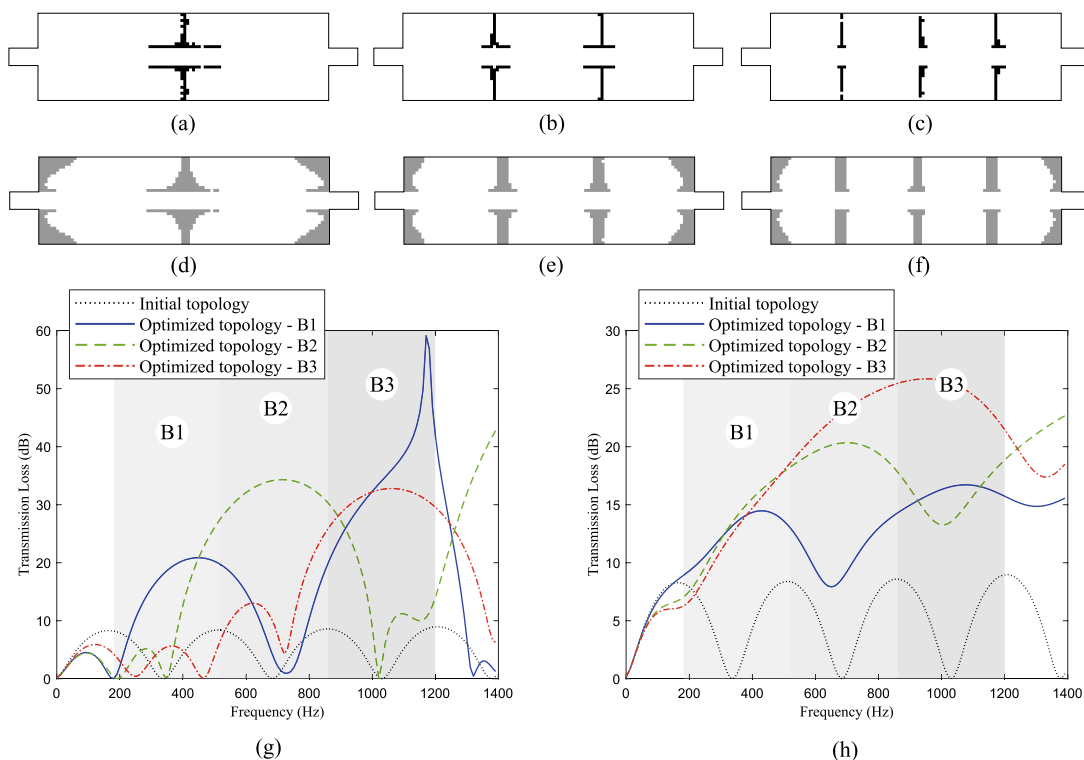


**Fig. 5** Optimized designs regarding the a AR-B1, b AR-B2, c AR-B3, d AP-B1, e AP-B2 and f AP-B3 cases, with the g AR and h AP corresponding transmission loss curves

Fig. 6, are mainly due to the distinctions found between the values chosen for  $\rho_r$  and  $\kappa_r$  in the investigations here conducted if compared to the aforementioned interrelated analysis, the supplementary material quantity considered by the researchers and their choice for specific target frequencies. In their study, for example, the rigid structure was somewhat softer (or less rigid) than the ones considered here, leading them to find major material concentrations in the areas of interest. Despite that, all the designs presented in Fig. 6 seem to agree with literature results (Lee and Kim 2009b; Lee et al. 2015), having rigid partitions in almost the same vertical locations.

Another point of interest regards the amount of rigid and porous materials chosen in the composition of the design problems investigated in this paper. After several numerical studies, the authors considered that 4% of rigid would be sufficient to demonstrate the plate-like design disposition in all the frequencies of interest, while also respecting the general trends of each of the topologies found. For porous structures, however, a few more aspects should be accounted for when deciding the amount of material that are to be adopted in an optimization process. From the five different JCA model parameters presented in Table 1, the static flow resistivity seems to be the most influential in the calculation of transmission loss values. This observation has found support in the works of Magliacano et al. (2020), who noted that by increasing  $\sigma$ , TL numbers also grow, meaning that flow resistivity can be viewed as an “acoustic hardness” of Biot-modeled foams. A similar statement was also made by Yoon (2013), when considering porous materials modeled by the empirical Delany-Bazley formulations.

Based on the above accounts, the authors investigated several quantities of porous materials along different optimization processes, as shown in Fig. 7. Here, final volume fractions of 10%, 15%, 20%, 25% and 30% are presented, for the AP-B2 case, aiming to make known the similarities of the obtained topologies. Therefore, a representative amount of material that actually comprises the above findings, but that does not provoke major computational cost

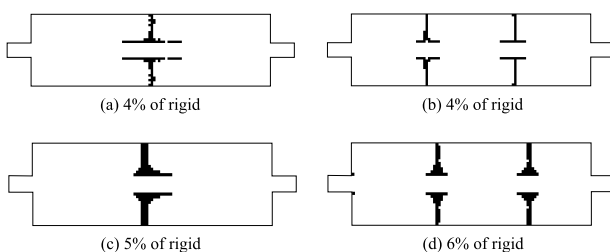


**Fig. 6** AR optimal topologies for the **a** B1 and **b** B2 frequency bands in the present approach, together with the AR results from Azevedo (2017) in **c** 346 Hz and **d** 690 Hz

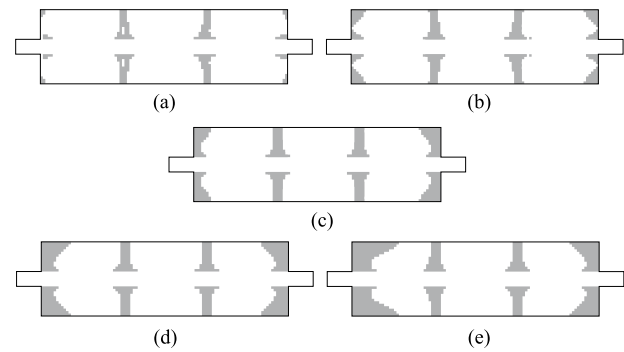


**Fig. 7** Optimized designs of the AP-B2 case comprising final volume fractions of **a** 10%, **b** 15%, **c** 20%, **d** 25% and **e** 30% of porous materials

increase is obtained when the final volume fraction of 20% is considered.

## 5.2 Single-chamber muffler design: the APR case

In this multi-phase APR scenario, Fig. 8 shows the optimal designs resulted from the solution of Eqs. (25) and (26), when adopting  $m = 1$  and  $n = 3$ , while also presenting its corresponding TL curves. In the B1, B2 and B3 bands here treated, items a, b and c respectively, a clear combination between the AR and AP configurations is noticeable, presenting porous materials attached to rigid structures without

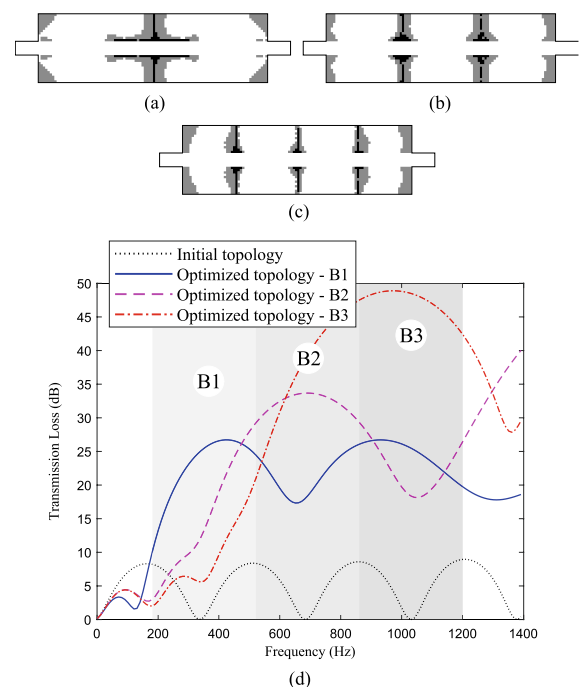


**Fig. 8** Optimized designs regarding the **a** APR-B1, **b** APR-B2 and **c** APR-B3 cases, with **d** its corresponding transmission loss curves

the need for further manipulations. If one only focus on the AP case (Fig. 5d–f), it is perceptible that little balance is given to the rock-wool when stacking it vertically inside the system, making such AP configuration very difficult to build and sustain (Yoon 2013). In this way, a common procedure to proper support porous materials is to connect them to stiffer structures, as naturally resulted from the proposed approach, in addition to using a grid to prevent drag by the fluid flow (Ferrándiz et al. 2020).

To further illustrate the correlations between the response behaviors of the AR, AP and APR designs, Fig. 9 is given. Here, only the partitions regarding the B1, B2 and B3 transmission loss curves of the AR (Fig. 5g), AP (Fig. 5h) and APR (Fig. 8d) cases are presented. It is clear that the APR approach takes the upper-hand in relation the AR and AP cases alone, as the hybrid chamber combines their respective reactive and dissipative characteristics. This is especially observed in higher frequency bands, such as B3, when the dissipative attributes are more pronounced, helping to boost the overall sound attenuation performance.

Furthermore, Fig. 10 presents the evolutionary history of mean TL values calculated in the B1, B2 and B3 frequency bands, while also showing intermediate design configurations gathered in the identifiable iterations ① to ⑥. From early stages, it is clear that porous materials are first introduced in the design until the previously set  $V_p^*$  value is reached. Then, rigid structures are brought into  $\Omega$ , but only inside the regions immediately after being occupied by the porous bodies. This methodological approach, in addition to the sensitivity historical average procedure adopted and the relatively small addition/removal of material per iteration, enhances the stability of the iterative process, especially when rigid elements are introduced in the design domain.

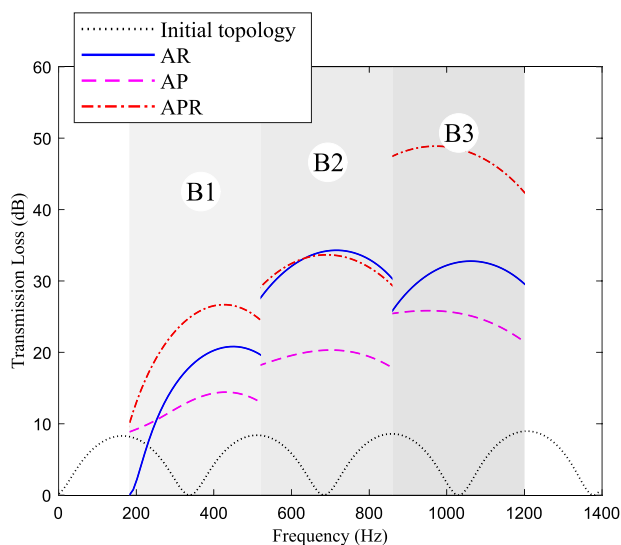


Fig. 9 The AR, AP and APR response comparison

Despite that, expressive mean TL variations are still visible at the final stages of the evolution, due to the major impact that a simple porous-rigid change may provoke in the objective function. Such feature can be considered as a typical behavior of discrete optimizers, as has been observed before in the design of acoustic-rigid metasurfaces (Pereira et al. 2022).

Lastly, a compelling facet that is worth investigating regards the mesh size information adopted in the current methodology. Based on that, Fig. 11 shows the optimized topologies obtained from the APR optimization case, with element sizes of 5.0 mm, 2.5 mm and 1.0 mm, while also considering B1, B2 and B3 frequency bands in the objective function determination. Beyond the clear designs obtained in all investigated scenarios, it is insighted that the chosen projection filter accomplishes its role in aggregating rigid and porous materials, in addition to providing closely related topologies in these frequency based optimizations, despite of the considered mesh variations.

Delving further into the details of the topologies found, one can note that porous materials are placed in different chamber locations, especially when looking at its sidewalls, in practically all the cases here presented. This is due to the marginal acoustic attenuation effects that such structures have when attached to any of the sides of a single chamber muffler (Panigrahi and Munjal 2005). Hence, it may be inferred that, in the case of the impossibility of placement of a large amount of porous elements in such regions, the algorithm may change their sidewall locations without inflicting great variations on the objective function values. Finally, it is important to point out that minor variations are noted in the middle parts of the chamber; regions in which the interference of porous/rigid materials in the sound attenuation is more pronounced.

### 5.3 Multi-chamber muffler design with the APR system settings

This last group of analyses considers a combination of multi-domains and multi-phase materials to maximize transmission loss values in a broad range of frequencies. For this, the internal partitions of two and three-chamber mufflers ( $m = 2$  and  $m = 3$ , respectively) are designed by the mdBESO approach, as presented in Algorithm 1, while also letting acoustic, porous and rigid ( $n = 3$ ) elements to be introduced in the design domain. To further enrich the study, not only mdBESO-based results are shown, but also two more BESO related concepts are explored. The first one consists in the union of separately investigated domains, according to the observed frequency band, in order to compose the required multi-chamber composition. The second one simply considers the optimization of a bigger  $\Omega_d$ , which encompass two, for  $m = 2$ , or three, for  $m = 3$ , muffler chambers in an unified

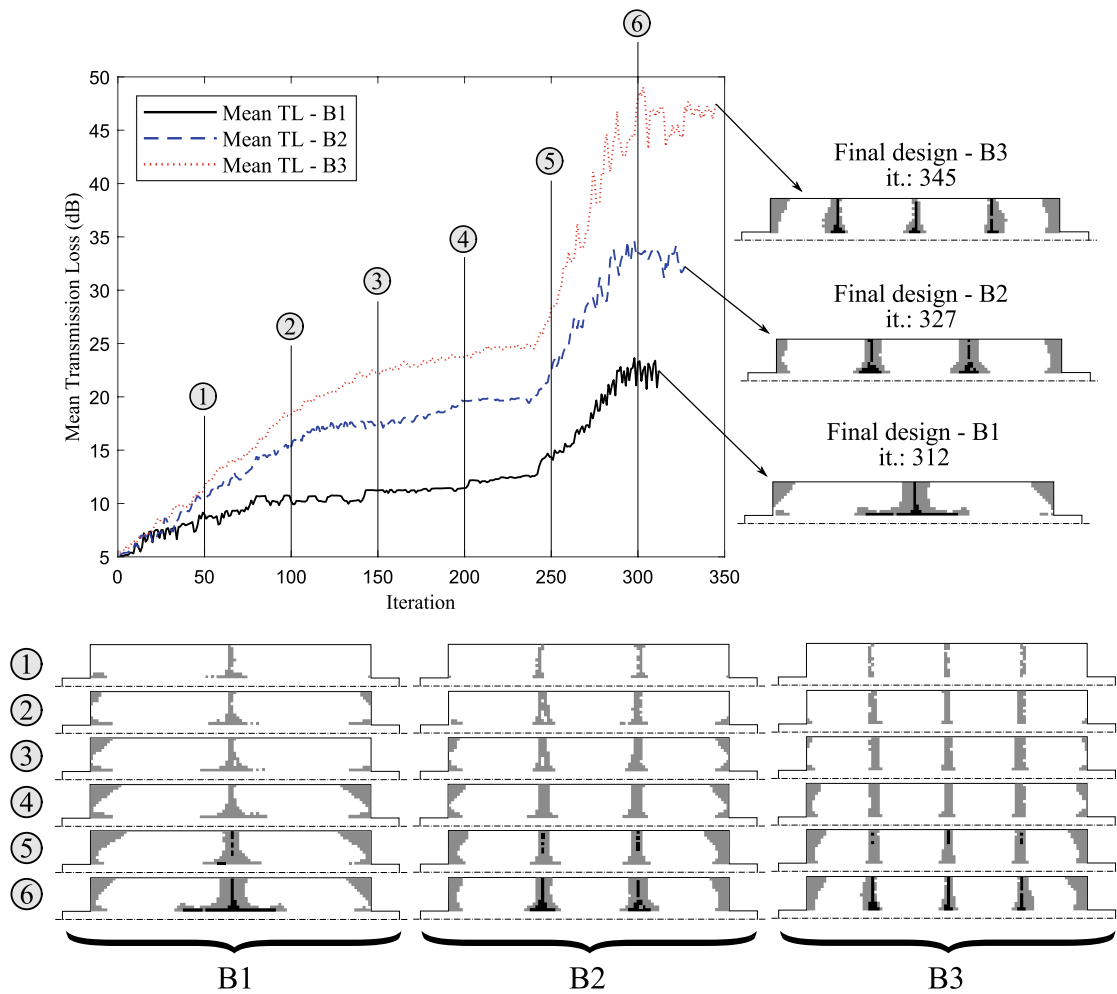
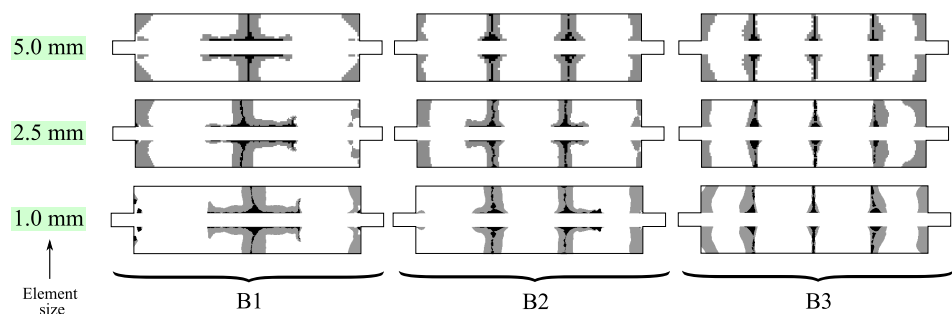


**Fig. 10** Evolutionary history of the objective function calculated in the B1, B2 and B3 frequency bands, as well as intermediate topologies of interest

**Fig. 11** Optimized topologies obtained from the APR optimization case, with meshes of 5.0 mm, 2.5 mm and 1.0 mm, while considering the B1, B2 and B3 frequency bands in the objective function determination



manner. These approaches are here referred as BESO-C (as in “Coupled”) and BESO-F (as in “Full”), respectively.

### 5.3.1 Two-chamber muffler design

Figure 12 presents a direct comparison between the two-chamber mdBESO, BESO-C and BESO-F approaches,

with its optimal topologies given, in a respectively manner, through items a, b and c. The TL final values and the objective function evolutionary behaviors are bestowed in items d and e. These studies clearly show similarities in the optimal results regarding the mdBESO and BESO-C techniques, items a and b, being apparent that B1 and B2 bands have been particularly targeted by the optimization in the

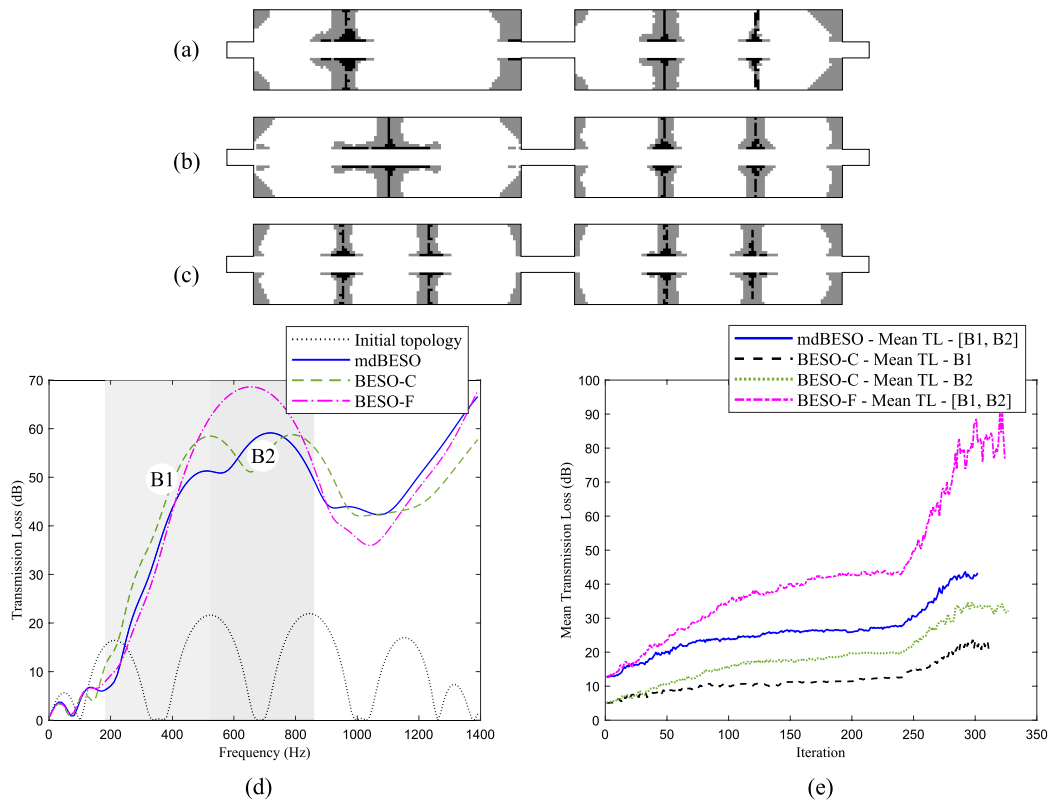


**Fig. 12** Optimized designs regarding the **a** mdBESO, **b** BESO-C and **c** BESO-F methodologies when considering the B1–B2 frequency band configuration, in addition to **d** its corresponding transmission loss curves and **e** objective function evolutionary behaviors

first and second chambers, from a left to right disposition, respectively. As previously mentioned, the main differences between the two results are due to the adoption of distinct approaches; while the first uses the mdBESO algorithm to consider the B1 and B2 bands simultaneously, the second simply joins two single chamber mufflers together, where the optimization for APR-B1 is placed on the left domain (see Fig. 8a) and for APR-B2 is connected to the right (see Fig. 8b).

In relation to the results found for BESO-F, it is visible that the influence of B2 surpass B1 regarding the final topology obtained, as can be seen by the spatial arrangement of rigid plates and its porous wraps, presented in Fig. 12c. Similarly to the mdBESO, this case also treats B1 at the same time as B2, but without restricting the design domain, that is, the elements are always free to enter the left and right chambers, following the mean TL values calculated in each iteration step. In this sense, the higher the frequencies considered, the greater the influence over topologies that break the formation of higher horizontal eigenmodes at the expense of the minors.

This finding is reinforced by the observation of Fig. 12d, which shows that the final TL curve of the BESO-F topology is the largest in the range encompassed by B2, but the

lowest in B1. It is also worth noting that, due to the nodal lines that appear in the connecting tube of both chambers (see Fig. 14), the mdBESO-Left topology seems to have been pushed laterally, resulting in a TL decrease in B1, but with an increase in B2, when compared to the BESO-C case. Lastly, Fig. 12e shows that the BESO-F case in fact leads to greater objective function values, but at the cost of the evolutionary process stability.

Furthermore, a complementary scenario is presented in Fig. 13, as the B2 and B3 frequency bands are contemplated along the iterations. In items a and c, for example, closely related topologies are found, since, in the mdBESO case, an additional vertical barrier is created at the zone dominated by B2. However, in the BESO-F approach, a mischaracterization of porous materials is perceived by its scatteredness throughout  $\Omega_d$ . Such observations are reflected in the calculation of the optimized TL, Fig. 13d, with the results of mdBESO and BESO-F being very close to each other and way more advantageous than the one found by the BESO-C methodology. Nevertheless, the greatest evolutionary instabilities are attributed to the BESO-F, as shown in Fig. 13e.

To emphasize the influence that the x-axial eigenfrequencies have under the mdBESO topology results, Fig. 14 is displayed. The TL curve is obtained for an empty two-chamber

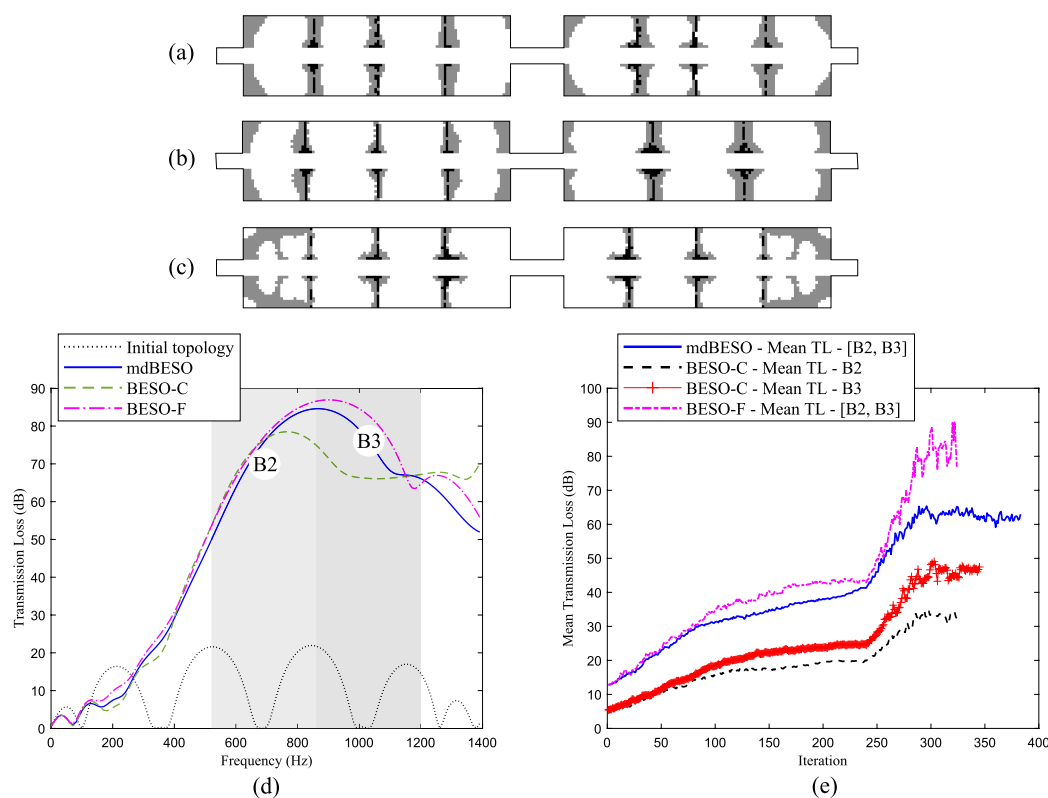


**Fig. 13** Optimized designs regarding the **a** mdBESO, **b** BESO-C and **c** BESO-F methodologies when considering the B2-B3 frequency band configuration, in addition to **d** its corresponding transmission loss curves and **e** objective function evolutionary behaviors

muffler, where its eigenfrequencies have been pointed out by the numbers ① and ② for B1, ③ and ④ for B2, and ⑤ and ⑥ for B3. The related eigenmodes have also been presented. Since the inlet/outlet tubes have marginal effect on the behavior of the investigated acoustic modes, the authors chose to replace them by rigid walls as a way to simplify the analysis (Lee and Kim 2009b). As a consequence, all the boundary conditions described by Eqs. (2) and (4) have been changed to the one of Eq. (3). In a general sense, the main observations are related to the similar impedance characteristics found near the ends of the muffler, allowing energy to be transmitted from one side to the other almost without losses, and the consequent nodal lines (blue lines) that appear in the maximum particle velocity regions (Lee and Kim 2009b; Lee et al. 2015).

Another interesting finding is done by looking at the pairs of modes located close to the valley frequencies comprised by B1, B2 and B3. In this particular bi-chamber case, the two modes of each pair are very close to each other, in the frequency spectrum, and quite similar in form, being the main difference attributed to the additional nodal line that appears in the connecting tube of chambers. These characteristics may lead the mdBESO to a certain instability in the optimization procedure when compared to the BESO-C

case, since more than one acoustic mode directly influence the design process of the considered mufflers. However, these same attributes are also responsible for a superior performance in many situations, as shown in the B2-B3 case (Fig. 13d), for example.

The methodological choice of considering the domains separately in each iterative step, but simultaneously in the overall optimization process, lead the mdBESO to be way more stable than the BESO-F approach (see Figs. 12e, 13e). Finally, it is remarked that such peculiar acoustic mode aspects are also observed for the empty three-chamber system, where three related acoustic modes are obtained in each TL valley. These results have not been shown here due to close similarities to the empty two-chamber setting.

### 5.3.2 Three-chamber muffler design

One additional aspect that may be considered in the optimization of multi-chamber mufflers is related to the arrangement of the domains treated in the analysis. Based on that, Figs. 15 and 16 present comparisons between the mdBESO, BESO-C and BESO-F applications for the design of three-chamber mufflers. The TL values are maximized in the first, second and third domains (in a left to right disposition)

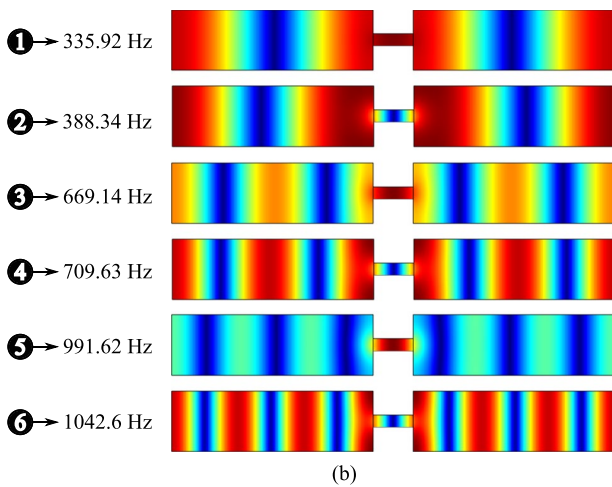
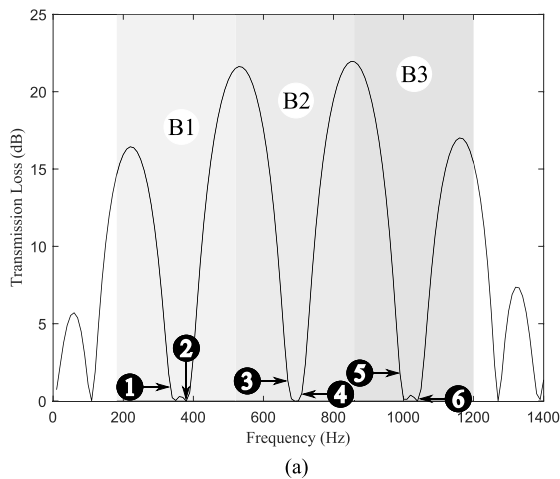


**Fig. 14** **a** Transmission loss curve of an empty two-chamber muffler, with highlight of the eigenfrequencies encompassed by the B1, B2 and B3 bands. **b** Related eigenmodes and eigenfrequency values

by considering the following order of bands: B1–B3–B2, Fig. 15, and B3–B2–B1, Fig. 16. The mdBESO approach successfully allocates 4% of rigid and 20% of porous materials in each  $\Omega_d$  considered, beyond providing topologies that are able to enhance the objective function in all investigated scenarios. Nevertheless, it is perceived that the B2–B3 relations led to designs with three plate-like barriers in the domains targeted by these both bands, similarly to the one shown in Fig. 13. While this disposition enhances TL in these bands, it may also provide decrease in the overall values comprised by B1.

Furthermore, one may note that TL values of the mdBESO-B1-B3-B2 configuration, Fig. 15d, are greater than the ones from the mdBESO-B3-B2-B1, Fig. 16d, while all the others remain practically the same. This observation allows the idea of considering not only the maximization of the objective function in specific domains, but also of including the search for the optimal configuration of domains in

the optimization problem. As this work deals with the design of multi-domain systems composed of multi-phase materials for enhancement of transmission loss values in a broad range of frequencies, the authors chose to let this even more challenging multi-objective scenario to be explored in future research.

In both Figs. 15c and 16c, the BESO-F optimal topology is organized with the aim of generate three vertical barriers in all considered chambers, making use of almost the entirety of porous materials in just one place to increase the stiffness of the composition. This corroborates with the fact that BESO-F tends to produce topologies that greatly contributes to the breakage of higher x-axial eigenmodes at the cost of the minors. Finally, it is also noticeable that, due to the presence of the two connecting tubes in the three-chamber scenario, the nodal lines that appear inside of these tubes seem to push away the left and right chamber lines further from its center, causing a small barrier to appear in the first half of the chamber target by B1. A similar effect is also visible in Fig. 14, for the two domain setting, especially in the pair ① – ②.

### 5.3.3 Investigations on the periodicity of the muffler configuration

A final attention factor treated in this work concerns with the periodic nature that the topologies may present when multiple domains are considered, but only one frequency band is applied. Based on that, Fig. 17 is bestowed, which shows the transmission loss responses of one, two and three empty, and mdBESO optimized chambers, when the B2 frequency band is considered (item d). The correspondent optimized designs are also shown in items a, b and c. Here, the main TL curve indications are maintained in both empty and optimized domains, in a way that almost the same responses appear to be repeated, when considering the empty from the optimized cases, but with greater TL intensification for larger chamber numbers. These results suggest that it is possible to use multiple periodic chambers optimized only once at a target frequency band, without the need to generate new topologies, if the design goal is to locally boost TL values. Yet, the system will significantly increase its global size, being the main setback of said application.

## 6 Conclusions

The design of internal partitions of acoustic mufflers for transmission loss maximization has been addressed in many works over the years. When it comes to the adoption of topology optimization techniques, such specific application has also been well covered, since these numerical methods can provide non-intuitive results regarding the

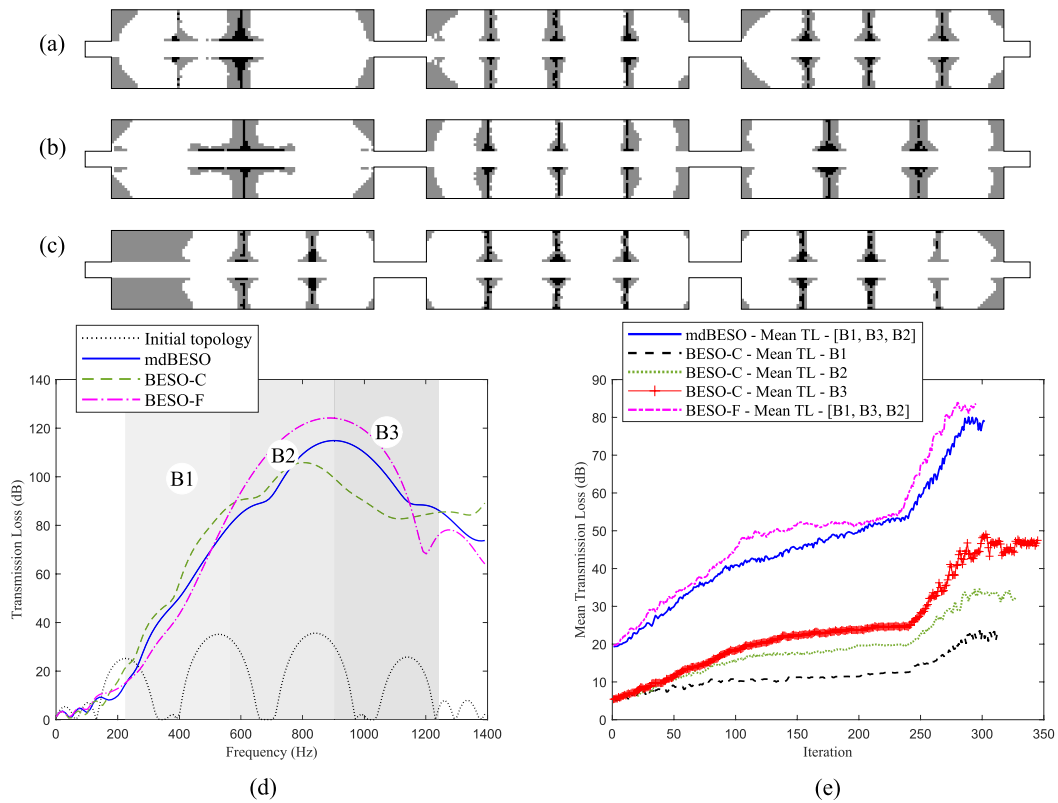


**Fig. 15** Optimized designs regarding the **a** mdBESO, **b** BESO-C and **c** BESO-F methodologies when considering the B1–B3–B2 frequency band configuration, in addition to **d** its corresponding transmission loss curves and **e** objective function evolutionary behaviors

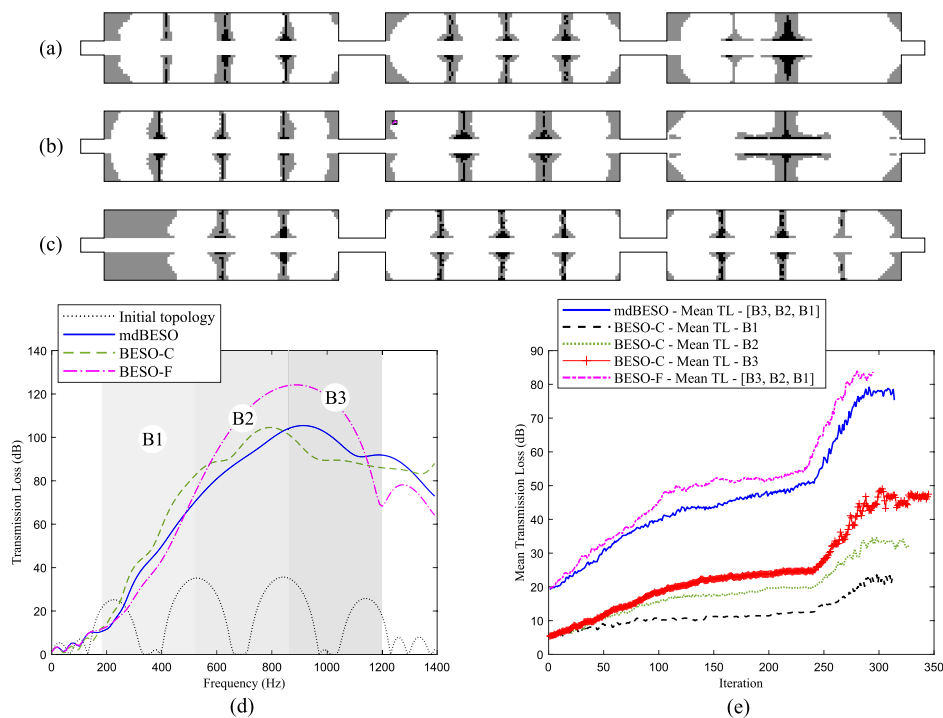
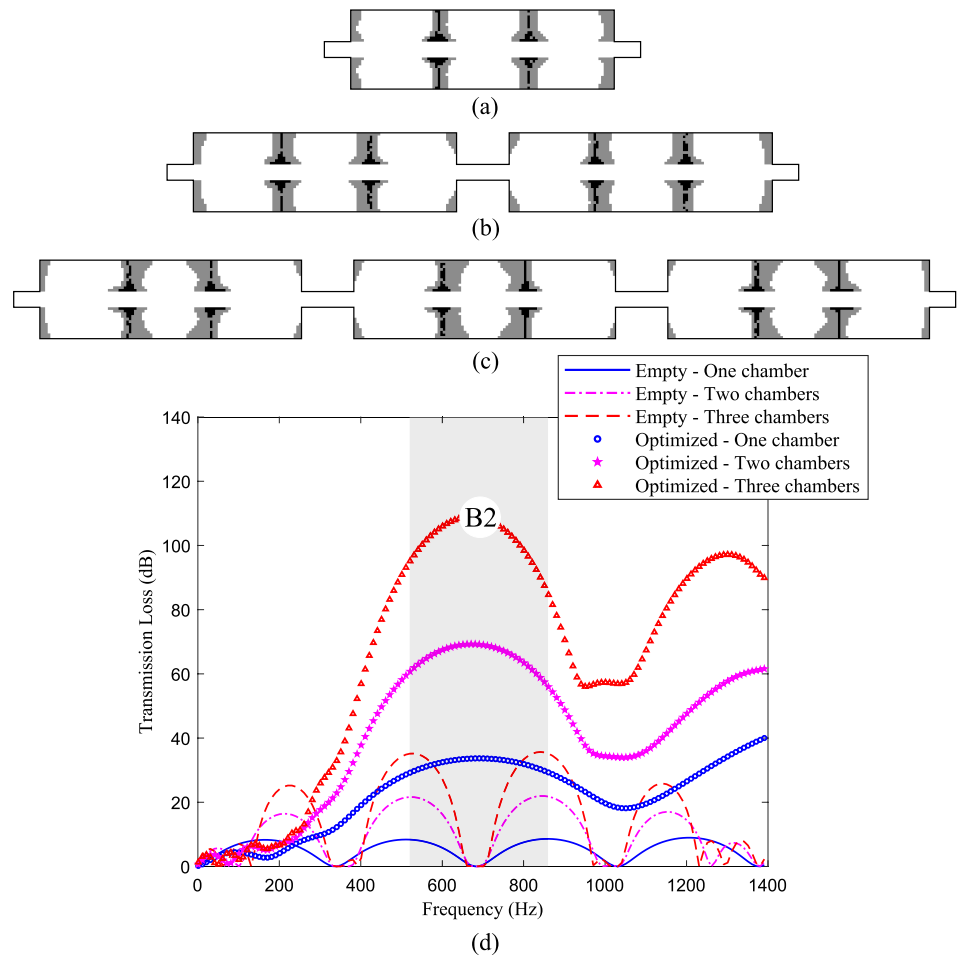


**Fig. 16** Optimized designs regarding the **a** mdBESO, **b** BESO-C and **c** BESO-F methodologies when considering the B3–B2–B1 frequency band configuration, in addition to **d** its corresponding transmission loss curves and **e** objective function evolutionary behaviors

**Fig. 17** mdBESO optimized designs regarding **a** one, **b** two and **c** three muffler chambers, with **d** TL responses of the same one to three empty and optimized domains, when only the B2 frequency band is considered



overall disposition and form of the treated system. Nevertheless, the design of multi-chamber mufflers composed of multi-phase materials for enhancement of transmission loss values in a broad range of frequencies is still rare, being, therefore, the purpose of this study.

To achieve this goal, the multi-phase Bi-directional Evolutionary Structural Optimization (BESO) methodology was combined with a novel multi-domain algorithm, named as mdBESO. Here, the standard BESO approach was modified to consider multi-chambers simultaneously throughout the global iterative procedure, but without allowing interference between these chambers in the same iteration.

Before that, the simulation of the acoustic muffler composition occurred with the adoption of the finite element method to solve the Helmholtz equation that, in turn, described the system. In this scenario, a new multi-phase material interpolation scheme was introduced, being able to systematically reproduce acoustic, porous and rigid material phases according to the need imposed by the optimization process. At this point, rigid and porous materials with rigid frame were approximated by the over amplification of

acoustic properties and by the Johnson–Champoux–Allard (JCA) formulations, respectively.

The optimization problem was then established as to maximize mean transmission loss values in one, two and three reactive/dissipative chamber mufflers, considering multiple materials and domains, but keeping only volume constraints in this case. A common trait of these analyzes regarded the consideration of three different frequency bands in the objective function calculation, being chosen in a way that each of them comprised one of the three first horizontal eigenfrequencies of a nominal expansion chamber muffler.

Particularly, in the mono-domain scenario, the AR and AP optimization results showed to be strongly depend on the valley frequencies comprehended by the corresponding target bands, being, therefore, consistent with results from the literature. Furthermore, the APR designs presented clear combinations of the AR and AP ones, without the need for further manipulations to obtain porous materials wrapped around rigid structures. In all these outcomes, the breakage of acoustic modes was perceptible, leading the topologies to deviate the valley frequencies to regions far from the ones of interest.

The multi-phase analyses were then conducted with the help of the mdBESO methodology and compared with two additional BESO-based settings, named as BESO-C and BESO-F. The first one was composed by the union of separately optimized chambers and, the second, by the design of a bigger domain, comprising two or three chambers. Due to the influence of the connecting tube nodal lines, the mdBESO optimized topologies succeeded in attenuate sound more effectively than BESO-C, while also being more stable than BESO-F.

Finally, the periodic nature of the topologies resulted from a multi-chamber, mono-band, optimization was also investigated. In this case, TL values presented predictable patterns, with strong influence of the number of domains as a way to boost them, however causing the system to increase its size. Therefore, it can be concluded that the mdBESO algorithm is a viable choice in the design of internal partitions of reactive and dissipative mufflers, in a general sense. Besides, it is worth noting that the inclusion of the search for the optimal configuration of domains was left to be treated in future research, as well as the investigation of three-dimensional domains with axisymmetry or even under asymmetric conditions.

**Author Contributions** RLP: Conceptualization, Methodology, Software, Validation, Data Curation, Writing—Original Draft preparation, Visualization, Writing—Review & Editing. HNL: Conceptualization, Methodology, Writing—Review & Editing. MSM: Conceptualization, Writing—Review & Editing. RP: Conceptualization, Resources, Writing—Review & Editing, Supervision, Project administration.

**Funding** The authors would like to acknowledge the financial support given by the Fundação de Amparo à Pesquisa do Estado de São Paulo (FAPESP), Project Numbers 2013/08293-7 and 2019/05393-7, and by the Coordenação de Aperfeiçoamento de Pessoal do Nível Superior (CAPES), finance code 001.

## Declarations

**Competing interests** The authors have no competing interests to declare that are relevant to the content of this article.

**Replication of results** The MATLAB® code of the proposed mdBESO algorithm is available upon request to the corresponding author.

## References

- Allard JF, Atalla N (2009) Propagation of sound in porous media: modelling sound absorbing materials. Wiley, Hoboken
- Atalla N, Panneton R, Debergue P (1998) A mixed displacement-pressure formulation for poroelastic materials. *J Acoust Soc Am* 104(3):1444–1452. <https://doi.org/10.1121/1.424355>
- Atalla N, Hamdi MA, Panneton R (2001) Enhanced weak integral formulation for the mixed (u, p) poroelastic equations. *J Acoust Soc Am* 109(6):3065–3068. <https://doi.org/10.1121/1.1365423>
- Atalla N, Sgard F (2015) Finite element and boundary methods in structural acoustics and vibration. CRC Press, Boca Raton
- Atkinson KE (1989) An introduction to numerical analysis. Wiley, Hoboken
- Azevedo FM (2017) Bi-directional evolutionary acoustic topology optimization for muffler design. Dissertation, School of Mechanical Engineering, University of Campinas
- Azevedo FM, Moura MS, Vicente WM, Picelli R, Pavanello R (2018) Topology optimization of reactive acoustic mufflers using a bi-directional evolutionary optimization method. *Struct Multidisc Optim* 58:2239–2252. <https://doi.org/10.1007/s00158-018-2012-5>
- Barbieri R, Barbieri N (2006) Finite element acoustic simulation based shape optimization of a muffler. *Appl Acoust* 67(4):346–357. <https://doi.org/10.1016/j.apacoust.2005.06.007>
- Bendsøe MP, Kikuchi N (1988) Generating optimal topologies in structural design using a homogenization method. *Comput Methods Appl Mech Eng* 71(2):197–224. [https://doi.org/10.1016/0045-7825\(88\)90086-2](https://doi.org/10.1016/0045-7825(88)90086-2)
- Bilawchuk S, Fyfe KR (2003) Comparison and implementation of the various numerical methods used for calculating transmission loss in silencer systems. *Appl Acoust* 64(9):903–916. [https://doi.org/10.1016/S0003-682X\(03\)00046-X](https://doi.org/10.1016/S0003-682X(03)00046-X)
- Bo Z, Tianning C (2009) Calculation of sound absorption characteristics of porous sintered fiber metal. *Appl Acoust* 70(2):337–346. <https://doi.org/10.1016/j.apacoust.2008.03.004>
- Bruns TE, Tortorelli DA (2001) Topology optimization of non-linear elastic structures and compliant mechanisms. *Comput Methods Appl Mech Eng* 190(26–27):3443–3459. [https://doi.org/10.1016/S0045-7825\(00\)00278-4](https://doi.org/10.1016/S0045-7825(00)00278-4)
- Cao L, Fu Q, Si Y, Ding B, Yu J (2018) Porous materials for sound absorption. *Compos Commun* 10:25–35. <https://doi.org/10.1016/j.coco.2018.05.001>
- Champoux Y, Allard J (1991) Dynamic tortuosity and bulk modulus in air-saturated porous media. *J Appl Phys* 70(4):1975–1979. <https://doi.org/10.1063/1.349482>
- Chang YC, Chiu MC (2008) Shape optimization of one-chamber perforated plug/non-plug mufflers by simulated annealing method. *Int J Numer Methods Eng* 74(10):1592–1620. <https://doi.org/10.1002/nme.2226>
- Chiu MC (2011) Optimization design of hybrid mufflers on broadband frequencies using the genetic algorithm. *Arch Acoust* 36(4):795–822. <https://doi.org/10.2478/v10168-011-0053-5>
- Delany ME, Bazley EN (1970) Acoustical properties of fibrous absorbent materials. *Appl Acoust* 3(2):105–116. [https://doi.org/10.1016/0003-682X\(70\)90031-9](https://doi.org/10.1016/0003-682X(70)90031-9)
- Denia FD, Sánchez-Orgaz EM, Martínez-Casas J, Kirby R (2015) Finite element based acoustic analysis of dissipative silencers with high temperature and thermal-induced heterogeneity. *Finite Elem Anal Des* 101:46–57. <https://doi.org/10.1016/j.finel.2015.04.004>
- Dilgen CB, Dilgen SB, Aage N, Jensen JS (2019) Topology optimization of acoustic mechanical interaction problems: a comparative review. *Struct Multidisc Optim* 60:779–801. <https://doi.org/10.1007/s00158-019-02236-4>
- Dong HW, Zhao SD, Wang YS, Cheng L, Zhang C (2020) Robust 2d/3d multi-polar acoustic metamaterials with broadband double negativity. *J Mech Phys Solids* 137(103):889. <https://doi.org/10.1016/j.jmps.2020.103889>
- Dong HW, Shen C, Zhao SD, Qiu W, Zheng H, Zhang C, Cummer SA, Wang YS, Fang D, Cheng L (2022) Achromatic metasurfaces by dispersion customization for ultra-broadband acoustic beam engineering. *Natl Sci Rev*. <https://doi.org/10.1093/nsr/nwac030>
- Dühring MB, Jensen JS, Sigmund O (2008) Acoustic design by topology optimization. *J Sound Vib* 317(3–5):557–575. <https://doi.org/10.1016/j.jsv.2008.03.042>
- Fahy FJ (2000) Foundations of engineering acoustics. Elsevier, Amsterdam

- Ferrández B, Denia FD, Martínez-Casas J, Nadal E, Ródenas JJ (2020) Topology and shape optimization of dissipative and hybrid mufflers. *Struct Multidisc Optim* 62:269–284. <https://doi.org/10.1007/s00158-020-02490-x>
- Huang X, Xie YM (2007) Convergent and mesh-independent solutions for the bi-directional evolutionary structural optimization method. *Finite Elem Anal Des* 43(14):1039–1049. <https://doi.org/10.1016/j.finel.2007.06.006>
- Huang X, Xie YM (2009) Bi-directional evolutionary topology optimization of continuum structures with one or multiple materials. *Comput Mech* 43:393–401. <https://doi.org/10.1007/s00466-008-0312-0>
- Huang X, Xie YM (2010) Evolutionary topology optimization of continuum structures: methods and applications. Wiley, Hoboken
- Jog CS, Haber RB (1996) Stability of finite element models for distributed-parameter optimization and topology design. *Comput Methods Appl Mech Eng* 130(3–4):203–226. [https://doi.org/10.1016/0045-7825\(95\)00928-0](https://doi.org/10.1016/0045-7825(95)00928-0)
- Johnson DL, Koplik J, Dashen R (1987) Theory of dynamic permeability and tortuosity in fluid-saturated porous media. *J Fluid Mech* 176:379–402. <https://doi.org/10.1017/s0022112087000727>
- Lazarov BS, Sigmund O (2011) Filters in topology optimization based on Helmholtz-type differential equations. *Int J Numer Methods Eng* 86(6):765–781. <https://doi.org/10.1002/nme.3072>
- Lee JS, Kang YJ, Kim YY (2012) Unified multiphase modeling for evolving, acoustically coupled systems consisting of acoustic, elastic, poroelastic media and septa. *J Sound Vib* 331(25):5518–5536. <https://doi.org/10.1016/j.jsv.2012.07.027>
- Lee JS, Göransson P, Kim YY (2015) Topology optimization for three-phase materials distribution in a dissipative expansion chamber by unified multiphase modeling approach. *Comput Methods Appl Mech Eng* 287:191–211. <https://doi.org/10.1016/j.cma.2015.01.011>
- Lee JW (2015) Optimal topology of reactive muffler achieving target transmission loss values: design and experiment. *Appl Acoust* 88:104–113. <https://doi.org/10.1016/j.apacoust.2014.08.005>
- Lee JW, Jang GW (2012) Topology design of reactive mufflers for enhancing their acoustic attenuation performance and flow characteristics simultaneously. *Int J Numer Methods Eng* 91(5):552–570. <https://doi.org/10.1002/nme.4329>
- Lee JW, Kim YY (2009) Rigid body modeling issue in acoustical topology optimization. *Comput Methods Appl Mech Eng* 198(9–12):1017–1030. <https://doi.org/10.1016/j.cma.2008.11.008>
- Lee JW, Kim YY (2009) Topology optimization of muffler internal partitions for improving acoustical attenuation performance. *Int J Numer Methods Eng* 80(4):455–477. <https://doi.org/10.1002/nme.2645>
- de Lima KF, Lenzi A, Barbieri R (2011) The study of reactive silencers by shape and parametric optimization techniques. *Appl Acoust* 72(4):142–150. <https://doi.org/10.1016/j.apacoust.2010.11.008>
- Liu T, Liang S, Chen F, Zhu J (2018) Inherent losses induced absorptive acoustic rainbow trapping with a gradient metasurface. *J Appl Phys* 123(9):091702. <https://doi.org/10.1063/1.4997631>
- Magliacano D, Ouisse M, Rosa SD, Franco F, Khelif A (2020) Computation of acoustic properties and design guidelines of periodic Biot-modeled foams. *Appl Acoust* 168(107):428. <https://doi.org/10.1016/j.apacoust.2020.107428>
- Munjal ML (2014) Acoustics of ducts and mufflers. Wiley, Hoboken
- Oh KS, Lee JW (2017) Topology optimization for enhancing the acoustic and thermal characteristics of acoustic devices simultaneously. *J Sound Vib* 401:54–75. <https://doi.org/10.1016/j.jsv.2017.04.027>
- Panigrahi SN, Munjal ML (2005) Combination mufflers: theory and parametric study. *Noise Control Eng J* 53(6):247–255. <https://doi.org/10.3397/1.2839260>
- Pereira RL, Lopes HN, Pavanello R (2022) Topology optimization of acoustic systems with a multiconstrained beso approach. *Finite Elem Anal Des* 201(103):701. <https://doi.org/10.1016/j.finel.2021.103701>
- Selamet A, Lee I, Huff N (2003) Acoustic attenuation of hybrid silencers. *J Sound Vib* 262(3):509–527. [https://doi.org/10.1016/S0022-460X\(03\)00109-3](https://doi.org/10.1016/S0022-460X(03)00109-3)
- Sigmund O (1997) On the design of compliant mechanisms using topology optimization. *Mech Struct Mach* 25(4):493–524. <https://doi.org/10.1080/08905459708945415>
- Wadbro E, Berggren M (2006) Topology optimization of an acoustic horn. *Comput Methods Appl Mech Eng* 196(1–3):420–436. <https://doi.org/10.1016/j.cma.2006.05.005>
- Wu TW, Wan GC (1996) Muffler performance studies using a direct mixed-body boundary element method and a three-point method for evaluating transmission loss. *J Vib Acoust* 118(3):479–484. <https://doi.org/10.1115/1.2888209>
- Xie YM, Steven GP (1993) A simple evolutionary procedure for structural optimization. *Comput Struct* 49(5):885–896. [https://doi.org/10.1016/0045-7949\(93\)90035-c](https://doi.org/10.1016/0045-7949(93)90035-c)
- Yang XY, Xie YM, Steven GP, Querin OM (1999) Bidirectional evolutionary method for stiffness optimization. *AIAA J* 37(11):1483–1488. <https://doi.org/10.2514/2.626>
- Yedeg EL, Wadbro E, Berggren M (2016) Interior layout topology optimization of a reactive muffler. *Struct Multidisc Optim* 53:645–656. <https://doi.org/10.1007/s00158-015-1317-x>
- Yoon GH (2013) Acoustic topology optimization of fibrous material with Delany-Bazley empirical material formulation. *J Sound Vib* 332(5):1172–1187. <https://doi.org/10.1016/j.jsv.2012.10.018>
- Young CII, Crocker MJ (1975) Prediction of transmission loss in mufflers by the finite-element method. *J Acoust Soc Am* 57(1):144–148. <https://doi.org/10.1121/1.380424>
- Zoutendijk G (1960) Methods of feasible directions: a study in linear and nonlinear programming. Elsevier, Amsterdam

**Publisher's Note** Springer Nature remains neutral with regard to jurisdictional claims in published maps and institutional affiliations.

Springer Nature or its licensor (e.g. a society or other partner) holds exclusive rights to this article under a publishing agreement with the author(s) or other rightsholder(s); author self-archiving of the accepted manuscript version of this article is solely governed by the terms of such publishing agreement and applicable law.

## 6 | Evolutionary Design of Multiphysics Systems with Poroelastic Materials

In this chapter, the original research article entitled “Evolutionary topology optimization approach to design multiphase soundproof systems with poroelastic media” by Rodrigo Lima Pereira, Lidy Marcela Anaya Jaimes and Renato Pavanello is presented. The paper is currently *under review*.

The work proposes a novel evolutionary approach to design closed-space structures for sound attenuation, including combinations of acoustic, poroelastic and elastic domains in the composition. The multiphysics involved in the analysis are fully detailed by the use of Helmholtz, Biot and elastodynamic equations, together with the Unified Multiphase methodology. New material interpolation schemes are also proposed to deal with such multiphysics scenario. Moreover, the objective function contemplates different combinations of structural, viscous and thermal dissipated power levels in its application. The resultant topologies present high manufacturability and dissipative effects.

Chapter 7 presents further discussions on the topics and results given here and Appendix A displays detailed extensions of the procedures introduced in the sensitivity analysis section.

# Evolutionary topology optimization approach to design multiphase soundproof systems with poroelastic media

Rodrigo L. Pereira<sup>a,\*</sup>, Lidy M. Anaya-Jaimes<sup>a</sup>, Renato Pavanello<sup>a</sup>

<sup>a</sup>*Department of Computational Mechanics, School of Mechanical Engineering,  
University of Campinas, Rua Mendeleev 200, 13083-860 Campinas, Brazil*

---

## Abstract

With the constant development of cities, noise sources have become increasingly present inside and outside living environments. Consequently, soundproof systems comprised of porous materials have been widely adopted as filling fabric of closed-space structures, such as in the components of buildings, airplanes or automobiles. However, in many situations, simply filling spaces may not be the most effective approach. In that scenario, this work introduces a multiphase acoustic topology optimization methodology to design closed-space structures for sound attenuation. Based on the Bi-directional Evolutionary Structural Optimization (BESO) algorithm, the proposed approach combines Biot's poroelasticity equations, expressed in the mixed  $\mathbf{u}/p$  form, and the Unified Multiphase (UMP) technique to fully describe the multiphysics involved in the acoustic, poroelastic and elastic model relations. An objective function contemplating different combinations of structural, viscous and thermal dissipated powers is maximized over multiple frequencies. Volume constraints in each material phase and a novel material interpolation scheme are also considered. The resultant topologies present enhanced dissipated power levels and manufacturability, even when compared with various baseline configurations of similar volume fractions.

*Keywords:* Topology optimization, Multiphase optimization, BESO, Poroelastic materials, Multiphysics

---

## 1. Introduction

Despite sound being a social mechanism used for communication, recognition, avoidance of dangerous situations, etc, when in excess or inadequate, it may be perceived negatively and defined as noise. Although such concept relies on the preferences of people and societies, the sounds emitted by washing machines, vacuum cleaners, blenders, roads of high traffic, jet planes, garbage trucks or construction sites are often

---

\*Corresponding author

*Email addresses:* pereira@fem.unicamp.br (Rodrigo L. Pereira), lidy@fem.unicamp.br (Lidy M. Anaya-Jaimes), pava@fem.unicamp.br (Renato Pavanello)

noted as harmful [1]. As a consequence, health issues may arise, such as high annoyance, tinnitus, hearing loss, sleep disturbances, learning disorders and even ischemic heart diseases [2].

10 In light of these challenges, porous materials have been commonly used for sound absorption applications, especially at high frequencies and inside enclosures [3]. The sound waves are generally trapped in the many interconnected openings and apertures of its basic cellular (as in foams) or fibrous compositions, entailing structural, viscous, and thermal energy losses [4]. In more detail, the fluid phase placed in the pores and  
15 external surfaces are overly excited when a sound wave impinges these structures. This physical phenomenon leads to greater contact between the fluid and the pore walls, increasing frictions and vibrations. Besides, the sound energy is also affected by the structural damping effect, common to its solid phase.

Porous structures can be simulated by a great deal of semi-phenomenological and  
20 empirical formulations that may or may not consider these dissipative effects [5]. According to Cao et al. [6], among the empirical models, the one proposed by Delany and Bazley [7] is the most adopted because it only requires flow resistivity data of the porous material as input. However, no thermal or structural aspects are considered in this proposition, limiting the accuracy of predictions. On the other hand, the Johnson–  
25 Champoux–Allard (JCA) [8, 9] methodology is the most employed of the equivalent fluid approaches. Such formulation encompasses both thermal and viscous effects, but since it treats the solid phase as rigid, prediction errors in the low-frequency spectrum are often obtained [10]. In a more general view, the poroelastic model may be thought  
30 of as a collection of fluid and structural phases superimposed in a homogenized manner. Being formulated by Biot [11, 12] to gather the main multiphysical aspects of such porous structures, this theory comprises all three dissipative aspects, in addition to deeming the pores to be fully saturated with fluid (air) and the entire poroelastic domain as isotropic [13].

From an engineering point of view, many are the ways to design and manufacture  
35 noise-controlling structures, with and without porous materials. Noise barriers, for example, have been considered in many different scenarios [14], followed by the use of Helmholtz resonators [15], perforated panels [16], acoustic metasurfaces/metamaterials [17, 18] and piezoelectric combined devices [19]. The use of such structures aims to broaden not only frequency bands with it but also different problem specificities. Nev-  
40 ertheless, such applications are generally based on try-and-error studies that demand complex experimental apparatuses for their verification.

An interesting alternative presented over the last few decades is the adoption of topology optimization techniques to design sound-related structures. Since the pion-  
45 eering study of Bendsøe and Kikuchi [20] and the later developments of the field regarding the use of continuous [21, 22] and discrete design variables [23, 24], Wadbro and Berggren [25] were the first to publish results combining topology optimization approaches with Helmholtz-based systems to enhance the sound radiation characteristics of an acoustic horn. Afterwards, several sound barrier configurations were also inves-  
50 tigated [26, 27], as well as rigid/elastic multifunctional metasurfaces [28, 29], mufflers/silencers [30, 31, 32, 33], poro-rigid systems [34, 35, 36], among others [37, 38].

Within the field of multiphysics interactions, groundbreaking works have been performed by Yamamoto et al. [39] and Lee et al. [40, 41], who developed methodologies

to avoid boundary tracking along the optimization of poroelastic structures. In their study, Yamamoto et al. [39] considered three different poroelastic materials, where one was to be degenerated to air (following Helmholtz equations), the other to an elastic structure (governed by elastodynamic expressions), and the last would remain in a Biot's like form. In the set of analyzes conducted by Lee et al. [40, 41], a similar approach named as Unified Multiphase (UMP) modeling technique was proposed and applied in later papers [42]. The methodology required only one poroelastic domain and started from the  $\mathbf{u}/p$  enhanced form of Biot's equations [43]. By setting limiting values to variables of interest, the description of acoustic, poroelastic and elastic domains was successfully conducted. In both studies, the boundaries were fully coupled throughout the entire optimizations. Recently, Hu et al. [44] placed these same kinds of materials as sandwich core structures of a biphasic soundproof system. In this case, the ersatz material model was adopted, together with the floating projection topology optimization technique [45], for maximizing sound transmission loss values in specific frequency points.

Despite all that, many gaps still exist in implementing topology optimization techniques, especially when considering multiple materials of different physics subjected to broad frequency ranges, in order to achieve greater proximity to real-world applications. Hence, this work presents a new evolutionary methodology to design closed-space systems for sound attenuation. Based on the Bi-directional Evolutionary Structural Optimization (BESO) algorithm, acoustic, poroelastic, and elastic material elements are systematically changed over the iterations due to the adoption of a novel Material Interpolation Scheme (MIS). The optimization problem is then posed as to maximize dissipated power levels, and different combinations of its structural, viscous and thermal partitions, throughout single and multiple frequencies. Pertinent results comparisons are then made with non-optimized configurations, treated here as baselines, in order to highlight the physical aspects of the compositions found.

The organization of this paper is presented as follows: In section 2, the governing equations and the finite element procedures employed in the simulation of multiphysics domains are thoroughly detailed. Section 3 introduces the basic features of the UMP approach and provides information about acoustic, poroelastic and elastic material characterization. Also, MISs are given for all the considered variables. The acoustic topology optimization problem is presented in section 4, where sensitivity analysis and the BESO algorithm are also detailed. In section 5, numerical examples and their discussions are treated, with conclusions drawn in section 6.

## 2. Governing equations

Consider the system shown in Fig. 1, where the poroelastic domain,  $\Omega_p$ , displayed in the hashed region, is secluded by two thin elastic structures,  $\Omega_e$ , representing a closed-space configuration for sound attenuation. In general, purely acoustic elements are placed in the two areas outside the limits imposed by the thin structures, symbolized by  $\Omega_a$ , while purely elastic elements are used in  $\Omega_e$ . Throughout the entire process, the hashed sector is also considered to be the design domain ( $\Omega_d = \Omega_p$ ), while the non-design domain is set as  $\Omega_{nd} = \Omega_a \cup \Omega_e$ .

In a closer look at Fig. 1(a), it is noticeable that the entire domain is treated as vertically periodic (the acoustic panel is formed by the repetition of the periodic cell), while a plane wave enters at the left side boundary and an anechoic termination is set at the right. With this disposition, nodal and elemental variables, such as displacements, pressure and sensitivities, assume equal values in both parts of the periodic system divided by the line of symmetry. Therefore, a symmetric unit cell is adopted here, without loss of generality, as shown in Fig. 1(b). The system dimensions, such as the thickness,  $b$ , height,  $D$ , and lengths,  $L_a$  and  $L_p$ , are defined later in the numerical examples section. Finally, it is remarked that the properties of acoustic, poroelastic and elastic regions are mostly referred to the subscripts  $a$ ,  $p$  and  $e$ , respectively. The structural and fluid phases of the poroelastic domain are subjected to the subscripts  $s$  and  $f$ .

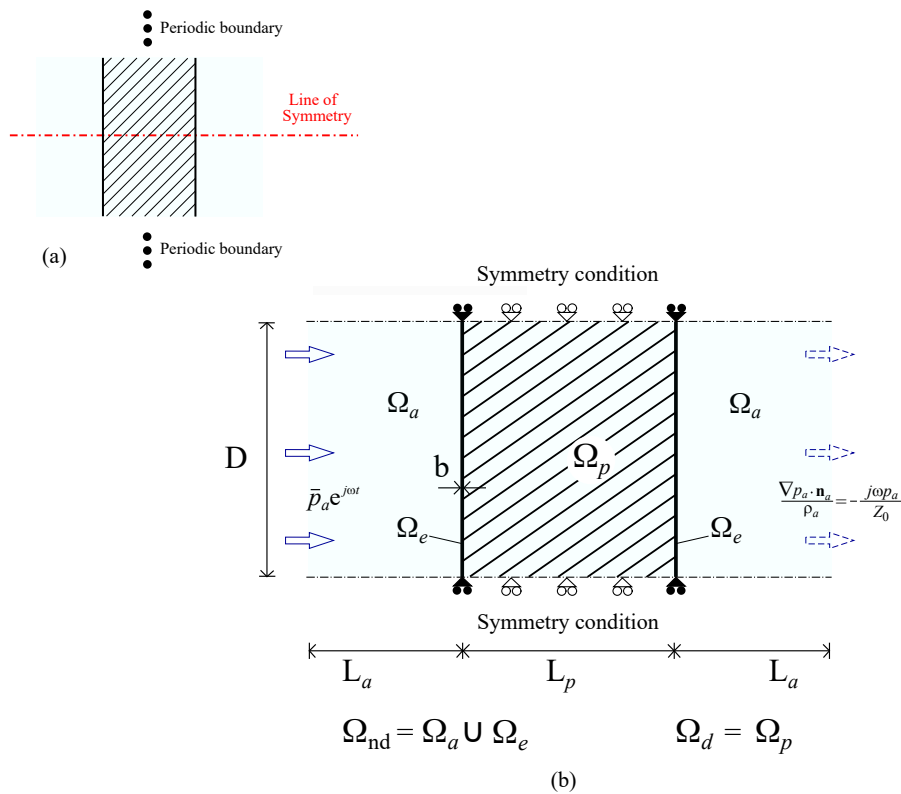


Figure 1: Initial closed-space system configuration with (a) periodic and (b) symmetry conditions

### 2.1. Poroelastic media formulation

The poroelastic media is here considered as macroscopically homogeneous [46] and subjected to time-harmonic motion ( $\mathbf{u}_s e^{j\omega t}$  and  $p_f e^{j\omega t}$ ). In this scenario, the subsequent set of relations may describe, in the frequency domain, the wave behavior inside

of it, that is,

$$\nabla \cdot \hat{\boldsymbol{\sigma}}^s + \omega^2 \tilde{\rho} \mathbf{u}_s + \tilde{\gamma} \nabla p_f = \mathbf{0}, \quad (1)$$

$$\nabla^2 p_f + \omega^2 \frac{\tilde{\rho}_{22}}{\tilde{R}} p_f - \omega^2 \frac{\tilde{\rho}_{22}}{\phi^2} \tilde{\gamma} \nabla \cdot \mathbf{u}_s = 0, \quad (2)$$

where  $p_f$  is the interstitial fluid phase pressure,  $\mathbf{u}_s$  is the solid phase displacement,  $j^2 = -1$  is the imaginary unit number,  $\omega$  is the angular frequency,  $t$  is time,  $\nabla$  is the gradient operator,  $\nabla^2$  is the Laplacian operator and  $\phi$  is the porosity. The tilde symbol indicates a frequency-dependent and complex valued variable. To find the combined effective density,  $\tilde{\rho}$ , and the coupling coefficient,  $\tilde{\gamma}$ , one may write,

$$\tilde{\rho} = \tilde{\rho}_{11} - \frac{\tilde{\rho}_{12}^2}{\tilde{\rho}_{22}}, \quad \tilde{\gamma} = \phi \left( \frac{\tilde{\rho}_{12}}{\tilde{\rho}_{22}} - \frac{\tilde{Q}}{\tilde{R}} \right), \quad (3)$$

with the individual effective densities being defined as,

$$\tilde{\rho}_{11} = \rho_{11} + \frac{\tilde{b}}{j\omega}, \quad \tilde{\rho}_{22} = \rho_{22} + \frac{\tilde{b}}{j\omega}, \quad \tilde{\rho}_{12} = \rho_{12} - \frac{\tilde{b}}{j\omega}. \quad (4)$$

The homogenized densities  $\rho_{11}$  and  $\rho_{22}$  account for the inertia effects in the structural and fluid phases, respectively, while  $\rho_{12}$  considers the interactions between the inertia forces of both phases. The physical interpretation of  $\tilde{b}$  may be divided into two aspects, depending on its real and imaginary parts. The first is related to the dissipative effect of viscous forces, and the second with the added mass effect that happens due to these same viscous interactions [13]. Following Allard and Atalla [10], these last terms may also be expressed as,

$$\rho_{11} = (1 - \phi)\rho_s - \rho_{12}, \quad \rho_{22} = \phi\rho_f - \rho_{12}, \quad (5)$$

$$\rho_{12} = -\phi\rho_f(\alpha_\infty - 1), \quad \tilde{b} = \phi^2\sigma\tilde{G}, \quad (6)$$

where  $\alpha_\infty$  is the tortuosity,  $\sigma$  is the static flow resistivity,  $\rho_f$  is the fluid phase density and  $\rho_s$  is the solid phase density. As  $\tilde{G}$  defines  $\tilde{b}$ , it also accounts for viscous effects. Based on Johnson et al. [8], this variable is written as,

$$\tilde{G} = \sqrt{1 + j \frac{4\alpha_\infty^2 \eta_0 \rho_f \omega}{\sigma^2 \Lambda^2 \phi^2}}, \quad (7)$$

with  $\Lambda$  being the viscous characteristic length and  $\eta_0$  the dynamic viscosity of the interstitial fluid.

Related only to the structural skeleton, the stress tensor of the porous material in vacuum,  $\hat{\boldsymbol{\sigma}}^s$ , also has a mathematical expression associated with it,

$$\hat{\boldsymbol{\sigma}}^s = \underbrace{\left( \tilde{A} - \frac{\tilde{Q}^2}{\tilde{R}} \right)}_{\tilde{A}} \nabla \cdot \mathbf{u}_s \mathbf{I} + 2\tilde{N} \boldsymbol{\epsilon}^s, \quad (8)$$

where  $\mathbf{I}$  is the identity tensor,  $\boldsymbol{\varepsilon}^s$  is the structural phase strain tensor and  $\tilde{A}$  is the first Lamé constant of the poroelastic material, which has  $\tilde{N}$  as its shear modulus. The variables  $\tilde{Q}$  and  $\tilde{R}$  are coupling coefficients that account for volumetric changes in both phases, and  $\tilde{A}$  is the first Lamé constant of the structural phase (poroelastic material in vacuum). Since the majority of poroelastic media has high porosity values, the variables  $\tilde{N}$ ,  $\tilde{A}$ ,  $\tilde{Q}$  and  $\tilde{R}$  can be written in a simplified manner,

$$\tilde{N} = \frac{E_p(1 + j\eta_p)}{2(1 + \nu_p)}, \quad \tilde{A} = \frac{\nu_p E_p(1 + j\eta_p)}{(1 + \nu_p)(1 - 2\nu_p)}, \quad (9)$$

$$\tilde{Q} = (1 - \phi)\tilde{K}_f, \quad \tilde{R} = \phi\tilde{K}_f, \quad (10)$$

with  $E_p$ ,  $\eta_p$  and  $\nu_p$  being the Young's modulus, the loss factor and the Poisson's ratio of the poroelastic material, respectively, while  $\tilde{K}_f$  represents the bulk modulus of the fluid in the pores. As highlighted by Cao et al. [6], one of the most used models to account for thermal losses inside porous domains is attributed to Champoux and Allard [9] due to the relatively low amount of variables introduced in the formulations. So, with the adoption of this model in the present work,  $\tilde{K}_f$  can finally be defined,

$$\tilde{K}_f = \gamma_0 P_0 \left[ \gamma_0 - (\gamma_0 - 1) \left( 1 - j \frac{8\eta_0}{\Lambda'^2 P_d \rho_f \omega} \sqrt{1 + j \frac{\Lambda'^2 P_d \rho_f \omega}{16\eta_0}} \right)^{-1} \right]^{-1}, \quad (11)$$

where  $\gamma_0$  is the specific heat ratio,  $P_d$  is the Prandtl number,  $P_0$  is the atmospheric pressure and  $\Lambda'$  is the thermal characteristic length.

The variational formulation (or weak form) of the coupled problem stated in Eqs. (1) and (2) may then be obtained by the application of the Weighted Residuals Method and the Divergence Theorem,

$$\int_{\Omega_p} \left\{ \hat{\boldsymbol{\sigma}}^s(\mathbf{u}_s) : \boldsymbol{\varepsilon}^s(\delta \mathbf{u}_s) - \omega^2 \tilde{\rho} \mathbf{u}_s \cdot \delta \mathbf{u}_s - (\tilde{\gamma} + \tilde{\xi}) \nabla p_f \cdot \delta \mathbf{u}_s - \tilde{\xi} p_f \nabla \cdot \delta \mathbf{u}_s \right\} d\Omega_p - \int_{\Gamma_p} (\boldsymbol{\sigma}^t \cdot \mathbf{n}_p) \cdot \delta \mathbf{u}_s d\Gamma_p = 0, \quad (12)$$

$$\int_{\Omega_p} \left\{ \frac{\phi^2}{\omega^2 \tilde{\rho}_{22}} \nabla p_f \cdot \nabla \delta p_f - \frac{\phi^2}{\tilde{R}} p_f \delta p_f - (\tilde{\gamma} + \tilde{\xi}) \nabla \delta p_f \cdot \mathbf{u}_s - \tilde{\xi} \delta p_f \nabla \cdot \mathbf{u}_s \right\} d\Omega_p - \int_{\Gamma_p} \phi(\mathbf{U}_f - \mathbf{u}_s) \cdot \mathbf{n}_p \delta p_f d\Gamma_p = 0, \quad (13)$$

where  $\delta \mathbf{u}_s$  and  $\delta p_f$  are admissible functions,  $\Gamma_p$  is the outer boundary of the poroelastic domain  $\Omega_p$ ,  $\mathbf{n}_p$  is the outward unit normal vector to  $\Gamma_p$ ,  $\boldsymbol{\sigma}^t = \hat{\boldsymbol{\sigma}}^s - \tilde{\xi} p_f \mathbf{I}$  is the total stress tensor,  $\phi(\mathbf{U}_f - \mathbf{u}_s)$  is the average relative displacement vector and  $\tilde{\xi} = \phi(1 + \tilde{Q}/\tilde{R})$  is a coupling coefficient introduced for conciseness [41]. An interesting aspect of Eqs. (12) and (13) is that the couplings between the structural and fluid phases are of volumetric nature, while the boundary quantities  $\boldsymbol{\sigma}^t \cdot \mathbf{n}_p$  and  $\phi(\mathbf{U}_f - \mathbf{u}_s) \cdot \mathbf{n}_p$  allow for a natural coupling between poroelastic-elastic domains, as well as two dissimilar poroelastic materials. Finally, according to Sgard et al. [47], the following relations  $\tilde{\gamma} + \tilde{\xi} = \rho_f(\phi^2/\tilde{\rho}_{22})$  are also valid.

## 2.2. Coupled equilibrium equation

160 As this work also deals with interactions of explicit acoustic-elastic nature (not to be confused with the implicit kind of poroelastic media), it is useful that both domains are formulated together. In this sense, the standard Helmholtz and elastodynamic expressions that govern the harmonic wave behavior in both regions are respectively presented,

$$\frac{1}{\rho_a} \left( \nabla^2 p_a + \frac{\omega^2}{c_a^2} p_a \right) = 0 \quad \text{in } \Omega_a, \quad (14)$$

$$\nabla \cdot \boldsymbol{\sigma}_e + \rho_e \omega^2 \mathbf{u}_e = \mathbf{0} \quad \text{in } \Omega_e, \quad (15)$$

165 with  $\rho_a$  and  $\rho_e$  being the acoustic and elastic densities,  $c_a$  the speed of sound in air and  $\boldsymbol{\sigma}_e$  the elastic stress tensor.

In a general view, the acoustic boundary conditions are related to pressure imposition, Eq. (16), hard wall condition, Eq. (17), impedance matching, Eq. (18), and normal displacements continuity, Eq. (19), that is,

$$p_a = \bar{p}_a \quad \text{over } \Gamma_{aD}, \quad (16)$$

$$\nabla p_a \cdot \mathbf{n}_a = 0 \quad \text{over } \Gamma_{aN}, \quad (17)$$

$$\frac{\nabla p_a \cdot \mathbf{n}_a}{\rho_a} = -\frac{j\omega p_a}{Z_0} \quad \text{over } \Gamma_{aR}, \quad (18)$$

$$\frac{\nabla p_a \cdot \mathbf{n}_a}{\rho_a} = \omega^2 \mathbf{u}_e \cdot \mathbf{n}_a \quad \text{over } \Gamma_{ae}. \quad (19)$$

170 For the elastic domain, the displacement imposition, Eq. (20), external load distribution, Eq. (21), and equilibrium between fluid pressures and surface tractions, Eq. (22), are considered,

$$\mathbf{u}_e = \bar{\mathbf{u}}_e \quad \text{over } \Gamma_{eD}, \quad (20)$$

$$\boldsymbol{\sigma}_e \cdot \mathbf{n}_e = \mathbf{f}_e \quad \text{over } \Gamma_{eN}, \quad (21)$$

$$\boldsymbol{\sigma}_e \cdot \mathbf{n}_e = p_a \mathbf{n}_a \quad \text{over } \Gamma_{ae}. \quad (22)$$

The subscripts  $D$ ,  $N$  and  $R$  refer to Dirichlet, Neumann and Robin boundary types of both regions, while  $ae$  concerns to the acoustic-elastic frontier.

175 Following similar procedures to those performed for poroelastic materials, Eqs. (16) to (22) are respectively combined with Eqs. (14) and (15), leading to their weak forms,

$$\begin{aligned} & \frac{1}{\rho_a} \int_{\Omega_a} \nabla p_a \cdot \nabla \delta p_a \, d\Omega_a - \frac{\omega^2}{\kappa_a} \int_{\Omega_a} p_a \delta p_a \, d\Omega_a \\ & + \int_{\Gamma_{aR}} \frac{j\omega p_a}{Z_0} \delta p_a \, d\Gamma_{aR} - \omega^2 \int_{\Gamma_{ae}} \mathbf{u}_e \cdot \mathbf{n}_a \delta p_a \, d\Gamma_{ae} = 0, \end{aligned} \quad (23)$$

$$\begin{aligned} & \int_{\Omega_e} \boldsymbol{\sigma}_e(\mathbf{u}_e) : \boldsymbol{\varepsilon}_e(\delta \mathbf{u}_e) \, d\Omega_e - \int_{\Omega_e} \rho_e \omega^2 \mathbf{u}_e \cdot \delta \mathbf{u}_e \, d\Omega_e \\ & - \int_{\Gamma_{eN}} \mathbf{f}_e \cdot \delta \mathbf{u}_e \, d\Gamma_{eN} - \int_{\Gamma_{ae}} p_a \mathbf{n}_a \cdot \delta \mathbf{u}_e \, d\Gamma_{ae} = 0, \end{aligned} \quad (24)$$

where  $\bar{p}_a$  and  $\bar{\mathbf{u}}_e$  are imposed pressure and displacement values, respectively,  $\mathbf{f}_e$  is a load vector applied over  $\Gamma_{eN}$ ,  $\boldsymbol{\varepsilon}_e$  is the elastic strain tensor,  $Z_0 = \rho_a c_a$  is the acoustic characteristic impedance and both  $\delta p_a$ ,  $\delta \mathbf{u}_e$  are admissible functions.

The coupling conditions at the poroelastic-elastic boundary,  $\Gamma_{ep}$ , are defined in a way that the continuity of the total stress, Eq. (25), the lack of relative mass flux through the impervious wall, Eq. (26), and the continuity of the solid phase vectors, Eq. (27), are all ensured,

$$\boldsymbol{\sigma}^t \cdot \mathbf{n}_p = \boldsymbol{\sigma}_e \cdot \mathbf{n}_p, \quad (25)$$

$$\phi(\mathbf{U}_f - \mathbf{u}_s) \cdot \mathbf{n}_p = 0, \quad (26)$$

$$\mathbf{u}_s = \mathbf{u}_e. \quad (27)$$

This means that when Eqs. (25), (26) and (27) are applied to the poroelastic-elastic surface integrals,

$$I^p + I^e = - \int_{\Gamma_{ep}} (\boldsymbol{\sigma}^t \cdot \mathbf{n}_p) \cdot \delta \mathbf{u}_s \, d\Gamma_{ep} - \int_{\Gamma_{ep}} \phi(\mathbf{U}_f - \mathbf{u}_s) \cdot \mathbf{n}_p \delta p_f \, d\Gamma_{ep} + \int_{\Gamma_{ep}} (\boldsymbol{\sigma}_e \cdot \mathbf{n}_p) \cdot \delta \mathbf{u}_e \, d\Gamma_{ep}, \quad (28)$$

where  $\mathbf{n}_e = -\mathbf{n}_p$ , the coupling is natural ( $I^p + I^e = 0$ ).

However, at the poroelastic-acoustic interface,  $\Gamma_{ap}$ , the conditions are,

$$\boldsymbol{\sigma}^t \cdot \mathbf{n}_p = -p_a \mathbf{n}_p, \quad (29)$$

$$\frac{\nabla p_a \cdot \mathbf{n}_p}{\rho_a} = \mathbf{u}_s \cdot \mathbf{n}_p + \phi(\mathbf{U}_f - \mathbf{u}_s) \cdot \mathbf{n}_p, \quad (30)$$

$$p_f = p_a, \quad (31)$$

where the continuity of all normal stresses, acoustic and total poroelastic displacements, and pressure are respectively represented by Eqs. (29), (30) and (31). Substituting these later expressions in Biot's and Helmholtz surface integrals,

$$I^p + I^a = - \int_{\Gamma_{ap}} (\boldsymbol{\sigma}^t \cdot \mathbf{n}_p) \cdot \delta \mathbf{u}_s \, d\Gamma_{ap} - \int_{\Gamma_{ap}} \phi(\mathbf{U}_f - \mathbf{u}_s) \cdot \mathbf{n}_p \delta p_f \, d\Gamma_{ap} + \int_{\Gamma_{ap}} \frac{\nabla p_a \cdot \mathbf{n}_p}{\rho_a} \delta p_a \, d\Gamma_{ap}, \quad (32)$$

for  $\mathbf{n}_a = -\mathbf{n}_p$ , the following coupling condition appear,

$$I^p + I^a = \int_{\Gamma_{ap}} \delta(p_a \mathbf{n}_p \cdot \mathbf{u}_s) \, d\Gamma_{ap}, \quad (33)$$

which is the standard acoustic-elastic coupling term applied over  $\Gamma_{ap}$ .

Finally, to proper couple two dissimilar poroelastic materials the conditions are of four types. The first one concerns to the continuity of normal stresses, Eq. (34), while the second ensures continuity of mass flow across the boundary, Eq. (35). The third and fourth ones, Eqs. (36) and (37), establish the solid phase displacements and pore

fluid pressure fields across the poroelastic-poroelastic interface,  $\Gamma_{pp}$ , hence,

$$\boldsymbol{\sigma}'_1 \cdot \mathbf{n}_p = \boldsymbol{\sigma}'_2 \cdot \mathbf{n}_p, \quad (34)$$

$$\phi(\mathbf{U}_{f_1} - \mathbf{u}_{s_1}) \cdot \mathbf{n}_p = \phi(\mathbf{U}_{f_1} - \mathbf{u}_{s_1}) \cdot \mathbf{n}_p, \quad (35)$$

$$\mathbf{u}_{s_1} = \mathbf{u}_{s_2}, \quad (36)$$

$$p_{f_1} = p_{f_2}, \quad (37)$$

which also leads to a natural coupling.

200 The Finite Element Method (FEM) is employed in the discretization of Eqs. (12), (13), (23) and (24). Combining with Galerkin's approach, the following coupled system of equations is found,

$$\underbrace{\begin{bmatrix} \mathbf{K}_e - \omega^2 \mathbf{M}_e & \mathbf{0} & \mathbf{0} & -\mathbf{L}_{ae} \\ \mathbf{0} & \tilde{\mathbf{K}}_p - \omega^2 \tilde{\mathbf{M}}_p & -(\tilde{\mathbf{C}}_{p1} + \tilde{\mathbf{C}}_{p2}) & -\mathbf{L}_{ap} \\ \mathbf{0} & -(\tilde{\mathbf{C}}_{p1} + \tilde{\mathbf{C}}_{p2})^T & \tilde{\mathbf{H}}_p / \omega^2 - \tilde{\mathbf{Q}}_p & \mathbf{0} \\ -\mathbf{L}_{ae}^T & -\mathbf{L}_{ap}^T & \mathbf{0} & \mathbf{H}_a / \omega^2 + j\mathbf{D}_a / \omega - \mathbf{Q}_a \end{bmatrix}}_{\tilde{\mathbf{z}}} \underbrace{\begin{bmatrix} \hat{\mathbf{u}}_e \\ \hat{\mathbf{u}}_s \\ \hat{\mathbf{p}}_f \\ \hat{\mathbf{p}}_a \end{bmatrix}}_{\hat{\boldsymbol{\theta}}} = \underbrace{\begin{bmatrix} \hat{\mathbf{f}}_e \\ \hat{\mathbf{f}}_s \\ \hat{\mathbf{f}}_f / \omega^2 \\ \mathbf{0} \end{bmatrix}}_{\hat{\mathbf{f}}}, \quad (38)$$

where  $\mathbf{K}$ ,  $\mathbf{M}$ ,  $\mathbf{H}$  and  $\mathbf{Q}$  are the global stiffness, mass, kinetic and compression matrices, respectively. The fluid-structure coupling matrices are  $\tilde{\mathbf{C}}_{p1}$ ,  $\tilde{\mathbf{C}}_{p2}$ ,  $\mathbf{L}_{ae}$  and  $\mathbf{L}_{ap}$ , 205 where the first two are related to both poroelastic phases, and the last ones regard the acoustic-elastic interactions present at  $\Gamma_{ae}$  and  $\Gamma_{ap}$ .  $\mathbf{D}_a$  is the acoustic damping matrix that appears due to the anechoic termination (see Eqs. (18)). The global displacement, pressure and load vectors are  $\hat{\mathbf{u}}$ ,  $\hat{\mathbf{p}}$  and  $\hat{\mathbf{f}}$ . From an elemental perspective, the above matrices and load vectors can be explicitly found in the works of Allard and Atalla 210 [10].

As previously stated, the adopted poroelasticity equations do not require coupling matrices to connect dissimilar poroelastic or poroelastic-elastic domains. However, for the acoustic-poroelastic case a  $\mathbf{L}_{ap}$  fluid-structural coupling matrix need to be implemented for the correct description of forces that are exchanged between both media. 215 To comply with this, two methodologies can be used. The first consists of tracking the boundaries between the different materials throughout the optimization process, in order to implement the  $\mathbf{L}_{ae}$  and  $\mathbf{L}_{ap}$  matrices in all acoustic-elastic and poroelastic-acoustic boundaries. The second methodology avoid such time consuming calculations by ignoring the tracking of borders, as Biot's equations are used to simulate all acoustic, elastic and poroelastic elements by the manipulation of specific variables. This last 220 approach, named as Unified Multiphase (UMP) [40, 41, 42] modeling technique, is the one adopted in this work.

### 3. Target Material Characterization

To characterize the multiphysical soundproof system, consider the following set of 225 variables that are present in the weak form of Biot's formulation (Eqs. (12) and (13)),

$$\tilde{\Psi} = \{\tilde{\xi}, \tilde{\rho}, \tilde{N}, \hat{A}, (\phi^2 / \tilde{\rho}_{22}), (\phi^2 / \tilde{R})\}. \quad (39)$$

Taking limiting values of the parameters contained in  $\tilde{\Psi}$ , the scalar Helmholtz and elastodynamic equations can be directly derived from the original Biot's expressions if ones goal is to simulate acoustic or elastic domains, respectively. Named as Unified Multiphase (UMP) approach by Lee et al. [40, 41, 42], these configurations are implemented as follows,

$$\tilde{\Psi}_p = \{\tilde{\xi}_p, \tilde{\rho}_p, \tilde{N}_p, \hat{A}_p, (\phi^2/\tilde{\rho}_{22})_p, (\phi^2/\tilde{R})_p\} \equiv \tilde{\Psi}, \quad (40)$$

$$\tilde{\Psi}_a = \{1, o_a \tilde{\rho}_p, o_a \tilde{N}_p, o_a \hat{A}_p, 1/\rho_a, 1/\kappa_a\}, \quad (41)$$

$$\tilde{\Psi}_e = \{o_e \tilde{\xi}_p, \rho_e, \tilde{N}_e, \tilde{A}_e, o_e (\phi^2/\tilde{\rho}_{22})_p, o_e (\phi^2/\tilde{R})_p\}, \quad (42)$$

for  $\tilde{\Psi}_p$ ,  $\tilde{\Psi}_a$  and  $\tilde{\Psi}_e$  being vectors of variables regarding poroelastic, acoustic and elastic media. To avoid numerical instabilities, small constants are adopted in  $\tilde{\Psi}_a$  and  $\tilde{\Psi}_e$  as  $o_a = o_e = 10^{-9}$ .

The UMP method is illustrated in Fig 2. In item (a), the acoustic, poroelastic and elastic domains are fully represented by the Helmholtz, Biot and elastodynamic formulations. With the adoption of the UMP approach, all these domains are characterized only by Biot's poroelasticity expressions, depending on the configuration of  $\tilde{\Psi}$ , as highlighted in Eqs. (40), (41) and (42), as well as shown in Fig 2(b). As a consequence of the degeneration caused by  $\tilde{\Psi}_a$  and  $\tilde{\Psi}_e$  in Eqs. (1) and (2), all the combinations of boundaries are naturally coupled, as also represented in Fig 2(b), hence solving the boundary tracking issue in the current acoustic topology optimization study. However, as the UMP considers that Biot's expressions describe the entire observed domain, the degrees of freedom of the system are augmented; that is, regardless of the domain that is simulated, each node will have three degrees of freedom in a 2D perspective, with two of them concerning displacements and one pressure. This methodological downside can be partially dealt with by adopting fully modeled acoustic and elastic elements in the non-design regions, with poroelastic elements only employed in the design domain. Such procedure is adopted in this work (see Eq. 38 for the coupled expressions).

### 3.1. Material interpolation scheme considering multiphysics

Recurrently in topology optimization approaches, the start design domain is considered to be completely (or partially) full of elastic/poroelastic elements in a way that the acoustic ones are often inserted into it. However, many of these methods provide different results if initialized with elastic or poroelastic. Therefore, seeing that the vast majority of vibroacoustic systems are, at first, designed to contain only air, the proposed Material Interpolation Scheme (MIS) is built in the following manner,

$$\tilde{\Psi}(x_{i_1}, x_{i_2}) = \tilde{\Psi}_e + x_{i_2}^{\xi_2} (\tilde{\Psi}_p - \tilde{\Psi}_e) + x_{i_1}^{\xi_1} (\tilde{\Psi}_a - \tilde{\Psi}_p), \quad (43)$$

with,

$$(x_{i_1}, x_{i_2}) = (1, 1), \quad \text{for acoustic elements}, \quad (44)$$

$$(x_{i_1}, x_{i_2}) = (x_{\min}, 1), \quad \text{for poroelastic elements}, \quad (45)$$

$$(x_{i_1}, x_{i_2}) = (x_{\min}, x_{\min}), \quad \text{for elastic elements}. \quad (46)$$

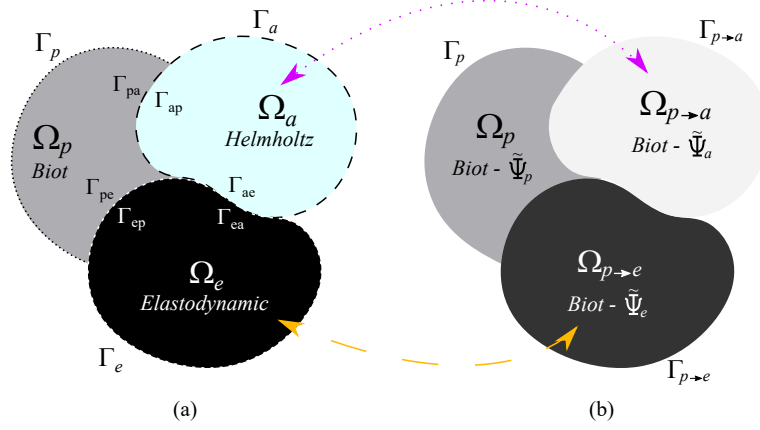


Figure 2: Schematic representation of the UMP methodology, where (a) the fully coupled acoustic-poroelastic-elastic region can be represented by (b) a unified Biot's governed domain. The variables  $\Gamma$  represent the inner/outer boundaries and the subscripts  $a$ ,  $p$  and  $e$  respectively refer to acoustic, poroelastic and elastic domains

In the above,  $x_{i_1}$  and  $x_{i_2}$  are elemental design variables, with  $x_{\min} = 0.001$ . The superscripts  $\zeta_1$  and  $\zeta_2$  are penalty coefficients.

260 One important point to note is that Eq. (43) is applied to all six variables comprised by  $\tilde{\Psi}$ , as explicitly shown in Eqs. (47) to (52),

$$\tilde{\zeta} = o_e \tilde{\zeta}_p + x_{i_2}^{\zeta_2} \tilde{\zeta}_p (1 - o_e) + x_{i_1}^{\zeta_1} (1 - \tilde{\zeta}_p), \quad (47)$$

$$\tilde{\rho} = \rho_e + x_{i_2}^{\zeta_2} (\tilde{\rho}_p - \rho_e) + x_{i_1}^{\zeta_1} \tilde{\rho}_p (o_a - 1), \quad (48)$$

$$\tilde{N} = \tilde{N}_e + x_{i_2}^{\zeta_2} (\tilde{N}_p - \tilde{N}_e) + x_{i_1}^{\zeta_1} \tilde{N}_p (o_a - 1), \quad (49)$$

$$\tilde{A} = \tilde{A}_e + x_{i_2}^{\zeta_2} (\tilde{A}_p - \tilde{A}_e) + x_{i_1}^{\zeta_1} \tilde{A}_p (o_a - 1), \quad (50)$$

$$\left( \frac{\phi^2}{\tilde{\rho}_{22}} \right) = o_e \left( \frac{\phi^2}{\tilde{\rho}_{22}} \right)_p + x_{i_2}^{\zeta_2} \left( \frac{\phi^2}{\tilde{\rho}_{22}} \right)_p (1 - o_e) + x_{i_1}^{\zeta_1} \left[ \frac{1}{\rho_a} - \left( \frac{\phi^2}{\tilde{\rho}_{22}} \right)_p \right], \quad (51)$$

$$\left( \frac{\phi^2}{\tilde{R}} \right) = o_e \left( \frac{\phi^2}{\tilde{R}} \right)_p + x_{i_2}^{\zeta_2} \left( \frac{\phi^2}{\tilde{R}} \right)_p (1 - o_e) + x_{i_1}^{\zeta_1} \left[ \frac{1}{\kappa_a} - \left( \frac{\phi^2}{\tilde{R}} \right)_p \right]. \quad (52)$$

265 Another interesting point regards the choice of only two penalty coefficients to be used in the above equations, when twelve different values of  $\zeta$  could be adopted. Although this last possibility gives dynamism to the proposed MIS, which can be adapted to several different scenarios, it also brings the burden of defining a high number of variables previous to the optimization. After a series of tests conducted by the authors, an effective mitigation approach is placed by simply setting the same values for all the penalty variables pegged to  $x_{i_1}$  or  $x_{i_2}$ , that is,  $\zeta_{2n-1} = \zeta_1$  and  $\zeta_{2n} = \zeta_2$ , where  $\{n \in \mathbb{N} \setminus 2 \leq n \leq 6\}$ . Table 1 presents the material properties needed to carry out the suggested approach. Here, the Polyurethane foam is treated as the poroelastic material, 270

while the Olefin sheet is regarded as elastic (viscoelastic characteristics are neglected) [39].

Table 1: Acoustic, poroelastic and elastic parameters

Poroelastic and Elastic Parameters	Polyurethane Foam	Olefin Sheet
Porosity $\phi$	0.97	–
Tortuosity $\alpha_\infty$	2.5	–
Static flow resistivity $\sigma$ (N s m <sup>-4</sup> )	$7 \times 10^4$	–
Viscous characteristic length $\Lambda$ (m)	$36 \times 10^{-6}$	–
Thermal characteristic length $\Lambda'$ (m)	$170 \times 10^{-6}$	–
Mass density $\rho_s, \rho_e$ (kg m <sup>-3</sup> )	1433	1790
Young's modulus $E_p, E_e$ (Pa)	$2.67 \times 10^5$	$1.75 \times 10^8$
Poisson's ratio $\nu_p, \nu_e$	0.4	0.4
Loss factor $\eta_p, \eta_e$	0.11	0.205
Acoustic Parameters		Air (20°C)
Dynamic viscosity $\eta_0$ (kg m <sup>-1</sup> s <sup>-1</sup> )	$1.84 \cdot 10^{-5}$	
Specific heat ratio $\gamma_0$	1.401	
Prandtl number $P_d$	0.710	
Atmospheric pressure $P_0$ (Pa)	101,325	

The final aspect that needs to be addressed is the fact that the design domain is solely composed of air in its initial configuration. This statement contrasts with the first presentation of the investigated setting, Fig. 1(b), where  $\Omega_d$  and  $\Omega_p$  are attributed as equals. However, the elements contained in  $\Omega_d$  are, throughout the investigations carried out here, considered as initially governed by Biot's equations of poroelasticity, but with the possibility of degeneration to the Helmholtz and elastodynamic forms. Moreover, the elements of  $\Omega_{nd}$  are purely governed by the equations of their own domains (Helmholtz for acoustic elements and elastodynamics for elastic elements), with no possibility of change. In this way,  $\Omega_d$  is characterized as being initially composed of air, even though the elements that compose this region are poroelastic elements degenerated to represent acoustic ones by the UMP method.

#### 4. Topology Optimization Problem Description

The topology optimization problem investigated in this work can be defined, for a specific target frequency, as to maximize the dissipated power level,  $PL_D$ , that in turn is a combination of the time-averaged dissipated powers of structural,  $\Pi_D^s$ , viscous,  $\Pi_D^v$ , and thermal,  $\Pi_D^t$ , nature, while subjected to volume constraints. Throughout the numerical procedure, a multifrequency band of  $[\omega_s, \omega_f]$  is also considered in a way that the objective function becomes the mean  $PL_D$  (or  $MPL_D$ ), as shown in the following

expressions,

$$\text{Maximize: } \text{MPL}_D = \frac{1}{\omega_f - \omega_s} \int_{\omega_s}^{\omega_f} \underbrace{10 \log_{10} \left( \frac{\vartheta_1 \Pi_D^s + \vartheta_2 \Pi_D^v + \vartheta_3 \Pi_D^t}{\Pi_{\text{ref}}} \right)}_{\text{PL}_D} d\Omega_p, \quad (53)$$

$$\text{Subjected to: } \begin{cases} \tilde{\mathbf{Z}}\hat{\boldsymbol{\theta}} = \hat{\mathbf{f}}, \\ V_p^f - \sum_{i=1}^{N_{\text{el}}} V_{i_p} x_{i_1} = 0, \\ V_e^f - \sum_{i=1}^{N_{\text{el}}} V_{i_e} x_{i_2} = 0, \\ x_{i_1} = x_{\text{min}} \text{ or } 1, \\ x_{i_2} = x_{\text{min}} \text{ or } 1. \end{cases} \quad (54)$$

In Eq. (53),  $\vartheta_1$ ,  $\vartheta_2$  and  $\vartheta_3$  are used as switching variables, that is, they assume unit values when  $\Pi_D^s$ ,  $\Pi_D^v$  or  $\Pi_D^t$  are respectively considered in the objective function, otherwise assuming null values. This artifice is here applied to facilitate the combination of different dissipative portions of power without necessarily rewriting the objective function. Furthermore,  $\Pi_{\text{ref}} = 1 \times 10^{-12}$  W represents the reference power. In Eq. (54), the prescribed final volume fraction is  $V^f$ , with the design domain volume fraction being  $\sum_{i=1}^{N_{\text{el}}} V_i x_i$ .  $N_{\text{el}}$  is the number of elements contained in the design domain. As  $\Omega_d$  initially contains only air, the porous materials are first introduced in the design until the attainment of  $V_p^f$ . Then, elastic structures are brought in, but only inside the regions immediately after being occupied by the porous bodies, in an acoustic-poroelastic-elastic sequential manner. As this methodology entails a larger number of iterations to complete the optimization process, it also enhances the stability of the application, since do not allow that significant variations of the acoustic-elastic type occur in the same iteration.

Knowing that harmonic motion is considered in the definition of all domain formulations, the dissipated powers may then be established in time-averaged forms. A common way to obtain these expressions for the poroelastic media was introduced by Sgard et al. [48], which applied  $\delta \mathbf{u}_s = -j\omega \mathbf{u}_s^*$  and  $\delta p_f = -j\omega p_f^*$  as admissible functions of Eqs. (12) and (13), generating,

$$\Pi_D^s = \frac{\omega}{2} \text{Im} \left( \hat{\mathbf{u}}_s^H \tilde{\mathbf{K}}_p \hat{\mathbf{u}}_s \right), \quad (55)$$

$$\Pi_D^v = -\frac{\omega}{2} \text{Im} \left( \omega^2 \hat{\mathbf{u}}_s^H \tilde{\mathbf{M}}_p \hat{\mathbf{u}}_s - \frac{1}{\omega^2} \hat{\mathbf{p}}_f^H \tilde{\mathbf{H}}_p \hat{\mathbf{p}}_f + 2 \hat{\mathbf{u}}_s^H \tilde{\mathbf{C}}_{p1} \hat{\mathbf{p}}_f \right), \quad (56)$$

$$\Pi_D^t = -\frac{\omega}{2} \text{Im} \left( \hat{\mathbf{p}}_f^H \tilde{\mathbf{Q}}_p \hat{\mathbf{p}}_f \right), \quad (57)$$

where  $\text{Im}(\cdot)$  is the imaginary part of a function. The superscripts  $*$  and  $H$  are, respectively, the conjugate and the transpose conjugate of a complex variable. When considering the thin elastic structures and the anechoic termination in the composition of the general domain ( $\Omega = \Omega_d \cup \Omega_{\text{nd}}$ ), two more time-averaged dissipated powers should be added to the above equations. However, the current double-wall composition causes a natural pressure reduction in the outlet region, which is even more pronounced with the

addition of materials between such walls, so that the acoustic power contribution can be neglected. Thus, Eq. (55) is rewritten to encompass only the purely elastic power portion,

$$\Pi_D^s = \frac{\omega}{2} \text{Im}(\hat{\mathbf{u}}_e^H \mathbf{K}_e \hat{\mathbf{u}}_e) + \frac{\omega}{2} \text{Im}(\hat{\mathbf{u}}_s^H \tilde{\mathbf{K}}_p \hat{\mathbf{u}}_s). \quad (58)$$

#### 320 4.1. Sensitivity Analysis

The sensitivity analysis must be performed in order to identify the effect of an elemental change on the objective function. Here, the derivation of  $\text{MPL}_D$  with respect to  $x_i$  is  $\alpha_i$ , so,

$$\alpha_i = \frac{1}{\omega_f - \omega_s} \int_{\omega_s}^{\omega_f} \frac{10}{\ln 10} \left( \frac{\vartheta_1 \frac{d\Pi_D^s}{dx_i} + \vartheta_2 \frac{d\Pi_D^v}{dx_i} + \vartheta_3 \frac{d\Pi_D^t}{dx_i}}{\vartheta_1 \Pi_D^s + \vartheta_2 \Pi_D^v + \vartheta_3 \Pi_D^t} \right) d\Omega_p. \quad (59)$$

At this moment, consider  $\hat{\boldsymbol{\theta}} = \boldsymbol{\theta}_{\text{Re}} + j\boldsymbol{\theta}_{\text{Im}}$ , where  $\boldsymbol{\theta}_{\text{Re}}$  and  $\boldsymbol{\theta}_{\text{Im}}$  stand for the real and  
325 imaginary parts of  $\hat{\boldsymbol{\theta}}$ . The sum of the time-averaged dissipated powers can thus be rewritten as,

$$\Pi_D(\boldsymbol{\theta}_{\text{Re}}, \boldsymbol{\theta}_{\text{Im}}, x_i) = \vartheta_1 \Pi_D^s + \vartheta_2 \Pi_D^v + \vartheta_3 \Pi_D^t. \quad (60)$$

With the introduction of Lagrange multipliers,  $\boldsymbol{\lambda}$ , the augmented performance index appears,

$$\Pi_D = \Pi_D(\boldsymbol{\theta}_{\text{Re}}, \boldsymbol{\theta}_{\text{Im}}, x_i) + \boldsymbol{\lambda}^T (\tilde{\mathbf{Z}}\hat{\boldsymbol{\theta}} - \hat{\mathbf{f}}) + \boldsymbol{\lambda}^H (\tilde{\mathbf{Z}}^*\hat{\boldsymbol{\theta}}^* - \hat{\mathbf{f}}^*), \quad (61)$$

where its derivative is,

$$\begin{aligned} \frac{d\Pi_D}{dx_i} &= \frac{\partial \Pi_D}{\partial x_i} + \left( \frac{\partial \Pi_D}{\partial \boldsymbol{\theta}_{\text{Re}}} + \boldsymbol{\lambda}^T \tilde{\mathbf{Z}} + \boldsymbol{\lambda}^H \tilde{\mathbf{Z}}^* \right) \frac{\partial \boldsymbol{\theta}_{\text{Re}}}{\partial x_i} \\ &\quad + \left( \frac{\partial \Pi_D}{\partial \boldsymbol{\theta}_{\text{Im}}} + j\boldsymbol{\lambda}^T \tilde{\mathbf{Z}} - j\boldsymbol{\lambda}^H \tilde{\mathbf{Z}}^* \right) \frac{\partial \boldsymbol{\theta}_{\text{Im}}}{\partial x_i} \\ &\quad + \boldsymbol{\lambda}^T \left( \frac{\partial \tilde{\mathbf{Z}}}{\partial x_i} \hat{\boldsymbol{\theta}} - \frac{\partial \hat{\mathbf{f}}}{\partial x_i} \right) + \boldsymbol{\lambda}^H \left( \frac{\partial \tilde{\mathbf{Z}}^*}{\partial x_i} \hat{\boldsymbol{\theta}}^* - \frac{\partial \hat{\mathbf{f}}^*}{\partial x_i} \right). \end{aligned} \quad (62)$$

330 Since  $\boldsymbol{\lambda}$  can take any value, the unknown variables  $\partial \boldsymbol{\theta}_{\text{Re}} / \partial x_i$  and  $\partial \boldsymbol{\theta}_{\text{Im}} / \partial x_i$  may be removed from Eq. (62), generating,

$$\begin{cases} \boldsymbol{\lambda}^T \tilde{\mathbf{Z}} + \boldsymbol{\lambda}^H \tilde{\mathbf{Z}}^* = -\frac{\partial \Pi_D}{\partial \boldsymbol{\theta}_{\text{Re}}}, \\ j\boldsymbol{\lambda}^T \tilde{\mathbf{Z}} - j\boldsymbol{\lambda}^H \tilde{\mathbf{Z}}^* = -\frac{\partial \Pi_D}{\partial \boldsymbol{\theta}_{\text{Im}}}. \end{cases} \quad (63)$$

Multiplying the second expression in Eq. (63) by  $-j$ , adding it to the first and transposing both sides ( $\tilde{\mathbf{Z}}^T = \tilde{\mathbf{Z}}$ ), the adjoint equation is found,

$$\tilde{\mathbf{Z}}\boldsymbol{\lambda} = -\frac{1}{2} \left( \frac{\partial \Pi_D}{\partial \boldsymbol{\theta}_{\text{Re}}} - j \frac{\partial \Pi_D}{\partial \boldsymbol{\theta}_{\text{Im}}} \right)^T = \mathbf{f}_{\text{ad}}, \quad (64)$$

with its right side being the adjoint load vector,  $\mathbf{f}_{\text{ad}}$ . As  $\Pi_D$  is represented by Eq. (61),  
335 the next step consists in finding the expressions for the structural,  $\mathbf{f}_{\text{ad}}^s$ , viscous,  $\mathbf{f}_{\text{ad}}^v$ ,

and thermal,  $\mathbf{f}_{\text{ad}}^t$ , adjoint load vectors that compose  $\mathbf{f}_{\text{ad}}$ . After a series of mathematical manipulations, one may write,

$$\mathbf{f}_{\text{ad}}^s = -\frac{\omega}{2} \left[ \hat{\mathbf{u}}_e^H \text{Im}(\mathbf{K}_e) + \hat{\mathbf{u}}_s^H \text{Im}(\tilde{\mathbf{K}}_p) \right]^T, \quad (65)$$

$$\mathbf{f}_{\text{ad}}^v = \frac{\omega}{2} \left[ \omega^2 \hat{\mathbf{u}}_s^H \text{Im}(\tilde{\mathbf{M}}_p) - \frac{1}{\omega^2} \hat{\mathbf{p}}_f^H \text{Im}(\tilde{\mathbf{H}}_p) + \hat{\mathbf{p}}_f^H \text{Im}(\tilde{\mathbf{C}}_{p1})^T + \hat{\mathbf{u}}_s^H \text{Im}(\tilde{\mathbf{C}}_{p1}) \right]^T, \quad (66)$$

$$\mathbf{f}_{\text{ad}}^t = \frac{\omega}{2} \left[ \hat{\mathbf{p}}_f^H \text{Im}(\tilde{\mathbf{Q}}_p) \right]^T. \quad (67)$$

The aforementioned procedure also leads to the final form of Eq. (62),

$$\frac{d\Pi_{\text{D}}}{dx_i} = \frac{\partial\Pi_{\text{D}}}{\partial x_i} + 2 \text{Re} \left[ \lambda^T \left( \frac{\partial\tilde{\mathbf{Z}}}{\partial x_i} \hat{\boldsymbol{\theta}} - \frac{\partial\hat{\mathbf{f}}}{\partial x_i} \right) \right], \quad (68)$$

with,

$$\frac{\partial\Pi_{\text{D}}}{\partial x_i} = \text{Im} \left( \left\{ \begin{array}{c} \hat{\mathbf{u}}_s \\ \hat{\mathbf{p}}_f \end{array} \right\}^H \frac{\omega}{2} \left[ \begin{array}{cc} \vartheta_1 \frac{\partial\tilde{\mathbf{K}}_p}{\partial x_i} - \vartheta_2 \omega^2 \frac{\partial\tilde{\mathbf{M}}_p}{\partial x_i} & -\vartheta_2 \frac{\partial\tilde{\mathbf{C}}_{p1}}{\partial x_i} \\ -\vartheta_2 \frac{\partial\tilde{\mathbf{C}}_{p1}^T}{\partial x_i} & \frac{\vartheta_2}{\omega^2} \frac{\partial\tilde{\mathbf{H}}_p}{\partial x_i} - \vartheta_3 \frac{\partial\tilde{\mathbf{Q}}_p}{\partial x_i} \end{array} \right] \left\{ \begin{array}{c} \hat{\mathbf{u}}_s \\ \hat{\mathbf{p}}_f \end{array} \right\} \right), \quad (69)$$

and,

$$\frac{\partial\tilde{\mathbf{Z}}}{\partial x_i} = \left[ \begin{array}{cccc} \frac{\partial\mathbf{K}_e}{\partial x_i} - \omega^2 \frac{\partial\mathbf{M}_e}{\partial x_i} & \mathbf{0} & \mathbf{0} & -\frac{\partial\mathbf{L}_{\text{ac}}}{\partial x_i} \\ \mathbf{0} & \frac{\partial\tilde{\mathbf{K}}_p}{\partial x_i} - \omega^2 \frac{\partial\tilde{\mathbf{M}}_p}{\partial x_i} & -\frac{\partial}{\partial x_i}(\tilde{\mathbf{C}}_{p1} + \tilde{\mathbf{C}}_{p2}) & -\frac{\partial\mathbf{L}_{\text{ap}}}{\partial x_i} \\ \mathbf{0} & -\frac{\partial}{\partial x_i}(\tilde{\mathbf{C}}_{p1} + \tilde{\mathbf{C}}_{p2})^T & \frac{1}{\omega^2} \frac{\partial\tilde{\mathbf{H}}_p}{\partial x_i} - \frac{\partial\tilde{\mathbf{Q}}_p}{\partial x_i} & \mathbf{0} \\ -\frac{\partial\mathbf{L}_{\text{ac}}^T}{\partial x_i} & -\frac{\partial\mathbf{L}_{\text{ap}}^T}{\partial x_i} & \mathbf{0} & \frac{1}{\omega^2} \frac{\partial\mathbf{H}_a}{\partial x_i} + \frac{j}{\omega} \frac{\partial\mathbf{D}_a}{\partial x_i} - \frac{\partial\mathbf{Q}_a}{\partial x_i} \end{array} \right], \quad (70)$$

$$\frac{\partial\hat{\mathbf{f}}}{\partial x_i} = \mathbf{0}. \quad (71)$$

In the above expressions,  $\partial\mathbf{K}_e/\partial x_i = \partial\mathbf{M}_e/\partial x_i = \partial\mathbf{L}_{\text{ac}}/\partial x_i = \partial\mathbf{L}_{\text{ap}}/\partial x_i = \partial\mathbf{H}_a/\partial x_i = \partial\mathbf{Q}_a/\partial x_i = \partial\mathbf{D}_a/\partial x_i = \mathbf{0}$ , since the purely acoustic and elastic domains compose  $\Omega_{\text{nd}}$ . At last, the values  $\partial\tilde{\mathbf{K}}_p/\partial x_i$ ,  $\partial\tilde{\mathbf{M}}_p/\partial x_i$ ,  $\partial\tilde{\mathbf{C}}_{p1}/\partial x_i$ ,  $\partial\tilde{\mathbf{C}}_{p2}/\partial x_i$ ,  $\partial\tilde{\mathbf{H}}_p/\partial x_i$  and  $\partial\tilde{\mathbf{Q}}_p/\partial x_i$  can be obtained with the derivation of the proposed MIS, Eq. (43), with respect to  $x_{i_1}$  and  $x_{i_2}$ .

#### 4.2. Evolutionary Algorithm

With the possibility of using several iterative algorithms, structural topology optimization techniques may provide the best possible material arrangement in a closed design space, even though its initial form is of arbitrary nature. The advantages of such approach are diverse, ranging from economic savings, such as reductions of time

invested in try-and-error simulations and in raw materials used, to the improvement of structural aspects [49].

Due to its robustness and simplicity, beyond the flexibility to remove and add material elements at any time in the design domain, the BESO algorithm is the one chosen to compose this work. As a discrete, gradient-based optimization approach, this technique seems suitable to solve the current investigated problem since it allows that any topologies obtained during the iterative process to be eventually used in practical applications, especially if combined with advanced fabrication techniques [50]. On that basis, Algorithm 1 presents the general steps considered here.

---

**Algorithm 1:** BESO procedure

---

**Input:** Geometry and FEM information – section 5

BESO parameters:  $x_{i_1}, x_{i_2}, \zeta_1, \zeta_2, V_p^f, V_e^f, r_{\min}, ER, AR_{\max}$  – section 5

$\hat{\theta}$  for the initial topology – Eq. (38)

Start iteration counter:  $r \leftarrow 0$

**while**  $err < 0.005$  **or**  $V_p^{(r)} + V_e^{(r)} \neq V_p^f + V_e^f$  **do**

$r = r + 1$

    Calculate sensitivity numbers – section 4.1

    Filter sensitivities – Eqs. (76) and (77)

    Apply sensitivity historical averaging – Eq. (78)

    Apply normalization of sensitivity numbers – Eq. (79)

    Update multiphase topology – section 4.2

    Update volume fraction – Eq. (75)

    Evaluate  $\hat{\theta}$  – Eq. (38)

    Evaluate  $MPL_D$  (or  $PL_D$  for a specific target frequency) – Eq. (53)

    Verify convergency by tolerance:

$$err = \left| \frac{\sum_{b=1}^{10} MPL_D^{(r-b+1)} - \sum_{b=1}^{10} MPL_D^{(r-9-b)}}{\sum_{b=1}^{10} MPL_D^{(r-b+1)}} \right| \quad (72)$$

**Output:** Optimized topology

---

After defining the basic geometrical and FEM parameters, the BESO variables should also be provided. As previously stated,  $x_i$  can only assume two well-established values: the minimum,  $x_{\min} = 0.001$ , or the maximum,  $x_i = 1$ , depending on the investigated configuration. The penalty coefficients,  $\zeta_1$  and  $\zeta_2$ , as well as the final volume fractions,  $V_p^f$  and  $V_e^f$ , also compose the set of variables that need to be known beforehand, as are the Evolutionary Ratio (ER) and the maximum Addition Ratio ( $AR_{\max}$ ). With the definition of these last two, the sequential control of the amount of material that leaves and enters the design domain is set.

For example, consider that acoustic, poroelastic and elastic elements are all allowed in the design domain, meaning that two different sensitivity analyses would have to be performed in order to relate acoustic to poroelastic and then to elastic materials. In other words, the procedure that starts in Eq. (59) has to be done twice since it takes two design variables to fully describe the type of element occupying a predefined po-

sition (see Eqs. (44), (45) and (46) for completeness). With this, two sets of sensitivity  
 375 numbers are generated, becoming then subject to the following relations,

$$\text{if } \alpha_i \leq \alpha_{\text{th}} \quad \text{then } x_i = x_{\text{min}}, \quad (73)$$

$$\text{else-if } \alpha_i > \alpha_{\text{th}} \quad \text{then } x_i = 1, \quad (74)$$

where  $\alpha_{\text{th}}$  is the threshold sensitivity number. Such aspect is mainly based on the target  
 volume of the following iteration,  $V^{(r+1)}$ , that is,

$$V^{(r+1)} = V^{(r)}(1 \pm \text{ER}), \quad (75)$$

with the superscript ( $r$ ) representing the ongoing iteration.

To avoid checkboard patterns and mesh dependent solutions, the projection filter  
 380 scheme, as proposed by Huang and Xie [51], is adopted. Firstly, the elemental sensi-  
 tivity numbers are transformed into nodal ones,  $\alpha_n$ , by setting,

$$\alpha_n = \sum_{i=1}^M \frac{1}{M-1} \left( 1 - \frac{r_{in}}{\sum_{i=1}^M r_{in}} \right) \alpha_i, \quad (76)$$

where  $M$  is the number of elements connected to the  $n$ th node and  $r_{in}$  is the distance  
 from the centroid of the  $i$ th element to the  $n$ th node (when  $M = 1$ ,  $\alpha_n = \alpha_i$ ). Then, the  
 recovery of the filtered  $\alpha_i$  values is performed in accordance with the number of nodes,  
 385  $G$ , that are inside the filter subdomain,

$$\alpha_i = \frac{\sum_{n=1}^G \max(0, r_{\text{min}} - r_{in}) \alpha_n}{\sum_{n=1}^G \max(0, r_{\text{min}} - r_{in})}, \quad (77)$$

with  $r_{\text{min}}$  being a mesh independent filter radius.

The historical averaging and the Min-Max normalization concepts [52] are also  
 considered, as stated in Eqs. (78) and (79), to enhance sensitivity stabilization effects,

$$\alpha_i^{(r)} = \frac{\alpha_i^{(r-1)} + \alpha_i^{(r)}}{2}, \quad (78)$$

$$\alpha_i^{(r)} = \frac{\alpha_i^{(r)} - \alpha_{\text{min}}^{(r)}}{\alpha_{\text{max}}^{(r)} - \alpha_{\text{min}}^{(r)}}, \quad (79)$$

390 where  $\alpha_{\text{max}}^{(r)}$  and  $\alpha_{\text{min}}^{(r)}$  are the maximum and minimum sensitivity number values of  
 iteration ( $r$ ), respectively. The convergence is reached by the attainment of  $\text{err} < 0.005$ ,  
 in Eq. (72), and the verification that  $V_p^{(r)} + V_e^{(r)} = V_p^f + V_e^f$ .

## 5. Numerical Results

In this section, numerical results regarding the newly proposed evolutionary method-  
 395 ology are presented and thoroughly discussed. The investigated closed-space configura-  
 tion is initially built as shown in Fig. 1, where the design domain is filled with poro-  
 elastic elements ( $\Omega_d = \Omega_p$ ) and the non-design domain is composed of fully modeled

acoustic and elastic ones ( $\Omega_{nd} = \Omega_a \cup \Omega_e$ ). It is remarked that the initial  $\Omega_d$  configuration is set to represent an acoustic region simulated by the UMP (Biot's equations degenerated to Helmholtz), hence being composed of nodes with three degrees of freedom each. The Polyurethane foam and Olefin sheet are, respectively, the poroelastic and elastic materials considered in all the cases (see Table 1).

The geometrical aspects of the studied system, Fig. 1(b), are defined as  $b = 1$  mm,  $D = 150$  mm and  $L_a = L_p = 50$  mm. The purely acoustic domains,  $\Omega_a$ , are filled with 1000 first-order quadrilateral elements each, while the purely elastic ones,  $\Omega_e$ , have 200 elements of the same type when considering both thin structures. In the poroelastic region,  $\Omega_p$ , 5000 elements are placed, which are first-order quadrilaterals of size  $1 \times 1.5$  mm<sup>2</sup>. Being mainly based on the appearance of a steep descent in the dissipated power level,  $PL_D$ , values of the initial configuration (see Fig. 3(b)), two different frequencies are targeted, that is 380 Hz and 430 Hz, as well as the entire multifrequency band encompassed between both. In this sense, the composite Simpson's numerical integration rule [53] is adopted to solve the integral existing in the objective function, Eq. (53), with a frequency step of 5 Hz. Still regarding this same equation, the switching variables  $\vartheta_1$ ,  $\vartheta_2$  and  $\vartheta_3$  that respectively account for the presence of  $\Pi_D^s$ ,  $\Pi_D^v$  and  $\Pi_D^t$ , if assuming unit values, or their absence when zeroed, are initially set as  $\vartheta_1 = \vartheta_2 = \vartheta_3 = 1$ . The BESO parameters are defined as  $ER = AR_{max} = 1\%$ ,  $r_{min} = 20$  mm,  $V_p^f = 60\%$ ,  $V_e^f = 5\%$ ,  $\zeta_1 = 2$  and  $\zeta_2 = 1$  for all cases.

This section is then divided into three main parts where, in the first, the optimized topologies, their evolutions and dissipated power levels are presented. As poroelastic and elastic materials are introduced in the design domain, which, in itself, already brings an increase of the general dissipative effects, the second part regards the comparison of the optimized designs with non-optimized geometries, referred here as baselines, as a way of investigating the effectiveness of the topologies found. Finally, the third one deals with several other combinations of powers as the objective function.

### 5.1. Dissipated power level as the objective function

Figure 3(a) shows the Top-F1, Top-F2 and Top-BD obtained topologies when considering, in a respectively manner, 380 Hz and 430 Hz as targeted frequencies, as well as the band that it is comprised between both. Henceforth, the gray areas are referred to poroelastic materials, while the light blue and black ones are attributed to acoustic and elastic domains, respectively. Fig. 3(b) presents the correspondent dissipated power levels of the optimized and initial configurations. Since the primary geometry is composed of two thin elastic structures, with acoustic regions filling the rest of the system (see Fig. 1), only contributions of a purely structural nature are visible, with particularly small values between 380 to 430 Hz. With the end of the optimization procedure, it is noticeable, in Fig. 3(a), that all topologies create poroelastic barriers on the left side of the design domain to enhance the dissipative effects in the impinging wave section. Such point is reinforced by the presence of acoustic holes in the center-to-right sides of  $\Omega_d$  and the appearance of elastic structures in small concentrated areas, mostly to provide structural stability to the overall system. As also highlighted in Fig. 3(b), the proposed approach is able to significantly enhance the  $PL_D$  function in all the cases treated, with the Top-BD configuration achieving the highest values in and out of the optimization band.

Another interesting point to note regards the type of dissipative effect that mainly causes the enhancements of  $\Pi_D$ . Figs. 3(c), (d) and (e) present such aspects, respectively for Top-F1, Top-F2 and Top-BD, where the total time-averaged dissipated power,  $\Pi_D$ , has been divided in its structural,  $\Pi_D^s$ , viscous,  $\Pi_D^v$ , and thermal,  $\Pi_D^t$ , portions and plotted along a wide frequency spectrum. In all obtained topologies, the structural aspect takes the lead in relation to other forms of dissipation, since it has an average of 85% of  $\Pi_D$ , being even higher after 430 Hz. The viscous portion is mostly influential at two different regions: around 50 Hz to 150 Hz, in which the structural power has a valley, and in the targeted frequency band, with the thermal aspects being mostly insignificant.

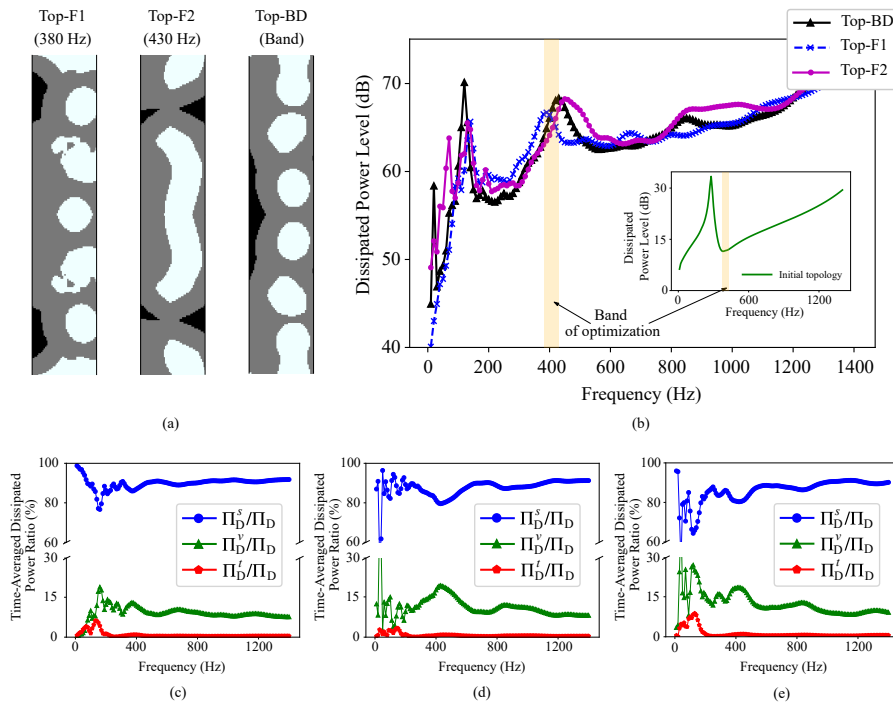


Figure 3: (a) One periodic topology design cells obtained when considering 380 Hz (Top-F1), 430 Hz (Top-F2) and the band of frequencies encompassed by the two (Top-BD), together with its (b) dissipated power levels. The time-averaged dissipated power ratios are also given for (c) Top-F1, (d) Top-F2 and (e) Top-BD

As previously reported by Dauchez et al. [54], the small influence of viscous and thermal effects can be attributed to the low constriction of the saturated fluid that composes the poroelastic domain; that is, the presence of an elastic layer between the acoustic excitation, that comes from the input region, and the porous section, in addition to the presence of infinitely periodic (or symmetric) boundaries, do not sufficiently constrain the fluid to enhance the particle frictions and vibrations. Furthermore, despite of polyurethane foam being highly porous, fact that increases its attenuation effects [55], it is known that the flow resistivity variable,  $\sigma$ , is usually the main indicator of vis-

cous actions in the low-frequency range, having a negative correlation with the overall thickness (when one goes up, the other goes down). Hence, since the polymeric foam here adopted has a quite stiff elastic skeleton ( $E_p = 2.67e5(1 + j\eta_p)$  Pa) and a considerable flow resistivity ( $\sigma = 7e4$  N s m<sup>-4</sup>), the increase in thickness would have to be significant for the viscous portion to be more expressive than the structural one.

Such findings can also be perceived by looking at Fig. 4 that shows the positions in which the dissipation mechanisms most occur within the design domain, followed by absolute pressure values,  $|p|$ , and the sum of the displacement amplitudes in the x and y directions,  $|u_x| + |u_y|$ . Calculating these aspects in 380 Hz, 430 Hz and in its frequency band, respectively for the Top-F1, Top-F2 and Top-BD topologies of Fig. 3(a), it is seen, in Figs. 4(a), (b) and (c), a high particle displacement in regions close to the left side poroelastic boundary, where the incoming wave is most strong, and close to the air holes, as the particles are more unconstrained (or free of particle packing). However, the elastic areas, filled with Olefin sheet material, seem to have little displacement, mostly due to the high stiffness of it. In this scenario,  $PL_D^s$  values are the biggest contributors to the general  $PL_D$ , especially because of the poroelastic skeleton movement. When looking at  $PL_D^v$  and  $PL_D^t$ , one may note a combination of pressure and displacements in the areas of high dissipation, with displacements improving more  $PL_D^v$  values, while pressure mildly augmenting  $PL_D^t$  (see also Eqs. (56) and (57)). Finally, it is important to state that  $PL_D^s$ ,  $PL_D^v$  and  $PL_D^t$  presented in Fig. 4 are obtained by the calculation of Eq. (38) for each element of the design domain and then of Eqs. (55), (56) and (57). Afterwards, such elemental values are relatively expressed by color in the contour plots, similarly to the procedures employed by Park et al. [56].

Figure 5 shows the evolutionary history of the mean dissipated power level,  $MPL_D$ , as well as intermediate topologies of interest regarding the Top-BD case. In the observed scenarios, a poroelastic material is firstly introduced in the system, causing the  $MPL_D$  to rapidly grow, as if the simple placement of a poroelastic barrier in the left region of  $\Omega_d$  would already be sufficient to greatly increase the objective function. With the observation of the next topologies, such as the ones from  $\textcircled{1}$  to  $\textcircled{4}$ , it is apparent that the porous material behaves in an irregular manner along the iterations, as the  $MPL_D$  varies harshly with simple changes of element types. Such aspect is still visible until the very last iteration of the evolutionary procedure, but with some softening when the elastic material finally reaches its final volume fraction, as can be seen in iterations 100 to 111, and in the little topological variability of  $\textcircled{5}$  to  $\textcircled{6}$ .

Notwithstanding the adoption of the proposed acoustic-poroelastic-elastic sequential methodology, together with the use of stabilization procedures, this behavior is also present in the majority of the optimizations here investigated. With the examination of previous studies, such as the ones conducted by Pereira et al. [29] who designed biphasic soundproof systems with pororigid and rigid elements, expressive oscillations are also noticed in those evolutionary processes, especially when rigid elements return to  $\Omega_d$  due to the use of manufacturing constraints. In the current investigation, a similar scenario is observed, i.e., there is the introduction, in a discrete manner, of poroelastic and elastic materials inside the acoustic design region, leading to fluctuations of the objective function of choice. Moreover, relatively high values of ER and  $AR_{\max}$  are here chosen, with the aim of accelerating the optimization process, thus recovering from the computational delays caused by the characteristic excess of degrees of freedom in  $\Omega_d$ .

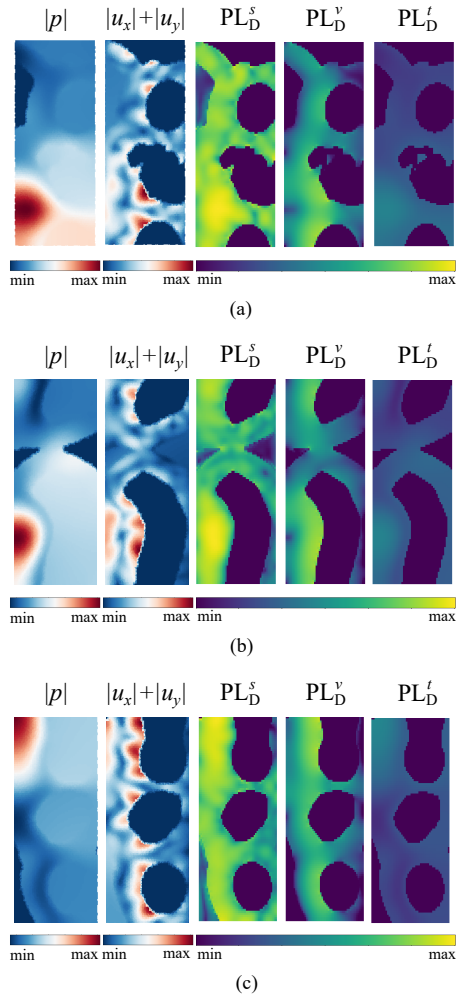
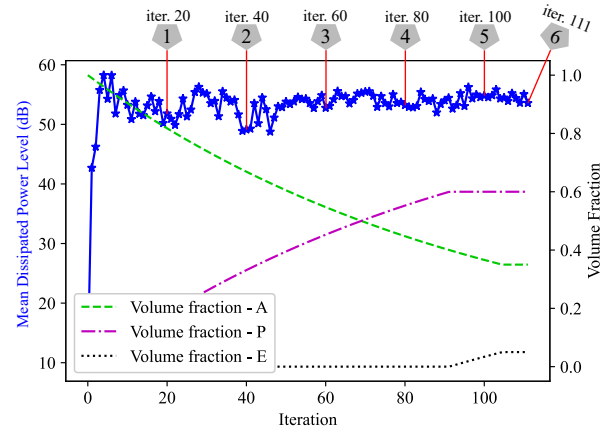


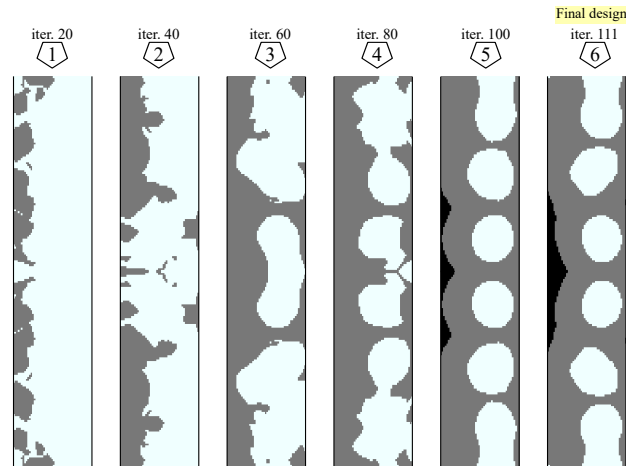
Figure 4: Dissipative power levels of structural,  $PL_D^s$ , viscous,  $PL_D^v$ , and thermal,  $PL_D^t$ , natures, as well as absolute pressure values,  $|p|$ , and the sum of displacement amplitudes in the x and y directions,  $|u_x| + |u_y|$ . One symmetric cell of the (a) Top-F1 topology, calculated in 380 Hz, (b) Top-F2 topology, determined in 430 Hz, and (c) Top-BD topology, obtained in the 380 to 430 Hz band, are considered

### 5.2. Comparison of the Top-BD configuration with baseline topologies

As this work deals with the introduction of poroelastic and elastic material elements in a  $\Omega_d$  full of air, it becomes interesting to compare  $PL_D$  values of the obtained topologies with the ones of some non-optimized structures, referred here as baselines. At this point, let A be acoustic, P poroelastic and E elastic elements. Hence, the baseline configurations adopted are of the form APEPA, EAPAE, PAEAP and EPAPE, with the materials being distributed in layers, as shown in Fig. 6(a), and with volume fractions of 60% of Polyurethane foam and 5% of Olefin sheet. In Fig. 6(b), the dissipated power



(a)



(b)

Figure 5: (a) Evolutionary history of the mean dissipated power level, (b) and intermediate topologies of interest, of the Top-BD case. The A, P and E letters used in the volume fraction descriptions regard acoustic, poroelastic and elastic materials, respectively

515 levels of such baselines and of the configuration Top-BD (Fig. 3(a)) are presented.

520 When looking at the detail shown in Fig. 6(b) regarding the results obtained in the band of optimization, it is clear that the Top-BD configuration shows the highest  $PL_D$  along the most part of the targeted frequencies, with a mean value of 66.4 dB, against 65.9 dB, 59.0 dB, 57.0 dB and 57.8 for the APEPA, EAPAE, PAEAP and EPAPE geometries, respectively. Nevertheless, it must be noted that EAPAE and APEPA reach high dissipative characteristics around 200 Hz and 300 Hz, mainly due to their thick poroelastic layer located in the middle of  $\Omega_d$  and the air gap that is placed between both poroelastic and elastic domains, which enhance losses of viscous and thermal nature

[57]. Such aspects are even more noted in the APEPA case by the combination of  
 525 poroelastic and elastic materials, increasing both stiffness and thickness of the overall  
 topology. In the PAEAP and EPAPE baselines, the poroelastic material is distributed,  
 with half of it in both  $\Omega_d$  extremities, lowering the viscous dissipation, but giving rise  
 to the powerful structural mechanisms of  $PL_D$  [54, 57], especially visible in highest  
 frequencies. The Top-BD topology seems then to combine such structural and viscous  
 530 effects, as the poroelastic material is not concentrated in one specific  $\Omega_d$  location, but  
 in an improved way, since brings the elevated  $PL_D$  values of PAEAP and EPAPE, that  
 happens around 600 Hz, to the band of optimization. Besides, Top-BD  $PL_D$  results are  
 better than the ones from PAEAP and EPAPE at lower frequencies, and than the ones  
 from APEPA and EAPAE in the highest spectrum.

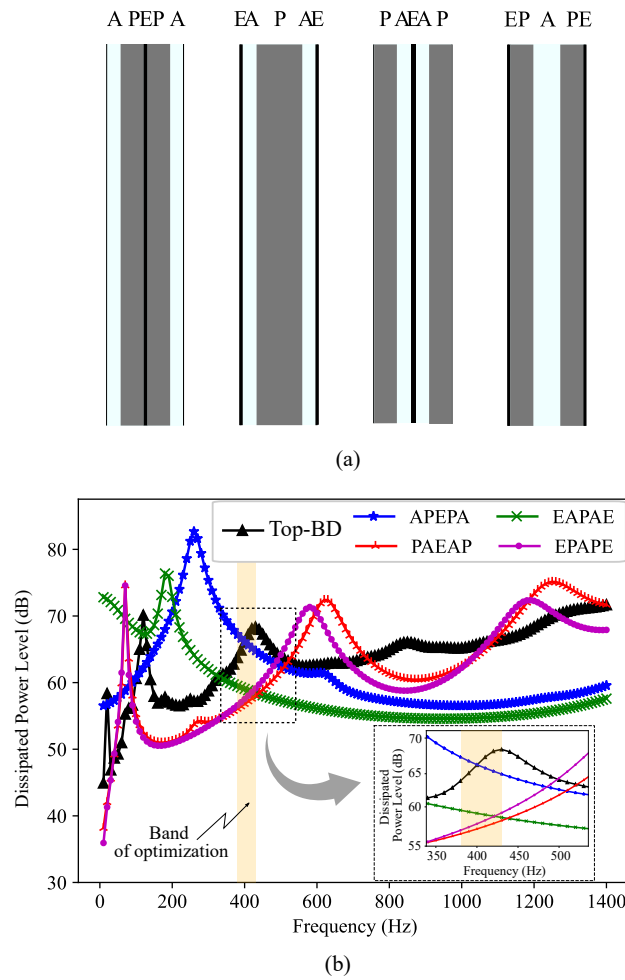


Figure 6: (a) Presentation of the baseline geometries considered, as well as (b) direct comparison of its dissipated power levels with the ones of the Top-BD configuration

### 5.3. Combinations of structural, viscous and thermal dissipative effects in the objective function

535

Aiming to investigate the unique influence that the structural,  $\Pi_D^s$ , viscous,  $\Pi_D^v$ , and thermal,  $\Pi_D^t$ , time-averaged dissipated power components, and its combinations, have on the proposed methodology, Fig. 7 is presented. For all the cases here treated, the band of frequencies comprised by 380 to 430 Hz is considered in the composition of Eq. (53). In this sense, Fig. 7(a) shows the topologies Top-S, Top-V, Top-SV, Top-ST and Top-VT obtained when taking into account, in a sequential manner, the following switching parameters:  $(\vartheta_1, \vartheta_2, \vartheta_3) = (1, 0, 0)$ ,  $(0, 1, 0)$ ,  $(1, 1, 0)$ ,  $(1, 0, 1)$ , and  $(0, 1, 1)$ . In Fig. 7(b) the dissipated power levels of all these topologies are displayed along with the results for the Top-BD case (see Fig. 3(a)), that in turn has a switching variable sequence of  $(\vartheta_1, \vartheta_2, \vartheta_3) = (1, 1, 1)$ . Finally, Table 2 present the mean values of  $\Pi_D^s/\Pi_D$ ,  $\Pi_D^v/\Pi_D$  and  $\Pi_D^t/\Pi_D$  calculated in the frequency band of optimization, while following the sequence of topologies of Fig. 7(a).

540

545

By looking at the configurations of Top-S, Top-SV and Top-ST, which respectively consider  $\Pi_D^s$ ,  $\Pi_D^s + \Pi_D^v$  and  $\Pi_D^s + \Pi_D^t$  in the objective function, material dispositions similar to those obtained in the Top-BD case are perceived, as well as comparable values of  $\Pi_D^s/\Pi_D$  and  $\Pi_D^v/\Pi_D$  shown in Table 2. The configuration in which a porous layer is established in the wave inlet region, along with the concentrated composition of Olefin sheet in areas connected to the thin elastic structures, promote a significant performance of  $\Pi_D^s$ , being responsible for more than 80% of  $\Pi_D$  in all cases. The Top-V and Top-VT topologies, that deals with  $\Pi_D^v$  and  $\Pi_D^v + \Pi_D^t$  in Eq. (53), present the highest values of  $\Pi_D^v$  (above 20%), being the compositions that most connect two different poroelastic layers inside  $\Omega_d$ ; either through a combination of thick porous and elastic material layers, either through several smaller polymeric connections. As expected, the structural dissipative percentage is reduced in these cases, reaching the lowest values observed in the study.

555

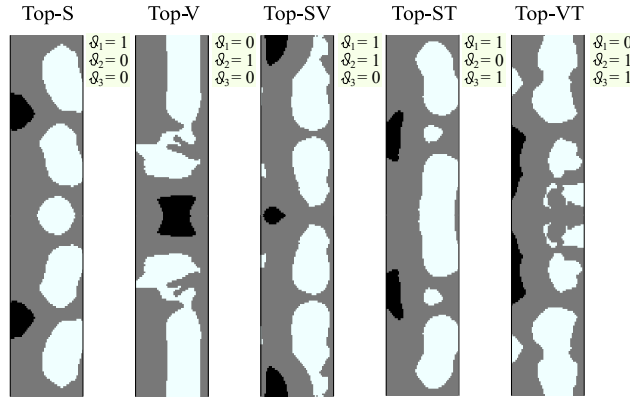
560

The enhanced viscous contributions are also perceived in the results shown in Fig. 7(b), with Top-VT being the topology that most increases  $PL_D$  in the optimization band. In this outline, both viscous and thermal effects have complementary mechanisms, helping to achieve higher dissipated power levels in the frequencies between 380 and 430 Hz. Finally, it is worth mentioning that the combination of all three dissipative mechanisms prove to be unfavorable, in a point of view of the maximization of general  $PL_D$  values, since the contributions of the viscous and thermal effects are more expressive in thicker layers than the ones obtained when considering the structural part. However, on a fabrication scenario, the Top-BD topology seems to be one of the most suitable for it.

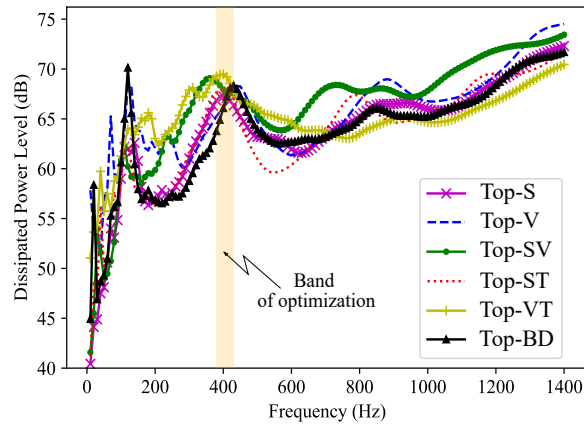
570

## 6. Conclusions

In many situations, simply filling spaces with porous foams may not be the most effective approach to enhance the dissipative performance of a system. Therefore, this work addressed the problem of designing closed-space soundproof systems, composed



(a)



(b)

Figure 7: Periodic design cells information obtained when considering the unique influence that the structural,  $\Pi_D^s$ , viscous,  $\Pi_D^v$ , and thermal,  $\Pi_D^t$ , time-averaged dissipated power components, and its combinations, have on the proposed methodology. (a) The topologies Top-S, Top-V, Top-SV, Top-ST and Top-VT are obtained when taking into account, in a sequential manner, the switching parameters  $(\vartheta_1, \vartheta_2, \vartheta_3) = (1, 0, 0), (0, 1, 0), (1, 1, 0), (1, 0, 1),$  and  $(0, 1, 1)$  in Eq. (53), for a frequency band that starts in 380 and ends in 430 Hz. (b) Dissipated power levels of all these topologies along with the results for the Top-BD case

575 of acoustic, poroelastic and elastic materials, for sound attenuation. A novel evolutionary  
 acoustic topology optimization methodology based on the BESO algorithm was  
 proposed, configuring a multiphase study of multiphysics nature. As part of the analy-  
 zes, the combination of the finite element method, the unified multiphase technique  
 and the mixed  $\mathbf{u}/p$  formulation was adopted, in order to simulate acoustic, poroelas-  
 580 tic and elastic domains with bases on Biot's expressions. The optimization problem  
 was then posed as to maximize the total dissipated power level, and different combina-  
 tions of its structural, viscous and thermal mechanisms, while respecting multiphysical  
 equilibrium equations and volume constraints.

Table 2: Mean values of time-averaged dissipated power ratios for the Top-S, Top-V, Top-SV, Top-ST, Top-VT and Top-BD topologies, when considering the frequency band that starts in 380 and ends in 430 Hz

Mean Power Ratios along 380 to 430 Hz Band	Resulted Topologies					
	Top-S	Top-V	Top-SV	Top-ST	Top-VT	Top-BD
$\Pi_D^s/\Pi_D$ (%)	84.55	77.48	84.63	82.94	77.45	80.63
$\Pi_D^v/\Pi_D$ (%)	14.60	21.02	14.47	16.00	21.41	18.47
$\Pi_D^t/\Pi_D$ (%)	0.85	1.50	0.90	1.06	1.14	0.90

As a general finding, poroelastic barriers were placed at the left  $\Omega_d$  side of the considered soundproof systems, enhancing the structural dissipative effects in the impinging wave section, at the cost of viscous and thermal ones. Nevertheless, such contributions were able to significantly increase dissipated power levels in all observed cases. When compared to the baselines, which are non-optimized configurations, the obtained Top-BD topology presented clear  $PL_D$  advantages in the band of optimization, and intermediary results when a broadband was considered.

In the multiple combination of structural, viscous and thermal dissipative effects study, topologies generated with focus on viscous aspects performed better, in a point of view of the maximization of  $PL_D$  values, than the ones considering structural mechanisms in the objective function. Nevertheless, on a fabrication perspective, these topologies seem to be filled with thin poroelastic compositions that may difficult practical applications. Finally, it must be pointed out that other common vibroacoustic indicators, such as insertion loss or mean quadratic velocities, have been left to be considered in future research.

### Acknowledgments

The authors would like to acknowledge the financial support given by the Fundação de Amparo à Pesquisa do Estado de São Paulo (FAPESP), project number 2013/08293-7, and by the Coordenação de Aperfeiçoamento de Pessoal do Nível Superior (CAPES), finance code 001.

### References

- [1] J. D. Miller, Effects of noise on people, *J. Acoust. Soc. Am.* 56 (3) (1974) 729–764. doi:10.1121/1.1903322.
- [2] EEA, Environmental noise in europe – 2020, Tech. Rep. 22, European Environment Agency, Luxembourg (2019).
- [3] J. P. Arenas, M. J. Crocker, Recent trends in porous sound-absorbing materials, *Sound Vib.* 44 (7) (2010) 12–17.
- [4] M. J. Crocker, *Handbook of Noise and Vibration Control*, first ed., John Wiley & Sons, Hoboken, New Jersey, 2007.

- [5] D. Oliva, V. Hongisto, Sound absorption of porous materials – accuracy of prediction methods, *Appl. Acoust.* 74 (12) (2013) 1473–1479. doi:<https://doi.org/10.1016/j.apacoust.2013.06.004>.  
615
- [6] L. Cao, Q. Fu, Y. Si, B. Ding, J. Yu, Porous materials for sound absorption, *Compos. Commun.* 10 (2018) 25–35. doi:[10.1016/j.coco.2018.05.001](https://doi.org/10.1016/j.coco.2018.05.001).
- [7] M. E. Delany, E. N. Bazley, Acoustical properties of fibrous absorbent materials, *Appl. Acoust.* 3 (2) (1970) 105–116. doi:[10.1016/0003-682X\(70\)90031-9](https://doi.org/10.1016/0003-682X(70)90031-9).
- [8] D. L. Johnson, J. Koplik, R. Dashen, Theory of dynamic permeability and tortuosity in fluid-saturated porous media, *J. Fluid Mech.* 176 (1987) 379–402. doi:[10.1017/s0022112087000727](https://doi.org/10.1017/s0022112087000727).  
620
- [9] Y. Champoux, J. Allard, Dynamic tortuosity and bulk modulus in air-saturated porous media, *J. Appl. Phys.* 70 (4) (1991) 1975–1979. doi:[10.1063/1.349482](https://doi.org/10.1063/1.349482).  
625
- [10] J. F. Allard, N. Atalla, *Propagation of Sound in Porous Media: Modelling Sound Absorbing Materials*, second ed., John Wiley & Sons, Hoboken, New Jersey, 2009.
- [11] M. A. Biot, Theory of propagation of elastic waves in a fluid-saturated porous solid. i. low-frequency range, *J. Acoust. Soc. Am.* 28 (1956) 168–178. doi:[10.1121/1.1908239](https://doi.org/10.1121/1.1908239).  
630
- [12] M. A. Biot, Theory of propagation of elastic waves in a fluid-saturated porous solid. ii. higher frequency range, *J. Acoust. Soc. Am.* 28 (1956) 179–191. doi:[10.1121/1.1908241](https://doi.org/10.1121/1.1908241).
- [13] O. Dazel, F. Sgard, F.-X. Becot, N. Atalla, Expressions of dissipated powers and stored energies in poroelastic media modeled by  $\{u, U\}$  and  $\{u, P\}$  formulations, *J. Acoust. Soc. Am.* 123 (4) (2008) 2054–2063. doi:[10.1121/1.2874520](https://doi.org/10.1121/1.2874520).  
635
- [14] I. Ekici, H. Bougdah, A review of research on environmental noise barriers, *Build. Acoust.* 10 (4) (2003) 289–323. doi:[10.1260/135101003772776712](https://doi.org/10.1260/135101003772776712).
- [15] C. Cai, C. M. Mak, Noise attenuation capacity of a helmholtz resonator, *Adv. Eng. Softw.* 116 (2018) 60–66. doi:<https://doi.org/10.1016/j.advengsoft.2017.12.003>.  
640
- [16] U. Ingard, Perforated facing and sound absorption, *J. Acoust. Soc. Am.* 26 (2) (1954) 151–154. doi:[10.1121/1.1907299](https://doi.org/10.1121/1.1907299).
- [17] G. Ji, Y. Fang, J. Zhou, X. Huang, Porous labyrinthine acoustic metamaterials with high transmission loss property, *J. Appl. Phys.* 125 (21) (2019) 215110. doi:[10.1063/1.5085880](https://doi.org/10.1063/1.5085880).  
645
- [18] G. Ji, Y. Fang, J. Zhou, Porous acoustic metamaterials in an inverted wedge shape, *Extreme Mech. Lett.* 36 (2020) 100648. doi:[10.1016/j.eml.2020.100648](https://doi.org/10.1016/j.eml.2020.100648).

- 650 [19] M.-A. Galland, B. Mazeaud, N. Sellen, Hybrid passive/active absorbers for flow ducts, *Appl. Acoust.* 66 (6) (2005) 691–708. doi:<https://doi.org/10.1016/j.apacoust.2004.09.007>.
- [20] M. P. Bendsøe, N. Kikuchi, Generating optimal topologies in structural design using a homogenization method, *Comput. Methods Appl. Mech. Eng.* 71 (2) (1988) 197–224. doi:[10.1016/0045-7825\(88\)90086-2](https://doi.org/10.1016/0045-7825(88)90086-2).
- 655 [21] M. P. Bendsøe, Optimal shape design as a material distribution problem, *Struct. Optim.* 1 (1989) 193–202. doi:[10.1007/bf01650949](https://doi.org/10.1007/bf01650949).
- [22] M. Zhou, G. I. N. Rozvany, The coc algorithm, part ii: Topological, geometrical and generalized shape optimization, *Comput. Methods Appl. Mech. Eng.* 89 (1-3) 660 (1991) 309–336. doi:[10.1016/0045-7825\(91\)90046-9](https://doi.org/10.1016/0045-7825(91)90046-9).
- [23] Y. Xie, G. P. Steven, Shape and layout optimization via an evolutionary procedure, in: *Proceedings of the international conference on computational engineering science*, 1992.
- [24] X. Huang, Y. M. Xie, Bi-directional evolutionary topology optimization of continuum structures with one or multiple materials, *Comput. Mech.* 43 (2009) 393–401. doi:[10.1007/s00466-008-0312-0](https://doi.org/10.1007/s00466-008-0312-0).
- 665 [25] E. Wadbro, M. Berggren, Topology optimization of an acoustic horn, *Comput. Methods Appl. Mech. Eng.* 196 (1–3) (2006) 420–436. doi:[10.1016/j.cma.2006.05.005](https://doi.org/10.1016/j.cma.2006.05.005).
- 670 [26] M. B. Dühring, J. S. Jensen, O. Sigmund, Acoustic design by topology optimization, *J. Sound Vib.* 317 (3–5) (2008) 557–575. doi:[10.1016/j.jsv.2008.03.042](https://doi.org/10.1016/j.jsv.2008.03.042).
- [27] J. Kook, K. Koo, J. Hyun, J. S. Jensen, S. Wang, Acoustical topology optimization for Zwicker’s loudness model – Application to noise barriers, *Comput. Methods Appl. Mech. Eng.* 237-240 (2012) 130–151. doi:[10.1016/j.cma.2012.05.004](https://doi.org/10.1016/j.cma.2012.05.004).
- 675 [28] K. Miyata, Y. Noguchi, T. Yamada, K. Izui, S. Nishiwaki, Optimum design of a multi-functional acoustic metasurface using topology optimization based on Zwicker’s loudness model, *Comput. Methods Appl. Mech. Eng.* 331 (2018) 116–137. doi:[10.1016/j.cma.2017.11.017](https://doi.org/10.1016/j.cma.2017.11.017).
- 680 [29] R. L. Pereira, H. N. Lopes, R. Pavanello, Topology optimization of acoustic systems with a multiconstrained beso approach, *Finite Elem. Anal. Des.* 201 (2022) 103701. doi:[10.1016/j.finel.2021.103701](https://doi.org/10.1016/j.finel.2021.103701).
- [30] J. W. Lee, Y. Y. Kim, Topology optimization of muffler internal partitions for improving acoustical attenuation performance, *Int. J. Numer. Meth. Eng.* 80 (4) 685 (2009) 455–477. doi:[10.1002/nme.2645](https://doi.org/10.1002/nme.2645).

- [31] K. S. Oh, J. W. Lee, Topology optimization for enhancing the acoustical and thermal characteristics of acoustic devices simultaneously, *J. Sound Vib.* 401 (2017) 54–75. doi:10.1016/j.jsv.2017.04.027.
- 690 [32] F. M. Azevedo, M. S. Moura, W. M. Vicente, R. Picelli, R. Pavanello, Topology optimization of reactive acoustic mufflers using a bi-directional evolutionary optimization method, *Struct. Multidiscipl. Optim.* 58 (2018) 2239–2252. doi:10.1007/s00158-018-2012-5.
- 695 [33] R. L. Pereira, H. N. Lopes, M. S. Moura, R. Pavanello, Multi-domain acoustic topology optimization based on the beso approach: applications on the design of multi-phase material mufflers, *Struct. Multidiscipl. Optim.* 66 (1) (2023) 25. doi:10.1007/s00158-022-03479-4.
- [34] F. I. Silva, R. Pavanello, Synthesis of porous-acoustic absorbing systems by an evolutionary optimization method, *Eng. Optim.* 42 (10) (2010) 887–905. doi:10.1080/03052150903477184.
- 700 [35] G. H. Yoon, Acoustic topology optimization of fibrous material with delany-bazley empirical material formulation, *J. Sound Vib.* 332 (5) (2013) 1172–1187. doi:10.1016/j.jsv.2012.10.018.
- [36] W. U. Yoon, J. H. Park, J. S. Lee, Y. Y. Kim, Topology optimization design for total sound absorption in porous media, *Comput. Methods Appl. Mech. Eng.* 360 (2020) 112723. doi:10.1016/j.cma.2019.112723.
- 705 [37] C. B. Dilgen, S. B. Dilgen, N. Aage, J. S. Jensen, Topology optimization of acoustic mechanical interaction problems: a comparative review, *Struct. Multidiscipl. Optim.* 60 (2019) 779–801. doi:10.1007/s00158-019-02236-4.
- 710 [38] V. T. Ramamoorthy, E. Özcan, A. J. Parkes, A. Sreekumar, L. Jaouen, F.-X. Bécot, Comparison of heuristics and metaheuristics for topology optimisation in acoustic porous materials, *J. Acoust. Soc. Am.* 150 (4) (2021) 3164–3175. doi:10.1121/10.0006784.
- [39] T. Yamamoto, S. Maruyama, S. Nishiwaki, M. Yoshimura, Topology design of multi-material soundproof structures including poroelastic media to minimize sound pressure levels, *Comput. Methods Appl. Mech. Eng.* 198 (17-20) (2009) 1439–1455. doi:10.1016/j.cma.2008.12.008.
- 715 [40] J. S. Lee, Unified multi-phase modeling and topology optimization for complex vibro-acoustic systems consisting of acoustic, poroelastic and elastic media, Ph.D. thesis, School of Mechanical and Aerospace Engineering, The Graduate School, Seoul National University (2009).
- 720 [41] J. S. Lee, Y. J. Kang, Y. Y. Kim, Unified multiphase modeling for evolving, acoustically coupled systems consisting of acoustic, elastic, poroelastic media and septa, *J. Sound Vib.* 331 (25) (2012) 5518–5536. doi:10.1016/j.jsv.2012.07.027.
- 725

- [42] J. S. Lee, P. Göransson, Y. Y. Kim, Topology optimization for three-phase materials distribution in a dissipative expansion chamber by unified multiphase modeling approach, *Comput. Methods Appl. Mech. Eng.* 287 (2015) 191–211. doi:10.1016/j.cma.2015.01.011.
- 730 [43] N. Atalla, M. A. Hamdi, R. Panneton, Enhanced weak integral formulation for the mixed (u,p) poroelastic equations, *J. Acoust. Soc. Am.* 109 (6) (2001) 3065–3068. doi:10.1121/1.1365423.
- [44] J. Hu, S. Yao, X. Huang, Topological design of sandwich structures filling with poroelastic materials for sound insulation, *Finite Elem. Anal. Des.* 199 (2022) 103650. doi:10.1016/j.finel.2021.103650.
- 735 [45] J. Hu, S. Yao, X. Huang, Topology optimization of dynamic acoustic–mechanical structures using the ersatz material model, *Comput. Method Appl. Mech. Eng.* 372 (2020) 113387. doi:10.1016/j.cma.2020.113387.
- [46] F.-X. Bécot, L. Jaouen, An alternative biot’s formulation for dissipative porous media with skeleton deformation, *J. Acoust. Soc. Am.* 134 (6) (2013) 4801. doi:10.1121/1.4826175.
- 740 [47] F. C. Sgard, X. Olny, N. Atalla, F. Castel, On the use of perforations to improve the sound absorption of porous materials, *Appl. Acoust.* 66 (6) (2005) 625–651. doi:10.1016/j.apacoust.2004.09.008.
- [48] F. C. Sgard, N. Atalla, J. Nicolas, A numerical model for the low frequency diffuse field sound transmission loss of double-wall sound barriers with elastic porous linings, *J. Acoust. Soc. Am.* 108 (6) (2000) 2865–2872. doi:10.1121/1.1322022.
- 745 [49] R. Das, R. Jones, Y.-M. Xie, Optimal topology design of industrial structures using an evolutionary algorithm, *Optim. Eng.* 12 (4) (2011) 681–717. doi:10.1007/s11081-010-9132-0.
- [50] H. N. Lopes, D. C. Cunha, R. Pavanello, J. Mahfoud, Numerical and experimental investigation on topology optimization of an elongated dynamic system, *Mech. Syst. Signal Process.* 165 (2022) 108356. doi:https://doi.org/10.1016/j.ymsp.2021.108356.
- 755 [51] X. Huang, Y. M. Xie, Convergent and mesh-independent solutions for the bi-directional evolutionary structural optimization method, *Finite Elem. Anal. Des.* 43 (14) (2007) 1039–1049. doi:10.1016/j.finel.2007.06.006.
- [52] E. L. Zhou, Y. Wu, X. Y. Lin, Q. Q. Li, Y. Xiang, A normalization strategy for beso-based structural optimization and its application to frequency response suppression, *Acta Mech.* 232 (2021) 1307–1327. doi:10.1007/s00707-020-02862-w.
- 760 [53] K. E. Atkinson, *An Introduction to Numerical Analysis*, second ed., John Wiley & Sons, Hoboken, New Jersey, 1989.

- <sup>765</sup> [54] N. Dauchez, S. Sahraoui, N. Atalla, Investigation and modelling of damping in a plate with a bonded porous layer, *J. Sound Vib.* 265 (2) (2003) 437–449. doi: 10.1016/S0022-460X(02)01454-2.
- [55] P. N. J. Rasolofosaon, Plane acoustic waves in linear viscoelastic porous media: Energy, particle displacement, and physical interpretation, *J. Acoust. Soc. Am.* <sup>770</sup> 89 (4) (1991) 1532–1550. doi:10.1121/1.400989.
- [56] J. H. Park, J. S. Lee, Y. Y. Kim, Directional quantification of power dissipation in sound-absorbing metaporous layers, *J. Sound Vib.* 512 (2021) 116375. doi: 10.1016/j.jsv.2021.116375.
- <sup>775</sup> [57] N. Atalla, R. Panneton, The effects of multilayer sound-absorbing treatments on the noise field inside a plate backed cavity, *Noise Control Eng. J.* 44 (5) (1996) 235–243. doi:10.3397/1.2828408.

## 7 | Discussion

Topology optimization techniques, combined with the finite element method, have been part of the structural design methodologies for more than 30 years, being present in the most diverse engineering applications. With the current programming packages and modern commercial/open-source software, the simulation of structures has reached unprecedented levels. It is worth noting that such methods require little financial resources if compared to the predictive benefits they can bring. Despite these significant advances, the design of sound insulation systems by evolutionary topology optimization approaches is still an object of limited attention, which motivated the author to thoroughly explore such field of research in many different scenarios.

Hence, this chapter presents further discussions on the topics and results brought in the papers entitled “Topology optimization of acoustic systems with a multiconstrained BESO approach” by Rodrigo Lima Pereira, Heitor Nigro Lopes and Renato Pavanello, fully presented in Chapter 4 and referred here as  $\mathcal{A}1$  (or Application 1); “Multi-domain acoustic topology optimization based on the BESO approach: applications on the design of multi-phase material mufflers” by Rodrigo Lima Pereira, Heitor Nigro Lopes, Marcio da Silva Moura and Renato Pavanello, fully presented in Chapter 5 and referred here as  $\mathcal{A}2$  (or Application 2); “Evolutionary topology optimization approach to design multiphase soundproof systems with poroelastic media” by Rodrigo Lima Pereira, Lidy Marcela Anaya Jaimes and Renato Pavanello, fully presented in Chapter 6 and referred here as  $\mathcal{A}3$  (or Application 3).

### 7.1 Number of Elements per Wavelength and Mesh Configuration

Firstly, it is important to note that the maximum frequencies here considered have been chosen based on the observed spectrum. For the acoustic metasurface application of paper  $\mathcal{A}1$  the maximum frequency is 4000 Hz. Hence, the entire region has approximately 68 elements/per x axial wavelength and element size of 0.00125 m in the x direction. For the poro-acoustic

application of the same paper the maximum frequency is 2000 Hz, meaning that the entire region has approximately 171 elements/per x axial wavelength and element size of 0.001 m in the x direction. The meshes considered in both problems are respectively illustrated in Figs. 7.1 and 7.2.

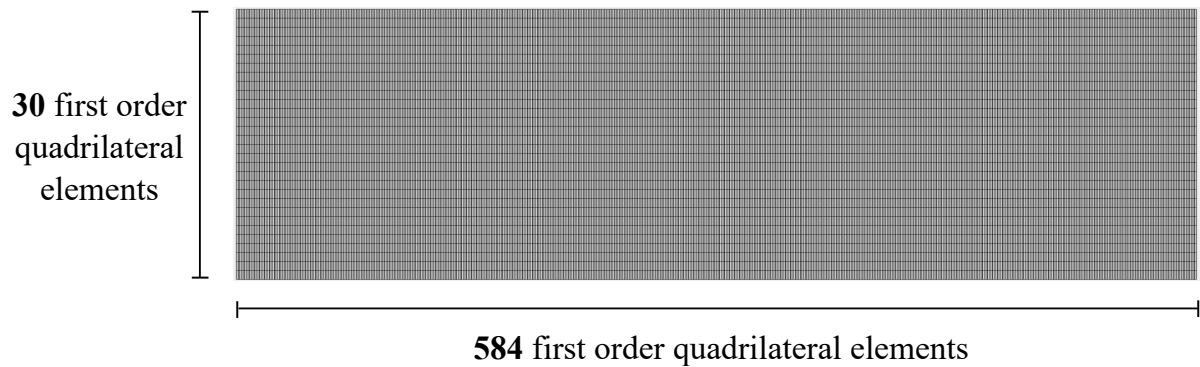


Figure 7.1 – Mesh configuration of Problem 1 – Application 1

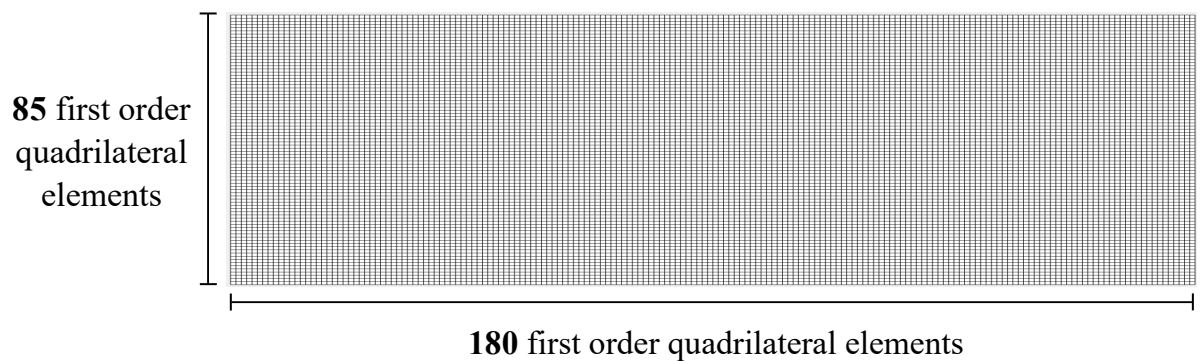


Figure 7.2 – Mesh configuration of Problem 2 – Application 1

For the one-chamber muffler application of paper  $\mathcal{A}2$  the maximum frequency is considered to be 1400 Hz, in a way that the entire region has approximately 49 elements/per x axial wavelength and element size of 0.005 m in the x direction. In this methodology, as the domain increases, the number of elements per wavelength remains the same. Furthermore, for the multiphysics application of paper  $\mathcal{A}3$  the maximum frequency is also considered to be 1400 Hz. This entails in an acoustic region of approximately 49 elements/per x axial wavelength, with element size of 0.005 m in the x direction, an elastic region of approximately 245 elements/per x axial wavelength, with element size of 0.001 m in the x direction, and a poroelastic region of approximately 245 elements/per x axial wavelength, with element size of 0.001 m in the x direc-

tion. The mesh configuration for the one-chamber muffler scenario, Application 2, is presented in Fig. 7.3, while the mesh considered in Application 3 is illustrated in Fig. 7.4.

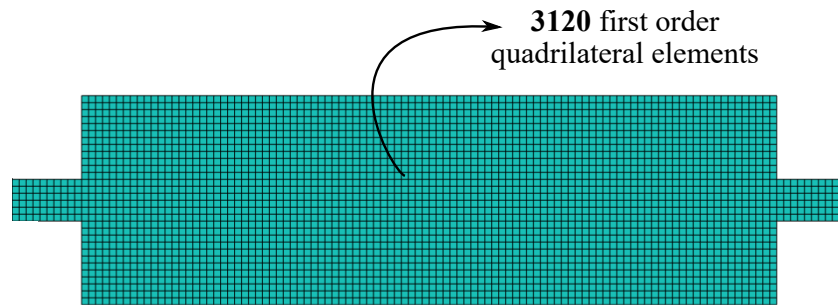


Figure 7.3 – Mesh configuration of Application 2

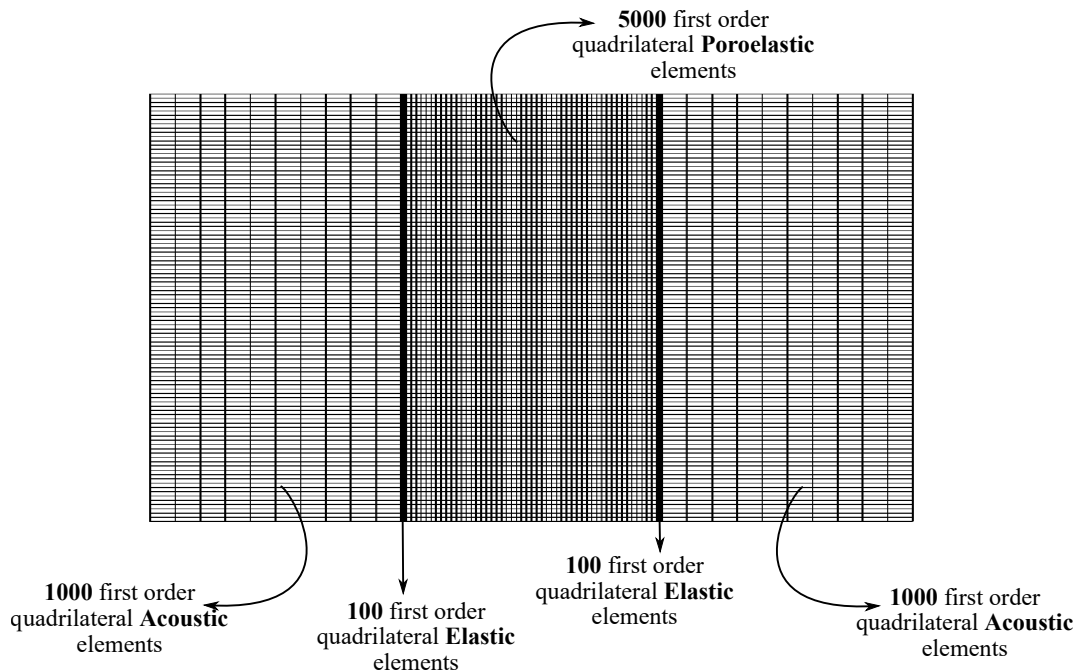


Figure 7.4 – Mesh configuration of Application 3

## 7.2 Definition of Target Volume Fractions

In general topology optimization problems one of the key factors is to set the volume of the final design. In the cases observed in paper  $\mathcal{A}1$ , the general geometries were based on previous works, such as the ones conducted by [Miyata \*et al.\* \(2018\)](#), for the metasurface design, and [Silva and Pavanello \(2010\)](#), for the poro-acoustic study. Since both applications made use of additional constraints to enhance the manufacturability, it would be interesting to observe how the topologies would behave in situations where the volume remained the same,

as well as it is reduced along the iterations. Therefore, the methodological choice was made to keep the volume fractions constant in the first application, while reducing it in the second. It is noteworthy that the reduction to 90% of  $\Omega_d$  was adopted in the second application so that it could be compared to [Silva Júnior \(2007\)](#) and [Silva and Pavanello \(2010\)](#) results. Besides, the constant value of 50% of  $\Omega_d$  was chosen in the design of acoustic metasurfaces only for the purposes of observing if internal holes would naturally appear with the “spreading” of the barrier inside the design domain, which actually happened, and how the manufacture constraint would deal with such effect.

Moreover, along the development of the methodology detailed in paper  $\mathcal{A}3$ , a few different volume fraction,  $V^f$ , values were tested, such as  $V_p^f = 40\%$ ,  $V_p^f = 50\%$  and  $V_p^f = 60\%$  of porous materials, in relation to the design domain volume, while keeping  $V_e^f = 5\%$  of elastic material in all the analysis. By considering  $V_p^f = 40\%$  or  $V_p^f = 50\%$  as the final volume fraction of the porous domain, most topologies presented a scattered configuration (formation of material islands) of both porous and elastic structures throughout the design domain, especially after the introduction of the elastic phase. With the adoption of  $V_p^f = 60\%$ , however, the inclusion of elastic structures in the porous design space actually enhanced the stabilization of the composition, since the elastic phase was compactly organized to increase the stiffness of the overall design. This motivated the choice of such value to compose the methodology. For the works presented in paper  $\mathcal{A}2$ , similar discussions are given in its Section 5.1 (see Figs. 6 and 7 of paper  $\mathcal{A}2$ ).

### 7.3 Computational Costs of the Multidomain/Multiphase Application

The current  $\mathcal{A}2$  methodology expands  $n$  times the basic acoustic domain (the one-chamber muffler), and its building elements, to compose the multi-domain system. This, by itself, already represents an increase of the computational costs related to each domain expansion. Moreover, in an effort to enhance the stability of the evolutionary process, the porous material is firstly introduced in the design domain to only then include the rigid elements, which stands for the multi-phase part of the methodology (see section 4.3 of paper  $\mathcal{A}2$  for more details on this matter).

In a general setting, the entire process takes about 240 and 70 iterations to include the 20% of porous and 5% of rigid materials, respectively, totaling 310 iterations in average. For a basic computer with an Intel® Core™ i7-8550U CPU @ 1.80GHz, 16.00 GB of RAM and NVIDIA GeForce MX150 graphics card with dedicated memory of 4GB GDDR4, the single-chamber muffler case (3120 first order quadrilateral elements of size 5 mm) leads to a run time

of 921 seconds, while the cases for 6240 and 9360 elements of the same type and size leads to the run times of 2826 and 5794 seconds. Its worth mentioning that the Matlab<sup>®</sup> software was here considered without any kind of parallel computing.

It is importante to note that these times may vary broadly, depending on the application (mufflers were chosen in this case), the BESO variables (such as ER,  $AR_{\max}$  and filters), the computer specifications and so on. What is interesting to know here, however, is that the run times are somewhat tripled when one more domain is added, which can be related not only to the increase in the number of elements, but also to the increase in the amount of porous and rigid materials that are introduced and their influence in the objective function evolution. Since the purpose of this work is not necessarily to provide computational performance improvement strategies to the muffler configuration in particular, more studies on this matter are to be included in future research.

#### **7.4 Performance Against Design Complexity of the Multiphysics Application**

During the  $\mathcal{A}3$  study the main goal was to propose a methodology that would entail the interplay of multiphysical domains throughout an evolutionary topology optimization process. To achieve this, a combination of the BESO method and the Unified Multiphase modeling approach was employed to account for the interactions between different domains, without the need to track element boundaries throughout the iterative process. Consequently, a set of topologies was obtained that maximized the dissipated power level at particular frequencies and bands. Furthermore, these optimized topologies were compared with a few parametrically obtained configurations, called baselines, to assess its capabilities.

The topologies obtained through parametric methods that included thick porous regions showed relevant results at low frequencies due to the high viscous dissipation present in such configurations, but lower values in the higher spectrum. Within this same set of results, those that included separate porous materials tended to be relevant mostly at medium to higher frequencies, within the observed bandwidth. As a combination of these two, the topologies found from the proposed methodology were able to achieve the best dissipated power values within the optimization band (between 380 and 430 Hz) and an intermediate behavior compared to those found through parametric methods, that is, intermediary dissipative levels in both lower and higher frequency spectra, while maintaining a high degree of manufacturability. Thus, the topologies found by the proposed method can be quite useful for applications that require sound dissipation over a wide range of frequencies.

## 8 | Concluding Remarks

Throughout this work, comprehensive information about evolutionary optimization methods were provided, while sougning to expand the concept to several applications involving different materials, physics, domains and frequencies. Moreover, a broad theoretical basis regarding multiphysics interactions was presented, not only encompassing expressions of acoustic or elastic nature, such as the scalar Helmholtz and the linear elastodynamic ones, but also presenting the highly complex equations and concepts that are relevant to the understanding of fluid-structure interactions. Here, the explicit interactions that occur between purely acoustic and elastic domains was detailed, as well as the implicit ones that happen in the simulation of poroelastic materials. The simultaneous interactions between all these domains were also discussed, further increasing the degree of difficulty of the application.

In Chapter 1 the problem involving excessive noise was presented, together with brief discussions about the various health issues that continued exposure to such levels can cause. A few questions were then raised regarding the performance enhancements that porous (pororigid or poroelastic) and elastic/rigid materials could provide to sound attenuation systems, in order to create environments with greater acoustic comfort. The suggestion of using topology optimization methods to help solve this problem was posed. Such methodologies were concisely introduced, with highlights given to evolutionary methods, since these were the subject of this work.

The general vibroacoustic systems governing equations were presented in Chapter 2, detailing the main conditions for the use of Helmholtz, Biot's and elastodynamic equations, as well as the boundary information involved in the studied compositions. These discussions were part of the theoretical background provided for this work, and represent an expansion of the information provided in all sections number 2 of the embedded papers. The theoretical background also encompassed Chapter 3, which introduced the Bi-directional Evolutionary Structural Optimization methodology applied in the solution of the compliance minimization problem. Here, the main parts of the approach, such as material interpolation schemes, sen-

sitivity analysis, mesh-independent filters, stabilization and normalization procedures, update schemes and stop criteria were explored, and further condensate in a BESO flowchart illustration.

The novelties brought in this work were mainly presented in the embedded papers that composed Chapters 4, 5 and 6. Using the basic BESO approach, some optimized topologies presented internal air holes, which brought problems concerning the rigid material hypothesis and the manufacturability of the obtained structures. This motivated the addition of the Virtual Temperature Method (VTM) as a connectivity constraint, expanding the BESO algorithm to a multiconstrained form, shown in Chapter 4. In this approach, bi-phase optimizations were considered, being the first one composed of acoustic and rigid elements, and the second of poro-rigid (simulated by the Johnson–Champoux–Allard formulations) and acoustic. Particularly in the former analysis, rigid-acoustic metasurfaces were designed for minimization of Sound Pressure Levels (SPL) in specific domain regions. They presented well defined topologies, with no air inclusions, high manufacturability and reduced SPL values in the frequencies targeted. Additionally, the trade-off between the amount of wind that is able to pass through the metasurface holes and its soundproofing effects was successfully established for all cases. It is remarked that the above study sought to answer the question posed in the introduction about how rigid structures should be built to increase acoustic comfort, while maintaining permissibility.

In the latter application, a coupled poro-acoustic absorptive system was investigated, aiming to maximize the sound absorption coefficient of the considered porous material, while adopting the VTM as a connectivity constraint. In a direct comparison with the available literature, it was noted that the obtained topologies presented slightly lower sound absorption coefficient values in the target frequencies of optimization, due to the additional constraint imposed by the VTM. Nonetheless, this same fact also contributed to the improved performances of the obtained topologies in low-to-mid frequency ranges. A common feature of most multiconstrained problems here solved regarded the increase of the iterations required to convergence. The material reorganization that was imposed by the VTM proved to be computationally expensive, and, especially when rigid materials were involved, difficult to converge. However, the method succeeded in provide topologies free of air hole seclusion, easy to manufacture and with enhanced characteristics in all the applications considered.

Chapter 5 regarded the design of muffler chambers composed of up to three distinct materials for enhancement of transmission loss values in a broad range of frequencies. The BESO method was extended to encompass not only a multiphase application, by the proposition of a novel material interpolation scheme that systematically reproduced acoustic, porous and rigid material phases, but also to investigate multiple domains in a methodology called

mdBESO. Rigid and porous materials with rigid frame were approximated by the over amplification of acoustic properties and by the JohnsonChampouxAllard formulations, respectively. A common trait of these analyzes regarded the consideration of three different frequency bands in the objective function calculation, being chosen in a way that each of them comprised one of the three first horizontal eigenfrequencies of a nominal expansion chamber muffler.

The bi-phase acoustic-rigid and acoustic-pororigid optimization result showed to be strongly depend on the lowest frequencies comprehended by the corresponding target bands, being, therefore, consistent with results from the literature. The acoustic-pororigid-rigid designs presented clear combinations of the acoustic-rigid and acoustic-pororigid analyzes, without the need for further manipulations to obtain porous materials wrapped around rigid structures. In all these outcomes, the breakage of acoustic modes was perceptible, leading the topologies to deviate the lowest frequencies to regions far from the ones of interest. When comparing the mdBESO with two additional BESO-based settings, named as BESO-C (union of separately optimized muffler chambers) and BESO-F (all domains are considered as design region), it was noted that the influence of the connecting tube nodal lines gave the mdBESO results enhanced effectiveness in the attenuation of sound regarding the BESO-C ones, while also being more stable than BESO-F.

Finally, Chapter 6 addressed the problem of designing closed-space systems, composed of acoustic, poroelastic and elastic materials, for sound attenuation. The finite element method, the Unified Multiphase technique and the mixed u/p formulation were combined to simulate the behavior of all these materials, while based on Biot's expressions. Besides, novel material interpolation schemes were proposed to encompass the multiphysics elemental changes throughout the iterative procedure. The optimization problem was posed as to maximize the total dissipated power level, and different combinations of its structural, viscous and thermal mechanisms, while respecting multiphysical equilibrium equations and volume constraints. In general, poroelastic barriers were placed at the left side of the design domain, enhancing structural dissipative effects in the impinging wave section, at the cost of viscous and thermal ones. Nevertheless, such contributions were able to significantly increase dissipated power levels in all observed cases. When compared to non-optimized structures, known as baselines, the obtained topologies presented higher dissipative effects in the target frequency band. To the best of the author's knowledge, such investigations were not conducted before. These last two chapters also tried to answer the question related with the proper arrangement of porous and elastic/rigid materials to reduce general noise levels, also posed at the introductory discussion. It is worth to point out that several counter-intuitive, manufacturable, highly effective and novel topology optimizations for sound attenuation were presented as result of all the aforementioned analyzes.

Despite the fact that the proposed modifications to the standard BESO method proved to be adequate not only to structural, but also to acoustic applications with multiple materials, domains, physics and frequencies, further discussions were presented in Chapter 7, highlighting the conditions adopted in the overall investigations. On that scenario, studies on broader aspects are still needed in order to make the current propositions be fully considered for real-world applications. Hence, future research directions may be given as to:

- Investigate the optimal size of air holes and their repercussions on the airflow throughout the optimization problem in the metasurfaces scenario;
- Obtain global values of VTM variables, in order to broaden the applications presented in Chapter 4 for other acoustic settings;
- Investigate the computational costs of the VTM implementation in different domain applications;
- Broaden the acoustic multiconstrained methodology to encompass multi-materials, as well as develop a composed VTM for such multiphase setting;
- Include the search for the optimal domain disposition in the mdBESO algorithm;
- Include the possibility of considering mean flow, thermal loads and perforated tubes in the mdBESO algorithm;
- Apply the mdBESO algorithm in other acoustic systems, including multiscale analysis and different boundary conditions;
- Investigate alternatives to reduce the computational costs involved in the mdBESO methodology;
- Consider other objective functions, such as transmission loss, absorption coefficient and sound pressure levels, in the design of acoustic-poroelastic-elastic systems to investigate which vibroacoustic indicator better contributes to the reduction of noise in predefined regions;
- Expand the above methodologies to the 3D scenario by combining commercial or open-source softwares with the ones here adopted;
- Build and test 3D printed prototypes experimentally.

# Bibliography

Aage, N.; Andreassen, E.; Lazarov, B. S.; Sigmund, O. Giga-voxel computational morphogenesis for structural design. **Nature**, v. 550, p. 84–86, 2017.

Allaire, G.; Jouve, F.; Toader, A.-M. A level-set method for shape optimization. **Comptes Rendus Mathématique**, v. 334, n. 12, p. 1125–1130, 2002.

Allard, J. F.; Atalla, N. **Propagation of Sound in Porous Media: Modelling Sound Absorbing Materials**. Second ed. New Jersey: John Wiley & Sons, 2009. ISBN 978-0-470-74661-5.

Almeida, B. V. de; Cunha, D. C.; Pavanello, R. Topology optimization of bimorph piezoelectric energy harvesters considering variable electrode location. **Smart Materials and Structures**, v. 28, n. 8, p. 085030, 2019.

Anaya-Jaimes, L. M.; Vicente, W. M.; Pavanello, R. Metamaterials design with a desired thermal expansion using a multi-material beso method. **Structural and Multidisciplinary Optimization**, v. 65, n. 12, p. 355, 2022.

Arora, R. K. **Optimization: Algorithms and Applications**. First ed. Florida: CRC Press, Taylor & Francis Group, 2015. ISBN 978-1-4987-2115-8.

Atalla, N.; Hamdi, M. A.; Panneton, R. Enhanced weak integral formulation for the mixed (u,p) poroelastic equations. **Journal of the Acoustical Society of America**, v. 109, n. 6, p. 3065–3068, 2001.

Atalla, N.; Panneton, R.; Debergue, P. A mixed displacement-pressure formulation for poroelastic materials. **Journal of the Acoustical Society of America**, v. 104, n. 3, p. 1444–1452, 1998.

Atalla, N.; Sgard, F. **Finite Element and Boundary Methods in Structural Acoustics and Vibration**. First ed. Florida: CRC Press, 2015. ISBN 9781138749177.

Azevedo, F. M.; Moura, M. S.; Vicente, W. M.; Picelli, R.; Pavanello, R. Topology optimization of reactive acoustic mufflers using a bi-directional evolutionary optimization method. **Structural and Multidisciplinary Optimization**, v. 58, p. 2239–2252, 2018.

Bala, M.; Verma, D. Investigation & examination of noise pollution - definition, sources, effects, monitoring and control. **International Journal of Research in Social Sciences**, v. 10, n. 07, p. 182–207, 2020.

Bazaraa, M. S.; Sherali, H. D.; Shetty, C. M. **Nonlinear Programming: Theory and Algorithms**. Third ed. New Jersey: John Wiley & Sons, 2006. ISBN 978-0-471-48600-8.

Bendsøe, M. P. Optimal shape design as a material distribution problem. **Structural Optimization**, v. 1, p. 193–202, 1989.

Bendsøe, M. P.; Kikuchi, N. Generating optimal topologies in structural design using a homogenization method. **Computer Methods in Applied Mechanics and Engineering**, v. 71, n. 2, p. 197–224, 1988.

Bendsøe, M. P.; Sigmund, O. Material interpolation schemes in topology optimization. **Archive of Applied Mechanics**, v. 69, p. 635–654, 1999.

Bendsøe, M. P.; Sigmund, O. **Topology Optimization: Theory, Methods, and Applications**. Second ed. Berlin: Springer-Verlag, 2004. ISBN 978-3-662-05086-6.

Biot, M. A. Theory of propagation of elastic waves in a fluidsaturated porous solid. i. lowfrequency range. **Journal of the Acoustical Society of America**, v. 28, p. 168–178, 1956.

Biot, M. A. Theory of propagation of elastic waves in a fluidsaturated porous solid. ii. higher frequency range. **Journal of the Acoustical Society of America**, v. 28, p. 179–191, 1956.

Biot, M. A.; Willis, D. G. The elastic coefficients of the theory of consolidation. **Journal of Applied Mechanics**, v. 24, n. 4, p. 594–601, 1957.

Birgitta, B.; Lindvall, H. **A Draft Document of Community Noise**. London, 1995.

Bourdin, B.; Chambolle, A. Design-dependent loads in topology optimization. **ESAIM: Control, Optimisation and Calculus of Variations**, v. 9, p. 19–48, 2003.

Bruns, T. E.; Tortorelli, D. A. Topology optimization of non-linear elastic structures and compliant mechanisms. **Computer Methods in Applied Mechanics and Engineering**, v. 190, n. 26–27, p. 3443–3459, 2001.

Bécot, F.-X.; Jaouen, L. An alternative biot's formulation for dissipative porous media with skeleton deformation. **Journal of the Acoustical Society of America**, v. 134, n. 6, p. 4801, 2013.

Cao, L.; Fu, Q.; Si, Y.; Ding, B.; Yu, J. Porous materials for sound absorption. **Composites Communications**, v. 10, p. 25–35, 2018.

Cavalcante, F.; Ferrite, S.; Meira, T. C. Exposure to noise in the manufacturing industry in brazil. **Revista CEFAC**, v. 15, n. 5, p. 1364 – 1370, 2013.

Champoux, Y.; Allard, J. Dynamic tortuosity and bulk modulus in airsaturated porous media. **Journal of Applied Physics**, v. 70, n. 4, p. 1975–1979, 1991.

Christensen, P. W.; Klarbring, A. **An Introduction to Structural Optimization**. First ed. Berlin: Springer Science & Business Media, 2009. v. 153.

Cook, R. D.; Malkus, D. S.; Plesha, M. E.; Witt, R. J. **Concepts and Applications of Finite Element Analysis**. Fourth ed. New Jersey: John Wiley & Sons, 2001.

Cunha, D. C.; Almeida, B. V. de; Lopes, H. N.; Pavanello, R. Finite variation sensitivity analysis for discrete topology optimization of continuum structures. **Structural and Multidisciplinary Optimization**, v. 64, n. 6, p. 3877–3909, 2021.

Das, R.; Jones, R.; Xie, Y.-M. Optimal topology design of industrial structures using an evolutionary algorithm. **Optimization and Engineering**, v. 12, n. 4, p. 681–717, 2011.

Dazel, O.; Sgard, F.; Becot, F.-X.; Atalla, N. Expressions of dissipated powers and stored energies in poroelastic media modeled by  $\{u, U\}$  and  $\{u, P\}$  formulations. **Journal of the Acoustical Society of America**, v. 123, n. 4, p. 2054–2063, 2008.

Dilgen, C. B.; Dilgen, S. B.; Aage, N.; Jensen, J. S. Topology optimization of acoustic mechanical interaction problems: a comparative review. **Structural and Multidisciplinary Optimization**, v. 60, p. 779–801, 2019.

Ding, Y. Shape optimization of structures: a literature survey. **Computers & Structures**, v. 24, n. 6, p. 985–1004, 1986.

Dühring, M. B.; Jensen, J. S.; Sigmund, O. Acoustic design by topology optimization. **Journal of Sound and Vibration**, v. 317, n. 3–5, p. 557–575, 2008.

EEA. **Environmental noise in Europe – 2020**. Luxembourg, 2019.

Flanders, H. Differentiation under the integral sign. **The American Mathematical Monthly**, v. 80, n. 6, p. 615–627, 1973.

Haftka, R. T.; Grandhi, R. V. Structural shape optimization a survey. **Computer Methods in Applied Mechanics and Engineering**, v. 57, n. 1, p. 91–106, 1986.

Hashin, Z.; Shtrikman, S. A variational approach to the theory of the elastic behaviour of multiphase materials. **Journal of the Mechanics and Physics of Solids**, v. 11, n. 2, p. 127–140, 1963.

Huang, X.; Xie, Y. Convergent and mesh-independent solutions for the bi-directional evolutionary structural optimization method. **Finite Elements in Analysis and Design**, v. 43, n. 14, p. 1039 – 1049, 2007.

Huang, X.; Xie, Y. M. Bi-directional evolutionary topology optimization of continuum structures with one or multiple materials. **Computational Mechanics**, v. 43, p. 393–401, 2009.

Huang, X.; Xie, Y. M. **Evolutionary Topology Optimization of Continuum Structures: Methods and Applications**. First ed. New Jersey: John Wiley & Sons, 2010. ISBN 9780470746530.

Huang, X.; Xie, Y. M. Evolutionary topology optimization of continuum structures with an additional displacement constraint. **Structural and Multidisciplinary Optimization**, v. 40, p. 409–416, 2010.

Huang, X.; Xie, Y. M. A further review of eso type methods for topology optimization. **Structural and Multidisciplinary Optimization**, v. 41, p. 671–683, 2010.

Jog, C. S.; Haber, R. B. Stability of finite element models for distributed-parameter optimization and topology design. **Computer Methods in Applied Mechanics and Engineering**, v. 130, n. 3–4, p. 203–226, 1996.

Johnson, D. L.; Koplik, J.; Dashen, R. Theory of dynamic permeability and tortuosity in fluid-saturated porous media. **Journal of Fluid Mechanics**, v. 176, p. 379–402, 1987.

Jokel, C.; Yankaskas, K.; Robinette, M. B. Noise of military weapons, ground vehicles, planes and ships. **The Journal of the Acoustical Society of America**, v. 146, n. 5, p. 3832–3838, 2019.

Kim, H.; Querin, O.; Steven, G. On the development of structural optimisation and its relevance in engineering design. **Design Studies**, v. 23, n. 1, p. 85–102, 2002.

Kirsch, U. **Structural Optimization: Fundamentals and Applications**. First ed. Berlin: Springer-Verlag, 1993. ISBN 978-3-540-55919-1.

Kook, J. Evolutionary topology optimization for acoustic-structure interaction problems using a mixed u/p formulation. **Mechanics Based Design of Structures and Machines**, v. 47, n. 3, p. 356–374, 2019.

Kook, J.; Koo, K.; Hyun, J.; Jensen, J. S.; Wang, S. Acoustical topology optimization for Zwicker's loudness model Application to noise barriers. **Computer Methods in Applied Mechanics and Engineering**, v. 237-240, p. 130–151, 2012.

Lazarov, B. S.; Sigmund, O. Filters in topology optimization based on helmholtz-type differential equations. **International Journal for Numerical Methods in Engineering**, v. 86, n. 6, p. 765–781, 2011.

Lee, J. S. **Unified Multi-Phase Modeling and Topology Optimization for Complex Vibro-Acoustic Systems Consisting of Acoustic, Poroelastic and Elastic Media**. PhD Thesis (PhD Thesis) — School of Mechanical and Aerospace Engineering, The Graduate School, Seoul National University, 2009.

Lee, J. S.; Göransson, P.; Kim, Y. Y. Topology optimization for three-phase materials distribution in a dissipative expansion chamber by unified multiphase modeling approach. **Computer Methods in Applied Mechanics and Engineering**, v. 287, p. 191–211, 2015.

Lee, J. S.; Kang, Y. J.; Kim, Y. Y. Unified multiphase modeling for evolving, acoustically coupled systems consisting of acoustic, elastic, poroelastic media and septa. **Journal of Sound and Vibration**, v. 331, n. 25, p. 5518–5536, 2012.

Lee, J. S.; Kim, Y. Y.; Kim, J. S.; Kang, Y. J. Two-dimensional poroelastic acoustical foam shape design for absorption coefficient maximization by topology optimization method. **Journal of the Acoustical Society of America**, v. 123, p. 2094–2106, 2008.

Lee, J. W.; Kim, Y. Y. Topology optimization of muffler internal partitions for improving acoustical attenuation performance. **International Journal for Numerical Methods in Engineering**, v. 80, n. 4, p. 455–477, 2009.

Liu, S.; Li, Q.; Chen, W.; Tong, L.; Cheng, G. An identification method for enclosed voids restriction in manufacturability design for additive manufacturing structures. **Frontiers in Mechanical Engineering**, v. 10, p. 126–137, 2015.

Lopes, H. N.; Mahfoud, J.; Pavanello, R. High natural frequency gap topology optimization of bi-material elastic structures and band gap analysis. **Structural and Multidisciplinary Optimization**, v. 63, p. 1–16, 2021.

- Maute, K.; Schwarz, S. T.; Ramm, E. Structural optimization the interaction between form and mechanics. **Journal of Applied Mathematics and Mechanics**, v. 79, n. 10, p. 651 – 673, 1999.
- Miyata, K.; Noguchi, Y.; Yamada, T.; Izui, K.; Nishiwaki, S. Optimum design of a multi-functional acoustic metasurface using topology optimization based on Zwicker's loudness model. **Computer Methods in Applied Mechanics and Engineering**, v. 331, p. 116–137, 2018.
- Munjal, M. L. **Acoustics of Ducts and Mufflers**. Second ed. New Jersey: John Wiley & Sons, 2014.
- Munk, D. J.; Kipouros, T.; Vio, G. A.; Parks, G. T.; Steven, G. P. Multiobjective and multi-physics topology optimization using an updated smart normal constraint bi-directional evolutionary structural optimization method. **Structural and Multidisciplinary Optimization**, v. 57, n. 2, p. 665–688, 2018.
- Pereira, R. L.; Lopes, H. N.; Moura, M. S.; Pavanello, R. Multi-domain acoustic topology optimization based on the beso approach: applications on the design of multi-phase material mufflers. **Structural and Multidisciplinary Optimization**, v. 66, n. 1, p. 25, 2023.
- Pereira, R. L.; Lopes, H. N.; Pavanello, R. Topology optimization of acoustic systems with a multiconstrained beso approach. **Finite Elements in Analysis and Design**, v. 201, p. 103701, 2022.
- Picelli, R.; Vicente, W.; Pavanello, R.; Xie, Y. Evolutionary topology optimization for natural frequency maximization problems considering acoustic structure interaction. **Finite Elements in Analysis and Design**, v. 106, p. 56–64, 2015.
- Querin, O. M.; Steven, G. P.; Xie, Y. M. Evolutionary structural optimisation (eso) using a bidirectional algorithm. **Engineering Computations**, v. 15, n. 8, p. 1031–1048, 1998.
- Querin, O. M.; Young, V.; Steven, G. P.; Xie, Y. M. Computational efficiency and validation of bi-directional evolutionary structural optimisation. **Computer Methods in Applied Mechanics and Engineering**, v. 189, n. 2, p. 559–573, 2000.
- Ramamoorthy, V. T.; Özcan, E.; Parkes, A. J.; Sreekumar, A.; Jaouen, L.; Bécot, F.-X. Comparison of heuristics and metaheuristics for topology optimisation in acoustic porous materials. **The Journal of the Acoustical Society of America**, v. 150, n. 4, p. 3164–3175, 2021.
- Rigobert, S.; Atalla, N.; Sgard, F. C. Investigation of the convergence of the mixed displacement-pressure formulation for three-dimensional poroelastic materials using hierarchical elements. **Journal of the Acoustical Society of America**, v. 114, n. 5, p. 2607–2617, 2003.
- Rozvany, G. I. N.; Bendsøe, M. P.; Kirsch, U. Layout optimization of structures. **Applied Mechanics Reviews**, v. 48, n. 2, p. 41–119, 02 1995.
- Rozvany, G. I. N.; Querin, O. M. Combining eso with rigorous optimality criteria. **International Journal of Vehicle Design**, v. 28, n. 4, p. 294–299, 2002.

Sgard, F.; Atalla, N.; Nicolas, J. A numerical model for the low frequency diffuse field sound transmission loss of double-wall sound barriers with elastic porous linings. **The Journal of the Acoustical Society of America**, v. 108, n. 6, p. 2865–2872, 2000.

Sgard, F.; Olny, X.; Atalla, N.; Castel, F. On the use of perforations to improve the sound absorption of porous materials. **Applied Acoustics**, v. 66, n. 6, p. 625–651, 2005, innovative Applications of Materials for Acoustic Purposes.

Sigmund, O. On the Design of Compliant Mechanisms Using Topology Optimization. **Mechanics of Structures and Machines**, v. 25, n. 4, p. 493–524, 1997.

Sigmund, O. A 99 line topology optimization code written in matlab. **Structural and Multidisciplinary Optimization**, v. 21, p. 120–127, 2001.

Sigmund, O.; Maute, K. Topology optimization approaches: A comparative review: A comparative review. **Structural and Multidisciplinary Optimization**, v. 48, p. 1031–1055, 2013.

Sigmund, O.; Petersson, J. Numerical instabilities in topology optimization: A survey on procedures dealing with checkerboards, mesh-dependencies and local minima. **Structural Optimization**, v. 16, n. 1, p. 68–75, 1998.

Silva, F. I.; Pavanello, R. Synthesis of porousacoustic absorbing systems by an evolutionary optimization method. **Engineering Optimization**, v. 42, n. 10, p. 887–905, 2010.

Silva Júnior, F. I. da. **Síntese Computacional de Absorvedores Acústicos Poroelásticos [Computational Synthesis of Poroelastic Acoustic Absorbers]**. PhD Thesis (PhD Thesis) — Department of Computational Mechanics, School of Mechanical Engineering, University of Campinas, 2007.

Singh, N.; Davar, S. C. Noise pollution-sources, effects and control. **Journal of Human Ecology**, v. 16, n. 3, p. 181–187, 2004.

Sivapuram, R.; Picelli, R. Topology optimization of binary structures using integer linear programming. **Finite Elements in Analysis and Design**, v. 139, p. 49–61, 2018.

Sokolowski, J.; Zochowski, A. On the topological derivative in shape optimization. **SIAM Journal on Control and Optimization**, v. 37, p. 12511272, 1999.

Tortorelli, D. A.; Michaleris, P. Design sensitivity analysis: overview and review. **Inverse Problems in Engineering**, v. 1, n. 1, p. 71–105, 1994.

Vicente, W.; Picelli, R.; Pavanello, R.; Xie, Y. Topology optimization of frequency responses of fluid structure interaction systems. **Finite Elements in Analysis and Design**, v. 98, p. 1–13, 2015.

Vicente, W.; Zuo, Z.; Pavanello, R.; Calixto, T.; Picelli, R.; Xie, Y. Concurrent topology optimization for minimizing frequency responses of two-level hierarchical structures. **Computer Methods in Applied Mechanics and Engineering**, v. 301, p. 116–136, 2016.

Wang, M. Y.; Wang, X.; Guo, D. A level set method for structural topology optimization. **Computer Methods in Applied Mechanics and Engineering**, v. 192, n. 1, p. 227–246, 2003.

- Wu, T. W.; Wan, G. C. Muffler performance studies using a direct mixed-body boundary element method and a three-point method for evaluating transmission loss. **Journal of Vibration and Acoustics**, v. 118, n. 3, p. 479–484, 07 1996.
- Xia, L.; Breitkopf, P. Recent advances on topology optimization of multiscale nonlinear structures. **Archives of Computational Methods in Engineering**, v. 24, n. 2, p. 227–249, 2017.
- Xia, L.; Zhang, L.; Xia, Q.; Shi, T. Stress-based topology optimization using bi-directional evolutionary structural optimization method. **Computer Methods in Applied Mechanics and Engineering**, v. 333, p. 356–370, 2018.
- Xie, Y.; Steven, G. P. Shape and layout optimization via an evolutionary procedure. In: **Proceedings of the International Conference on Computational Engineering Science**. Hong Kong: [s.n.], 1992.
- Xie, Y. M.; Steven, G. P. A simple evolutionary procedure for structural optimization. **Computers & Structures**, v. 49, n. 5, p. 885–896, 1993.
- Xie, Y. M.; Steven, G. P. **Evolutionary Structural Optimization**. First ed. London: Springer-Verlag, 1997. ISBN 978-1-4471-0985-3.
- Yamamoto, T.; Maruyama, S.; Nishiwaki, S.; Yoshimura, M. Topology design of multi-material soundproof structures including poroelastic media to minimize sound pressure levels. **Computer Methods in Applied Mechanics and Engineering**, v. 198, n. 17, p. 1439–1455, 2009.
- Yan, X.; Huang, X.; Sun, G.; Xie, Y. M. Two-scale optimal design of structures with thermal insulation materials. **Composite Structures**, v. 120, p. 358–365, 2015.
- Yang, X. Y.; Xie, Y. M.; Steven, G. P.; Querin, O. M. Bidirectional evolutionary method for stiffness optimization. **AIAA Journal**, v. 37, n. 11, p. 1483–1488, 1999.
- Yoon, G. H. Acoustic topology optimization of fibrous material with delanybazley empirical material formulation. **Journal of Sound and Vibration**, v. 332, n. 5, p. 1172–1187, 2013.
- Zhao, F. A nodal variable eso (beso) method for structural topology optimization. **Finite Elements in Analysis and Design**, v. 86, p. 34–40, 2014.
- Zhou, E. L.; Wu, Y.; Lin, X. Y.; Li, Q. Q.; Xiang, Y. A normalization strategy for beso-based structural optimization and its application to frequency response suppression. **Acta Mechanica**, v. 232, p. 1307–1327, 2021.
- Zhou, M.; Rozvany, G. I. N. The coc algorithm, part ii: Topological, geometrical and generalized shape optimization. **Computer Methods in Applied Mechanics and Engineering**, v. 89, p. 309–336, 1991.
- Zhou, M.; Rozvany, G. I. N. On the validity of eso type methods in topology optimization. **Structural and Multidisciplinary Optimization**, v. 21, n. 1, p. 80–83, 2001.
- Zuo, Z. H.; Xie, Y. M.; Huang, X. Evolutionary topology optimization of structures with multiple displacement and frequency constraints. **Advances in Structural Engineering**, v. 15, n. 2, p. 359–372, 2012.

## A | Extended Sensitivity Analysis

This appendix presents detailed extensions of the procedures introduced in the sensitivity analysis sections of papers  $\mathcal{A}1$ ,  $\mathcal{A}2$  and  $\mathcal{A}3$  (Chapters 4, 5 and 6, respectively). For this, some recurring variables of the papers needed to be modified to maintain the uniformity established in Chapters 1, 2 and 3 of this thesis. Thus, Table A.1 indicates such variables that have undergone symbolic changes and their respective descriptions.

Table A.1 – Indication of variable changes: papers to thesis

Variables		Description
Papers	Thesis	
$\mathbf{K}_e$	$\mathbf{H}_a^i$	elemental kinetic energy (acoustic stiffness) matrix
$\mathbf{M}_e$	$\mathbf{Q}_a^i$	elemental compression (acoustic mass) matrix
$\mathbf{C}_e$	$\mathbf{D}_a^i$	elemental damping matrix
$\mathbf{p}$	$\hat{\mathbf{p}}_a$	acoustic pressure vector
$\mathbf{f}$	$\hat{\mathbf{f}}_a$	acoustic load vector
$V^*$	$V^f$	final volume fraction
$\gamma_e$	$x_i$	design variable
$T^*$	$T_{\text{adm}}$	admissible temperature
$\mathbf{N}_e$	$\mathbf{N}_a$	acoustic shape function matrix
$\Omega_e$	$\Omega_a^i$	elemental acoustic domain
$\psi, \eta$	$\psi_1, \dots, \psi_4$	penalty variables of $\mathcal{A}1$
$\Phi$	$\Phi_{\mathcal{A}1}$	objective function of $\mathcal{A}1$
$\Phi$	$\Phi_{\mathcal{A}2}$	objective function of $\mathcal{A}2$

## A.1 Sound Pressure Level

The developments presented here are detailed extensions of the procedures introduced in Section 6.1 of paper  $\mathcal{A}1$  and, therefore, a direct continuation of the sensitivity analysis started in Section 5.1 of the same work. The optimization problem of designing acoustic metasurfaces (referred here as  $\mathcal{P}1$ ) consists of reducing regional sound pressure levels in a set of observed frequencies, while subjected to volume and manufacturing constraints,

$$\text{Maximize: } \Phi_{\mathcal{A}1}^{\mathcal{P}1} = -\frac{1}{N_f} \sum_{n=1}^{N_f} \text{SPL}_n, \quad (\text{A.1})$$

$$\text{Subjected to: } \begin{cases} \mathbf{Z}\hat{\mathbf{p}}_a = \hat{\mathbf{f}}_a, \\ \mathbf{K}_T \mathbf{T} = \mathbf{q}, \\ V^f - \sum_{i=1}^{N_{\text{el}}} V_i x_i = 0, \\ T_j - T_{\text{adm}} \leq 0, \\ x_i = x_{\text{min}} \text{ or } 1, \end{cases} \quad (\text{A.2})$$

where the objective function  $\Phi_{\mathcal{A}1}^{\mathcal{P}1}$  corresponds to the arithmetic mean of the SPL values for  $N_f$  target frequencies. In Eq. (A.1), the negative sign is used to turn a maximization problem into a minimization one (Huang; Xie, 2010a). Considering the reference pressure equal to  $P_{\text{ref}} = 20 \times 10^{-6}$  Pa, the mathematical expression for the frequency dependent SPL calculation is presented by,

$$\text{SPL} = 10 \log_{10} \left( \frac{P_{\text{avg}}^2}{P_{\text{ref}}^2} \right), \quad (\text{A.3})$$

where the average squared pressure amplitude is (Dühring *et al.*, 2008; Kook *et al.*, 2012),

$$P_{\text{avg}}^2 = \frac{1}{\int_{\Omega_r} d\Omega_r} \int_{\Omega_r} |p_a(\omega, x_i)|^2 d\Omega_r. \quad (\text{A.4})$$

In the equation above,  $\Omega_r$  corresponds to the receiver domain, the region in which the SPL values must be minimized.

Since, in this case,  $\Phi_{\mathcal{A}1} = \Phi_{\mathcal{A}1}^{\mathcal{P}1}$ , the sensitivity analysis can now be completely described by solving the first term of the right-hand side of the following,

$$\alpha_i = \frac{dL}{dx_i} = \frac{\partial \Phi_{\mathcal{A}1}}{\partial x_i} + \lambda \frac{\partial (T_j - T_{\text{adm}} + S_k^2)}{\partial x_i}. \quad (\text{A.5})$$

Therefore,

$$\frac{\partial \Phi_{\mathcal{A}1}}{\partial x_i} = \frac{d\Phi_{\mathcal{A}1}^{\mathcal{P}1}}{dx_i} = -\frac{1}{N_f} \sum_{n=1}^{N_f} \left[ \frac{10}{\ln 10} \left( \frac{dP_{\text{avg}}^2/dx_i}{P_{\text{avg}}^2} \right) \right]. \quad (\text{A.6})$$

To find  $dP_{\text{avg}}^2/dx_i$ , first consider that,

$$\hat{\mathbf{p}}_a = \hat{\mathbf{p}}_{\text{Re}} + j\hat{\mathbf{p}}_{\text{Im}}, \quad (\text{A.7})$$

where  $\hat{\mathbf{p}}_{\text{Re}}$  and  $\hat{\mathbf{p}}_{\text{Im}}$  are the real and imaginary parts of  $\hat{\mathbf{p}}_a$ , respectively. Knowing that  $P_{\text{avg}}^2$  is a function of  $\hat{\mathbf{p}}_{\text{Re}}$ ,  $\hat{\mathbf{p}}_{\text{Im}}$  and  $x_i$ , the adjoint method (Tortorelli; Michaleris, 1994) can be applied by the introduction of Lagrange Multipliers,  $\lambda_{\mathcal{A}1}$ ,

$$P_{\text{avg}}^2 = P_{\text{avg}}^2(\hat{\mathbf{p}}_{\text{Re}}, \hat{\mathbf{p}}_{\text{Im}}, x_i) + \lambda_{\mathcal{A}1}^T (\mathbf{Z}\hat{\mathbf{p}}_a - \hat{\mathbf{f}}_a) + \lambda_{\mathcal{A}1}^H (\mathbf{Z}^*\hat{\mathbf{p}}_a^* - \hat{\mathbf{f}}_a^*). \quad (\text{A.8})$$

The superscript  $(\cdot)^*$  is the complex conjugate and  $(\cdot)^H$  is the same as  $((\cdot)^T)^*$ . It is important to note that all pressure vectors are also dependent on  $x_i$ , being hid in Eqs. (A.7) and (A.8) to simplify the notation. Taking the derivative of Eq. (A.8) with respect to the design variable, one gets,

$$\begin{aligned} \frac{dP_{\text{avg}}^2}{dx_i} = & \frac{\partial P_{\text{avg}}^2}{\partial x_i} + \frac{\partial P_{\text{avg}}^2}{\partial \hat{\mathbf{p}}_{\text{Re}}} \frac{\partial \hat{\mathbf{p}}_{\text{Re}}}{\partial x_i} + \frac{\partial P_{\text{avg}}^2}{\partial \hat{\mathbf{p}}_{\text{Im}}} \frac{\partial \hat{\mathbf{p}}_{\text{Im}}}{\partial x_i} \\ & + \lambda_{\mathcal{A}1}^T \left( \frac{\partial \mathbf{Z}}{\partial x_i} \hat{\mathbf{p}}_a + \mathbf{Z} \frac{\partial \hat{\mathbf{p}}_{\text{Re}}}{\partial x_i} + j\mathbf{Z} \frac{\partial \hat{\mathbf{p}}_{\text{Im}}}{\partial x_i} - \frac{\partial \hat{\mathbf{f}}_a}{\partial x_i} \right) \\ & + \lambda_{\mathcal{A}1}^H \left( \frac{\partial \mathbf{Z}^*}{\partial x_i} \hat{\mathbf{p}}_a^* + \mathbf{Z}^* \frac{\partial \hat{\mathbf{p}}_{\text{Re}}}{\partial x_i} - j\mathbf{Z}^* \frac{\partial \hat{\mathbf{p}}_{\text{Im}}}{\partial x_i} - \frac{\partial \hat{\mathbf{f}}_a^*}{\partial x_i} \right), \end{aligned} \quad (\text{A.9})$$

which becomes,

$$\begin{aligned} \frac{dP_{\text{avg}}^2}{dx_i} = & \frac{\partial P_{\text{avg}}^2}{\partial x_i} + \left( \frac{\partial P_{\text{avg}}^2}{\partial \hat{\mathbf{p}}_{\text{Re}}} + \lambda_{\mathcal{A}1}^T \mathbf{Z} + \lambda_{\mathcal{A}1}^H \mathbf{Z}^* \right) \frac{\partial \hat{\mathbf{p}}_{\text{Re}}}{\partial x_i} \\ & + \left( \frac{\partial P_{\text{avg}}^2}{\partial \hat{\mathbf{p}}_{\text{Im}}} + j\lambda_{\mathcal{A}1}^T \mathbf{Z} - j\lambda_{\mathcal{A}1}^H \mathbf{Z}^* \right) \frac{\partial \hat{\mathbf{p}}_{\text{Im}}}{\partial x_i} \\ & + \lambda_{\mathcal{A}1}^T \left( \frac{\partial \mathbf{Z}}{\partial x_i} \hat{\mathbf{p}}_a - \frac{\partial \hat{\mathbf{f}}_a}{\partial x_i} \right) + \lambda_{\mathcal{A}1}^H \left( \frac{\partial \mathbf{Z}^*}{\partial x_i} \hat{\mathbf{p}}_a^* - \frac{\partial \hat{\mathbf{f}}_a^*}{\partial x_i} \right). \end{aligned} \quad (\text{A.10})$$

The unknown expressions involving  $\partial \hat{\mathbf{p}}_{\text{Re}}/\partial x_i$  and  $\partial \hat{\mathbf{p}}_{\text{Im}}/\partial x_i$  can be eliminated by satisfying,

$$\begin{cases} \lambda_{\mathcal{A}1}^T \mathbf{Z} + \lambda_{\mathcal{A}1}^H \mathbf{Z}^* = -\frac{\partial P_{\text{avg}}^2}{\partial \hat{\mathbf{p}}_{\text{Re}}}, \\ j\lambda_{\mathcal{A}1}^T \mathbf{Z} - j\lambda_{\mathcal{A}1}^H \mathbf{Z}^* = -\frac{\partial P_{\text{avg}}^2}{\partial \hat{\mathbf{p}}_{\text{Im}}}. \end{cases} \quad (\text{A.11})$$

Multiplying the second expression by  $-j$ , adding to the first and transposing both sides ( $\mathbf{Z}^T = \mathbf{Z}$ ), the adjoint equation is found,

$$\mathbf{Z}\lambda_{\mathcal{A}1} = \underbrace{-\frac{1}{2} \left( \frac{\partial P_{\text{avg}}^2}{\partial \hat{\mathbf{p}}_{\text{Re}}} - j \frac{\partial P_{\text{avg}}^2}{\partial \hat{\mathbf{p}}_{\text{Im}}} \right)^T}_{\mathbf{f}_{\text{ad}}^{\mathcal{A}1}}, \quad (\text{A.12})$$

where,

$$\mathbf{f}_{\text{ad}}^{\mathcal{A}1} = - \left( \frac{1}{\int_{\Omega_r} d\Omega_r} (\hat{\mathbf{P}}_{\text{Re}}^T - j\hat{\mathbf{P}}_{\text{Im}}^T) \int_{\Omega_r} \mathbf{N}_a^T \mathbf{N}_a d\Omega_r \right)^T. \quad (\text{A.13})$$

Furthermore, with the use of Eq. (A.11) it is now possible to simplify Eq. (A.10), hence,

$$\frac{dP_{\text{avg}}^2}{dx_i} = \frac{\partial P_{\text{avg}}^2}{\partial x_i} + 2 \text{Re} \left[ \boldsymbol{\lambda}_{\mathcal{A}1}^T \left( \frac{\partial \mathbf{Z}}{\partial x_i} \hat{\mathbf{P}}_a - \frac{\partial \hat{\mathbf{f}}_a}{\partial x_i} \right) \right]. \quad (\text{A.14})$$

As,

$$\frac{\partial P_{\text{avg}}^2}{\partial x_i} = \hat{\mathbf{P}}_a^H \left[ \frac{\partial}{\partial x_i} \left( \frac{1}{\int_{\Omega_r} d\Omega_r} \int_{\Omega_r} \mathbf{N}_a^T \mathbf{N}_a d\Omega_r \right) \right] \hat{\mathbf{P}}_a = 0, \quad (\text{A.15})$$

and

$$\frac{\partial \hat{\mathbf{f}}_a}{\partial x_i} = 0, \quad (\text{A.16})$$

$dP_{\text{avg}}^2/dx_i$  can finally be found by the use of the MIS,

$$\begin{cases} \frac{1}{\rho(x_i)} = \frac{1}{\rho_a} + x_i^{\psi_1} \left( \frac{1}{\rho_r} - \frac{1}{\rho_a} \right), \\ \frac{1}{\kappa(x_i)} = \frac{1}{\kappa_a} + x_i^{\psi_2} \left( \frac{1}{\kappa_r} - \frac{1}{\kappa_a} \right), \end{cases} \quad (\text{A.17})$$

in the  $\partial \mathbf{Z}/\partial x_i$  determination. Therefore,

$$\frac{\partial \mathbf{Z}}{\partial x_i} = \frac{\partial \mathbf{H}_a}{\partial x_i} - \omega^2 \frac{\partial \mathbf{Q}_a}{\partial x_i}, \quad (\text{A.18})$$

where,

$$\frac{\partial \mathbf{H}_a^i}{\partial x_i} = \frac{\partial}{\partial x_i} \left[ \frac{1}{\rho(x_i)} \right] \int_{\Omega_a^i} (\nabla \mathbf{N}_a)^T \nabla \mathbf{N}_a d\Omega_a^i, \quad (\text{A.19})$$

$$\frac{\partial \mathbf{Q}_a^i}{\partial x_i} = \frac{\partial}{\partial x_i} \left[ \frac{1}{\kappa(x_i)} \right] \int_{\Omega_a^i} \mathbf{N}_a^T \mathbf{N}_a d\Omega_a^i, \quad (\text{A.20})$$

and,

$$\frac{\partial}{\partial x_i} \left[ \frac{1}{\rho(x_i)} \right] = \psi_1 x_i^{(\psi_1-1)} \left( \frac{1}{\rho_r} - \frac{1}{\rho_a} \right), \quad (\text{A.21})$$

$$\frac{\partial}{\partial x_i} \left[ \frac{1}{\kappa(x_i)} \right] = \psi_2 x_i^{(\psi_2-1)} \left( \frac{1}{\kappa_r} - \frac{1}{\kappa_a} \right), \quad (\text{A.22})$$

in the element domain  $\Omega_a^i$ . It is also noted that all pressure related sensitivity expressions have been validated via finite differences method.

## A.2 Absorption Coefficient

The developments presented here are detailed extensions of the procedures introduced in Section 6.2 of paper  $\mathcal{A}1$  and, therefore, a direct continuation of the sensitivity analysis started in Section 5.1 of the same work. The acoustic topology optimization problem of designing poro-acoustic structures (referred here as  $\mathcal{P}2$ ) with maximized absorption coefficient in predefined frequencies can be written as,

$$\begin{aligned} \text{Maximize: } & \Phi_{\mathcal{A}1}^{\mathcal{P}2} = 1 - |R|^2, & (\text{A.23}) \\ \text{Subjected to: } & \left\{ \begin{array}{l} \mathbf{Z}\hat{\mathbf{p}}_a = \hat{\mathbf{f}}_a, \\ \mathbf{K}_T \mathbf{T} = \mathbf{q}, \\ V^f - \sum_{i=1}^{N_{\text{el}}} V_i x_i = 0, \\ T_j - T_{\text{adm}} \leq 0, \\ x_i = x_{\text{min}} \text{ or } 1, \end{array} \right. & (\text{A.24}) \end{aligned}$$

where the objective function  $\Phi_{\mathcal{A}1}^{\mathcal{P}2}$  is the sound absorption coefficient of the considered porous material and  $R$  is the reflection coefficient, which in turn can be represented by the following frequency dependent expression (Lee *et al.*, 2008),

$$R = \frac{-P_2 \exp(-jk_a X_1) + P_1 \exp(-jk_a X_2)}{P_2 \exp(jk_a X_1) - P_1 \exp(jk_a X_2)}. \quad (\text{A.25})$$

$P_1$  and  $P_2$  are pressure amplitudes measured in positions  $X_1$  and  $X_2$ , and  $k_a = \omega/c_a$  is the air wavenumber.

Knowing that  $\Phi_{\mathcal{A}1} = \Phi_{\mathcal{A}1}^{\mathcal{P}2}$ , the first term of the right-hand side of Eq. (A.5) can be specified as,

$$\frac{\partial \Phi_{\mathcal{A}1}^{\mathcal{P}2}}{\partial x_i} = -2 \left( \text{Re}(R) \frac{\partial \text{Re}(R)}{\partial x_i} + \text{Im}(R) \frac{\partial \text{Im}(R)}{\partial x_i} \right), \quad (\text{A.26})$$

with  $\text{Re}(R)$  and  $\text{Im}(R)$  denoting the real and imaginary parts of  $R$ . After a series of mathematical manipulations, the derivative of  $R$  can be found (Lee *et al.*, 2008),

$$\begin{aligned} \frac{\partial R}{\partial x_i} = & \frac{\left[ -\frac{\partial P_2}{\partial x_i} \exp(-jk_a X_1) + \frac{\partial P_1}{\partial x_i} \exp(-jk_a X_2) \right] [P_2 \exp(jk_a X_1) - P_1 \exp(jk_a X_2)]}{[P_2 \exp(jk_a X_1) - P_1 \exp(jk_a X_2)]^2} - \\ & \frac{[-P_2 \exp(-jk_a X_1) + P_1 \exp(-jk_a X_2)] \left[ \frac{\partial P_2}{\partial x_i} \exp(jk_a X_1) - \frac{\partial P_1}{\partial x_i} \exp(jk_a X_2) \right]}{[P_2 \exp(jk_a X_1) - P_1 \exp(jk_a X_2)]^2}, & (\text{A.27}) \end{aligned}$$

with  $\partial \text{Re}(R)/\partial x_i$  and  $\partial \text{Im}(R)/\partial x_i$  obtained by taking the real and imaginary parts of  $\partial R/\partial x_i$ .

To find  $\partial P_1/\partial x_i$  and  $\partial P_2/\partial x_i$ , consider the adjoint load vector  $\partial P_j/\partial \hat{\mathbf{p}}_a$  of size [dof, 1], where dof is the total number of degrees of freedom of the system. Since  $P_j$  is the target pressure value, located in a specific dof,  $\partial P_j/\partial \hat{\mathbf{p}}_a$  is completely full of zeros, except at the degree of freedom referred to  $P_j$ , where a value of 1 is placed (Lee *et al.*, 2015). The differentiation of  $P_j$  can then be written,

$$\frac{\partial P_j}{\partial x_i} = \left( \frac{\partial P_j}{\partial \hat{\mathbf{p}}_a} \right)^T \frac{\partial \hat{\mathbf{p}}_a}{\partial x_i}, \quad (\text{A.28})$$

with the subscript  $(\cdot)_j$  representing both microphone positions where  $P_1$  and  $P_2$  are measured. Based on Eq. (2.21), one may write,

$$\frac{\partial \hat{\mathbf{p}}_a}{\partial x_i} = -\mathbf{Z}^{-1} \frac{\partial \mathbf{Z}}{\partial x_i} \hat{\mathbf{p}}_a, \quad (\text{A.29})$$

which can be applied to Eq. (A.28), generating,

$$\frac{\partial P_j}{\partial x_i} = -\hat{\mathbf{p}}_j^T \frac{\partial \mathbf{Z}}{\partial x_i} \hat{\mathbf{p}}_a, \quad (\text{A.30})$$

where  $\hat{\mathbf{p}}_j = \mathbf{Z}^{-1}(\partial P_j/\partial \hat{\mathbf{p}}_a)$ . Lastly,  $\partial \mathbf{Z}/\partial x_i$  is calculated with Eq. (A.18) and then Eqs. (A.19) and (A.20). Here, the appropriate MIS is,

$$\begin{cases} \frac{1}{\rho(x_i)} = \frac{1}{\rho_a} + x_i^{\psi_3} \left( \frac{1}{\rho_p} - \frac{1}{\rho_a} \right), \\ \frac{1}{\kappa(x_i)} = \frac{1}{\kappa_a} + x_i^{\psi_4} \left( \frac{1}{\kappa_p} - \frac{1}{\kappa_a} \right), \end{cases} \quad (\text{A.31})$$

with its derivation being,

$$\frac{\partial}{\partial x_i} \left[ \frac{1}{\rho(x_i)} \right] = \psi_3 x_i^{(\psi_3-1)} \left( \frac{1}{\rho_p} - \frac{1}{\rho_a} \right), \quad (\text{A.32})$$

$$\frac{\partial}{\partial x_i} \left[ \frac{1}{\kappa(x_i)} \right] = \psi_4 x_i^{(\psi_4-1)} \left( \frac{1}{\kappa_p} - \frac{1}{\kappa_a} \right). \quad (\text{A.33})$$

Once again, all pressure related sensitivity expressions have been validated via finite differences method.

### A.3 Transmission Loss

The developments presented here are detailed extensions of the procedures introduced in Section 4.1 of paper  $\mathcal{A}2$ . At this moment, consider a topology optimization problem where the goal is to maximize the mean transmission loss,  $\Phi_{\mathcal{A}2}$ , over the angular frequency range  $[\omega_s^{(1)}, \omega_f^{(m)}]$ , when subjected to the acoustic equilibrium system (Eq. (2.21)) and  $n_p - 1$  volume

constraints,

$$\text{Maximize: } \Phi_{\mathcal{A}2} = \frac{1}{\omega_f^{(m)} - \omega_s^{(1)}} \left( \int_{\omega_s^{(1)}}^{\omega_f^{(1)}} \text{TL} \, d\Omega_{d1} + \dots + \int_{\omega_s^{(m)}}^{\omega_f^{(m)}} \text{TL} \, d\Omega_{dm} \right), \quad (\text{A.34})$$

$$\text{Subjected to: } \left\{ \begin{array}{l} \mathbf{Z}\hat{\mathbf{p}}_a = \hat{\mathbf{f}}_a, \\ \left\{ \begin{array}{l} V_1^f - \left( \sum_{i=1}^{N_{\text{el}}} V_i x_i \right)_1 \\ \vdots \\ V_{n_p-1}^f - \left( \sum_{i=1}^{N_{\text{el}}} V_i x_i \right)_{n_p-1} \end{array} \right\} = \left\{ \begin{array}{l} 0 \\ \vdots \\ 0 \end{array} \right\}, \\ \mathbf{x} = \left[ \left\{ \begin{array}{l} x_1 \\ \vdots \\ x_{N_{\text{el}}} \end{array} \right\}_1, \dots, \left\{ \begin{array}{l} x_1 \\ \vdots \\ x_{N_{\text{el}}} \end{array} \right\}_{n_p-1} \right]. \end{array} \right. \quad (\text{A.35})$$

In the above equations,  $m$  is the number of design domains (or muffler chambers) considered in the optimization, while  $\Omega_{dm}$  refers to the specific domain where the mean TL is calculated over the  $[\omega_s^{(m)}, \omega_f^{(m)}]$  frequency range. Additionally,  $n_p$  indicates the number of material phases treated in the iterative procedure, which are controlled by the relations between the prescribed final volume fractions,  $V^f$ , and the domain volume fractions,  $\sum_{i=1}^{N_{\text{el}}} V_i x_i$ . The general design domain matrix,  $\mathbf{x}$ , encompass all the column design domain vectors,  $\mathbf{x}$ , of each individual material phase.

Considering the same cross sectional areas of the inlet and outlet tubes, and knowing that only plane waves propagate themselves in those regions, the TL formula can be obtained with the help of the three-point methodology (Wu; Wan, 1996),

$$\text{TL} = 10 \log_{10} \frac{|p_{\text{in}}|^2}{|p_{\text{out}}|^2} = 20 \log_{10} \left( \left| \frac{1}{p_3} \frac{p_1 - p_2 \exp(-jk_a X_{12})}{1 - \exp(-jk_a X_{12})} \right| \right), \quad (\text{A.36})$$

where the sound pressure amplitudes measured at the inlet receivers are  $p_1$  and  $p_2$ , being located  $X_{12}$  from each other, and the sound pressure amplitude taken from the outlet end is  $p_3$ .

In this muffler optimization problem, the sensitivity analysis is done by the derivation of  $\Phi_{\mathcal{A}2}$  with respect to  $x_i$ ,

$$\alpha_i = \frac{d\Phi_{\mathcal{A}2}}{dx_i} = \frac{1}{\omega_f^{(m)} - \omega_s^{(1)}} \left( \frac{d}{dx_i} \int_{\omega_s^{(1)}}^{\omega_f^{(1)}} \text{TL} \, d\Omega_{d1} + \dots + \frac{d}{dx_i} \int_{\omega_s^{(m)}}^{\omega_f^{(m)}} \text{TL} \, d\Omega_{dm} \right). \quad (\text{A.37})$$

By the adoption of the Leibniz integral rule (Flanders, 1973), Eq. (A.37) can be rewritten,

$$\alpha_i = \frac{1}{\omega_f^{(m)} - \omega_s^{(1)}} \left( \int_{\omega_s^{(1)}}^{\omega_f^{(1)}} \frac{\partial \text{TL}}{\partial x_i} \, d\Omega_{d1} + \dots + \int_{\omega_s^{(m)}}^{\omega_f^{(m)}} \frac{\partial \text{TL}}{\partial x_i} \, d\Omega_{dm} \right). \quad (\text{A.38})$$

To properly solve Eq. (A.38), one may first calculate the partial TL derivative (Lee; Kim, 2009; Azevedo *et al.*, 2018),

$$\frac{\partial \text{TL}}{\partial x_i} = \frac{10}{\ln 10} \left( \frac{\partial |p_{\text{in}}|^2}{\partial x_i} \frac{1}{|p_{\text{in}}|^2} - \frac{\partial |p_{\text{out}}|^2}{\partial x_i} \frac{1}{|p_{\text{out}}|^2} \right), \quad (\text{A.39})$$

where,

$$|p_{\text{in}}|^2 = \frac{[\text{Re}(p_1) - \text{Re}(p_2) \cos(k_a X_{12}) - \text{Im}(p_2) \sin(k_a X_{12})]^2}{[1 - \cos(2k_a X_{12})]^2 + [\sin(2k_a X_{12})]^2} + \frac{[\text{Im}(p_1) - \text{Im}(p_2) \cos(k_a X_{12}) + \text{Re}(p_2) \sin(k_a X_{12})]^2}{[1 - \cos(2k_a X_{12})]^2 + [\sin(2k_a X_{12})]^2}, \quad (\text{A.40})$$

$$|p_{\text{out}}|^2 = \text{Re}(p_3)^2 + \text{Im}(p_3)^2, \quad (\text{A.41})$$

and,

$$\begin{aligned} \frac{\partial |p_{\text{in}}|^2}{\partial x_i} &= \frac{2 [\text{Re}(p_1) - \text{Re}(p_2) \cos(k_a X_{12}) - \text{Im}(p_2) \sin(k_a X_{12})]}{[1 - \cos(2k_a X_{12})]^2 + [\sin(2k_a X_{12})]^2} \times \\ &\quad \left[ \frac{\frac{\partial \text{Re}(p_1)}{\partial x_i} - \frac{\partial \text{Re}(p_2)}{\partial x_i} \cos(k_a X_{12}) - \frac{\partial \text{Im}(p_2)}{\partial x_i} \sin(k_a X_{12})}{[1 - \cos(2k_a X_{12})]^2 + [\sin(2k_a X_{12})]^2} \right] + \\ &\quad \frac{2 [\text{Im}(p_1) - \text{Im}(p_2) \cos(k_a X_{12}) + \text{Re}(p_2) \sin(k_a X_{12})]}{[1 - \cos(2k_a X_{12})]^2 + [\sin(2k_a X_{12})]^2} \times \\ &\quad \left[ \frac{\frac{\partial \text{Im}(p_1)}{\partial x_i} - \frac{\partial \text{Im}(p_2)}{\partial x_i} \cos(k_a X_{12}) + \frac{\partial \text{Re}(p_2)}{\partial x_i} \sin(k_a X_{12})}{[1 - \cos(2k_a X_{12})]^2 + [\sin(2k_a X_{12})]^2} \right], \end{aligned} \quad (\text{A.42})$$

$$\frac{\partial |p_{\text{out}}|^2}{\partial x_i} = 2 \frac{\partial \text{Re}(p_3)}{\partial x_i} \text{Re}(p_3) + 2 \frac{\partial \text{Im}(p_3)}{\partial x_i} \text{Im}(p_3). \quad (\text{A.43})$$

In Eqs. (A.40) to (A.43),  $\text{Re}(p_j)$  and  $\text{Im}(p_j)$  denote the real and imaginary parts of the  $j$ th pressure amplitude, with the values of  $\partial \text{Re}(p_j)/\partial x_i$  and  $\partial \text{Im}(p_j)/\partial x_i$  obtained by respectively taking the real and imaginary parts of  $\partial p_j/\partial x_i$ . This last term may be calculated by the adoption of the procedures stated in Eqs. (A.28), (A.29) and (A.30), when  $P_j$  is similar to  $p_j$  in this case.

As a final action, one may find  $\partial \mathbf{Z}/\partial x_i$  with the assistance of,

$$\frac{\partial \mathbf{Z}}{\partial x_i} = \frac{\partial \mathbf{H}_a}{\partial x_i} + j\omega \frac{\partial \mathbf{D}_a}{\partial x_i} - \omega^2 \frac{\partial \mathbf{Q}_a}{\partial x_i}, \quad (\text{A.44})$$

where,

$$\frac{\partial \mathbf{H}_a^i}{\partial x_i} = \frac{\partial}{\partial x_i} \left[ \frac{1}{\rho(x_i)} \right] \int_{\Omega_a^i} (\nabla \mathbf{N}_a)^T \nabla \mathbf{N}_a d\Omega_a^i, \quad (\text{A.45})$$

$$\frac{\partial \mathbf{Q}_a^i}{\partial x_i} = \frac{\partial}{\partial x_i} \left[ \frac{1}{\kappa(x_i)} \right] \int_{\Omega_a^i} \mathbf{N}_a^T \mathbf{N}_a d\Omega_a^i, \quad (\text{A.46})$$

$$\frac{\partial \mathbf{D}_a^i}{\partial x_i} = \mathbf{0}, \quad (\text{A.47})$$

as well as the appropriate material interpolation schemes created for this application. In the broader scenario, where acoustic, pororigid and rigid material elements are all considered in the design domain, the MIS is,

$$\begin{cases} \frac{1}{\rho(x_{i_1}, x_{i_2})} = \Theta_3(1 - x_{i_2}^{\iota_2}) + \frac{1}{\rho_p}(x_{i_2}^{\iota_2} - x_{i_1}^{\iota_1}) + x_{i_1}^{\iota_1} \frac{1}{\rho_a}, \\ \frac{1}{\kappa(x_{i_1}, x_{i_2})} = \Theta_4(1 - x_{i_2}^{\iota_4}) + \frac{1}{\kappa_p}(x_{i_2}^{\iota_4} - x_{i_1}^{\iota_3}) + x_{i_1}^{\iota_3} \frac{1}{\kappa_a}, \end{cases} \quad (\text{A.48})$$

with,

$$\Theta_3 = \frac{1}{\rho_r} - \left[ \frac{1}{\rho_p}(x_{\min}^{\iota_2} - x_{\min}^{\iota_1}) + x_{\min}^{\iota_1} \frac{1}{\rho_a} \right], \quad (\text{A.49})$$

$$\Theta_4 = \frac{1}{\kappa_r} - \left[ \frac{1}{\kappa_p}(x_{\min}^{\iota_4} - x_{\min}^{\iota_3}) + x_{\min}^{\iota_3} \frac{1}{\kappa_a} \right]. \quad (\text{A.50})$$

Furthermore, its derivation with respect to both design variables  $(x_{i_1}, x_{i_2})$  is then,

$$\frac{\partial}{\partial x_{i_1}} \left[ \frac{1}{\rho(x_{i_1}, x_{i_2})} \right] = \iota_1 x_{i_1}^{(\iota_1-1)} \left( \frac{1}{\rho_a} - \frac{1}{\rho_p} \right), \quad (\text{A.51})$$

$$\frac{\partial}{\partial x_{i_2}} \left[ \frac{1}{\rho(x_{i_1}, x_{i_2})} \right] = \iota_2 x_{i_2}^{(\iota_2-1)} \left( \frac{1}{\rho_p} - \Theta_3 \right), \quad (\text{A.52})$$

and

$$\frac{\partial}{\partial x_{i_1}} \left[ \frac{1}{\kappa(x_{i_1}, x_{i_2})} \right] = \iota_3 x_{i_1}^{(\iota_3-1)} \left( \frac{1}{\kappa_a} - \frac{1}{\kappa_p} \right), \quad (\text{A.53})$$

$$\frac{\partial}{\partial x_{i_2}} \left[ \frac{1}{\kappa(x_{i_1}, x_{i_2})} \right] = \iota_4 x_{i_2}^{(\iota_4-1)} \left( \frac{1}{\kappa_p} - \Theta_4 \right). \quad (\text{A.54})$$

All aforementioned expressions have been validated via finite differences method.

#### A.4 Dissipated Power Level

The developments presented here are detailed extensions of the procedures introduced in Section 4.1 of paper  $\mathcal{A}3$ . The topology optimization problem investigated in the multiphysics application can be defined, for a specific target frequency, as to maximize the dissipated power level,  $\text{PL}_D$ , that in turn is a combination of the time-averaged dissipated powers of structural,  $\Pi_D^s$ , viscous,  $\Pi_D^v$ , and thermal,  $\Pi_D^t$ , nature, while subjected to volume constraints. Throughout the numerical procedure, a multifrequency band of  $[\omega_s, \omega_f]$  is also considered, in a way that the objective function becomes the mean  $\text{PL}_D$  (also referred as  $\text{MPL}_D$ ), as shown in the following

expressions,

$$\text{Maximize: } \text{MPL}_D = \frac{1}{\omega_f - \omega_s} \int_{\omega_s}^{\omega_f} \underbrace{10 \log_{10} \left( \frac{\vartheta_1 \Pi_D^s + \vartheta_2 \Pi_D^v + \vartheta_3 \Pi_D^t}{\Pi_{\text{ref}}} \right)}_{\text{PL}_D} d\Omega_p, \quad (\text{A.55})$$

$$\text{Subjected to: } \begin{cases} \tilde{\mathbf{Z}} \hat{\boldsymbol{\theta}} = \hat{\mathbf{f}}, \\ V_p^f - \sum_{i=1}^{N_{\text{el}}} V_{i_p} x_{i_1} = 0, \\ V_e^f - \sum_{i=1}^{N_{\text{el}}} V_{i_e} x_{i_2} = 0, \\ x_{i_1} = x_{\min} \text{ or } 1, \\ x_{i_2} = x_{\min} \text{ or } 1. \end{cases} \quad (\text{A.56})$$

In Eq. (A.55),  $\vartheta_1$ ,  $\vartheta_2$  and  $\vartheta_3$  are simply used as switching variables, that is, they assume unit values when  $\Pi_D^s$ ,  $\Pi_D^v$  or  $\Pi_D^t$  are respectively considered in the objective function, otherwise assuming null values. This artifice is here applied to facilitate the combination of different dissipative portions of power without necessarily rewriting the objective function. Furthermore,  $\Pi_{\text{ref}} = 1 \times 10^{-12} \text{ W}$  represents the reference power. In Eq. (A.56), the prescribed final volume fraction is  $V^f$ , with the design domain volume fraction being  $\sum_{i=1}^{N_{\text{el}}} V_i x_i$ .

Since harmonic motion is considered in the definition of all domain formulations, the dissipated powers may then be established in time-averaged forms. One way to obtain such expressions for the porous medium was given by [Sgard \*et al.\* \(2000\)](#), being latter formalized by [Dazel \*et al.\* \(2008\)](#). Due to the simplicity of [Sgard \*et al.\* \(2000\)](#) formulations, the expressions that follow are therefore the result of their work. Considering the unification of Eqs. (2.47) and (2.48), and that both admissible functions are  $\delta \mathbf{u}_s = -j\omega \mathbf{u}_s^*$  and  $\delta p_f = -j\omega p_f^*$ , the weak form of the aforementioned expressions may be rewritten as,

$$\begin{aligned} & \underbrace{-j\omega \int_{\Omega_p} \hat{\boldsymbol{\sigma}}^s(\mathbf{u}_s) : \boldsymbol{\varepsilon}^s(\mathbf{u}_s^*) d\Omega_p}_{\Pi_{\text{elas}}^s} + \underbrace{j\omega^3 \int_{\Omega_p} \tilde{\rho} \mathbf{u}_s \cdot \mathbf{u}_s^* d\Omega_p}_{\Pi_{\text{iner}}^s} \\ & \underbrace{-j\omega \int_{\Omega_p} \frac{\phi^2}{\omega^2 \tilde{\rho}_{22}} \nabla p_f \cdot \nabla p_f^* d\Omega_p}_{\Pi_{\text{iner}}^f} + \underbrace{j\omega \int_{\Omega_p} \frac{\phi^2}{\tilde{R}} p_f p_f^* d\Omega_p}_{\Pi_{\text{elas}}^f} \\ & \underbrace{+ j\omega (\tilde{\gamma} + \tilde{\xi}) \int_{\Omega_p} (\nabla p_f \cdot \mathbf{u}_s^* + \nabla p_f^* \cdot \mathbf{u}_s) d\Omega_p + j\omega \tilde{\xi} \int_{\Omega_p} (p_f \nabla \cdot \mathbf{u}_s^* + p_f^* \nabla \cdot \mathbf{u}_s) d\Omega_p}_{\Pi_{\text{coup}}^f} \\ & \underbrace{+ j\omega \int_{\Gamma_p} (\boldsymbol{\sigma}^t \cdot \mathbf{n}_p) \cdot \mathbf{u}_s^* d\Gamma_p + j\omega \int_{\Gamma_p} \phi(\mathbf{U}_f - \mathbf{u}_s) \cdot \mathbf{n}_p p_f^* d\Gamma_p}_{\Pi_{\text{ext}}} = 0. \end{aligned} \quad (\text{A.57})$$

Based on the above equations, the power balance yields,

$$\Pi_{\text{elas}}^s + \Pi_{\text{iner}}^s + \Pi_{\text{iner}}^f + \Pi_{\text{elas}}^f + \Pi_{\text{coup}}^{sf} + \Pi_{\text{ext}} = 0, \quad (\text{A.58})$$

where  $\Pi_{\text{elas}}^s$  and  $\Pi_{\text{iner}}^s$  are the power developed by the internal and inertial forces in the solid phase in vacuum, respectively. These same internal and inertial forces also generate contributions in the interstitial fluid, respectively being the powers  $\Pi_{\text{elas}}^f$  and  $\Pi_{\text{iner}}^f$ . The power exchanged between both phases is  $\Pi_{\text{coup}}^{sf}$ , while the one developed by external loading is  $\Pi_{\text{ext}}$ . Knowing that the time-averaged dissipated power,  $\Pi_{\text{D}}$ , can be divided into its structural,  $\Pi_{\text{D}}^s$ , viscous,  $\Pi_{\text{D}}^v$ , and thermal,  $\Pi_{\text{D}}^t$ , parts, as highlighted in Eq. (A.55), and based on the Eqs. (A.57), the Eqs.(A.59), (A.60) and (A.61) are defined,

$$\Pi_{\text{D}}^s = \frac{\omega}{2} \text{Im} \left[ \int_{\Omega_p} \hat{\boldsymbol{\sigma}}^s(\mathbf{u}_s) : \boldsymbol{\varepsilon}^s(\mathbf{u}_s^*) d\Omega_p \right], \quad (\text{A.59})$$

$$\Pi_{\text{D}}^v = -\frac{\omega}{2} \text{Im} \left[ \omega^2 \int_{\Omega_p} \tilde{\rho} \mathbf{u}_s \cdot \mathbf{u}_s^* d\Omega_p - \int_{\Omega_p} \frac{\phi^2}{\omega^2 \tilde{\rho}_{22}} \nabla p_f \cdot \nabla p_f^* d\Omega_p + 2\tilde{\gamma} \int_{\Omega_p} \text{Re}(\nabla p_f \cdot \mathbf{u}_s^*) d\Omega_p \right] \quad (\text{A.60})$$

$$\Pi_{\text{D}}^t = -\frac{\omega}{2} \text{Im} \left[ \int_{\Omega_p} \frac{\phi^2}{\tilde{R}} p_f p_f^* d\Omega_p \right], \quad (\text{A.61})$$

where,  $\Pi_{\text{D}}^s$  is obtained from  $\Pi_{\text{elas}}^s$ ,  $\Pi_{\text{D}}^v$  from  $\Pi_{\text{iner}}^s + \Pi_{\text{iner}}^f + \Pi_{\text{coup}}^{sf}$  and  $\Pi_{\text{D}}^t$  from  $\Pi_{\text{elas}}^f$ . It is also noticeably that  $\text{Im}(\tilde{\gamma} + \tilde{\xi}) = \text{Im}(\tilde{\gamma})$ , as  $\tilde{Q}/\tilde{R}$  is a real number (see Eqs. (2.40) and (2.41)).

Finally, it is possible to apply the FEM to the aforementioned relations, generating the time-averaged dissipated powers as functions of the elementary matrices,

$$\Pi_{\text{D}}^s = \frac{\omega}{2} \text{Im} \left( \hat{\mathbf{u}}_s^H \tilde{\mathbf{K}}_p \hat{\mathbf{u}}_s \right), \quad (\text{A.62})$$

$$\Pi_{\text{D}}^v = -\frac{\omega}{2} \text{Im} \left( \omega^2 \hat{\mathbf{u}}_s^H \tilde{\mathbf{M}}_p \hat{\mathbf{u}}_s - \frac{1}{\omega^2} \hat{\mathbf{p}}_f^H \tilde{\mathbf{H}}_p \hat{\mathbf{p}}_f + 2 \hat{\mathbf{u}}_s^H \tilde{\mathbf{C}}_{p1} \hat{\mathbf{p}}_f \right), \quad (\text{A.63})$$

$$\Pi_{\text{D}}^t = -\frac{\omega}{2} \text{Im} \left( \hat{\mathbf{p}}_f^H \tilde{\mathbf{Q}}_p \hat{\mathbf{p}}_f \right), \quad (\text{A.64})$$

where  $\text{Im}(\cdot)$  is the imaginary part of a function, and the superscripts  $(\cdot)^*$  and  $(\cdot)^H$  are, respectively, the conjugate and the transpose conjugate of a complex variable. An important point to note is that, when considering the thin elastic structures and the anechoic termination in the composition of the observed domain ( $\Omega = \Omega_d \cup \Omega_{\text{nd}}$ ), two more time-averaged dissipated powers should be included in Eqs. (A.62), (A.63) and (A.64). However, the current double-wall composition causes a natural pressure reduction in the outlet region, which is even more pronounced with the addition of materials between such walls, so that the acoustic power contribution can be neglected. Thus, Eq. (A.62) can be rewritten to encompass the purely elastic power portion,

$$\Pi_{\text{D}}^s = \frac{\omega}{2} \text{Im} \left( \hat{\mathbf{u}}_e^H \mathbf{K}_e \hat{\mathbf{u}}_e \right) + \frac{\omega}{2} \text{Im} \left( \hat{\mathbf{u}}_s^H \tilde{\mathbf{K}}_p \hat{\mathbf{u}}_s \right). \quad (\text{A.65})$$

Furthermore, the derivation of  $\text{MPL}_D$  with respect to  $x_i$  is referred as  $\alpha_i$ , so,

$$\alpha_i = \frac{1}{\omega_f - \omega_s} \int_{\omega_s}^{\omega_f} \frac{10}{\ln 10} \left( \frac{\vartheta_1 \frac{d\Pi_D^s}{dx_i} + \vartheta_2 \frac{d\Pi_D^v}{dx_i} + \vartheta_3 \frac{d\Pi_D^t}{dx_i}}{\vartheta_1 \Pi_D^s + \vartheta_2 \Pi_D^v + \vartheta_3 \Pi_D^t} \right) d\Omega_p. \quad (\text{A.66})$$

At this moment, consider  $\hat{\boldsymbol{\theta}} = \boldsymbol{\theta}_{\text{Re}} + j\boldsymbol{\theta}_{\text{Im}}$ , where  $\boldsymbol{\theta}_{\text{Re}}$  and  $\boldsymbol{\theta}_{\text{Im}}$  stands for the real and imaginary parts of  $\hat{\boldsymbol{\theta}}$ . The sum of the time-averaged dissipated powers can thus be rewritten as,

$$\Pi_D(\boldsymbol{\theta}_{\text{Re}}, \boldsymbol{\theta}_{\text{Im}}, x_i) = \vartheta_1 \Pi_D^s + \vartheta_2 \Pi_D^v + \vartheta_3 \Pi_D^t. \quad (\text{A.67})$$

By the introduction of Lagrange multipliers,  $\boldsymbol{\lambda}_{A3}$ , the augmented performance index appear,

$$\Pi_D = \Pi_D(\boldsymbol{\theta}_{\text{Re}}, \boldsymbol{\theta}_{\text{Im}}, x_i) + \boldsymbol{\lambda}_{A3}^T (\tilde{\mathbf{Z}}\hat{\boldsymbol{\theta}} - \hat{\mathbf{f}}) + \boldsymbol{\lambda}_{A3}^H (\tilde{\mathbf{Z}}^*\hat{\boldsymbol{\theta}}^* - \hat{\mathbf{f}}^*), \quad (\text{A.68})$$

with its derivation being,

$$\begin{aligned} \frac{d\Pi_D}{dx_i} &= \frac{\partial \Pi_D}{\partial x_i} + \frac{\partial \Pi_D}{\partial \boldsymbol{\theta}_{\text{Re}}} \frac{\partial \boldsymbol{\theta}_{\text{Re}}}{\partial x_i} + \frac{\partial \Pi_D}{\partial \boldsymbol{\theta}_{\text{Im}}} \frac{\partial \boldsymbol{\theta}_{\text{Im}}}{\partial x_i} \\ &+ \boldsymbol{\lambda}_{A3}^T \left( \frac{\partial \tilde{\mathbf{Z}}}{\partial x_i} \hat{\boldsymbol{\theta}} + \tilde{\mathbf{Z}} \frac{\partial \boldsymbol{\theta}_{\text{Re}}}{\partial x_i} + j\tilde{\mathbf{Z}} \frac{\partial \boldsymbol{\theta}_{\text{Im}}}{\partial x_i} - \frac{\partial \hat{\mathbf{f}}}{\partial x_i} \right) \\ &+ \boldsymbol{\lambda}_{A3}^H \left( \frac{\partial \tilde{\mathbf{Z}}^*}{\partial x_i} \hat{\boldsymbol{\theta}}^* + \tilde{\mathbf{Z}}^* \frac{\partial \boldsymbol{\theta}_{\text{Re}}}{\partial x_i} - j\tilde{\mathbf{Z}}^* \frac{\partial \boldsymbol{\theta}_{\text{Im}}}{\partial x_i} - \frac{\partial \hat{\mathbf{f}}^*}{\partial x_i} \right), \end{aligned} \quad (\text{A.69})$$

that becomes,

$$\begin{aligned} \frac{d\Pi_D}{dx_i} &= \frac{\partial \Pi_D}{\partial x_i} + \left( \frac{\partial \Pi_D}{\partial \boldsymbol{\theta}_{\text{Re}}} + \boldsymbol{\lambda}_{A3}^T \tilde{\mathbf{Z}} + \boldsymbol{\lambda}_{A3}^H \tilde{\mathbf{Z}}^* \right) \frac{\partial \boldsymbol{\theta}_{\text{Re}}}{\partial x_i} \\ &+ \left( \frac{\partial \Pi_D}{\partial \boldsymbol{\theta}_{\text{Im}}} + j\boldsymbol{\lambda}_{A3}^T \tilde{\mathbf{Z}} - j\boldsymbol{\lambda}_{A3}^H \tilde{\mathbf{Z}}^* \right) \frac{\partial \boldsymbol{\theta}_{\text{Im}}}{\partial x_i} \\ &+ \boldsymbol{\lambda}_{A3}^T \left( \frac{\partial \tilde{\mathbf{Z}}}{\partial x_i} \hat{\boldsymbol{\theta}} - \frac{\partial \hat{\mathbf{f}}}{\partial x_i} \right) + \boldsymbol{\lambda}_{A3}^H \left( \frac{\partial \tilde{\mathbf{Z}}^*}{\partial x_i} \hat{\boldsymbol{\theta}}^* - \frac{\partial \hat{\mathbf{f}}^*}{\partial x_i} \right). \end{aligned} \quad (\text{A.70})$$

The unknown variables  $\partial \boldsymbol{\theta}_{\text{Re}}/\partial x_i$  and  $\partial \boldsymbol{\theta}_{\text{Im}}/\partial x_i$  may finally be removed from Eq. (A.70) by setting,

$$\begin{cases} \boldsymbol{\lambda}_{A3}^T \tilde{\mathbf{Z}} + \boldsymbol{\lambda}_{A3}^H \tilde{\mathbf{Z}}^* = -\frac{\partial \Pi_D}{\partial \boldsymbol{\theta}_{\text{Re}}}, \\ j\boldsymbol{\lambda}_{A3}^T \tilde{\mathbf{Z}} - j\boldsymbol{\lambda}_{A3}^H \tilde{\mathbf{Z}}^* = -\frac{\partial \Pi_D}{\partial \boldsymbol{\theta}_{\text{Im}}}. \end{cases} \quad (\text{A.71})$$

Multiplying the second expression by  $-j$ , adding to the first and transposing both sides ( $\tilde{\mathbf{Z}}^T = \tilde{\mathbf{Z}}$ ), the adjoint equation is found,

$$\tilde{\mathbf{Z}} \boldsymbol{\lambda}_{A3} = \underbrace{-\frac{1}{2} \left( \frac{\partial \Pi_D}{\partial \boldsymbol{\theta}_{\text{Re}}} - j \frac{\partial \Pi_D}{\partial \boldsymbol{\theta}_{\text{Im}}} \right)^T}_{\mathbf{f}_{\text{ad}}^{A3}}, \quad (\text{A.72})$$

with its right side being the adjoint load vector,  $\mathbf{f}_{\text{ad}}^{\mathcal{A}3}$ . Since  $\Pi_{\text{D}}$  is represented by Eq. (A.67), the next step consists in finding the expressions for the structural,  $\mathbf{f}_{\text{ad}}^s$ , viscous,  $\mathbf{f}_{\text{ad}}^v$ , and thermal,  $\mathbf{f}_{\text{ad}}^t$ , adjoint load vectors that compose  $\mathbf{f}_{\text{ad}}^{\mathcal{A}3}$ . After a series of mathematical manipulations, one may write,

$$\mathbf{f}_{\text{ad}}^s = -\frac{\omega}{2} \left[ \hat{\mathbf{u}}_e^H \text{Im}(\mathbf{K}_e) + \hat{\mathbf{u}}_s^H \text{Im}(\tilde{\mathbf{K}}_p) \right]^T, \quad (\text{A.73})$$

$$\mathbf{f}_{\text{ad}}^v = \frac{\omega}{2} \left[ \omega^2 \hat{\mathbf{u}}_s^H \text{Im}(\tilde{\mathbf{M}}_p) - \frac{1}{\omega^2} \hat{\mathbf{p}}_f^H \text{Im}(\tilde{\mathbf{H}}_p) + \hat{\mathbf{p}}_f^H \text{Im}(\tilde{\mathbf{C}}_{p1})^T + \hat{\mathbf{u}}_s^H \text{Im}(\tilde{\mathbf{C}}_{p1}) \right]^T, \quad (\text{A.74})$$

$$\mathbf{f}_{\text{ad}}^t = \frac{\omega}{2} \left[ \hat{\mathbf{p}}_f^H \text{Im}(\tilde{\mathbf{Q}}_p) \right]^T. \quad (\text{A.75})$$

The aforementioned procedures also lead to the final form of Eq. (A.70),

$$\frac{d\Pi_{\text{D}}}{dx_i} = \frac{\partial \Pi_{\text{D}}}{\partial x_i} + 2 \text{Re} \left[ \boldsymbol{\lambda}_{\mathcal{A}3}^T \left( \frac{\partial \tilde{\mathbf{Z}}}{\partial x_i} \hat{\boldsymbol{\theta}} - \frac{\partial \hat{\mathbf{f}}}{\partial x_i} \right) \right], \quad (\text{A.76})$$

with,

$$\frac{\partial \tilde{\mathbf{Z}}}{\partial x_i} = \begin{bmatrix} \frac{\partial \mathbf{K}_e}{\partial x_i} - \omega^2 \frac{\partial \mathbf{M}_e}{\partial x_i} & \mathbf{0} & \mathbf{0} & -\frac{\partial \mathbf{L}_{\text{ae}}}{\partial x_i} \\ \mathbf{0} & \frac{\partial \tilde{\mathbf{K}}_p}{\partial x_i} - \omega^2 \frac{\partial \tilde{\mathbf{M}}_p}{\partial x_i} & -\frac{\partial}{\partial x_i}(\tilde{\mathbf{C}}_{p1} + \tilde{\mathbf{C}}_{p2}) & -\frac{\partial \mathbf{L}_{\text{ap}}}{\partial x_i} \\ \mathbf{0} & -\frac{\partial}{\partial x_i}(\tilde{\mathbf{C}}_{p1} + \tilde{\mathbf{C}}_{p2})^T & \frac{1}{\omega^2} \frac{\partial \tilde{\mathbf{H}}_p}{\partial x_i} - \frac{\partial \tilde{\mathbf{Q}}_p}{\partial x_i} & \mathbf{0} \\ -\frac{\partial \mathbf{L}_{\text{ae}}^T}{\partial x_i} & -\frac{\partial \mathbf{L}_{\text{ap}}^T}{\partial x_i} & \mathbf{0} & \frac{1}{\omega^2} \frac{\partial \mathbf{H}_a}{\partial x_i} - \frac{1}{j\omega} \frac{\partial \mathbf{D}_a}{\partial x_i} - \frac{\partial \mathbf{Q}_a}{\partial x_i} \end{bmatrix}, \quad (\text{A.77})$$

where,

$$\frac{\partial \mathbf{K}_e}{\partial x_i} = \frac{\partial \mathbf{M}_e}{\partial x_i} = \mathbf{0}, \quad (\text{A.78})$$

$$\frac{\partial \mathbf{L}_{\text{ae}}}{\partial x_i} = \frac{\partial \mathbf{L}_{\text{ap}}}{\partial x_i} = \frac{\partial \mathbf{L}_{\text{ae}}^T}{\partial x_i} = \frac{\partial \mathbf{L}_{\text{ap}}^T}{\partial x_i} = \mathbf{0}, \quad (\text{A.79})$$

$$\frac{\partial \mathbf{H}_a}{\partial x_i} = \frac{\partial \mathbf{Q}_a}{\partial x_i} = \frac{\partial \mathbf{D}_a}{\partial x_i} = \mathbf{0}, \quad (\text{A.80})$$

$$(\text{A.81})$$

and, in an element domain  $\Omega_p^i$ ,

$$\frac{\partial \tilde{\mathbf{K}}_p^i}{\partial x_i} = \int_{\Omega_p^i} (\nabla \mathbf{N}_e)^T \frac{\partial}{\partial x_i} [\mathbf{E}_p(x_{i_1}, x_{i_2})] \nabla \mathbf{N}_e d\Omega_p^i, \quad (\text{A.82})$$

$$\frac{\partial \tilde{\mathbf{M}}_p^i}{\partial x_i} = \frac{\partial}{\partial x_i} [\tilde{\rho}(x_{i_1}, x_{i_2})] \int_{\Omega_p^i} \mathbf{N}_e^T \mathbf{N}_e d\Omega_p^i, \quad (\text{A.83})$$

$$\frac{\partial \tilde{\mathbf{H}}_p^i}{\partial x_i} = \frac{\partial}{\partial x_i} \left[ \frac{\phi^2}{\tilde{\rho}_{22}}(x_{i_1}, x_{i_2}) \right] \int_{\Omega_p^i} (\nabla \mathbf{N}_a)^T \nabla \mathbf{N}_a d\Omega_p^i, \quad (\text{A.84})$$

$$\frac{\partial \tilde{\mathbf{Q}}_p^i}{\partial x_i} = \frac{\partial}{\partial x_i} \left[ \frac{\phi^2}{\tilde{R}}(x_{i_1}, x_{i_2}) \right] \int_{\Omega_p^i} \mathbf{N}_a^T \mathbf{N}_a d\Omega_p^i, \quad (\text{A.85})$$

$$\frac{\partial \tilde{\mathbf{C}}_{p1}^i}{\partial x_i} = \frac{\partial}{\partial x_i} \left[ \frac{\phi}{\tilde{\alpha}}(x_{i_1}, x_{i_2}) \right] \int_{\Omega_p^i} \mathbf{N}_e^T \nabla \mathbf{N}_a d\Omega_p^i, \quad (\text{A.86})$$

$$\frac{\partial \tilde{\mathbf{C}}_{p2}^i}{\partial x_i} = \frac{\partial}{\partial x_i} \left[ \tilde{\xi}(x_{i_1}, x_{i_2}) \right] \int_{\Omega_p^i} \phi (\nabla \cdot \mathbf{N}_e)^T \mathbf{N}_a d\Omega_p^i. \quad (\text{A.87})$$

In the above,  $\mathbf{E}_p(x_{i_1}, x_{i_2})$  can be written in terms of  $\tilde{N}(x_{i_1}, x_{i_2})$  and  $\hat{A}(x_{i_1}, x_{i_2})$  (see Eq. (2.67)), while  $(\phi/\tilde{\alpha})(x_{i_1}, x_{i_2})$  is equivalent to  $\tilde{\gamma} + \tilde{\xi}(x_{i_1}, x_{i_2})$ , where  $\tilde{\gamma}$  is not a function of the design variables (see Eq. (2.69) and Eqs. (A.91), (A.92) and (A.93)).

The final forms of Eqs. (A.82) to (A.87) are obtained by the derivation of the proposed multiphysical MIS,

$$\tilde{\Psi}(x_{i_1}, x_{i_2}) = \tilde{\Psi}_e + x_{i_2}^{\zeta_2} (\tilde{\Psi}_p - \tilde{\Psi}_e) + x_{i_1}^{\zeta_1} (\tilde{\Psi}_a - \tilde{\Psi}_p), \quad (\text{A.88})$$

with respect to  $x_{i_1}$  and  $x_{i_2}$ , that is,

$$\frac{\partial \tilde{\Psi}(x_{i_1}, x_{i_2})}{\partial x_{i_1}} = \zeta_1 x_{i_1}^{(\zeta_1-1)} (\tilde{\Psi}_a - \tilde{\Psi}_p), \quad (\text{A.89})$$

$$\frac{\partial \tilde{\Psi}(x_{i_1}, x_{i_2})}{\partial x_{i_2}} = \zeta_2 x_{i_2}^{(\zeta_2-1)} (\tilde{\Psi}_p - \tilde{\Psi}_e), \quad (\text{A.90})$$

with  $\tilde{\Psi}_p$ ,  $\tilde{\Psi}_a$  and  $\tilde{\Psi}_e$  being,

$$\tilde{\Psi}_p = \left\{ \tilde{\xi}_p, \tilde{\rho}_p, \tilde{N}_p, \hat{A}_p, (\phi^2/\tilde{\rho}_{22})_p, (\phi^2/\tilde{R})_p \right\} \equiv \tilde{\Psi}, \quad (\text{A.91})$$

$$\tilde{\Psi}_a = \left\{ 1, o_a \tilde{\rho}_p, o_a \tilde{N}_p, o_a \hat{A}_p, 1/\rho_a, 1/\kappa_a \right\}, \quad (\text{A.92})$$

$$\tilde{\Psi}_e = \left\{ o_e \tilde{\xi}_p, \rho_e, \tilde{N}_e, \tilde{A}_e, o_e (\phi^2/\tilde{\rho}_{22})_p, o_e (\phi^2/\tilde{R})_p \right\}. \quad (\text{A.93})$$

To avoid numerical instabilities, small constants are adopted as  $o_a = o_e = 10^{-9}$ , instead of being zeroed.

Lastly,  $\partial\Pi_D/\partial x_i$  and  $\partial\hat{\mathbf{f}}/\partial x_i$  are defined by the following,

$$\frac{\partial\Pi_D}{\partial x_i} = \text{Im} \left( \begin{array}{c} \left\{ \hat{\mathbf{u}}_s \right\} \\ \left\{ \hat{\mathbf{p}}_f \right\} \end{array} \right)^H \frac{\omega}{2} \begin{bmatrix} \vartheta_1 \frac{\partial\tilde{\mathbf{K}}_p}{\partial x_i} - \vartheta_2 \omega^2 \frac{\partial\tilde{\mathbf{M}}_p}{\partial x_i} & -\vartheta_2 \frac{\partial\tilde{\mathbf{C}}_{p1}}{\partial x_i} \\ -\vartheta_2 \frac{\partial\tilde{\mathbf{C}}_{p1}^T}{\partial x_i} & \frac{\vartheta_2}{\omega^2} \frac{\partial\tilde{\mathbf{H}}_p}{\partial x_i} - \vartheta_3 \frac{\partial\tilde{\mathbf{Q}}_p}{\partial x_i} \end{bmatrix} \begin{array}{c} \left\{ \hat{\mathbf{u}}_s \right\} \\ \left\{ \hat{\mathbf{p}}_f \right\} \end{array} \right), \quad (\text{A.94})$$

and

$$\frac{\partial\hat{\mathbf{f}}}{\partial x_i} = 0, \quad (\text{A.95})$$

which concludes the approach. All aforementioned expressions have been validated via finite differences method.

## **B | Publications in International Conferences**

This appendix presents the works published in annals of events throughout the PhD period. In chronological order, these works are:

Pereira, R. L.; Anaya-Jaimes, L. M.; Pavanello, R. Design of periodic noise barriers using the bi-directional evolutionary optimization method. In: *e-Forum Acusticum*. v. 1, p.209–215, 2020. <https://doi.org/10.48465/fa.2020.1068>. (Reproduced from the HAL open science repository. Visit: <https://hal.science/> for more information).

Pereira, R. L.; Anaya-Jaimes, L. M.; Pavanello, R. Topology optimization of acoustic-poroelastic-elastic structures for sound attenuation. In: *15th World Congress on Computational Mechanics & 8Th Asian Pacific Congress on Computational Mechanics*, 2022. <https://doi.org/10.23967/wccm-apcom.2022.117> (Reproduced from the Scipedia open science repository. Visit: <https://www.scipedia.com/> for more information).

Pereira, R. L.; Pavanello, R. Topology optimization design of acoustic-poroelastic-elastic structures by the BESO Approach. In: *8th International Symposium on Solid Mechanics*, 2022. <https://doi.org/10.26678/ABCM.MECSOL2022.MSL22-0197> (Reproduced with permission from ABCM – see the first page of the paper for the copyright clearance).



## Design of Periodic Acoustic Barriers Using an Evolutionary Topological Optimization Procedure

Rodrigo L. Pereira, Lidy Marcela Anaya Jaimes, Renato Pavanello

### ► To cite this version:

Rodrigo L. Pereira, Lidy Marcela Anaya Jaimes, Renato Pavanello. Design of Periodic Acoustic Barriers Using an Evolutionary Topological Optimization Procedure. Forum Acusticum, Dec 2020, Lyon, France. pp.209-215, 10.48465/fa.2020.1068 . hal-03235499

**HAL Id: hal-03235499**

**<https://hal.science/hal-03235499>**

Submitted on 27 May 2021

**HAL** is a multi-disciplinary open access archive for the deposit and dissemination of scientific research documents, whether they are published or not. The documents may come from teaching and research institutions in France or abroad, or from public or private research centers.

L'archive ouverte pluridisciplinaire **HAL**, est destinée au dépôt et à la diffusion de documents scientifiques de niveau recherche, publiés ou non, émanant des établissements d'enseignement et de recherche français ou étrangers, des laboratoires publics ou privés.

# DESIGN OF PERIODIC NOISE BARRIERS USING THE BI-DIRECTIONAL EVOLUTIONARY STRUCTURAL OPTIMIZATION METHOD

**Rodrigo L. Pereira<sup>1</sup>**      **Marcela Anaya-Jaimes<sup>1</sup>**      **Renato Pavanello<sup>1</sup>**

Department of Computational Mechanics, School of Mechanical Engineering,  
University of Campinas, Rua Mendeleev, 200, 13083-860 Campinas, Brazil

pereira@fem.unicamp.br, lidy@fem.unicamp.br, pava@fem.unicamp.br

## ABSTRACT

In the past few years, acoustic-mechanical devices have become widely used, which increased the demand for noise control solutions. One of the approaches to solve such problems consists in designing noise barriers. However, finding the best topology for these barriers can be a complex task. In this work it is proposed a methodology to design periodic noise barriers, composed of rigid materials, using the bi-directional evolutionary structural optimization (BESO) method. The acoustic problem is modeled using the Helmholtz equation and solved by the finite element procedure, while a material interpolation scheme is used for switching acoustic and rigid elements. The optimization problem is defined as the minimization of the average square pressure amplitude in a specific region of the acoustic domain, while the volume of the barrier is reduced. The sensitivity analysis was carried out by the gradient of the objective function with respect to the design variable. Two cases are presented in order to show the capabilities of the proposed approach. In the first one, periodic conditions are imposed in the entire system, while in the second non-periodic conditions are considered. The results showed that, although the barrier volume was reduced by 35% in both cases, the objective function decreased at least 68.80%.

## 1. INTRODUCTION

In the last decades, topology optimization methods have become powerful engineering tools since they provide non-intuitive structure designs for a large number of applications. Generally, what is sought is a lighter structure that is also able to enhance a few characteristics of the system, making the design even less costly. After the development and popularization of computing, many methods arose in order to make use of topology optimization.

The Evolutionary Structural Optimization (ESO) method, first introduced by Xie and Steven in the early 1990s [1], has as premise the removal of inefficient material from the structure. However, this could also result in non-optimal geometries due to inappropriate initial design settings [2]. Later, the Bi-directional Evolutionary Structural Optimization (BESO) method, proposed by Yang et al. [3], made possible not only to remove but also add elements to the structure during the optimization process. Shortly thereafter, the so-called new BESO algorithm [4]

has been used in many works, since also provides solutions for some important numerical problems, such as checkerboard pattern and mesh-dependence. All these improvements made the method even more popular and highly used in many engineering applications [5,6].

Acoustic-mechanical devices (AMDs), like microphones and speakerphones, are increasingly familiar and so is the noise control situation. As a result, the interest of many researchers, whose main focus is the design of acoustic barriers, enhanced. Due to the vast applicability of such acoustic components, going from houses, hospitals and schools to the automotive industry, for example, a great number of techniques have been implemented to design such systems.

It became common to design acoustic barriers, in repetitive domains, taking into account the complexities of fluid-structure interactions [7]. However, a more simplified approach, which consists of infinitely enlarge, in a theoretical point of view, the mass density and bulk modulus of the barrier material to generate a rigid structure, has gained many supporters [8–10]. This is due to the fact that it reduces the multiphysical fluid-structure problem to an acoustical one, ruled by the Helmholtz equation.

Acoustic topology optimization (ATO) problems have been solved, using the BESO method, in the works of Vicente et al. [11] and Picelli et al. [12], but their main focus was on the structural part of the problem and, in many situations, even neglected the effects of the acoustic domain. Kook [13] and Dilgen et al. [14] also used the bi-directional optimization method, together with a mixed u/p formulation, in order to solve classical acoustic-structure problems. Finally, Azevedo et al. [15] combined the BESO approach and the rigid material approximation with the goal of maximizing the transmission loss in the internal partitions of a reactive muffler.

With this in mind and seeking to enhance the use of the bi-directional evolutionary structural topology optimization method in the context of noise attenuation, this paper aims to optimize noise barriers when subjected to periodic and non-periodic conditions. The organization of this paper is presented as follows: In section 2 the acoustic problem is formulated using the finite element approach. In section 3 the optimization problem, as well as the material interpolation scheme and the design sensitivity analysis are discussed. Also in this section, the BESO method is described in detail. Section 4 presents numerical results,

intending to demonstrate the relevance of the presented methodology. Finally, conclusions are drawn in section 5.

## 2. ACOUSTIC PROBLEM FORMULATION

Considering an acoustic volume  $\Omega_f$  that includes the design,  $\Omega_d$ , non-design,  $\Omega_{nd}$ , and objective,  $\Omega_o$ , domains, as illustrated in Fig. 1. The boundaries are of Dirichlet,  $\Gamma_D$ , Neumann,  $\Gamma_N$ , and Robin,  $\Gamma_R$ , types where it is possible to prescribe the acoustic pressure, normal gradient pressure and acoustic admittance [16], respectively, according to the system of Eqn. (1).

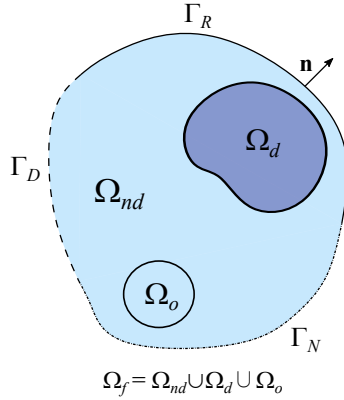


Figure 1. Acoustic continuum

$$\begin{cases} \nabla^2 \tilde{p} + \frac{\omega^2}{c^2} \tilde{p} = 0 & \text{in } \Omega_f \\ \tilde{p} = \bar{p} & \text{at } \Gamma_D \\ \nabla \tilde{p} \cdot \mathbf{n} = -\rho_0 \bar{a}_n & \text{at } \Gamma_N \\ \nabla \tilde{p} \cdot \mathbf{n} + i\rho_0 \omega \tilde{A} \tilde{p} = 0 & \text{at } \Gamma_R \end{cases} \quad (1)$$

Where  $\tilde{p}$  and  $\bar{p}$  are, respectively, the complex and prescribed acoustic pressure,  $\omega$  is the angular frequency,  $c$  is the speed of sound in air,  $\mathbf{n}$  is the outward unit normal vector,  $\rho_0$  is the fluid mass density,  $\bar{a}_n$  is the prescribed normal acceleration and  $\tilde{A}$  is the acoustic admittance.

In order to provide a discrete approximation of the continuum problem stated in Eqn. (1), the finite element (FE) method is considered [15–17]. Thus, multiplying the Helmholtz equation by a weight function  $\nu$  and integrating on the entire fluid domain (method of weighted residual) the strong form can be written as Eqn. (2).

$$\int_{\Omega_f} \nabla^2 \tilde{p} \nu \, d\Omega_f + \frac{\omega^2}{c^2} \int_{\Omega_f} \tilde{p} \nu \, d\Omega_f = 0 \quad (2)$$

Applying Green's theorem, Eqn. (2) becomes,

$$-\int_{\Omega_f} \nabla \tilde{p} \cdot \nabla \nu \, d\Omega_f + \int_{\Gamma} \nabla \tilde{p} \cdot \mathbf{n} \nu \, d\Gamma + \frac{\omega^2}{c^2} \int_{\Omega_f} \tilde{p} \nu \, d\Omega_f = 0 \quad (3)$$

for  $\Gamma = \Gamma_D \cup \Gamma_N \cup \Gamma_R$ . Substituting the boundary conditions presented in Eqn. (1), and knowing that  $\nabla \tilde{p} \cdot \mathbf{n} = 0$

for the rigid wall case, the weak form can then be written as Eqn. (4).

$$\int_{\Omega_f} \nabla \tilde{p} \cdot \nabla \nu \, d\Omega_f + \int_{\Gamma_N} \rho_0 \bar{a}_n \nu \, d\Gamma_N + \int_{\Gamma_R} i\rho_0 \omega \tilde{A} \tilde{p} \nu \, d\Gamma_R - \frac{\omega^2}{c^2} \int_{\Omega_f} \tilde{p} \nu \, d\Omega_f = 0 \quad (4)$$

The complex acoustic pressure and its normal gradient can be rewritten in a more suitable manner,

$$\tilde{p} = \mathbf{N} \tilde{\mathbf{p}}_i, \quad \nabla \tilde{p} = \partial \mathbf{N} \tilde{\mathbf{p}}_i \quad (5)$$

where  $\mathbf{N}$  is the FE shape function matrix, with  $\partial \mathbf{N}$  denoting its derivation, and  $\tilde{\mathbf{p}}_i$  is the complex acoustic pressure vector of the  $i$ th element. With the use of Galerkin method, the weight function can be written,

$$\nu = \mathbf{N} \nu_i, \quad \nabla \nu = \partial \mathbf{N} \nu_i \quad (6)$$

where  $\nu$  is the weight function vector of the  $i$ th element. Finally, substituting Eqns. (5) and (6) in Eqn. (4) and performing the FE assembly procedure, the global dynamic system arises,

$$\mathbf{S} \tilde{\mathbf{p}} = (\mathbf{K} + i\omega \mathbf{C} - \omega^2 \mathbf{M}) \tilde{\mathbf{p}} = \mathbf{f} \quad (7)$$

where  $\mathbf{S}$  corresponds to the system matrix and has contributions from  $\mathbf{K}$ ,  $\mathbf{C}$  and  $\mathbf{M}$ , denoting the acoustic stiffness, damping and mass matrices, respectively, while  $\mathbf{f}$  is the acoustic load vector. Besides,

$$\mathbf{K}_i = \frac{1}{\rho_0} \int_{\Omega_f} (\partial \mathbf{N})^t \partial \mathbf{N} \, d\Omega_f \quad (8)$$

$$\mathbf{C}_i = \tilde{A} \int_{\Gamma_R} \mathbf{N}^t \mathbf{N} \, d\Gamma_R \quad (9)$$

$$\mathbf{M}_i = \frac{1}{\kappa} \int_{\Omega_f} \mathbf{N}^t \mathbf{N} \, d\Omega_f \quad (10)$$

$$\mathbf{f}_i = -\bar{a}_n \int_{\Gamma_N} \mathbf{N}^t \, d\Gamma_N \quad (11)$$

where the subscript  $i$  represents elementary variables. The bulk modulus of the acoustic medium is denoted by  $\kappa$ , which is equal to  $\rho_0 c^2$ .

## 3. RIGID BARRIER TOPOLOGY OPTIMIZATION

In this section, the optimization problem is presented, as well as the adopted material interpolation scheme, the design sensitivity analysis and the evolutionary procedure. Eqn. (12) states the topology optimization problem as the minimization of the average square acoustic pressure amplitude at  $\Omega_o$  [7–9, 13] subject to restrictions stated in Eqns. (13), (14) and (15).

$$\text{Minimize: } \Phi = \frac{1}{\int_{\Omega_o} d\mathbf{r}} \int_{\Omega_o} |\tilde{p}(\mathbf{r}, \chi(\mathbf{r}))|^2 \, d\mathbf{r} \quad (12)$$

$$\text{Subjected to: } V^* - \frac{1}{\int_{\Omega_d} d\mathbf{r}} \int_{\Omega_d} \chi(\mathbf{r}) \, d\mathbf{r} = 0 \quad (13)$$

$$\mathbf{S}(\chi(\mathbf{r})) \tilde{\mathbf{p}}(\mathbf{r}, \chi(\mathbf{r})) = \mathbf{f} \quad (14)$$

$$\chi(\mathbf{r}) = 0 \text{ or } 1 \quad \forall \mathbf{r} \in \Omega_d \quad (15)$$

Where  $\Phi$  is the objective function and  $V^*$  is the imposed volume fraction, which varies from 0 to 1. Eqn. (14) exposes that  $\tilde{\mathbf{p}}$  depends on the binary design variable,  $\chi$ , and the position,  $\mathbf{r}$ , vectors. The elemental values of  $\chi$  can only be 0 for air or 1 for rigid materials.

### 3.1 Material interpolation scheme

As discussed in section 2, three different regions are included in the fluid domain  $\Omega_f$  (see Fig. 1). In the non-design,  $\Omega_{nd}$ , and objective,  $\Omega_o$ , domains the medium is air. However, in the design domain,  $\Omega_d$ , the medium is composed of an acoustic barrier of rigid constitution. Following many researchers [7–10, 18], this so-called rigid material is the result of a mathematical resource in which the air density and bulk modulus are infinitely amplified, from a purely theoretical point of view, in order to generate a material where the wave is totally reflected. However, to avoid numerical singularities in the calculation of the acoustic finite element matrices, adequate values need to be chosen for these variables. In this sense, the physical properties considered are  $\rho_{air} = 1.21 \text{ kg/m}^3$ ,  $\kappa_{air} = 1.42e5 \text{ Pa}$ ,  $\rho_{rigid} = 1.21e5 \text{ kg/m}^3$  and  $\kappa_{rigid} = 1.21e12 \text{ Pa}$ , where the subscripts *air* and *rigid* denote air and rigid material, respectively [9]. To find the optimal distribution of rigid in  $\Omega_d$ , the material interpolation scheme, presented in Eqns. (16) and (17), is adopted.

$$\frac{1}{\rho} = \frac{1}{\rho_{air}} + \chi \left( \frac{1}{\rho_{rigid}} - \frac{1}{\rho_{air}} \right) \quad (16)$$

$$\frac{1}{\kappa} = \frac{1}{\kappa_{air}} + \chi \left( \frac{1}{\kappa_{rigid}} - \frac{1}{\kappa_{air}} \right) \quad (17)$$

### 3.2 Design Sensitivity Analysis

It is discussed, in this section, the sensitivity numbers based on the average square acoustic pressure amplitude [7]. Thus, since  $\tilde{\mathbf{p}}$  is a complex vector, it can be written as follows,

$$\tilde{\mathbf{p}} = \mathbf{p}_R + i\mathbf{p}_I \quad (18)$$

with  $\mathbf{p}_R$  and  $\mathbf{p}_I$  denoting real and imaginary parts of  $\tilde{\mathbf{p}}$ . Knowing that  $\Phi$  is a function of,

$$\Phi = \Phi(\mathbf{p}_R, \mathbf{p}_I, \chi), \quad (19)$$

the adjoint method [19] is used by the introduction of Lagrangian multipliers,  $\tilde{\boldsymbol{\lambda}}$  and  $\bar{\boldsymbol{\lambda}}$ ,

$$\Phi = \Phi(\mathbf{p}_R, \mathbf{p}_I, \chi) + \tilde{\boldsymbol{\lambda}}^t (\mathbf{S}\tilde{\mathbf{p}} - \mathbf{f}) + \bar{\boldsymbol{\lambda}}^t (\bar{\mathbf{S}}\bar{\tilde{\mathbf{p}}} - \bar{\mathbf{f}}) \quad (20)$$

where the over bars denote complex conjugates. It is important to note that all pressure vectors are also dependent on  $\chi$ , but this was not shown in Eqns. (18), (19) and (20) in order to simplify the notation.

Taking the derivative of Eqn. (20), with respect to the

design domain variable, yields,

$$\begin{aligned} \frac{d\Phi}{d\chi} = & \frac{\partial\Phi}{\partial\chi} + \frac{\partial\Phi}{\partial\mathbf{p}_R} \frac{\partial\mathbf{p}_R}{\partial\chi} + \frac{\partial\Phi}{\partial\mathbf{p}_I} \frac{\partial\mathbf{p}_I}{\partial\chi} + \\ & \tilde{\boldsymbol{\lambda}}^t \left( \frac{\partial\mathbf{S}}{\partial\chi} \tilde{\mathbf{p}} + \mathbf{S} \frac{\partial\tilde{\mathbf{p}}}{\partial\chi} + i\mathbf{S} \frac{\partial\mathbf{p}_I}{\partial\chi} - \frac{\partial\mathbf{f}}{\partial\chi} \right) + \\ & \bar{\boldsymbol{\lambda}}^t \left( \frac{\partial\bar{\mathbf{S}}}{\partial\chi} \bar{\tilde{\mathbf{p}}} + \bar{\mathbf{S}} \frac{\partial\bar{\tilde{\mathbf{p}}}}{\partial\chi} - i\bar{\mathbf{S}} \frac{\partial\mathbf{p}_I}{\partial\chi} - \frac{\partial\bar{\mathbf{f}}}{\partial\chi} \right) \end{aligned} \quad (21)$$

which becomes,

$$\begin{aligned} \frac{d\Phi}{d\chi} = & \frac{\partial\Phi}{\partial\chi} + \tilde{\boldsymbol{\lambda}}^t \left( \frac{\partial\mathbf{S}}{\partial\chi} \tilde{\mathbf{p}} - \frac{\partial\mathbf{f}}{\partial\chi} \right) + \bar{\boldsymbol{\lambda}}^t \left( \frac{\partial\bar{\mathbf{S}}}{\partial\chi} \bar{\tilde{\mathbf{p}}} - \frac{\partial\bar{\mathbf{f}}}{\partial\chi} \right) + \\ & \left( \frac{\partial\Phi}{\partial\mathbf{p}_R} + \tilde{\boldsymbol{\lambda}}^t \mathbf{S} + \bar{\boldsymbol{\lambda}}^t \bar{\mathbf{S}} \right) \frac{\partial\mathbf{p}_R}{\partial\chi} + \\ & \left( \frac{\partial\Phi}{\partial\mathbf{p}_I} + i\tilde{\boldsymbol{\lambda}}^t \mathbf{S} - i\bar{\boldsymbol{\lambda}}^t \bar{\mathbf{S}} \right) \frac{\partial\mathbf{p}_I}{\partial\chi}. \end{aligned} \quad (22)$$

Since the Lagrangian multipliers can assume any number, the unknown expressions involving  $\frac{\partial\mathbf{p}_R}{\partial\chi}$  and  $\frac{\partial\mathbf{p}_I}{\partial\chi}$  can be eliminated by satisfying Eqns. (23) and (24).

$$\tilde{\boldsymbol{\lambda}}^t \mathbf{S} + \bar{\boldsymbol{\lambda}}^t \bar{\mathbf{S}} = -\frac{\partial\Phi}{\partial\mathbf{p}_R} \quad (23)$$

$$i\tilde{\boldsymbol{\lambda}}^t \mathbf{S} - i\bar{\boldsymbol{\lambda}}^t \bar{\mathbf{S}} = -\frac{\partial\Phi}{\partial\mathbf{p}_I} \quad (24)$$

Multiplying Eqn. (24) by  $-i$ , adding the result to Eqn. (23) and transposing both sides (knowing that  $\mathbf{S}^t = \mathbf{S}$ ), the adjoint equation is found,

$$\mathbf{S}\tilde{\boldsymbol{\lambda}} = -\frac{1}{2} \left( \frac{\partial\Phi}{\partial\mathbf{p}_R} - i\frac{\partial\Phi}{\partial\mathbf{p}_I} \right)^t \quad (25)$$

with  $\tilde{\boldsymbol{\lambda}}$  being the solution of the adjoint equation and with the right side of Eqn. (25) defined as the adjoint load. Finally, it is possible to rewrite Eqn. (22) in its final form,

$$\alpha_i = -\frac{d\Phi}{d\chi} = -\left\{ \frac{\partial\Phi}{\partial\chi} + 2Re \left[ \tilde{\boldsymbol{\lambda}}^t \left( \frac{\partial\mathbf{S}}{\partial\chi} \tilde{\mathbf{p}} - \frac{\partial\mathbf{f}}{\partial\chi} \right) \right] \right\} \quad (26)$$

where  $\alpha_i$  denotes the sensitivity number of the  $i$ th element. Also, it is noticeable that (26) has received a minus sign on its right side, which acts as a corrector of the BESO method towards minimization of the objective function.

Making use of the material interpolation scheme, Eqns. (16) and (17), the derivatives stated at Eqn. (26) can be easily written, at the elementary level, as follows,

$$\frac{\partial\Phi}{\partial\chi} = 0, \quad \frac{\partial\mathbf{f}}{\partial\chi} = 0 \quad (27)$$

$$\frac{\partial\mathbf{S}}{\partial\chi} = \frac{\partial\mathbf{K}}{\partial\chi} + i\omega \frac{\partial\mathbf{C}}{\partial\chi} - \omega^2 \frac{\partial\mathbf{M}}{\partial\chi} \quad (28)$$

with,

$$\frac{\partial\mathbf{C}}{\partial\chi} = 0 \quad (29)$$

$$\frac{\partial\mathbf{K}}{\partial\chi} = \left( \frac{1}{\rho_{rigid}} - \frac{1}{\rho_{air}} \right) \int_{\Omega_d} (\partial\mathbf{N})^t \partial\mathbf{N} d\Omega_d \quad (30)$$

$$\frac{\partial\mathbf{M}}{\partial\chi} = \left( \frac{1}{\kappa_{rigid}} - \frac{1}{\kappa_{air}} \right) \int_{\Omega_d} \mathbf{N}^t \mathbf{N} d\Omega_d. \quad (31)$$

Knowing that,

$$|\tilde{p}|^2 = p_R^2 + p_I^2 \quad (32)$$

$$p_R = \mathbf{N}\mathbf{p}_R \quad (33)$$

$$p_I = \mathbf{N}\mathbf{p}_I \quad (34)$$

the adjoint load can also be rewritten in an integral form as Eqn. (35).

$$-\frac{1}{2} \left( \frac{\partial \Phi}{\partial \mathbf{p}_R} - i \frac{\partial \Phi}{\partial \mathbf{p}_I} \right)^t = - \left( \frac{1}{\int_{\Omega_o} d\Omega_o} (\mathbf{p}_R^t - i \mathbf{p}_I^t) \int_{\Omega_o} \mathbf{N}^t \mathbf{N} d\Omega_o \right)^t \quad (35)$$

Since the optimization of periodic noise barriers is examined, an additional procedure needs to be performed in order to ensure the same topology in all barrier cells. In that way, when more than one cell is considered, a periodic vector of sensitivities is calculated by the following procedure:

1. Calculate all the sensitivity numbers inside the design domain using Eqns. (25) to (35).
2. Separate the sensitivity numbers by cell vectors, in order to identify the first, second, down to the last elements, of each periodic cell.
3. Average the sensitivity numbers of all the firsts, seconds, down to the last elements, and store those values inside another variable, called periodic sensitivity vector.
4. Use this new vector throughout the BESO methodology.

All this process ensures that the same barrier is obtained independently of the amount of cells considered.

### 3.3 Bi-directional Evolutionary Procedure

This section presents the Bi-directional evolutionary structural optimization (BESO) method related with acoustic problems [4, 5, 13, 15]. The main steps of the methodology are given as follows:

1. Execute the finite element procedure using Eqns. (7) to (11). This analysis should be performed in order to find the acoustic pressure in the fluid domain. At this point, it is important to differentiate air and rigid elements, that encompass the design domain, by attributing the correct physical properties to each case (see section 3.1).
2. Carry out the sensitivity analysis. In this case the sensitivity numbers were validated by comparing them to the ones obtained by the finite differences method.

3. Apply the filter scheme, Eqns. (36) to (38), in order to deal with numerical problems that arises with the use of low order elements [4, 20].

$$\alpha_j = \sum_{i=1}^M w_i \alpha_i \quad (36)$$

$$w_i = \frac{1}{M-1} \left( 1 - \frac{r_{ij}}{\sum_{i=1}^M r_{ij}} \right) \quad (37)$$

Where  $\alpha_j$  denotes the sensitivity number of the  $j$ th node,  $M$  is the total number of elements connected to the  $j$ th node,  $w_i$  is the weight factor of the  $i$ th element, with  $\sum_{i=1}^M w_i = 1$ , and  $r_{ij}$  corresponds to the distance between the center of the  $i$ th element and the  $j$ th node. Additionally, a length scale,  $r_{min}$ , is defined with the goal of identify the nodes that contribute to the sensitivity of the  $i$ th element as follows,

$$\alpha_i = \frac{\sum_{j=1}^{tnd} w(r_{ij}) \alpha_j}{\sum_{j=1}^{tnd} w(r_{ij})} \quad (38)$$

with  $tnd$  being the total number of nodes that has influence over  $\alpha_i$  and  $w(r_{ij})$  is the linear weight factor determined by  $r_{min} - r_{ij}$ , for all nodes inside the subdomain imposed by  $r_{min}$ .

4. Apply the sensitivity history. One of the main characteristics of the BESO method consists in the usage of discrete design variables, which may cause difficulties in the convergence of the objective function and its corresponding topology. One way to solve this issue is to average the sensitivity numbers with its historical information. A way to do that is by the application of Eqn. (39),

$$\alpha_i = \frac{\alpha_i^{it} + \alpha_i^{it-1}}{2} \quad (39)$$

where superscript  $it$  refers to the current iteration.

5. Define the volume target for the next iteration,

$$V_{it+1} = V_{it}(1 \pm ER) \quad (40)$$

where  $V_{it}$  is the volume fraction of the iteration  $it$  and  $ER$  is the evolutionary rate. When the final volume fraction,  $V^*$ , is reached, the next iterations must necessarily keep the volume constant until the stop criteria (step 7) is fulfilled.

6. Define element type. The definition of volume for the next iteration establishes a threshold for the amount of elements that will be air ( $\chi = 0$ ) or rigid ( $\chi = 1$ ). Looking at the sensitivity numbers in the context of minimization of the objective function, it is possible to write Eqns. (41) and (42).

$$\alpha_i \leq \alpha_{th} \quad \text{air elements} \quad (41)$$

$$\alpha_i > \alpha_{th} \quad \text{rigid elements} \quad (42)$$

Besides, another important parameter that needs to be addressed is the addition ratio,  $AR$ , which defines the additional volume that can return to the FE mesh. However, in order to restrict this amount, the maximum addition ratio,  $AR_{max}$ , is also stated. If the case  $AR > AR_{max}$  happens, only some elements with the lowest  $\alpha_i$  will be turned to air in order to respect the  $AR = AR_{max}$  restriction. This fact also implies that some elements with the highest  $\alpha_i$  will be turned to rigid, fulfilling  $V_{it+1}$  [12].

7. Repeat 1 to 6 until the final volume is reached and the stop criteria, Eqn. (43), is satisfied.

$$\frac{|\sum_{m=1}^5 \Phi_{it-m+1} - \sum_{m=1}^5 \Phi_{it-m-4}|}{\sum_{m=1}^5 \Phi_{it-m+1}} \leq \tau \quad (43)$$

The variable  $\tau$  denotes the allowable error tolerance.

#### 4. NUMERICAL RESULTS

This section presents the optimization of an acoustic barrier with periodic, case 1, and non-periodic, case 2, settings. Fig. 2 illustrates the geometry considered in the examples. The gray region denotes the design domain, initially full of rigid elements. The green and white areas are the objective and non-design domain regions, respectively, composed of air elements. The entire cell has 730 mm of length and 45 mm of height, with an initial barrier of 30x27 mm<sup>2</sup>. At boundary  $\Gamma_{in}$  different inputs are given in order to explore further the behavior of the optimization method when dealing with this kind of ATO problem, while  $\Gamma_{out}$  is considered closed in all examples.

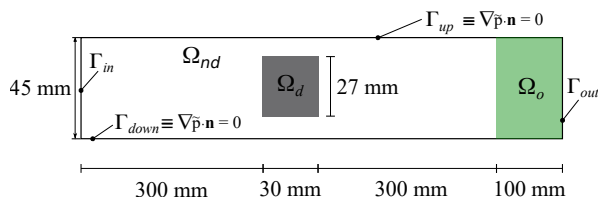


**Figure 2.** Geometric details of the structure adopted in the examples

##### 4.1 Case 1: Barrier optimization in a periodic system

Fig. 3(a) shows the sound pressure field of the acoustic tube with dimensions given in Fig. 2, when subjected to a plane wave caused by an acceleration of 1 m/s<sup>2</sup>, at  $\Gamma_{in}$ , and frequency of 2900 Hz. The fluid domain is discretized by 292x30 first order quadrilateral elements, which is above the minimum recommend per wavelength [16]. The speed of sound in air is 343 m/s, with the physical characteristics of air and rigid materials as stated in section 3.1. Fig. 3(b) illustrates the sound pressure field of the acoustic system with the optimized rigid barrier. The BESO parameters are:  $V^* = 0.65$ ,  $ER = 1.0\%$ ,  $AR_{max} = 1.4\%$ ,  $r_{min} = 10$  mm and  $\tau = 0.1\%$ . Fig. 3(c) is the representation of the same problem, but with three periodic cells, which makes a finite element mesh of size 292x90.

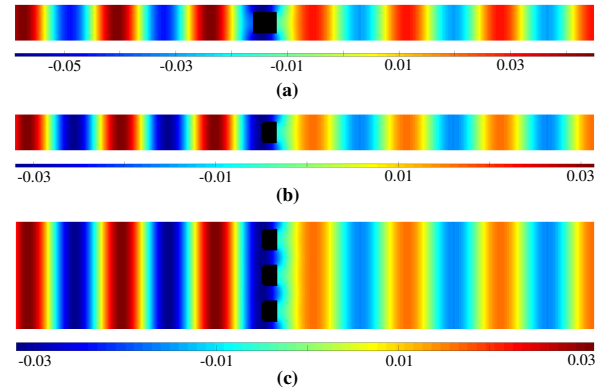


**Figure 3.** Sound pressure field of an acoustic tube (a) one cell with a non-optimized barrier (b) one cell with an optimized barrier (c) three cells and optimized barriers

It is observed from Fig. 3(b) and (c) that the same results are found after the optimization is complete due to the periodic conditions of the problem. Since the fluid domain is horizontally symmetric, it is possible to model rigid barriers with one or even half of a periodic cell, representing a significant reduction of computational cost. This becomes even clearer with the observation of Fig. 4, that presents the identical evolution of the objective function for the examples with one and three periodic cells, respectively. The barrier topology in iterations 10, 30 and 50 are also shown. The BESO method reveals great potential in the optimization of noise barriers with periodic conditions, since the average square pressure is reduced by 68.80%, while 35% of the barrier volume is also reduced. Additionally, there was no break of horizontal symmetry during the entire optimization process, resulting in a smooth behavior of the objective function.

##### 4.2 Case 2: Optimization of a non-periodic system

Fig. 5(a) illustrates the sound pressure field of a similar acoustic tube to the one presented in section 4.1 since the geometry, acceleration and frequency are maintained. However, a wave is generated by a cylindrical source of 45 mm in length, located at the center of  $\Gamma_{in}$ . In this case, since the boundary is non-periodic, the entire tube needs to be analyzed or Floquet-Bloch boundary conditions would have to be imposed in order to consider the different phases between cells [21]. Since this is an early study on the behavior of the BESO method in the optimization of noise barriers, the authors choose to only consider the case presented in Fig. 5(a). It is our hope to go deeper into this topic and even study the optimization of acoustic barriers composed of poroelastic materials [22, 23] in future work. Fig. 5(b) presents the results found after the optimization takes place. The BESO parameters considered in this case are:  $V^* = 0.65$ ,  $ER = 0.6\%$ ,  $AR_{max} = 0.8\%$ ,  $r_{min} = 18$  mm and  $\tau = 0.1\%$ . It must be pointed out that despite of the non-periodic setting, the barrier was considered as three cells, to which were applied the procedures described at the end of section 3.2.

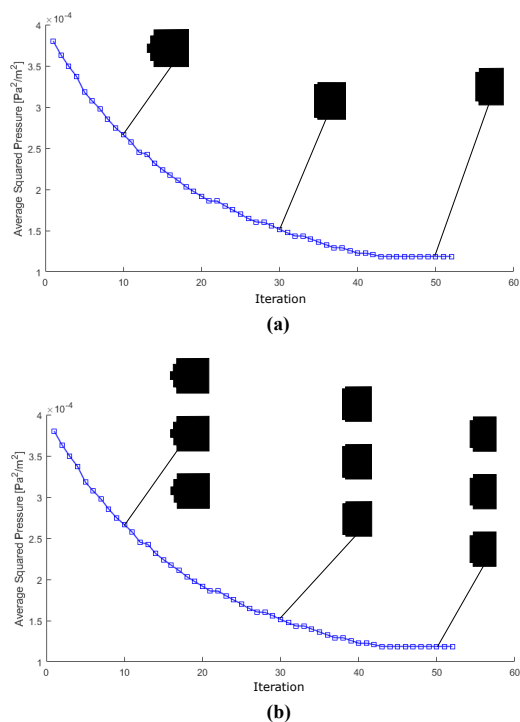


**Figure 4.** Objective function and barrier evolutions (a) one periodic cell (b) three periodic cells

From Fig. 5(b) it is noticed that the barrier converged to a non-symmetrical optimized form, completely different from the one presented in Fig. 3(c), even though its periodicity is maintained by the optimization method. This observation implies that, for the case of non-periodic boundaries, the optimization needs to be made for the whole fluid domain and not only for a small portion of it, as previously discussed. Additionally, the barrier may present some irregular behavior throughout the iterative procedure, due to abrupt variations of the objective function when the swap air-rigid is made. Sometimes, even elements located inside the barrier are turned to air, which does not affect the objective function at first, but sudden variations are usually observed when these elements meet the design domain surface. In this sense, the BESO parameters needed to be changed in order to slow down the optimization process and, therefore, reduce pressure variations.

Fig. 6 shows the evolution of the objective function with a presentation of the topologies for the 9th, 45th, 81st and 117th iterations. When looking at Fig. 4 and 6 it is noted that the number of iterations of the second case more than doubled in comparison to the first, showing an increase in computational cost. Despite that, the BESO method presents a reduction of the average square pressure by 83.39%, while the barrier suffers a 35% volume reduction.

## 5. CONCLUSIONS

In this paper the Bi-directional evolutionary structural optimization (BESO) methodology was implemented with the

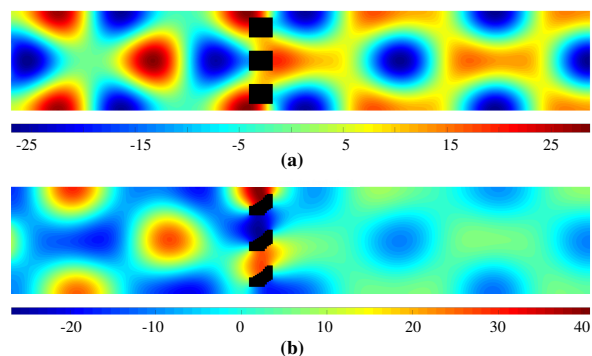


**Figure 5.** (a) Sound pressure field of an acoustic tube with a 45 mm cylindrical input (b) optimized result

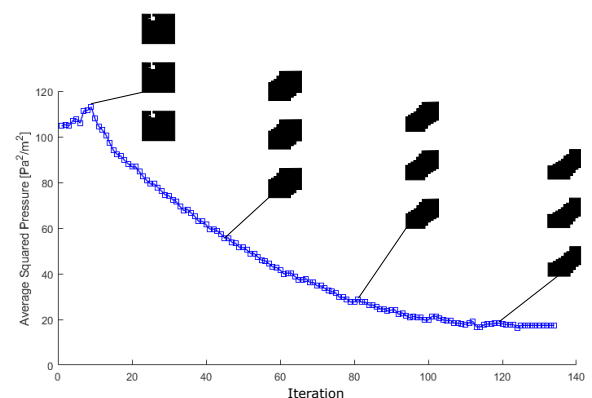


**Figure 6.** Evolution of the objective function for the non-symmetric case

goal of finding the best distribution of air ( $\chi = 0$ ) and rigid ( $\chi = 1$ ) elements in the design domain, thus building the most suitable noise barrier for the applications considered. The first case used one and three periodic cells. It is shown that the optimized results are, as expected, independent from the number of cells used, since the entire domain remained periodic, representing a low computational cost scenario. Additionally, the objective function has been reduced by 68.80%, with smooth behavior during the optimization procedure. In the second case, non-periodic inputs were examined. This made clear that, in those types of scenarios, the optimization needs to be made considering the entire acoustic tube, or Floquet-Bloch boundary conditions would have to be applied. In addition, BESO parameters were also required to change in order to deal with the abrupt variations of the evolutionary procedure. Despite of that, the objective function was reduced by 83.39% while the barrier volume decreased by 35%, showing that BESO is an applicable method to be used for the optimization of rigid acoustic barriers subjected to periodic and non-periodic conditions.

## 6. ACKNOWLEDGMENTS

The authors would like to thanks the financial support given by FAPESP (Fundação de Amparo à Pesquisa do

Estado de São Paulo), project number 2013/08293-7, and CAPES (Coordenação de Aperfeiçoamento de Pessoal do Nível Superior), finance code 001.

## 7. REFERENCES

- [1] Y. M. Xie and G. P. Steven, "A simple evolutionary procedure for structural optimization," *Computers & structures*, vol. 49, no. 5, pp. 885–896, 1993.
- [2] L. Xia, Q. Xia, X. Huang, and Y. M. Xie, "Bi-directional evolutionary structural optimization on advanced structures and materials: a comprehensive review," *Archives of Computational Methods in Engineering*, vol. 25, no. 2, pp. 437–478, 2018.
- [3] X. Yang, Y. Xie, G. Steven, and O. Querin, "Bidirectional evolutionary method for stiffness optimization," *AIAA journal*, vol. 37, no. 11, pp. 1483–1488, 1999.
- [4] X. Huang and M. Xie, *Evolutionary Topology Optimization of Continuum Structures: methods and applications*. West Sussex, UK: John Wiley & Sons, 1 ed., 2010.
- [5] X. Huang and Y. Xie, "Convergent and mesh-independent solutions for the bi-directional evolutionary structural optimization method," *Finite Elements in Analysis and Design*, vol. 43, no. 14, pp. 1039–1049, 2007.
- [6] X. Huang and Y.-M. Xie, "A further review of eso type methods for topology optimization," *Structural and Multidisciplinary Optimization*, vol. 41, no. 5, pp. 671–683, 2010.
- [7] J. Kook, K. Koo, J. Hyun, J. S. Jensen, and S. Wang, "Acoustical topology optimization for zwicker's loudness model—application to noise barriers," *Computer Methods in Applied Mechanics and Engineering*, vol. 237, pp. 130–151, 2012.
- [8] M. B. Dühring, J. S. Jensen, and O. Sigmund, "Acoustic design by topology optimization," *Journal of sound and vibration*, vol. 317, no. 3-5, pp. 557–575, 2008.
- [9] J. W. Lee and Y. Y. Kim, "Rigid body modeling issue in acoustical topology optimization," *Computer methods in applied mechanics and engineering*, vol. 198, no. 9-12, pp. 1017–1030, 2009.
- [10] J. W. Lee and Y. Y. Kim, "Topology optimization of muffler internal partitions for improving acoustical attenuation performance," *International journal for numerical methods in engineering*, vol. 80, no. 4, pp. 455–477, 2009.
- [11] W. Vicente, R. Picelli, R. Pavanello, and Y. Xie, "Topology optimization of frequency responses of fluid–structure interaction systems," *Finite Elements in Analysis and Design*, vol. 98, pp. 1 – 13, 2015.
- [12] R. Picelli, W. M. Vicente, R. Pavanello, and Y. Xie, "Evolutionary topology optimization for natural frequency maximization problems considering acoustic–structure interaction," *Finite Elements in Analysis and Design*, vol. 106, pp. 56–64, 2015.
- [13] J. Kook, "Evolutionary topology optimization for acoustic-structure interaction problems using a mixed u/p formulation," *Mechanics Based Design of Structures and Machines*, vol. 47, no. 3, pp. 356–374, 2019.
- [14] C. B. Dilgen, S. B. Dilgen, N. Aage, and J. S. Jensen, "Topology optimization of acoustic mechanical interaction problems: a comparative review," vol. 60, pp. 779–801, 2019.
- [15] F. M. Azevedo, M. S. Moura, W. M. Vicente, R. Picelli, and R. Pavanello, "Topology optimization of reactive acoustic mufflers using a bi-directional evolutionary optimization method," *Structural and Multidisciplinary Optimization*, vol. 58, no. 5, pp. 2239–2252, 2018.
- [16] N. Atalla and F. Sgard, *Finite Element and Boundary Methods in Structural Acoustics and Vibration*. Boca Raton, FL: CRC Press, 2015.
- [17] R. D. Cook, D. S. Malkus, M. E. Plesha, and R. J. Witt, *Concepts and Applications of Finite Element Analysis*. John wiley & sons, 2002.
- [18] W. U. Yoon, J. H. Park, J. S. Lee, and Y. Y. Kim, "Topology optimization design for total sound absorption in porous media," *Computer Methods in Applied Mechanics and Engineering*, vol. 360, p. 112723, 2020.
- [19] D. A. Tortorelli and P. Michaleris, "Design sensitivity analysis: overview and review," *Inverse problems in Engineering*, vol. 1, no. 1, pp. 71–105, 1994.
- [20] C. S. Jog and R. B. Haber, "Stability of finite element models for distributed-parameter optimization and topology design," *Computer methods in applied mechanics and engineering*, vol. 130, no. 3-4, pp. 203–226, 1996.
- [21] K. Miyata, Y. Noguchi, T. Yamada, K. Izui, and S. Nishiwaki, "Optimum design of a multi-functional acoustic metasurface using topology optimization based on zwicker's loudness model," *Computer Methods in Applied Mechanics and Engineering*, vol. 331, pp. 116–137, 2018.
- [22] F. I. Silva and R. Pavanello, "Synthesis of porous–acoustic absorbing systems by an evolutionary optimization method," vol. 42, pp. 887–905, 2010.
- [23] J. S. Lee, P. Göransson, and Y. Y. Kim, "Topology optimization for three-phase materials distribution in a dissipative expansion chamber by unified multiphase modeling approach," vol. 287, pp. 191–211, 2015.

# TOPOLOGY OPTIMIZATION OF ACOUSTIC-POROELASTIC-ELASTIC STRUCTURES FOR SOUND ATTENUATION

RODRIGO L. PEREIRA<sup>1</sup>, LIDY M. ANAYA-JAMES<sup>1</sup> AND RENATO PAVANELLO<sup>1</sup>

<sup>1</sup> Department of Computational Mechanics, School of Mechanical Engineering, University of  
Campinas, Rua Mendeleev 200, 13083-860, Campinas, Brazil  
pereira@fem.unicamp.br, lidy@fem.unicamp.br, pava@fem.unicamp.br

**Key words:** Topology optimization, BESO method, Multiphysics, Poroelastic materials, Vibroacoustics

**Abstract.** *Structures for sound attenuation have been explored in many scenarios, ranging from civil construction to automotive and aerospace industries. However, the proper multiphysics interactions of acoustic-poroelastic-elastic structures are still challenging, especially when topology optimization techniques are involved. This work entails a new topology optimization methodology based on the Bi-directional Evolutionary Structural Optimization (BESO) approach to design bidimensional structures for sound attenuation enhancements. The full modeling of poroelastic bodies is done by the mixed  $u/p$  technique. At the same time, the elastic and acoustic (air) materials are obtained by the degeneration of the latter, leading to the well-known elasto-dynamic and Helmholtz formulations, respectively. Such procedure is done in by the combination of the Finite Element Method (FEM) with the Unified Multi-phase (UMP) modeling approach, which in turn contributes to the development of material interpolation schemes suited for the application. In this scenario, the topology optimization problem is established as the maximization of the time-averaged dissipative power, composed by the summation of its structural, viscous and thermal dissipative components. The numerical examples show the effectiveness of the proposed methodology since it provides well-defined topologies with generally enhanced dissipative performances.*

## 1 INTRODUCTION

This paper presents a methodology to maximize the time-averaged dissipated power. It is considered a multiphysics system composed of acoustic, elastic and poroelastic elements. The Bi-directional Evolutionary Structural Optimization (BESO) method is chosen as the optimizer, since it provides clearly defined boundaries throughout the entire optimization process. The first ones to use a similar optimization methodology were Xie and Steven [1], with the proposition of the Evolutionary Structural Optimization (ESO) method. In this case, the aim was to gradually remove inefficient material from the structure, while enhancing some physical properties of the system. In 1999, Yang et al. [2] modified the ESO technique by allowing not only material removal, but also addition to the design domain. After a series of modifications that included sensitivity filters [3] and material interpolation schemes [4], Huang and Xie [5] proposed the new BESO approach, being extensively used ever since.

As this work also deals with acoustic, elastic and poroelastic materials, careful attention has to be paid to the boundary tracking problem in a context of topology optimizations. For example, when acoustic elements change to elastic or poroelastic, the coupling between the boundaries has to be properly imposed. However, such procedure is not straightforward, in a way that a few solutions have been proposed

to overcome this issue. Yamamoto et al. [6] considered three distinct poroelastic materials inside the design domain, modifying specific variables in order to fully simulate acoustic, elastic and poroelastic structures within the same region. The success of this approach was due to the fact that the materials were all derived from Biot's equation, therefore being naturally coupled with each other. In the same year, the Unified Multiphase (UMP) technique was proposed by Lee [7, 8], which used these same Biot's equations, in the  $\mathbf{u}/p$  form, as a foundation to describe the aforementioned medias. The main difference between both approaches concerns the amount of different porous materials needed in the methodology. While Yamamoto's [6] approach used three different poroelastic medias, Lee's [7, 8] considered only one.

Finally, this work also proposes a new material interpolation scheme for systematic material changes along the iterative procedure. According to Pereira et al. [9], the interpolations are generally polynomial functions of the design variables, first used in density-based approaches [4]. Besides, penalty variables are often used as degrees of freedom of the polynomial function. Although the BESO method does not need material interpolations, it has been shown that such a procedure contributes to the avoidance of singularities, as well as to the reduction of computational costs involved in multiphysics problems [10, 11].

## 2 FINITE ELEMENT FORMULATION FOR POROELASTIC MEDIA: THE MIXED U/P

As of 1956, Biot [12, 13] proposed expressions that were able to microscopically describe the behavior of the wave in poroelastic media, being mainly based on the displacements of the elastic ( $\mathbf{\ddot{u}}$ ) and fluid components ( $\mathbf{\ddot{U}}$ ), that is,

$$\nabla \cdot \mathbf{\sigma}^s = \rho_{11} \mathbf{\ddot{u}} + \rho_{12} \mathbf{\ddot{U}} + \tilde{b}(\mathbf{\dot{u}} - \mathbf{\dot{U}}), \quad (1)$$

$$\nabla \cdot \mathbf{\sigma}^f = \rho_{22} \mathbf{\ddot{U}} + \rho_{12} \mathbf{\ddot{u}} - \tilde{b}(\mathbf{\dot{u}} - \mathbf{\dot{U}}), \quad (2)$$

where  $\mathbf{\sigma}^s$  and  $\mathbf{\sigma}^f$  are the stress tensor of the solid and fluid phases, respectively. The homogenized densities related to the solid and fluid phases are  $\rho_{11}$  and  $\rho_{22}$ , while  $\rho_{12}$  relates to the interaction between the inertial forces of both phases. Finally, the viscous damping coefficient that accounts for the viscous iteration forces is  $\tilde{b}$ , while the gradient operator is  $\nabla$ .

In a mathematical perspective, the aforementioned homogenized densities and damping coefficient can also be defined as [14],

$$\rho_{12} = -\phi \rho_f (\alpha_\infty - 1), \quad \rho_{11} = (1 - \phi) \rho_s - \rho_{12}, \quad \rho_{22} = \phi \rho_f - \rho_{12}, \quad \tilde{b} = \phi^2 \sigma \tilde{G}(\omega), \quad (3)$$

with  $\phi$  being the porosity,  $\alpha_\infty$  the tortuosity,  $\sigma$  the static flow resistivity,  $\rho_f$  the fluid phase density and  $\rho_s$  the solid phase density. Following Johnson's model [15],  $\tilde{G}(\omega)$  is written [16] as,

$$\tilde{G}(\omega) = \left[ 1 + \left( \frac{2\alpha_\infty \eta}{\phi \Lambda \sigma} \right)^2 \frac{j\omega \rho_f}{\eta} \right]^{1/2}. \quad (4)$$

Here,  $\eta$  is the fluid kinematic viscosity,  $\Lambda$  is the viscous characteristic length,  $\omega$  is the angular frequency and  $j^2 = -1$  is the imaginary number.

Assuming that the porous material properties are homogeneous and subject to harmonic oscillations, a more suitable way to describe the wave behavior in poroelastic materials was proposed by Atalla et al.

[14, 17], by turning Eqs. (1) and (2) into a mixed displacement-pressure ( $\mathbf{u}/p$ ) formulation,

$$\nabla \cdot \underline{\hat{\boldsymbol{\sigma}}}^s + \omega^2 \tilde{\rho} \mathbf{u} + \tilde{\gamma} \nabla p = \mathbf{0}, \quad (5)$$

$$\nabla^2 p + \omega^2 \frac{\tilde{\rho}_{22}}{\tilde{R}} p - \omega^2 \frac{\tilde{\rho}_{22}}{\phi^2} \tilde{\gamma} \nabla \cdot \mathbf{u} = 0, \quad (6)$$

where the combined effective density  $\tilde{\rho}$  and the coupling coefficient  $\tilde{\gamma}$  are written as,

$$\tilde{\rho} = \tilde{\rho}_{11} - \frac{\tilde{\rho}_{12}^2}{\tilde{\rho}_{22}}, \quad \tilde{\gamma} = \phi \left( \frac{\tilde{\rho}_{12}}{\tilde{\rho}_{22}} - \frac{\tilde{Q}}{\tilde{R}} \right), \quad (7)$$

with the effective densities that account for the inertia effects in the solid ( $\tilde{\rho}_{11}$ ), fluid ( $\tilde{\rho}_{22}$ ) and in the viscous coupling that happens between the two ( $\tilde{\rho}_{12}$ ) being,

$$\tilde{\rho}_{11} = \rho_{11} + \frac{\tilde{b}}{j\omega}, \quad \tilde{\rho}_{22} = \rho_{22} + \frac{\tilde{b}}{j\omega}, \quad \tilde{\rho}_{12} = \rho_{12} - \frac{\tilde{b}}{j\omega}. \quad (8)$$

The stress tensor of the porous material in vacuo  $\underline{\hat{\boldsymbol{\sigma}}}^s$  also has a mathematical expression associated with it,

$$\underline{\hat{\boldsymbol{\sigma}}}^s = \left( \tilde{A} - \frac{\tilde{Q}^2}{\tilde{R}} \right) \nabla \cdot \mathbf{u} \mathbf{I} + 2N \underline{\boldsymbol{\epsilon}}^s = \hat{A} \nabla \cdot \mathbf{u} \mathbf{I} + 2N \underline{\boldsymbol{\epsilon}}^s, \quad (9)$$

where  $\mathbf{I}$  is the identity tensor,  $\tilde{A}$  is the first Lamé constant of the poroelastic material,  $N$  is the elastic shear modulus,  $\tilde{Q}$  is the coupling coefficient between the dilatation of both component phases,  $\tilde{R}$  is the bulk modulus of air occupying a fraction of volume aggregate and  $\hat{A}$  is the first Lamé constant of the elastic phase [14, 18]. At last, since the majority of poroelastic media has high porosity in the applications here considered, the variables  $N$ ,  $\tilde{A}$ ,  $\tilde{Q}$  and  $\tilde{R}$  can be written in a simplified manner,

$$N = \frac{E(1 + j\eta_e)}{2(1 + \nu)}, \quad \tilde{A} = \frac{\nu E(1 + j\eta_e)}{(1 + \nu)(1 - 2\nu)} \quad (10)$$

$$\tilde{Q} = (1 - \phi) \tilde{K}_f, \quad \tilde{R} = \phi \tilde{K}_f \quad (11)$$

where  $E$ ,  $\eta_e$  and  $\nu$  are the Young's modulus, the loss factor and the Poisson's ratio of the elastic material, respectively.  $\tilde{K}_f$  is the bulk modulus of the air in the poroelastic material pores.

The weak form of Eqs. (5) and (6) is then obtained by the combination of the Weighted Residuals Method and the divergence theorem, followed by the consideration of material isotropy, that is [8, 19],

$$\int_{\Omega_p} \left\{ \underline{\hat{\boldsymbol{\sigma}}}^s(\mathbf{u}) : \underline{\boldsymbol{\epsilon}}^s(\delta \mathbf{u}) - \omega^2 \tilde{\rho} \mathbf{u} \cdot \delta \mathbf{u} - (\tilde{\gamma} + \tilde{\xi}) \nabla p \cdot \delta \mathbf{u} - \tilde{\xi} p \nabla \cdot \delta \mathbf{u} \right\} d\Omega_p - \int_{\Gamma_p} (\underline{\hat{\boldsymbol{\sigma}}}^s \cdot \mathbf{n}) \cdot \delta \mathbf{u} d\Gamma_p = \mathbf{0}, \quad (12)$$

$$\int_{\Omega_p} \left\{ \frac{\phi^2}{\omega^2 \tilde{\rho}_{22}} \nabla p \cdot \nabla \delta p - \frac{\phi^2}{\tilde{R}} p \delta p - (\tilde{\gamma} + \tilde{\xi}) \nabla \delta p \cdot \mathbf{u} - \tilde{\xi} \delta p \nabla \cdot \mathbf{u} \right\} d\Omega_p - \int_{\Gamma_p} \phi (\mathbf{U} - \mathbf{u}) \cdot \mathbf{n} \delta p d\Gamma_p = 0, \quad (13)$$

where  $\delta \mathbf{u}$  and  $\delta p$  are test functions related to the solid phase displacement and the interstitial pressure, respectively, while  $\Omega_p$  represents the poroelastic domain with  $\Gamma_p$  as its boundary. The newly introduced variable  $\tilde{\xi} = \phi(1 + \tilde{Q}/\tilde{R})$  may be also viewed as a coupling coefficient, and  $\mathbf{n}$  is the outward unit normal vector.

The Finite Element Method (FEM) [20] is then considered in the discretization of the aforementioned continuous problem, being also followed by Galerkin's approach. The result is a linear system of equations [16], as can be seen next,

$$\begin{bmatrix} \mathbf{K} - \omega^2 \tilde{\mathbf{M}} & -(\tilde{\mathbf{C}}_1 + \tilde{\mathbf{C}}_2) \\ -(\tilde{\mathbf{C}}_1 + \tilde{\mathbf{C}}_2)^T & \tilde{\mathbf{H}}/\omega^2 - \tilde{\mathbf{Q}} \end{bmatrix} \begin{Bmatrix} \mathbf{u} \\ \mathbf{p} \end{Bmatrix} = \begin{Bmatrix} \mathbf{f}_s \\ \mathbf{f}_p/\omega^2 \end{Bmatrix}, \quad (14)$$

where  $\mathbf{K}$ ,  $\tilde{\mathbf{M}}$ ,  $\tilde{\mathbf{H}}$ ,  $\tilde{\mathbf{Q}}$ ,  $\tilde{\mathbf{C}}_1$ ,  $\tilde{\mathbf{C}}_2$  denote the global stiffness, mass, kinetic, compression and coupling matrices, respectively. The global displacement and acoustic pressure vectors, as well as the global structural and acoustic loads are respectively defined as  $\mathbf{u}$ ,  $\mathbf{p}$ ,  $\mathbf{f}_s$ ,  $\mathbf{f}_p$ .

### 3 UNIFIED MULTIPHASE MODELING: ACOUSTIC, ELASTIC AND POROELASTIC RELATIONS

In this technique, six variables are controlled, namely,  $\tilde{\xi}$ ,  $\tilde{\rho}$ ,  $N$ ,  $\hat{A}$ ,  $\phi^2/\tilde{\rho}_{22}$  and  $\phi^2/\tilde{R}$ . For the acoustic case, these variables take the following values: 1, 0, 0, 0,  $1/\rho_a$  and  $1/\kappa_a$ , where  $\kappa_a$  is the bulk modulus of the air (identified by the subscript  $a$ ). For the elastic case, one gets the sequence: 0,  $\rho_e$ ,  $N_e$ ,  $\hat{A}_e$ , 0 and 0, with the subscript  $e$  being related to the elastic material. In order to solve numerical issues that may appear with the above relations, small valued coefficients are assigned to each of the properties that have to be zero so that the final sequences get the following results,

$$\{\tilde{\xi}, \tilde{\rho}, N, \hat{A}, (\phi^2/\tilde{\rho}_{22}), (\phi^2/\tilde{R})\}_p = \{\tilde{\xi}, \tilde{\rho}, N, \hat{A}, \phi^2/\tilde{\rho}_{22}, \phi^2/\tilde{R}\}, \quad (15)$$

$$\{\tilde{\xi}, \tilde{\rho}, N, \hat{A}, (\phi^2/\tilde{\rho}_{22}), (\phi^2/\tilde{R})\}_a = \{1, \varepsilon_a \tilde{\rho}, \varepsilon_a N, \varepsilon_a \hat{A}, 1/\rho_a, 1/\kappa_a\}, \quad (16)$$

$$\{\tilde{\xi}, \tilde{\rho}, N, \hat{A}, (\phi^2/\tilde{\rho}_{22}), (\phi^2/\tilde{R})\}_e = \{\varepsilon_e \tilde{\xi}, \rho_e, N_e, \hat{A}_e, \varepsilon_e (\phi^2/\tilde{\rho}_{22}), \varepsilon_e (\phi^2/\tilde{R})\}, \quad (17)$$

where the subscript  $p$  refers to the poroelastic material. Here,  $\varepsilon_a = 1 \times 10^{-4}$  and  $\varepsilon_e = 1 \times 10^{-9}$  were chosen.

The multiphase material interpolation scheme is then written,

$$\tilde{\xi} = \tilde{\xi}_e + x_2^{\zeta_2} (\tilde{\xi}_p - \tilde{\xi}_e) + x_1^{\zeta_1} (\tilde{\xi}_a - \tilde{\xi}_p), \quad (18)$$

$$\tilde{\rho} = \tilde{\rho}_e + x_2^{\zeta_2} (\tilde{\rho}_p - \tilde{\rho}_e) + x_1^{\zeta_1} (\tilde{\rho}_a - \tilde{\rho}_p), \quad (19)$$

$$N = N_e + x_2^{\zeta_2} (N_p - N_e) + x_1^{\zeta_1} (N_a - N_p), \quad (20)$$

$$\hat{A} = \hat{A}_e + x_2^{\zeta_2} (\hat{A}_p - \hat{A}_e) + x_1^{\zeta_1} (\hat{A}_a - \hat{A}_p), \quad (21)$$

$$\phi^2/\tilde{\rho}_{22} = (\phi^2/\tilde{\rho}_{22})_e + x_2^{\zeta_2} [(\phi^2/\tilde{\rho}_{22})_p - (\phi^2/\tilde{\rho}_{22})_e] + x_1^{\zeta_1} [(\phi^2/\tilde{\rho}_{22})_a - (\phi^2/\tilde{\rho}_{22})_p], \quad (22)$$

$$\phi^2/\tilde{R} = (\phi^2/\tilde{R})_e + x_2^{\zeta_2} [(\phi^2/\tilde{R})_p - (\phi^2/\tilde{R})_e] + x_1^{\zeta_1} [(\phi^2/\tilde{R})_a - (\phi^2/\tilde{R})_p], \quad (23)$$

where  $x_{1,2}$  represents the design variables and the superscripts  $\zeta_{1,2}$  are the penalty coefficients. After a series of tests, the following values were chosen for the design variables,

$$\{x_1, x_2\} = \{1, 1\}, \quad \text{for acoustic elements}, \quad (24)$$

$$\{x_1, x_2\} = \{x_{\min}, 1\}, \quad \text{for poroelastic elements}, \quad (25)$$

$$\{x_1, x_2\} = \{x_{\min}, x_{\min}\}, \quad \text{for elastic elements}, \quad (26)$$

and for the penalty variables,  $\{\zeta_1, \zeta_2\} = \{2, 2\}$ . In order to avoid numerical singularities,  $x_{\min} = 0.001$  is adopted, being the lower limit that the design variable can get. Table 1 shows the poroelastic and elastic material properties adopted in this work, while the acoustic characteristics used have been the same as the ones brought by Pereira et al. [9].

**Table 1:** Poroelastic and elastic material properties [6]

Parameters	Polyurethane foam	Olefin sheet
Porosity $\phi$	0.97	–
Tortuosity $\alpha_\infty$	2.5	–
Static flow resistivity $\sigma$ (N s m <sup>-4</sup> )	$7 \times 10^4$	–
Viscous characteristic length $\Lambda$ ( $\mu\text{m}$ )	$36 \times 10^{-6}$	–
Thermal characteristic length $\Lambda'$ ( $\mu\text{m}$ )	$170 \times 10^{-6}$	–
Solid mass density $\rho$ (kg m <sup>-3</sup> )	1433	1790
Young's modulus $E$ (Pa)	$2.67 \times 10^5$	$1.75 \times 10^8$
Poisson ratio $\nu$	0.4	0.4
Loss factor $\eta$	0.11	0.205

#### 4 DESCRIPTION OF THE TOPOLOGY OPTIMIZATION PROBLEM

The topology optimization problem investigated in this work aims to maximize the time-averaged dissipated power ( $\Pi_{\text{diss}}$ ) composed of its structural, viscous and thermal components. Throughout the numerical procedure, a frequency band of  $[\omega_i, \omega_f]$  is also considered, together with the multimaterial and multiphysics constraints, therefore,

$$\text{Maximize: } \Phi = \frac{1}{\omega_f - \omega_i} \int_{\omega_i}^{\omega_f} 10 \log \frac{\Pi_{\text{diss}}}{\Pi_{\text{ref}}} d\Omega_p, \quad (\text{in dB units}) \quad (27)$$

$$\text{Subjected to: } \begin{cases} \begin{bmatrix} \mathbf{K} - \omega^2 \tilde{\mathbf{M}} & -(\tilde{\mathbf{C}}_1 + \tilde{\mathbf{C}}_2) \\ -(\tilde{\mathbf{C}}_1 + \tilde{\mathbf{C}}_2)^T & \tilde{\mathbf{H}}/\omega^2 - \tilde{\mathbf{Q}} \end{bmatrix} \begin{Bmatrix} \mathbf{u} \\ \mathbf{p} \end{Bmatrix} = \begin{Bmatrix} \mathbf{f}_s \\ \mathbf{f}_p/\omega^2 \end{Bmatrix}, \\ \begin{Bmatrix} V_1^* - \left( \sum_{i=1}^{N_{\text{el}}} V_i x_i \right)_1 \\ V_2^* - \left( \sum_{i=1}^{N_{\text{el}}} V_i x_i \right)_2 \end{Bmatrix} = \begin{Bmatrix} 0 \\ 0 \end{Bmatrix}, \\ \mathbf{x} = \left[ \begin{Bmatrix} x_1 \\ \vdots \\ x_{N_{\text{el}}} \end{Bmatrix}_1, \begin{Bmatrix} x_1 \\ \vdots \\ x_{N_{\text{el}}} \end{Bmatrix}_2 \right]. \end{cases} \quad (28)$$

In Eq. (28), the prescribed final volume fraction is  $V^*$ , with the design domain volume fraction being  $\sum_{i=1}^{N_{\text{el}}} V_i x_i$ .  $N_{\text{el}}$  is the number of elements of the entire porous domain and  $\mathbf{x}$  is the design variable matrix. The subscript numbers 1 and 2 represent the changes along the optimization process, in other words, the number 1 refers to variations from acoustic to poroelastic elements, while the number 2 regards the changes from poroelastic to elastic.

Generally, the  $\Pi_{\text{diss}}$  formula can be obtained as,

$$\Pi_{\text{diss}} = \frac{\omega}{2} \begin{Bmatrix} \mathbf{u} \\ \mathbf{p} \end{Bmatrix}^H \text{Im} \left( \begin{bmatrix} \mathbf{K} - \omega^2 \tilde{\mathbf{M}} & -(\tilde{\mathbf{C}}_1 + \tilde{\mathbf{C}}_2) \\ -(\tilde{\mathbf{C}}_1 + \tilde{\mathbf{C}}_2)^T & \tilde{\mathbf{H}}/\omega^2 - \tilde{\mathbf{Q}} \end{bmatrix} \right) \begin{Bmatrix} \mathbf{u} \\ \mathbf{p} \end{Bmatrix}, \quad (29)$$

where the superscript  $H$  represents the transpose conjugate of the solution vector,  $\text{Im}()$  is the imaginary part and  $\Pi_{\text{ref}}$  is the reference acoustic power ( $\Pi_{\text{ref}} = 1 \times 10^{-12}$  watts).

#### 4.1 Sensitivity analysis

As the current work adopts the BESO method as the optimizer, the sensitivity analysis needs to be carried out to identify each elemental contribution to the maximization of the objective function of choice. The derivation of Eq. (27) follows,

$$\alpha_i = \frac{d\Phi}{dx_i} = \frac{1}{\omega_f - \omega_i} \left( \int_{\omega_i}^{\omega_f} \frac{10}{\ln 10} \frac{d\Pi_{\text{diss}}/dx_i}{\Pi_{\text{diss}}} d\Omega_p \right), \quad (30)$$

with,

$$\frac{d\Pi_{\text{diss}}}{dx_i} = \frac{\partial \Pi_{\text{diss}}}{\partial x_i} + 2\text{Re} \left\{ \boldsymbol{\lambda}^T \left( \begin{bmatrix} \frac{\partial \mathbf{K}}{\partial x_i} - \omega^2 \frac{\partial \tilde{\mathbf{M}}}{\partial x_i} & -\left( \frac{\partial \tilde{\mathbf{C}}_1}{\partial x_i} + \frac{\partial \tilde{\mathbf{C}}_2}{\partial x_i} \right) \\ -\left( \frac{\partial \tilde{\mathbf{C}}_1}{\partial x_i} + \frac{\partial \tilde{\mathbf{C}}_2}{\partial x_i} \right)^T & \frac{1}{\omega^2} \frac{\partial \tilde{\mathbf{H}}}{\partial x_i} - \frac{\partial \tilde{\mathbf{Q}}}{\partial x_i} \end{bmatrix} \begin{Bmatrix} \mathbf{u} \\ \mathbf{p} \end{Bmatrix} - \begin{Bmatrix} \frac{\partial \mathbf{f}_s}{\partial x_i} \\ \frac{1}{\omega^2} \frac{\partial \mathbf{f}_p}{\partial x_i} \end{Bmatrix} \right) \right\} \quad (31)$$

and,

$$\begin{bmatrix} \mathbf{K} - \omega^2 \tilde{\mathbf{M}} & -(\tilde{\mathbf{C}}_1 + \tilde{\mathbf{C}}_2) \\ -(\tilde{\mathbf{C}}_1 + \tilde{\mathbf{C}}_2)^T & \tilde{\mathbf{H}}/\omega^2 - \tilde{\mathbf{Q}} \end{bmatrix} \boldsymbol{\lambda} = -\frac{1}{2} \left( \frac{\partial \Pi_{\text{diss}}}{\partial \left( \text{Re} \begin{Bmatrix} \mathbf{u} \\ \mathbf{p} \end{Bmatrix} \right)} - j \frac{\partial \Pi_{\text{diss}}}{\partial \left( \text{Im} \begin{Bmatrix} \mathbf{u} \\ \mathbf{p} \end{Bmatrix} \right)} \right)^T, \quad (32)$$

where  $\text{Re}()$  represents the real part.

## 5 NUMERICAL EXAMPLES

This section presents numerical examples regarding the optimization of the system illustrated in Fig. 1. Here, the design,  $\Omega_d$ , and the non-design,  $\Omega_{nd}$ , domains are represented by the grey region at the center of the system, and by the white and black areas located at the sides, respectively. Initially, poroelastic structures fill the entire  $\Omega_d$ , while acoustic and elastic elements are set in the major white areas and on the thin walls surrounding the design domain. At the upper and lower sides, symmetric boundary conditions are imposed (only the degrees of freedom in the y direction are blocked); a plane wave enters the composition at the left boundary, while at the right, an anechoic termination is set.

In the represented scenario, first order quadrilateral elements of size  $1 \times 1,25 \text{ mm}^2$  are considered, meaning that  $22 \times 40$  elements are placed at both sides of  $\Omega_{nd}$  and  $80 \times 40$  in  $\Omega_d$ . The BESO parameters are then set to be  $\text{ER} = \text{AR}_{\text{max}} = 1\%$  and  $r_{\text{min}} = 2 \text{ cm}$ . Besides,  $V_2^* = 0.05$  is fixed, defining the amount of elastic material that enters the design domain along the optimization procedure. Meanwhile,  $V_1^*$  is variable, that is, in some cases  $V_1^* = 0.5$  and in others  $V_1^* = 0.6$ . Besides, two distinct low-to-mid multifrequency bands are also treated in this work, namely  $\text{B1} = [150, 200] \text{ Hz}$  and  $\text{B2} = [200, 250]$ .

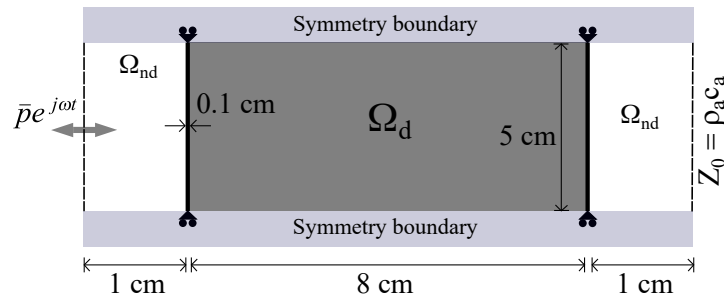


**Figure 1:** Schematic representation of the considered geometry

Fig. 2 shows the optimized results obtained from the maximization of the time-averaged dissipated powers when considering multiple frequency bands and distinct porous volume fractions. In Fig. 2 (a) and (c), the topologies are strongly related to one another, with the one of item (c) being the most effective in enhancing the objective function (see Fig. 2 (e)). This same aspect is not observed in Fig. 2 (b) and (d), where B2 is considered. In this case, the topologies are entirely different, with the case of 50% of porous material being similar, from a purely dissipative point of view, to its counterpart. This unsuspected result illustrates how efficient the proposed topology optimization methodology can be, as effective topologies may be generated with less material than expected. Finally, it is noted that even though some topologies may present disconnected porous materials, such characteristic does not affect, in a considerable manner, the dissipative effects of the main resulted topologies.

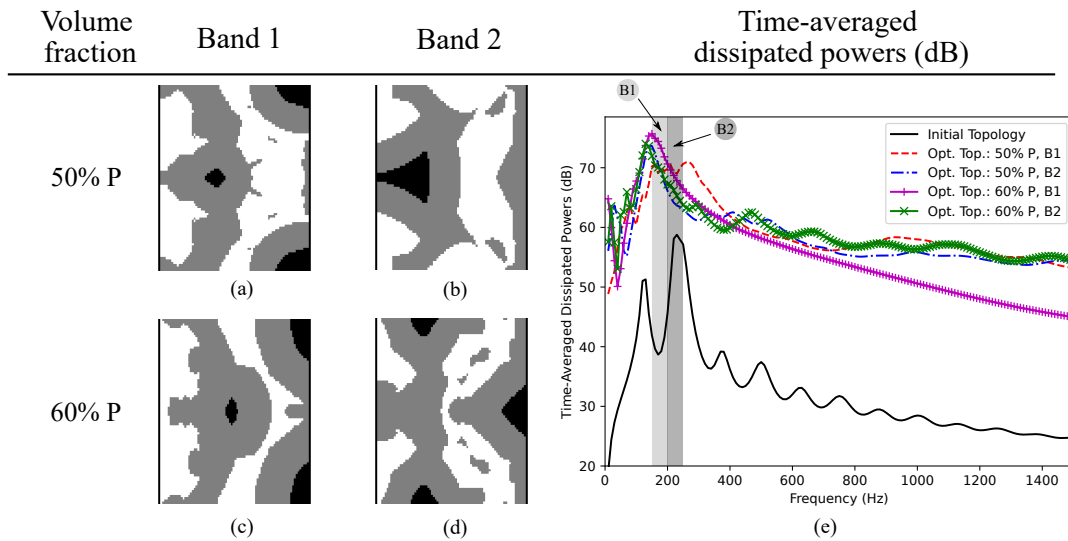


**Figure 2:** Optimized topologies when considering (a) 50% and (c) 60% of porous material in band 1, together with (b) 50% and (d) 60% in band 2. (e) The initial and final time averaged-dissipated powers are also shown

## 6 CONCLUSIONS

This work proposed a multifrequency topology optimization methodology to maximize time-averaged dissipated powers of an acoustic-poroelastic-elastic structure. For this, the Bi-directional Evolutionary Structural Optimization approach was considered as the optimizer, in order to provide clearly defined designs throughout the iterative procedure. The unified multiphase technique was then combined with the finite element method to fully describe elastic and acoustic systems, starting from Biot's poroelasticity equations. This combination proved to be an efficient solution to the boundary tracking problem, common to fluid-structure systems.

Furthermore, a newly introduced material interpolation scheme was also proposed, systematically combining acoustic-poroelastic-elastic properties. With this, the numerical examples showed to be highly effective in maximizing the objective function while generating topologies with low material disconnections.

## REFERENCES

- [1] Xie, Y. and Steven, G. P. A simple evolutionary procedure for structural optimization. *Comput. Struct.* (1993) **49**:885–896.
- [2] Yang, X. Y., Xie, Y. M., Steven, G. P. and Querin, O. M. Bidirectional evolutionary method for stiffness optimization. *AIAA J.* (1999) **37**:1483–1488.
- [3] Sigmund, O. and Petersson, J. Numerical instabilities in topology optimization: A survey on procedures dealing with checkerboards, mesh-dependencies and local minima. *Struct. Optim* (1998) **16**:68–75.
- [4] Bendsoe, M. P. and Sigmund, O. Material interpolation schemes in topology optimization. *Arch. Appl. Mech.* (1999) **69**:635–654.
- [5] Huang, X. and Xie, Y. M. *Evolutionary Topology Optimization of Continuum Structures: Methods and Applications*. Ed. John Wiley & Sons, Vol. I., (2010).
- [6] Yamamoto, T., Maruyama, S., Nishiwaki, S. and Yoshimura, M. Topology design of multi-material soundproof structures including poroelastic media to minimize sound pressure levels. *Comput. Method Appl. M.* (2009) **198**:1439–1455.
- [7] Lee, J. S. *Unified Multi-Phase Modeling and Topology Optimization for Complex Vibro-Acoustic Systems Consisting of Acoustic, Poroelastic and Elastic Media*. School of Mechanical and Aerospace Engineering, The Graduate School, Seoul National University, (2009).
- [8] Lee, J. S., Kang, Y. J. and Kim, Y. Y. Unified multiphase modeling for evolving, acoustically coupled systems consisting of acoustic, elastic, poroelastic media and septa. *J. Sound Vib.* (2012) **331**:5518–5536.
- [9] Pereira, R. L., Lopes, H. N. and Pavanello, R. Topology optimization of acoustic systems with a multiconstrained BESO approach. *Finite Elem. Anal. Des.* (2022) **201**:103701.
- [10] Picelli, R., Vicente, W., Pavanello, R. and Xie Y. Evolutionary topology optimization for natural frequency maximization problems considering acoustic–structure interaction. *Finite Elem. Anal. Des.* (2015) **106**:56–64.
- [11] Vicente, W., Picelli, R., Pavanello, R. and Xie Y. Topology optimization of frequency responses of fluid–structure interaction systems. *Finite Elem. Anal. Des.* (2015) **98**:1–13.
- [12] Biot, M. A. Theory of Propagation of Elastic Waves in a Fluid-Saturated Porous Solid: I. Low-Frequency Range. *J. Acoust. Soc. Am.* (1956) **28**:168–178.

- 
- [13] Biot, M. A. Theory of Propagation of Elastic Waves in a Fluid-Saturated Porous Solid: II. Higher-Frequency Range. *J. Acoust. Soc. Am.* (1956) **28**:179–191.
- [14] Atalla, N., Panneton, R. and Debergue, P. A mixed displacement-pressure formulation for poroelastic materials. *J. Acoust. Soc. Am.* (1998) **104**:1444–1452.
- [15] Johnson, D. L., Koplik, J. and Dashen, R. Theory of dynamic permeability and tortuosity in fluid-saturated porous media. *J. Fluid Mech.* (1987) **176**:379–402.
- [16] Allard, J. F. and Atalla, N. *Propagation of Sound in Porous Media: Modelling Sound Absorbing Materials*. Ed. John Wiley & Sons, Vol. I. (1993), Vol. II. (2009).
- [17] Atalla, N., Hamdi, M. A. and Panneton, R. Enhanced weak integral formulation for the mixed (u,p) poroelastic equations. *J. Acoust. Soc. Am.* (2001) **109**:3065–3068.
- [18] Lee, J. S., Göransson, P. and Kim, Y. Y. Topology optimization for three-phase materials distribution in a dissipative expansion chamber by unified multiphase modeling approach. *Comput. Method Appl. M.* (2015) **287**:191–211.
- [19] Rigobert, S., Atalla, N. and Sgard, F. C. Investigation of the convergence of the mixed displacement-pressure formulation for three-dimensional poroelastic materials using hierarchical elements. *J. Acoust. Soc. Am.* (2003) **114**:2607–2617.
- [20] Atalla, N. and Sgard, F. *Finite Element and Boundary Methods in Structural Acoustics and Vibration*. Ed. CRC Press, Vol. I., (2015).

## DECLARAÇÃO

Declaramos, para os devidos fins, que foi autorizada a inclusão do trabalho intitulado “*Topology Optimization Design of Acoustic-Poroelastic-Elastic Structures by the BESO Approach*” de autoria de Rodrigo Lima Pereira e Renato Pavanello, e publicado nos Anais do 8th International Symposium on Solid Mechanics – MECSOL 2022, na Tese de Doutorado do Sr. Rodrigo Lima Pereira. Informamos, ainda, que o copyright continua sendo da ABCeM.



Prof. Francis H. R. França  
Diretor Técnico Científico da ABCeM

## Topology Optimization Design of Acoustic-Poroelastic-Elastic Structures by the BESO Approach

Rodrigo L. Pereira<sup>1</sup> and Renato Pavanello<sup>1</sup>

<sup>1</sup> Department of Computational Mechanics, School of Mechanical Engineering, University of Campinas, Rua Mendeleev 200, 13083-860 Campinas, Brazil

*Porous materials are constantly the subject of study in the automotive and aerospace industries due to its sound insulation capabilities, lightweight characteristics, and vast degree of applicability, for example. Nevertheless, its mathematical formulations still pose a challenge, especially when topology optimization algorithms are considered, as multiphysics components must be contemplated for an enhanced degree of real-world simulation. In this work, the design of full modelled acoustic-poroelastic-elastic structures is formulated as a topology optimization problem. The Bi-directional Evolutionary Structural Optimization (BESO) algorithm is employed to offer non-intuitive design options with clearly defined boundaries. Biot's poroelasticity equations, expressed in the mixed  $\mathbf{u}/p$  form, and the Finite Element Method (FEM) comprise the basic expressions adopted in the description of all mediums and multiphysics interface conditions. With this unified multiphase (UMP) approach, it is possible to degenerate the poroelasticity expressions into the well-known scalar Helmholtz or elasto-dynamic equations, depending on the need for describing acoustic or elastic elements, respectively, without even implementing further coupling conditions. Additionally, this work also adopts a multiphase material interpolation scheme, which allows for systematic material changes, with only the elemental design variable information as input, and no boundary tracking. As Transmission Loss (TL) values are common indicators of the capability of a system in attenuate sound, the topology optimization problem is defined as the maximization of TL values at a specific target frequency. The proposed approach is tested through numerical examples that show the efficiency of the methodology.*

**Keywords:** *Topology optimization, BESO method, Multiphysics, Porous materials*

### INTRODUCTION

Generally speaking, porous materials can be viewed as micro (or sometimes meso) perforated solid structures that are saturated with air. When this solid frame is considered to be motionless, the porous material can be modeled only with modifications of the scalar Helmholtz equation (Johnson et al., 1987; Champoux and Allard, 1991). For more real-life based simulations, however, the frame may be derived from an elastic component, hence having considerable displacements along its structure. In this case, complex multiphysical expressions are used to fully model the fluid-structure coupling of domains that presents such configuration.

As of 1956, Biot (1956a, 1956b) proposed expressions that were able to macroscopically describe the behavior of the wave in poroelastic materials, being mainly based on the displacements of the elastic and fluid components. Later in 1998, an even more suitable formulation was proposed by Atalla et al. (1998, 2001), which considered not only the displacements of the elastic frame, but also the interstitial pressure of the fluid component. This so called mixed  $\mathbf{u}/p$  approach greatly reduced the Degrees of Freedom (dofs) involved in the Finite Element Method (FEM) implementation, being especially adopted in the works involving topology optimization procedures (Yamamoto et al., 2009; Lee et al., 2012, 2015, Hu et al. 2022).

Based on that, this work makes use of the Bi-directional Evolutionary Structural Optimization (BESO) method to maximize Transmission Loss (TL) values at a predefined target frequency. The investigated domains are mainly composed of poroelastic materials, represented by the mixed  $\mathbf{u}/p$  formulation, but with the possibility of degeneration to acoustic or elastic elements by means of the unified multiphase (UMP) approach (Lee, 2009; Lee et al., 2012). In this sense, multiphysical aspects compose the optimization, as acoustic-poroelastic-elastic domains interact throughout the entire procedure. In a systematic way, these components are rearranged in each iteration, in accordance with the adopted multiphase material interpolation scheme.

## THE MIXED U/P FINITE ELEMENT FORMULATION FOR POROELASTIC MEDIA

Assuming that the porous material properties are homogeneous and subject to harmonic oscillations ( $e^{j\omega t}$ ), the mixed displacement-pressure ( $\mathbf{u}/p$ ) formulation may be written in the following form,

$$\nabla \cdot \hat{\boldsymbol{\sigma}}^s + \omega^2 \tilde{\rho} \mathbf{u} + \tilde{\gamma} \nabla p = \mathbf{0}, \quad (1)$$

$$\nabla^2 p + \omega^2 \frac{\tilde{\rho}_{22}}{\tilde{R}} p - \omega^2 \frac{\tilde{\rho}_{22}}{\phi^2} \tilde{\gamma} \nabla \cdot \mathbf{u} = 0, \quad (2)$$

where  $\nabla$  is the gradient operator,  $\nabla^2$  is the Laplace operator,  $\omega$  is the angular frequency,  $j^2 = -1$  is the imaginary unit,  $t$  is time,  $\mathbf{u}$  is the solid phase displacement,  $p$  is the interstitial pressure and  $\phi$  is the porosity. The combined effective density  $\tilde{\rho}$  and coupling coefficient  $\tilde{\gamma}$  are defined as,

$$\tilde{\rho} = \tilde{\rho}_{11} - \frac{\tilde{\rho}_{12}^2}{\tilde{\rho}_{22}}, \quad \tilde{\gamma} = \phi \left( \frac{\tilde{\rho}_{12}}{\tilde{\rho}_{22}} - \frac{\tilde{Q}}{\tilde{R}} \right), \quad (3)$$

with  $\tilde{\rho}_{11}$ ,  $\tilde{\rho}_{22}$ ,  $\tilde{\rho}_{12}$  being the effective densities that account for the inertia effects in the solid, fluid and in the viscous coupling that happens between the two, respectively. The stress tensor of the porous material in vacuo  $\hat{\boldsymbol{\sigma}}^s$  has also a mathematical expression associated to it,

$$\hat{\boldsymbol{\sigma}}^s = \left( \tilde{A} - \frac{\tilde{Q}^2}{\tilde{R}} \right) \nabla \cdot \mathbf{u} \mathbf{I} + 2N \boldsymbol{\epsilon}^s = \hat{A} \nabla \cdot \mathbf{u} \mathbf{I} + 2N \boldsymbol{\epsilon}^s, \quad (4)$$

where  $\mathbf{I}$  is the identity tensor,  $\boldsymbol{\epsilon}^s$  is the solid phase strain tensor,  $\tilde{A}$  is the first Lamé constant of the poroelastic material,  $N$  is the elastic shear modulus,  $\tilde{Q}$  is the coupling coefficient between the dilatation of both component phases,  $\tilde{R}$  is the bulk modulus of air occupying a fraction of volume aggregate and  $\hat{A}$  is the first Lamé constant of the elastic phase in vacuo (Atalla et al., 1998; Lee et al. 2015).

The weak form of Eqs. (1) and (2) is then obtained by the combination of the Weighted Residuals Method and the divergence theorem, followed by the consideration of material isotropy, that is (Rigobert et al., 2003; Lee et al. 2015),

$$\int_{\Omega_p} \left\{ \hat{\boldsymbol{\sigma}}^s(\mathbf{u}) : \boldsymbol{\epsilon}^s(\delta \mathbf{u}) - \omega^2 \tilde{\rho} \mathbf{u} \cdot \delta \mathbf{u} - (\tilde{\gamma} + \tilde{\xi}) \nabla p \cdot \delta \mathbf{u} - \tilde{\xi} p \nabla \cdot \delta \mathbf{u} \right\} d\Omega_p - \int_{\Gamma_p} (\boldsymbol{\sigma}^t \cdot \mathbf{n}) \cdot \delta \mathbf{u} d\Gamma_p = 0, \quad (5)$$

$$\int_{\Omega_p} \left\{ \frac{\phi^2}{\omega^2 \tilde{\rho}_{22}} \nabla p \cdot \nabla \delta p - \frac{\phi^2}{\tilde{R}} p \delta p - (\tilde{\gamma} + \tilde{\xi}) \nabla \delta p \cdot \mathbf{u} - \tilde{\xi} \delta p \nabla \cdot \mathbf{u} \right\} d\Omega_p - \int_{\Gamma_p} \phi (\mathbf{U} - \mathbf{u}) \cdot \mathbf{n} \delta p d\Gamma_p = 0, \quad (6)$$

where  $\delta \mathbf{u}$  and  $\delta p$  are test functions related with the solid phase displacement and the interstitial pressure, respectively, while  $\Omega_p$  represents the poroelastic domain with  $\Gamma_p$  as its boundary. The newly introduced variable  $\tilde{\xi} = \phi(1 + \tilde{Q}/\tilde{R})$  may be also viewed as a coupling coefficient, and  $\mathbf{n}$  is the outward unit normal vector.

An important point is that Eqs. (5) and (6) have boundary related expressions that can be physically specified on the interface of two distinct poroelastic media, that is the traction vector,  $\boldsymbol{\sigma}^t \cdot \mathbf{n}$ , and the relative displacement vector,  $(\mathbf{U} - \mathbf{u}) \cdot \mathbf{n}$ . Joining this characteristic with the continuity of the nodal variables that it is common to the FEM, the coupling of poroelastic-poroelastic and poroelastic-elastic materials happens naturally and completely free of further approximations (Atalla et al., 2001).

The FEM is then considered in the discretization of the aforementioned continuous problem, being also followed by Galerkin's approach. The result is a linear system of equations (Allard and Atalla, 2009), as can be seen next,

$$\begin{bmatrix} \mathbf{K} - \omega^2 \tilde{\mathbf{M}} & -(\tilde{\mathbf{C}}_1 + \tilde{\mathbf{C}}_2) \\ -(\tilde{\mathbf{C}}_1 + \tilde{\mathbf{C}}_2)^T & \tilde{\mathbf{H}}/\omega^2 - \tilde{\mathbf{Q}} \end{bmatrix} \begin{Bmatrix} \mathbf{u} \\ \mathbf{p} \end{Bmatrix} = \begin{Bmatrix} \mathbf{f}_s \\ \mathbf{f}_p/\omega^2 \end{Bmatrix}, \quad (7)$$

where  $\mathbf{K}$ ,  $\tilde{\mathbf{M}}$ ,  $\tilde{\mathbf{H}}$ ,  $\tilde{\mathbf{Q}}$ ,  $\tilde{\mathbf{C}}_1$ ,  $\tilde{\mathbf{C}}_2$  denote the global stiffness, mass, kinetic, compression and coupling matrices, respectively. The global displacement and acoustic pressure vectors, as well as the global structural and acoustic loads are respectively defined as  $\mathbf{u}$ ,  $\mathbf{p}$ ,  $\mathbf{f}_s$ ,  $\mathbf{f}_p$ .

## UNIFIED MULTIPHASE MODELING APPROACH

Following the works of Lee (2009) and Lee et. al (2012), the UMP approach aims at using Biot's equations, in the  $\mathbf{u}/p$  form, to easily describe the three main medias considered in vibroacoustic systems applications. Hence, the scalar

Helmholtz and the elasto-dynamic equations are directly derived from Eqs. (1) and (2) if ones goal is to simulate acoustic or elastic materials, respectively. This happens by taking limit values of some material parameters, in order to degenerate the original Biot's equations in the ones of interest. As a direct consequence of the method, no boundary tracking is ever needed when changing from one element type to another.

In a numerical point of view, six variables are directly controlled by the UMP approach, in a way that the dynamic properties of the base poroelastic material are changed in accordance with the element configuration. In a purely poroelastic scenario, the variables are:  $\tilde{\xi}$ ,  $\tilde{\rho}$ ,  $N$ ,  $\hat{A}$ ,  $\phi^2/\tilde{\rho}_{22}$  and  $\phi^2/\tilde{R}$ . For the acoustic case, the same variables assume the following form: 1, 0, 0, 0,  $1/\rho_a$  and  $1/\kappa_a$ , where  $\kappa_a$  is the bulk modulus of the air (identified by the subscript  $a$ ). Lastly, for the elastic case, one gets the sequence: 0,  $\rho_e$ ,  $N_e$ ,  $\hat{A}_e$ , 0 and 0, with the subscript  $e$  being related with the elastic material.

A downside of this approach, in a finite element point of view, regards the singularity that happens when completely canceling one of the aforementioned variables. To solve this issue, small valued coefficients are assigned to each of the properties that have to be zero, in a way that all the sequences get the following results,

$$\{\tilde{\xi}, \tilde{\rho}, N, \hat{A}, (\phi^2/\tilde{\rho}_{22}), (\phi^2/\tilde{R})\}_p = \{\tilde{\xi}, \tilde{\rho}, N, \hat{A}, \phi^2/\tilde{\rho}_{22}, \phi^2/\tilde{R}\}, \quad (8)$$

$$\{\tilde{\xi}, \tilde{\rho}, N, \hat{A}, (\phi^2/\tilde{\rho}_{22}), (\phi^2/\tilde{R})\}_a = \{1, \varepsilon_a \tilde{\rho}, \varepsilon_a N, \varepsilon_a \hat{A}, 1/\rho_a, 1/\kappa_a\}, \quad (9)$$

$$\{\tilde{\xi}, \tilde{\rho}, N, \hat{A}, (\phi^2/\tilde{\rho}_{22}), (\phi^2/\tilde{R})\}_e = \{\varepsilon_e \tilde{\xi}, \rho_e, N_e, \hat{A}_e, \varepsilon_e (\phi^2/\tilde{\rho}_{22}), \varepsilon_e (\phi^2/\tilde{R})\}, \quad (10)$$

with the subscript  $p$  referring to the poroelastic materials. In this work, the values of  $\varepsilon_a$  and  $\varepsilon_e$  were carefully selected to be  $1 \times 10^{-4}$  and  $1 \times 10^{-9}$ , respectively.

### Material interpolation scheme: acoustic, elastic and poroelastic relations

As the main objective of this paper is to study the design of structures composed of acoustic-poroelastic-elastic medias, a multiphase material interpolation scheme is presented in Eqs. (11) to (16) with the goal of providing systematic material changes along the entire optimization process,

$$\tilde{\xi} = \tilde{\xi}_e + x_2^{\zeta_2} (\tilde{\xi}_p - \tilde{\xi}_e) + x_1^{\zeta_1} (\tilde{\xi}_a - \tilde{\xi}_p), \quad (11)$$

$$\tilde{\rho} = \tilde{\rho}_e + x_2^{\zeta_2} (\tilde{\rho}_p - \tilde{\rho}_e) + x_1^{\zeta_1} (\tilde{\rho}_a - \tilde{\rho}_p), \quad (12)$$

$$N = N_e + x_2^{\zeta_2} (N_p - N_e) + x_1^{\zeta_1} (N_a - N_p), \quad (13)$$

$$\hat{A} = \hat{A}_e + x_2^{\zeta_2} (\hat{A}_p - \hat{A}_e) + x_1^{\zeta_1} (\hat{A}_a - \hat{A}_p), \quad (14)$$

$$\phi^2/\tilde{\rho}_{22} = (\phi^2/\tilde{\rho}_{22})_e + x_2^{\zeta_2} [(\phi^2/\tilde{\rho}_{22})_p - (\phi^2/\tilde{\rho}_{22})_e] + x_1^{\zeta_1} [(\phi^2/\tilde{\rho}_{22})_a - (\phi^2/\tilde{\rho}_{22})_p], \quad (15)$$

$$\phi^2/\tilde{R} = (\phi^2/\tilde{R})_e + x_2^{\zeta_2} [(\phi^2/\tilde{R})_p - (\phi^2/\tilde{R})_e] + x_1^{\zeta_1} [(\phi^2/\tilde{R})_a - (\phi^2/\tilde{R})_p], \quad (16)$$

where  $x_{1,2}$  represent the design variables and the superscripts  $\zeta_{1,2}$  are the penalty coefficients. At this stage, it is important to note that even though the elastic and acoustic materials are indeed degenerated poroelastic ones, as highlighted in Eqs. (8), (9) and (10), comparisons between the UMP approach and the segregated formulations (scalar Helmholtz for acoustic, elasto-dynamic for elastic and Biot's equations for poroelastic) have been conducted by the authors, hence validating the current numerical approach. Another notable point is that, after a series of test, the following values were chosen for the design variables,

$$\{x_1, x_2\} = \{1, 1\}, \quad \text{for acoustic elements,} \quad (17)$$

$$\{x_1, x_2\} = \{x_{\min}, 1\}, \quad \text{for poroelastic elements,} \quad (18)$$

$$\{x_1, x_2\} = \{x_{\min}, x_{\min}\}, \quad \text{for elastic elements,} \quad (19)$$

and for the penalty variables,  $\{\zeta_1, \zeta_2\} = \{2, 1\}$ . The user defined  $x_{\min} = 0.001$  parameter is the lower limit that the design variable can get, being usually adopted to avoid numerical singularities. Finally, the poroelastic and elastic material properties adopted in this work are presented in Table 1, while the acoustic ones are the same as brought by Pereira et al. (2022).

**Table 1 – Poroelastic and elastic material properties (Yamamoto et al. 2009)**

Parameters	Polyurethane foam	Olefin sheet
Porosity $\phi$	0.97	–
Tortuosity $\alpha_\infty$	2.5	–
Static flow resistivity $\sigma$ (N s m <sup>-4</sup> )	$7 \times 10^4$	–
Viscous characteristic length $\Lambda$ ( $\mu\text{m}$ )	$36 \times 10^{-6}$	–
Thermal characteristic length $\Lambda'$ ( $\mu\text{m}$ )	$170 \times 10^{-6}$	–
Solid mass density $\rho$ (kg m <sup>-3</sup> )	1433	1790
Young's modulus $E$ (Pa)	$2.67 \times 10^5$	$1.75 \times 10^8$
Poisson ratio $\nu$	0.4	0.4
Loss factor $\eta$	0.11	0.205

## TOPOLOGY OPTIMIZATION FORMULATION

Since TL values are common vibroacoustic indicators regarding the attenuation of sound in acoustic systems, the topology optimization problem here investigated aims at the maximization of TL values at target frequencies, when subjected to equilibrium equations (Eq. 7) and volume constraints,

$$\text{Maximize: TL} = 20 \log_{10} \left( \left| \frac{1}{p_3} \frac{p_1 - p_2 \exp(-jk_a L)}{1 - \exp(-j2k_a L)} \right| \right), \quad (20)$$

$$\text{Subjected to: } \begin{cases} \begin{bmatrix} \mathbf{K} - \omega^2 \tilde{\mathbf{M}} & -(\tilde{\mathbf{C}}_1 + \tilde{\mathbf{C}}_2) \\ -(\tilde{\mathbf{C}}_1 + \tilde{\mathbf{C}}_2)^T & \tilde{\mathbf{H}}/\omega^2 - \tilde{\mathbf{Q}} \end{bmatrix} \begin{Bmatrix} \mathbf{u} \\ \mathbf{p} \end{Bmatrix} = \begin{Bmatrix} \mathbf{f}_s \\ \mathbf{f}_p/\omega^2 \end{Bmatrix}, \\ \begin{Bmatrix} V_1^* - \left( \sum_{i=1}^{N_{el}} V_i \gamma_i \right)_1 \\ V_2^* - \left( \sum_{i=1}^{N_{el}} V_i \gamma_i \right)_2 \end{Bmatrix} = \begin{Bmatrix} 0 \\ 0 \end{Bmatrix}, \\ \mathbf{x} = \left[ \begin{array}{c} \begin{Bmatrix} x_1 \\ \vdots \\ x_{N_{el}} \end{Bmatrix}_1 \\ \begin{Bmatrix} x_1 \\ \vdots \\ x_{N_{el}} \end{Bmatrix}_2 \end{array} \right]. \end{cases} \quad (21)$$

As observed in Eq. (20), the two sound pressure amplitudes that are collected at the left side of the system (inlet) are  $p_1$  and  $p_2$ , apart  $L$  from each other, while the one gathered at the right side (outlet) is  $p_3$  (see Fig. 1). Here, the wave number is denoted as  $k_a$ . In Eq. (21) the prescribed final volume fraction is  $V^*$ , with the design domain volume fraction being  $\sum_{i=1}^{N_{el}} V_i \gamma_i$ .  $N_{el}$  is the number of elements of the entire porous domain and  $\mathbf{x}$  is the design variable matrix. The subscript numbers 1 and 2 represents the changes that happens along the optimization process, in other words, the number 1 refers to variations from acoustic to poroelastic elements, while the number 2 regards the changes from poroelastic to elastic. It is remarked, however, that changes from acoustic to poroelastic happens prior to poroelastic to elastic, in a way that the final volume fraction of poroelastic materials have to be achieved to start the next set of alterations (poroelastic to elastic). Finally, it may also be noted that once  $V_1^*$  is reached, the value is kept constant until the achievement of  $V_2^*$  (Huang and Xie, 2010).

## Sensitivity analysis

As previously highlighted, TL values are often observed when dealing with acoustic systems, which motivated many researchers to conduct the derivation of Eq. (20) (Lee, 2009; Yoon, 2013; Lee et al. 2015; Azevedo et al., 2018; Ferrándiz et al. 2020; Hu et al., 2022). In a mathematical perspective, the elemental sensitivity number,  $\alpha_i$ , is usually obtained as,

$$\alpha_i = \frac{\partial \text{TL}}{\partial x_i} = \frac{10}{\ln 10} \left( \frac{\partial |p_{\text{in}}|^2}{\partial x_i} \frac{1}{|p_{\text{in}}|^2} - \frac{\partial |p_{\text{out}}|^2}{\partial x_i} \frac{1}{|p_{\text{out}}|^2} \right), \quad (22)$$

where,

$$|p_{\text{in}}| = |(p_1 - p_2 e^{-jk_a L}) / (1 - e^{-j2k_a L})| \quad (23)$$

$$|p_{\text{out}}| = |p_3|. \quad (24)$$

After open the expressions for  $\partial|p_{\text{in}}|^2/\partial x_i$  and  $\partial|p_{\text{out}}|^2/\partial x_i$ , one will need to find the partial derivatives of the observed pressures in the  $j$ th node, hence,

$$\frac{\partial p_j}{\partial x_i} = -\hat{\mathbf{p}}_j^T \begin{bmatrix} \frac{\partial \mathbf{K}}{\partial x_i} - \omega^2 \frac{\partial \tilde{\mathbf{M}}}{\partial x_i} & -\left(\frac{\partial \tilde{\mathbf{C}}_1}{\partial x_i} + \frac{\partial \tilde{\mathbf{C}}_2}{\partial x_i}\right) \\ -\left(\frac{\partial \tilde{\mathbf{C}}_1}{\partial x_i} + \frac{\partial \tilde{\mathbf{C}}_2}{\partial x_i}\right)^T & \frac{1}{\omega^2} \frac{\partial \tilde{\mathbf{H}}}{\partial x_i} - \frac{\partial \tilde{\mathbf{Q}}}{\partial x_i} \end{bmatrix} \begin{Bmatrix} \mathbf{u} \\ \mathbf{p} \end{Bmatrix}, \quad (25)$$

where,

$$\hat{\mathbf{p}}_j^T = \mathbf{f}_j^T \begin{bmatrix} \mathbf{K} - \omega^2 \tilde{\mathbf{M}} & -(\tilde{\mathbf{C}}_1 + \tilde{\mathbf{C}}_2) \\ -(\tilde{\mathbf{C}}_1 + \tilde{\mathbf{C}}_2)^T & \tilde{\mathbf{H}}/\omega^2 - \tilde{\mathbf{Q}} \end{bmatrix}^{-1}, \quad (26)$$

being the solution of the transposed problem. The partial derivatives resulted from Eq. (25) are easily obtained from the material interpolation schemes provided in Eqs. (11) to (16). Finally,  $\mathbf{f}_j$  may be viewed as a locator, that is a vector full of zeros, except on the dof referred to  $p_j$ .

## Overview of the BESO method

The BESO method is the topology optimization approach of choice in this work, as proposed by Huang and Xie (2010), since it provides clearly defined designs at all stages of the iterative problem. The following algorithm summarizes the entire method.

---

### Algorithm 1: BESO algorithm

---

**Input:** Define geometry and FEM parameters

Define BESO parameters:  $\underline{\mathbf{x}}, V^*, r_{\text{min}}, \text{ER}, \text{AR}_{\text{max}}, \zeta_{1,2}$

Evaluate  $\mathbf{u}$  and  $\mathbf{p}$

Start iteration counter:  $r = 0$

**while**  $\text{err} < 0.005$  **or**  $V_1^{(r)} + V_2^{(r)} \neq V_1^* + V_2^*$  **do**

$r = r + 1$

    Calculate sensitivity numbers

    Filter sensitivities (+ historical averaging + normalization)

    Update design domain

    Update volume domain

    Evaluate  $\mathbf{u}$  and  $\mathbf{p}$

    Evaluate TL

$$\text{err} = \frac{|\sum_{b=1}^{10} \text{TL}^{(r-b+1)} - \sum_{b=1}^{10} \text{TL}^{(r-9-b)}|}{\sum_{b=1}^{10} \text{TL}^{(r-b+1)}} \leq 0.005 \quad (27)$$

**Output:** Optimized topology

---

In Algorithm 1, it is perceptible that the domain geometry needs to be known beforehand, as well as the solution vectors  $\mathbf{u}$  and  $\mathbf{p}$ . Next, in the while loop, the sensitivities are calculated and then filtered, following a projection approach that is controlled by the filter radius,  $r_{\text{min}}$ . To increase the stability of the optimization, two more procedures are commonly performed, being the historical averaging of the elemental sensitivities and its normalization (Zhou et al., 2021). Before updating the design variables, it is necessary to first determine the volume of the next iteration,  $V^{(r+1)}$ , with the information of the current,  $V^{(r)}$ , and the Evolutionary Rate (ER), that is  $V^{(r+1)} = V^{(r)}(1 \pm \text{ER})$ .

The sensitivity numbers are then sorted from highest to lowest, in order to assign the elements with the biggest  $\alpha_i$  values as “full” and the smallest as “void”. The bi-directionality of the BESO approach is characterized by the allowance

of the contrary mechanism, that is “void” elements can turn back to be “full”, which is controlled by the Addition Ratio ( $AR_{\max}$ ). As the topology is updated, the solution vectors  $\mathbf{u}$  and  $\mathbf{p}$  are obtained, followed by the transmission loss values. The final step is done by the calculation of the iteration error, that has to be smaller than the tolerance of 0.5%.

## NUMERICAL EXAMPLES

In this section the optimization of two distinct systems composed of acoustic-poroelastic-elastic components are presented and discussed. Figure 1 shows two fairly similar systems, but with different boundary conditions. In the first one, shown in Fig. 1 (a), the top surface is considered to be a hard wall (all elastic dofs are blocked), while the bottom is a symmetry boundary (only the dofs in the  $y$  direction are blocked). A pressure imposed plane wave enters at the left side of the system, while an anechoic termination is considered to be present at the far right. It is remarked that, in all domains here considered, only poroelastic elements exist, being therefore modified to represent acoustic or elastic elements by the UMP technique. In this sense, all nodes have three dofs, even when they are in the “modified form”, where two are related with the displacements of the elastic frame and one with the interstitial pressure. As a consequence, the imposition of the boundary conditions here considered are not straightforward, being presented in detail in the works of Lee (2009) and Lee et al. (2012).

Still in Fig. 1 (a), the design domain,  $\Omega_d$ , is characterized by a light grey area of  $8 \times 5 \text{ cm}^2$ , and the non-design domain,  $\Omega_{nd}$ , by two white and small black areas of  $1 \times 5 \text{ cm}^2$  and  $0.1 \times 5 \text{ cm}^2$ , respectively. Three previously chosen points of observation of pressure (inside inverted triangles) are also present. Figure 1 (b) shows the same elements as previously highlighted, but with symmetry boundary conditions also in the top surface of the system. Another common fact regarding both scenarios is the number of finite elements. It is a known fact that to simulate poroelastic structures more elements are required per wavelength than common acoustic ones. Based on this, the entire system is composed of  $102 \times 40$  first order quadrilateral elements, being way above the recommended per wavelength (Atalla and Sgard, 2015).

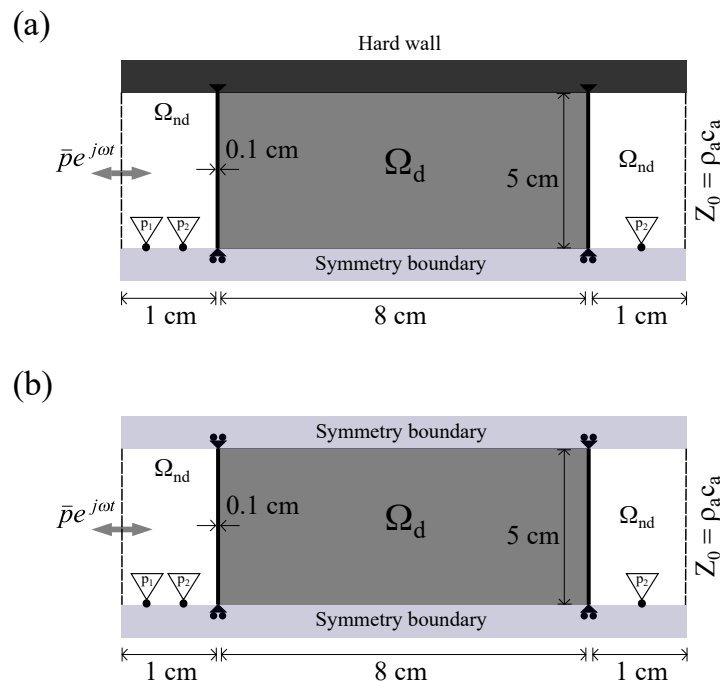


Figure 1 – Details of the geometries investigated.

In this study, the initial configuration is that acoustic elements fill the entire  $\Omega_d$  (light grey area), while  $\Omega_{nd}$  has both, acoustic (white areas) and elastic (black area) components. In this sense, the BESO parameters are chosen to be  $ER = 1\%$ ,  $AR = 0.5\%$ ,  $r_{\min}^1 = 3 \text{ cm}$  and  $r_{\min}^2 = 2 \text{ cm}$ . These two distinct filter radius were adopted as an effort to reduced isolated configurations throughout the design domain. Furthermore,  $V_1^*$  and  $V_2^*$  assume the values of 0.5 and 0.05, respectively, which guarantees that porous materials occupy 50% of the design domain, while the elastic component fills 5% of it. For the sake of conciseness, the scenarios shown in Figs. 1 (a) and (b) will be referred, from now on, as Hard-Symmetry (or simply HS) and Symmetry-Symmetry (SS).

## Topology Optimization of the Hard-Symmetry and Symmetry-Symmetry systems

Figure 2 shows the main results obtained from the analysis of the HS system (see Fig. 1 (a)) for the target frequency of 250 Hz. In Fig. 2 (b), the evolution of the volume fractions for acoustic (Vol.Frac - A), poroelastic (Vol.Frac - P) and elastic (Vol.Frac - E) components are shown, together with the behavior of the objective function along the iterative procedure. It is perceptible that TL values vary greatly throughout the course of the optimization, in a way that the procedure stops only due to the mean values obtained in the calculation of Eq. (27). This fact shows that the ER and AR<sub>max</sub> values chosen need to be reevaluated to an even lower number, as an effort to reduce such erratic behavior.

Nevertheless, the topology resulted seem to be effective in promoting the increase of TL values, not only in the target frequency, but also in the vast range of frequencies observed. Besides, the choice of different filter radius sizes is here justified, as the poroelastic-elastic structures appear quite close to each other, instead of generating expressive material disconnections (like porous structures floating on air); enhancing the manufacturability of the global optimized topologies.

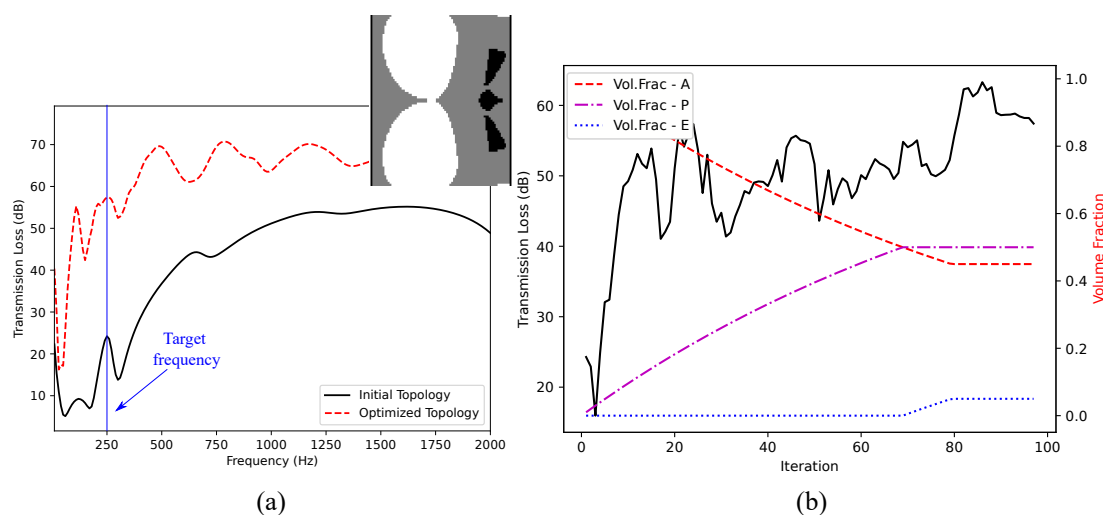


**Figure 2 – Main results of the Hard-Symmetry system case, with (a) the transmission loss responses of the initial and final configurations, highlighting the final topology, together with (b) the evolution of the objective function and volume fractions of the three materials under consideration.**

All of these findings can also be extended to the SS case (Fig. 3), given that the materials are close together in the resulted topology and the TL enhancements are of 41.67 dB, but with oscillatory evolution. A different point is that, in the HS configuration, both poroelastic and elastic materials seem to be drawn to the left and right sides of the domain, while in the SS scenario these components are mainly located on the top and bottom portions of it. Such behavior is clearly caused by the different boundary conditions considered, in a way that the HS case may represent a superior far end part of a periodic structure (being the hard wall on the top and the periodic boundary on the bottom) and the SS condition may be seen as the body part of said periodic structure (repeating themselves up and down).

## CONCLUSIONS

In this work a topology optimization problem was developed, in order to design systems composed of acoustic-poroelastic-elastic elements. Additionally, to ensure that clear design configurations are obtained at the end of the procedure, the BESO method was chosen. In this scenario, transmission loss values were maximized at 250 Hz, while poroelastic and elastic materials were introduced in a design domain initially filled of acoustic elements, hence configuring a multiphase approach. The modeling of such material phases was done by the unified multiphase technique, which made use of Biot's equations, in the mixed  $\mathbf{u}/p$ , to obtain the scalar Helmholtz and elasto-dynamic expressions.

These fully modeled components were then systematically changed along the optimization iterations by an introduced material interpolation scheme. In this scenario, two problems were investigated, being geometrically similar, but with differences in the boundary configuration. In both cases, the transmission loss values were successfully enhanced and the material disposition kept the components close to each other (with almost no material disconnection). As a drawback, a great deal of variations occurred in the evolution of the objection function due to the iterative step chosen (ER and AR<sub>max</sub>

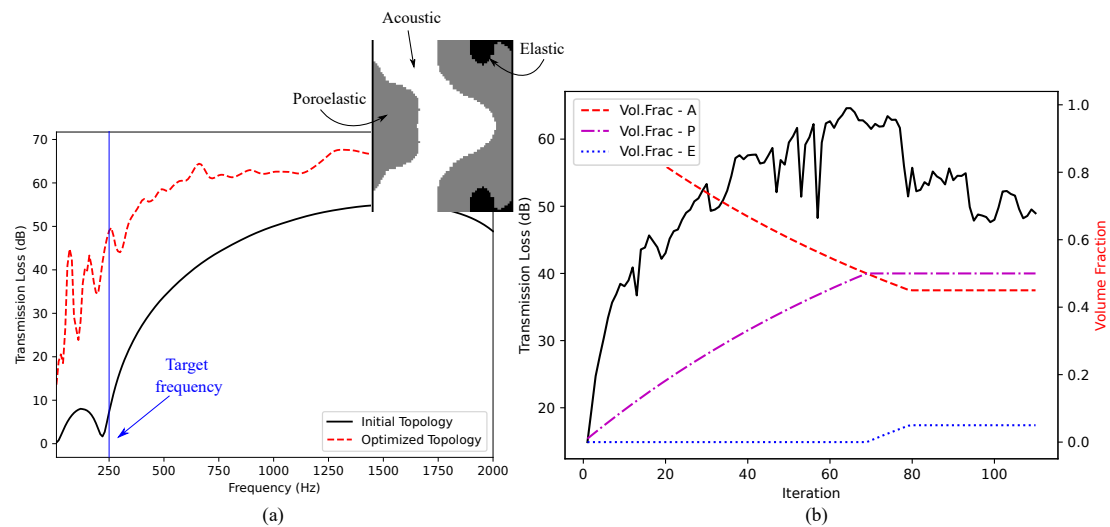


**Figure 3 – Main results of the Symmetry-Symmetry system case, with (a) the transmission loss responses of the initial and final configurations, highlighting the final topology, together with (b) the evolution of the objective function and volume fractions of the three materials under consideration.**

values).

## ACKNOWLEDGMENTS

The authors would like to acknowledge the financial support given by the Fundação de Amparo à Pesquisa do Estado de São Paulo (FAPESP), project numbers 2013/08293-7, and by the Coordenação de Aperfeiçoamento de Pessoal do Nível Superior (CAPES), finance code 001.

## REFERENCES

- Allard, J.F. and Atalla, N., 2009, “Propagation of Sound in Porous Media: Modelling Sound Absorbing Materials”, Ed. John Wiley & Sons, West Sussex, United Kingdom, 358 p.
- Atalla, N., Panneton, R. and Debergue, P., 1998, “A mixed displacement-pressure formulation for poroelastic materials”, *J. Acoust. Soc. Am.*, Vol. 104, pp. 1444-1452.
- Atalla, N., Hamdi, M.A. and Panneton, R., 2001, “Enhanced weak integral formulation for the mixed (u,p) poroelastic equations”, *J. Acoust. Soc. Am.*, Vol. 109, pp. 3065-3068.
- Atalla, N. and Sgard, F., 2015, “Finite Element and Boundary Methods in Structural Acoustics and Vibration”, Ed. CRC Press, Florida, United States, 441 p.
- Azevedo, F.M., Moura, M.S., Vicente, W.M., Picelli, R. and Pavanello, R., 2018, “Topology optimization of reactive acoustic mufflers using a bi-directional evolutionary optimization method”, *Struct. Multidiscip. Optim.*, Vol. 58, pp. 2239-2252.
- Biot, M.A., 1956, “Theory of Propagation of Elastic Waves in a Fluid-Saturated Porous Solid: I. Low-Frequency Range”, *J. Acoust. Soc. Am.*, Vol. 28, pp. 168-178.
- Biot, M.A., 1956, “Theory of Propagation of Elastic Waves in a Fluid-Saturated Porous Solid: II. Higher-Frequency Range”, *J. Acoust. Soc. Am.*, Vol. 28, pp. 179-191.
- Champoux, Y. and Allard, J., 1991, “Dynamic tortuosity and bulk modulus in air-saturated porous media”, *J. Appl. Phys.*, Vol. 70, pp. 1975-1979.
- Ferrández, B., Denia, F.D., Martínez-Casas, J., Nadal, E. and Ródenas, J.J., 2020, “Topology and shape optimization of dissipative and hybrid mufflers”, *Struct. Multidiscip. Optim.*, Vol. 62, pp. 269–284.
- Hu, J., Yao, S. and Huang, X., 2022, “Topological design of sandwich structures filling with poroelastic materials for sound insulation”, *Finite Elem. Anal. Des.*, Vol. 199, pp. 103650.
- Huang, X. and Xie, Y.M., 2010, “Evolutionary Topology Optimization of Continuum Structures: Methods and Applications”, Ed. John Wiley & Sons, West Sussex, United Kingdom, 223 p.

- Johnson, D.L., Koplik, J. and Dashen, R., 1987, “Theory of dynamic permeability and tortuosity in fluid-saturated porous media”, *J. Fluid Mech.*, Vol. 176, pp. 379-402.
- Lee, J.S., 2009, “Unified Multi-Phase Modeling and Topology Optimization for Complex Vibro-Acoustic Systems Consisting of Acoustic, Poroelastic and Elastic Media”, School of Mechanical and Aerospace Engineering, The Graduate School, Seoul National University.
- Lee, J.S., Göransson, P. and Kim, Y.Y., 2015, “Topology optimization for three-phase materials distribution in a dissipative expansion chamber by unified multiphase modeling approach”, *Comput. Method Appl. M.*, Vol. 287, pp. 191-211.
- Lee, J.S., Kang, Y.J. and Kim, Y.Y., 2012, “Unified multiphase modeling for evolving, acoustically coupled systems consisting of acoustic, elastic, poroelastic media and septa”, *J. Sound Vib.*, Vol. 331, pp. 5518-5536.
- Lee, J.W. and Kim, Y.Y., 2009, “Topology optimization of muffler internal partitions for improving acoustical attenuation performance”, *Int. J. Numer. Meth. Eng.*, Vol. 80, pp. 455-477.
- Pereira, R.L., Lopes, H.N. and Pavanello, R., 2022, “Topology optimization of acoustic systems with a multiconstrained BESO approach”, *Finite Elem. Anal. Des.*, Vol. 201, pp. 103701.
- Rigobert, S., Atalla, N. and Sgard, F.C., 2003, “Investigation of the convergence of the mixed displacement-pressure formulation for three-dimensional poroelastic materials using hierarchical elements”, *J. Acoust. Soc. Am.*, Vol. 114, pp. 2607-2617.
- Yamamoto, T., Maruyama, S., Nishiwaki, S. and Yoshimura, M., 2009, “Topology design of multi-material soundproof structures including poroelastic media to minimize sound pressure levels”, *Comput. Method Appl. M.*, Vol. 198, pp. 1439-1455.
- Yoon, G. H., 2013, “Acoustic topology optimization of fibrous material with Delany–Bazley empirical material formulation”, *J. Sound Vib.*, Vol. 332, pp. 1172-1187.
- Zhou, E. L., Wu, Y., Lin, X. Y., Li, Q. Q. and Xiang, Y., 2021, “A normalization strategy for BESO-based structural optimization and its application to frequency response suppression”, *Acta Mech.*, Vol. 232, pp. 1307-1327.

## RESPONSIBILITY NOTICE

The authors are the only parties responsible for the printed material included in this paper.

## C | Permission to Use Content – Elsevier and Springer Nature

Part of this work regarding the optimization of acoustic-rigid metasurfaces and poro-acoustic systems (Chapter 4) was reprinted from the publication: Pereira, R.L.; Lopes, H.N.; Pavanello, R. Topology optimization of acoustic systems with a multiconstrained BESO approach. *Finite Element in Analysis and Design*, v. 201, p. 103701, (2022), with permission from Elsevier. Part of this work referring to the multiphase optimization of muffler multichambers (Chapter 5) was first published in: Pereira, R.L.; Lopes, H.N.; Moura, M.S.; Pavanello R. Multi-domain acoustic topology optimization based on the BESO approach: applications on the design of multi-phase material mufflers. *Structural and Multidisciplinary Optimization*, v. 66, p. 25 (2023), and is reproduced with permission of Springer Nature. All copyright clearances are presented in the following:

### Institution rights

Regardless of how the author chooses to publish with Elsevier, their institution has the right to use articles for classroom teaching and internal training. Articles can be used for these purposes throughout the author's institution, not just by the author:

Institution rights in Elsevier's proprietary journals (providing full acknowledgement of the original article is given)	All articles
Copies can be distributed electronically as well as in physical form for classroom teaching and internal training purposes	√
Material can be included in coursework and courseware programs for use within the institution (but not in Massive Open Online Courses)	√
Articles can be included in applications for grant funding	√
Theses and dissertations which contain embedded final published articles as part of the formal submission can be posted publicly by the awarding institution with DOI links back to the formal publication on ScienceDirect	√

## Author rights

The below table explains the rights that authors have when they publish with Elsevier, for authors who choose to publish either open access or subscription. These apply to the corresponding author and all co-authors.

Author rights in Elsevier's proprietary journals	Published open access	Published subscription
Retain patent and trademark rights	✓	✓
Retain the rights to use their research data freely without any restriction	✓	✓
Receive proper attribution and credit for their published work	✓	✓
Re-use their own material in new works without permission or payment (with full acknowledgement of the original article): 1. Extend an article to book length 2. Include an article in a subsequent compilation of their own work 3. Re-use portions, excerpts, and their own figures or tables in other works.	✓	✓
Use and share their works for scholarly purposes (with full acknowledgement of the original article): 1. In their own classroom teaching. Electronic and physical distribution of copies is permitted 2. If an author is speaking at a conference, they can present the article and distribute copies to the attendees 3. Distribute the article, including by email, to their students and to research colleagues who they know for their personal use 4. Share and publicize the article via Share Links, which offers 50 days' free access for anyone, without signup or registration 5. Include in a thesis or dissertation (provided this is not published commercially) 6. Share copies of their article privately as part of an invitation-only work group on commercial sites with which the publisher has a hosting agreement	✓	✓
Publicly share the preprint on any website or repository at any time.	✓	✓
Publicly share the accepted manuscript on non-commercial sites	✓	✓ using a CC BY-NC-ND license and usually only after an embargo period (see <a href="#">Sharing Policy</a> for more information)
Publicly share the final published article	✓ in line with the author's choice of end user license	×
Retain copyright	✓	×

See <https://www.elsevier.com/about/policies/copyright> for a complete description of Elsevier's permissions and <https://www.elsevier.com/about/policies/copyright/permissions> for a quick and easy route to permissions guide.

08/02/2023 09:16

RightsLink Printable License

SPRINGER NATURE LICENSE  
TERMS AND CONDITIONS

Feb 08, 2023

---

---

This Agreement between Mr. Rodrigo Pereira ("You") and Springer Nature ("Springer Nature") consists of your license details and the terms and conditions provided by Springer Nature and Copyright Clearance Center.

License Number	5484170248689
License date	Feb 08, 2023
Licensed Content Publisher	Springer Nature
Licensed Content Publication	Structural and Multidisciplinary Optimization
Licensed Content Title	Multi-domain acoustic topology optimization based on the BESO approach: applications on the design of multi-phase material mufflers
Licensed Content Author	Rodrigo L. Pereira et al
Licensed Content Date	Jan 9, 2023
Type of Use	Thesis/Dissertation
Requestor type	non-commercial (non-profit)
Format	print and electronic
Portion	full article/chapter
Will you be translating?	no
Circulation/distribution	500 - 999

08/02/2023 09:16

RightsLink Printable License

Author of this Springer Nature content	yes
Title	Multi-domain acoustic topology optimization based on the BESO approach: applications on the design of multi-phase material mufflers
Institution name	Universidade Estadual de Campinas
Expected presentation date	Mar 2023
Requestor Location	[REDACTED]
Customer VAT ID	[REDACTED]
Total	0.00 USD

Terms and Conditions

### Springer Nature Customer Service Centre GmbH Terms and Conditions

The following terms and conditions ("Terms and Conditions") together with the terms specified in your [RightsLink] constitute the License ("License") between you as Licensee and Springer Nature Customer Service Centre GmbH as Licensor. By clicking 'accept' and completing the transaction for your use of the material ("Licensed Material"), you confirm your acceptance of and obligation to be bound by these Terms and Conditions.

#### 1. Grant and Scope of License

1.1. The Licensor grants you a personal, non-exclusive, non-transferable, non-sublicensable, revocable, world-wide License to reproduce, distribute, communicate to the public, make available, broadcast, electronically transmit or create derivative works using the Licensed Material for the purpose(s) specified in your RightsLink Licence Details only. Licenses are granted for the specific use requested in the order and for no other use, subject to these Terms and Conditions. You acknowledge and agree that the rights granted to you under this License do not include the right to modify, edit, translate, include in collective works, or create derivative works of the Licensed Material in whole or in part unless expressly stated in your RightsLink Licence Details. You may use the Licensed Material only as permitted under this Agreement and will not reproduce, distribute, display, perform, or otherwise use or exploit any Licensed Material in any way, in whole or in part, except as expressly

permitted by this License.

1. 2. You may only use the Licensed Content in the manner and to the extent permitted by these Terms and Conditions, by your RightsLink Licence Details and by any applicable laws.

1. 3. A separate license may be required for any additional use of the Licensed Material, e.g. where a license has been purchased for print use only, separate permission must be obtained for electronic re-use. Similarly, a License is only valid in the language selected and does not apply for editions in other languages unless additional translation rights have been granted separately in the License.

1. 4. Any content within the Licensed Material that is owned by third parties is expressly excluded from the License.

1. 5. Rights for additional reuses such as custom editions, computer/mobile applications, film or TV reuses and/or any other derivative rights requests require additional permission and may be subject to an additional fee. Please apply to [journalpermissions@springernature.com](mailto:journalpermissions@springernature.com) or [bookpermissions@springernature.com](mailto:bookpermissions@springernature.com) for these rights.

## 2. Reservation of Rights

Licensor reserves all rights not expressly granted to you under this License. You acknowledge and agree that nothing in this License limits or restricts Licensor's rights in or use of the Licensed Material in any way. Neither this License, nor any act, omission, or statement by Licensor or you, conveys any ownership right to you in any Licensed Material, or to any element or portion thereof. As between Licensor and you, Licensor owns and retains all right, title, and interest in and to the Licensed Material subject to the license granted in Section 1.1. Your permission to use the Licensed Material is expressly conditioned on you not impairing Licensor's or the applicable copyright owner's rights in the Licensed Material in any way.

## 3. Restrictions on use

3. 1. Minor editing privileges are allowed for adaptations for stylistic purposes or formatting purposes provided such alterations do not alter the original meaning or intention of the Licensed Material and the new figure(s) are still accurate and representative of the Licensed Material. Any other changes including but not limited to, cropping, adapting, and/or omitting material that affect the meaning, intention or moral rights of the author(s) are strictly prohibited.

3. 2. You must not use any Licensed Material as part of any design or trademark.

3. 3. Licensed Material may be used in Open Access Publications (OAP), but any such reuse must include a clear acknowledgment of this permission visible at the same time as the figures/tables/illustration or abstract and which must indicate that the Licensed Material is not part of the governing OA license but has been reproduced with permission. This may be indicated according to any standard referencing system but must include at a minimum 'Book/Journal title, Author, Journal Name (if applicable), Volume (if applicable), Publisher, Year, reproduced with permission from SNCSC'.

## 4. STM Permission Guidelines

4. 1. An alternative scope of license may apply to signatories of the STM Permissions Guidelines ("STM PG") as amended from time to time and made available at <https://www.stm-assoc.org/intellectual-property/permissions/permissions-guidelines/>.

4. 2. For content reuse requests that qualify for permission under the STM PG, and which may be updated from time to time, the STM PG supersedes the terms and conditions contained in this License.

4. 3. If a License has been granted under the STM PG, but the STM PG no longer apply at the time of publication, further permission must be sought from the Rightsholder. Contact [journalpermissions@springernature.com](mailto:journalpermissions@springernature.com) or [bookpermissions@springernature.com](mailto:bookpermissions@springernature.com) for these rights.

## 5. Duration of License

5. 1. Unless otherwise indicated on your License, a License is valid from the date of purchase ("License Date") until the end of the relevant period in the below table:

Reuse in a medical communications project	Reuse up to distribution or time period indicated in License
Reuse in a dissertation/thesis	Lifetime of thesis
Reuse in a journal/magazine	Lifetime of journal/magazine
Reuse in a book/textbook	Lifetime of edition
Reuse on a website	1 year unless otherwise specified in the License
Reuse in a presentation/slide kit/poster	Lifetime of presentation/slide kit/poster. Note: publication whether electronic or in print of presentation/slide kit/poster may require further permission.
Reuse in conference proceedings	Lifetime of conference proceedings
Reuse in an annual report	Lifetime of annual report
Reuse in training/CME materials	Reuse up to distribution or time period indicated in License
Reuse in newsmedia	Lifetime of newsmedia
Reuse in coursepack/classroom materials	Reuse up to distribution and/or time period indicated in license

## 6. Acknowledgement

6. 1. The Licensor's permission must be acknowledged next to the Licensed Material in print. In electronic form, this acknowledgement must be visible at the same time as the figures/tables/illustrations or abstract and must be hyperlinked to the journal/book's homepage.

6. 2. Acknowledgement may be provided according to any standard referencing system and at a minimum should include "Author, Article/Book Title, Journal name/Book imprint, volume, page number, year, Springer Nature".

## 7. Reuse in a dissertation or thesis

7. 1. Where 'reuse in a dissertation/thesis' has been selected, the following terms apply: Print rights of the Version of Record are provided for; electronic rights for use only on institutional repository as defined by the Sherpa guideline ([www.sherpa.ac.uk/romeo/](http://www.sherpa.ac.uk/romeo/)) and only up to what is required by the awarding institution.

7. 2. For theses published under an ISBN or ISSN, separate permission is required. Please contact [journalpermissions@springernature.com](mailto:journalpermissions@springernature.com) or [bookpermissions@springernature.com](mailto:bookpermissions@springernature.com) for these rights.

7. 3. Authors must properly cite the published manuscript in their thesis according to current citation standards and include the following acknowledgement: *'Reproduced with permission from Springer Nature'*.

## 8. License Fee

You must pay the fee set forth in the License Agreement (the "License Fees"). All amounts payable by you under this License are exclusive of any sales, use, withholding, value added or similar taxes, government fees or levies or other assessments. Collection and/or remittance of such taxes to the relevant tax authority shall be the responsibility of the party who has the legal obligation to do so.

## 9. Warranty

9. 1. The Licensor warrants that it has, to the best of its knowledge, the rights to license reuse of the Licensed Material. **You are solely responsible for ensuring that the material you wish to license is original to the Licensor and does not carry the copyright of another entity or third party (as credited in the published version).** If the credit line on any part of the Licensed Material indicates that it was reprinted or adapted with permission from another source, then you should seek additional permission from that source to reuse the material.

9. 2. EXCEPT FOR THE EXPRESS WARRANTY STATED HEREIN AND TO THE EXTENT PERMITTED BY APPLICABLE LAW, LICENSOR PROVIDES THE LICENSED MATERIAL "AS IS" AND MAKES NO OTHER REPRESENTATION OR WARRANTY. LICENSOR EXPRESSLY DISCLAIMS ANY LIABILITY FOR ANY CLAIM ARISING FROM OR OUT OF THE CONTENT, INCLUDING BUT NOT LIMITED TO ANY ERRORS, INACCURACIES, OMISSIONS, OR DEFECTS CONTAINED THEREIN, AND ANY IMPLIED OR EXPRESS WARRANTY AS TO MERCHANTABILITY OR FITNESS FOR A PARTICULAR PURPOSE. IN NO EVENT SHALL LICENSOR BE LIABLE TO YOU OR ANY OTHER PARTY OR ANY OTHER PERSON OR FOR ANY SPECIAL, CONSEQUENTIAL, INCIDENTAL, INDIRECT, PUNITIVE, OR EXEMPLARY DAMAGES, HOWEVER CAUSED, ARISING OUT OF OR IN CONNECTION WITH THE DOWNLOADING, VIEWING OR USE OF THE LICENSED MATERIAL REGARDLESS OF THE FORM OF ACTION, WHETHER FOR BREACH OF CONTRACT, BREACH OF WARRANTY, TORT, NEGLIGENCE, INFRINGEMENT OR OTHERWISE (INCLUDING, WITHOUT LIMITATION, DAMAGES BASED ON LOSS OF PROFITS, DATA, FILES, USE, BUSINESS OPPORTUNITY OR CLAIMS OF THIRD PARTIES), AND WHETHER OR NOT THE PARTY HAS BEEN ADVISED OF THE POSSIBILITY OF SUCH DAMAGES. THIS LIMITATION APPLIES NOTWITHSTANDING ANY FAILURE OF ESSENTIAL PURPOSE OF ANY LIMITED REMEDY PROVIDED HEREIN.

## 10. Termination and Cancellation

10. 1. The License and all rights granted hereunder will continue until the end of the applicable period shown in Clause 5.1 above. Thereafter, this license will be terminated and all rights granted hereunder will cease.

10. 2. Licensor reserves the right to terminate the License in the event that payment is not received in full or if you breach the terms of this License.

**11. General**

11. 1. The License and the rights and obligations of the parties hereto shall be construed, interpreted and determined in accordance with the laws of the Federal Republic of Germany without reference to the stipulations of the CISG (United Nations Convention on Contracts for the International Sale of Goods) or to Germany's choice-of-law principle.

11. 2. The parties acknowledge and agree that any controversies and disputes arising out of this License shall be decided exclusively by the courts of or having jurisdiction for Heidelberg, Germany, as far as legally permissible.

11. 3. This License is solely for Licensor's and Licensee's benefit. It is not for the benefit of any other person or entity.

**Questions?** For questions on Copyright Clearance Center accounts or website issues please contact [springernaturesupport@copyright.com](mailto:springernaturesupport@copyright.com) or +1-855-239-3415 (toll free in the US) or +1-978-646-2777. For questions on Springer Nature licensing please visit <https://www.springernature.com/gp/partners/rights-permissions-third-party-distribution>

**Other Conditions:**

Version 1.4 - Dec 2022

**Questions?** [customercare@copyright.com](mailto:customercare@copyright.com).

---

---